ITMF # 76-42217

ANALYSIS OF AIRCRAFT WING-MOUNTED ANTENNA PATTERNS

R. J. Marhefka

TECHNICAL REPORT 2902-25

June 1976

Grant NGL 36-008-138

The material contained in this report is also used as a dissertation submitted to the Ohio State University Electrical Engineering Department as partial fulfillment of the requirements for the degree Doctor of Philosophy.

National Aeronautics and Space Administration
Langley Research Center
Hampton, Virginia 23665

ACKNOWLEDGMENT

The author would like to express his sincere gratitude to his graduate adviser, Professor R. C. Rudduck, for all the guidance and encouragement that he has provided. The assistance and cooperation of all his associates at the ElectroScience Laboratory are greatly appreciated. Deserving special recognition is Dr. W. D. Burnside for all his stimulating discussions and suggestions. Thanks must, also, be extended to Dr. P. H. Pathak and Dr. C. L. Yu for their help and ideas. Professor C. H. Walter and Professor L. Peters have been most helpful in their critical review of the author's manuscript.

The efforts of Messrs. G. Ryno and J. Huang of the Naval Weapons Center, China Lake, California; and Messrs. W. Croswell and M. Gilreath of the National Aeronautics and Space Administration, Langley Research Center in providing measured results on scale model aircraft are greatly appreciated.

ABSTRACT

The analysis of high frequency radiation patterns of aircraft wing mounted antennas is the object of this research. This is an analytical study of basic antenna types using ray optical techniques. The aircraft is modelled in its most basic form so that this study is applicable to general-type aircraft. The fuselage is modelled as a perfectly conducting finite elliptic cylinder. The wings and horizontal and vertical stabilizers are modelled as perfectly conducting "n" sided flat plates that can be arbitrarily attached to the fuselage or to themselves. Presently, the antenna locations are assumed to be on the surfaces of the wings at locations removed from engines and stores such that these effects are negligible. Volumetric patterns are calculated for several aircraft. The validity of the solution is shown by comparing the results against scale model measurements. The application of this solution to practical airborne antenna problems has shown its versatility in designing antennas and predicting their radiation patterns in an accurate and efficient manner.

TABLE OF CONTENTS

LIST OF TABLES

LIST OF FIGURES

Figure

Figure'

CHAPTER I
INTRODUCTION

In order for modern airborne antenna systems to function properly, the antenna pattern must meet certain specifications. In fact, system performance often is very much dependent on the pattern performance of the antenna. This requires the aircraft antenna designer to not only concern himself with the development of an antenna element for a particular application, but to also be concerned with the performance of the antenna system in the presence of the aircraft structure. The location of the antenna on the aircraft, and even the element design, is critical if a reliable antenna system is to be achieved. An efficient and economical means of predicting the pattern performance of an antenna is, therefore, desirable.

The object of this research is to analyze radiation patterns for wing mounted antennas at high frequency. Wing locations have become increasingly desirable for many applications, as the available real estate for antennas becomes more difficult to find because of the large number of antenna systems on a modern aircraft. This, then, is an analytical study of basic antenna types for frequencies above 100 megahertz in which the antenna is mounted on or near the wing.

The aircraft is modelled in its most basic form so that this study is applicable to general-type aircraft. The fuselage is modelled as a perfectly conducting finite elliptic cylinder. The wings and horizontal and vertical stabilizers are modelled as perfectly conducting "n" sided flat plates that can be arbitrarily attached to the fuselage or to themselves. Presently, the antenna locations are assumed to be on the upper surfaces of the wings or at locations removed from engines and stores such that these effects are negligible. The theory, however, is applicable to the addition of engine and store effects by modelling these structures as flat plates or small finite elliptic cylinders.

This type of analytic solution enables antenna designers to investigate an antenna system's performance in the presence of the aircraft structure using a computer simulation method, in a manner that can save a great deal of engineering time and money. This allows airborne antennas to be located on the aircraft at the design stage of the aircraft. This means that optimum locations and necessary structural changes can be anticipated. Also, a future relocation or addition of antennas on an aircraft within its useful lifetime can be easily accomplished. Once an optimum region is determined using computer simulation models of the aircraft, the antenna can be experimentally tested to ascertain its actual performance.

It is not uncommon for antennas to be allocated specific locations which are not related to electronic system requirements. Typically, these locations are chosen primarily for convenience with regard to aircraft structural specifications. Scale model measurements, then, are used to evaluate the performance of the antenna system in terms of its desired pattern. This approach can be very time consuming and costly.

The computer simulation method can, also, be used to determine optimum antenna designs for a given application. Various antenna types can be easily examined on the analytical models and the results compared. These analyses are based on arbitrarily-oriented electric and magnetic delta function sources which can be used to solve for the pattern of an arbitrary antenna simply by integrating over the equivalent aperture currents.

Three basic methods have been used to compute on-aircraft antenna patterns. Among the first methods used were the modal solutions for infinitely long circular [1,2] and elliptic [3] cylinders. These solutions modelled the fuselage by a cylinder whose cross-section approximated the fuselage cross-section at the antenna location. Arbitrary antennas were considered in these studies in which the antenna was mounted either on or over the fuselage. This method could not consider the effects of the other scattering structures of the aircraft such as the wings and stabilizers. The effects of these additional structures can be quite large, in general.

The second method for analysis of aircraft radiation patterns is primarily a low frequency technique. This approach uses a moment method technique to solve for the unknowns to an integral equation. The surface currents and resulting scattered fields can be found by enforcing the boundary conditions on the aircraft structures. One of the first moment solutions applied to aircraft problems was the wire grid technique, developed by Richmond [4], which employed a point matching technique [5]. This solution required the determination of approximately 100 unknown currents per square wavelength in order that the wire grid adequately model the perfectly conducting surface. Richmond [6] has developed a more sophisticated approach in which the reaction technique is used to solve for the unknown currents. This solution still requires approximately 100 unknown currents per square wavelength. Another approach is to divide the surface of the conducting body into patches each having two orthogonal unknown complex currents [7]. This surface-current approach reduces the unknown currents to about 20 per square wavelength. This allows a larger surface to be considered. However, all these solutions are restricted to low frequencies due to the limitation on the size of matrices which modern computers can solve without excessive loss of accuracy.

The approach that has been taken in this study is the Geometrical Theory of Diffraction (GTD). This is basically a high frequency method that is applied in terms of two characteristic problems; these being wedge diffraction and curved surface diffraction. The wedge diffraction solution has been applied to determine the radiation patterns of such basic antennas as parallel plate antennas [8,9,10], parallel plate arrays [11,12], horn antennas [13,14], parabolic reflectors [15,16], and rectangular waveguide antennas [17]. Both of these types of diffraction solutions have been applied in computing the patterns of antennas mounted on cylinders [18,19,20] and rockets [21]. GTD has also been successfully applied to a number of problems involving antennas mounted on the fuselage of aircraft [22-30]. Antennas mounted on various isolated wing structures have been analyzed [31,32], however, these did not include the effects of the fuselage and other structures.

Using this approach, one applies a ray optics technique to determine components of the field incident on various scatterers. Components of the diffracted field are found using the GTD solutions in terms of rays which are summed with the geometrical optics terms in the far field. The rays from a given scatterer tend to interact with the other structures causing various higher order terms. In this way one can trace out the various possible combinations of rays that interact between scatterers and determine and include only the dominant terms. Thus, one need only be concerned with the important scattering components and neglect all other higher-order terms. This makes the GTD approach ideal for a general high frequency study of aircraft antennas in that only the most basic structural features of the aircraft need to be modelled.

Since GTD is essentially a high frequency solution, the lower frequency limit of this solution is dictated by the spacings between the various scattering centers. In practice, this means that the scattering centers should be greater than approximately a half-wavelength apart. In some cases even this requirement can be relaxed. For a general type aircraft, therefore, the low frequency limit will be around 100 MHz. The upper frequency limit is dependent on how well the theoretical model simulates the important details of the actual structure.

The basic approach applied in this study of antennas mounted on the wings of aircraft is to separately analyze the basic scattering shapes making up the computer simulated model of an aircraft. The single structures are analyzed using the ray optics approach such that only the dominant effects are included. The scattered fields of the various component parts of the structure are found using the Geometrical Theory of Diffraction. The basic solutions needed for this study are briefly discussed in Chapter II. This includes geometrical optics reflected fields from curved surfaces, the diffraction by a wedge and curved wedge, and the slope diffraction by a wedge using arbitrarily oriented dipole moment sources. A heuristic corner diffraction coefficient is also introduced. Curved surface diffraction is presented along with a newly developed transition function for the shadow boundaries of curved surfaces.

Chapter III describes the scattering from a number of finite flat plates. They can have an arbitrary orientation in space and can be attached to form bent plates. These plates are used to model the wings, horizontal and vertical stabilizers.

Chapter IV describes the scattering from a finite elliptic cylinder. This is used to model the fuselage and can be used to model engines and stores.

The complete aircraft model is described in Chapter V. The dominant scattering terms due to the interaction of the plates and cylinder are discussed. The analytic results are compared against scale model measurements to determine the validity of the approximations made in the analysis. Finally, a summary of the present study and a discussion of future topics are made in Chapter VI.

CHAPTER II

THEORETICAL BACKGROUND

A. Introduction

The analytical modelling of an aircraft to predict the radiation patterns of antennas mounted on the wings has been accomplished by the use of the Geometrical Theory of Diffraction (GTD). This is a high frequency technique that allows a complicated structure to be approximated by basic shapes representing canonical problems in the GTD. These shapes include flat and curved wedges and convex curved surfaces. The GTD is a ray optical technique and it therefore allows one to gain some physical insight into the various scattering and diffraction mechanisms involved. Consequently, one is able to quickly seek out the dominant or significant scattering and diffraction mechanism for a given geometrical configuration. This, in turn, leads to an accurate engineering solution to practical antenna problems. The basic GTD solutions needed are discussed in this chapter. These solutions are applied to specific structural scattering problems in the following chapters.

Two of the basic diffraction problems are illustrated in Figures 1a and b. In the format of GTD, the total electric field may be represented as

$$\overline{E} = \overline{E}^i u^i + \overline{E}^r u^r + \overline{E}^d \quad .$$

The field $\overline{E}^i$ is the electric field of the source in the absence of the surfaces. The field $\overline{E}^r$ is the electric field reflected from the surfaces. The field $\overline{E}^d$ is the diffracted field from the discontinuities of the structure, such as edges, corners, curved surfaces, etc. The step functions u^i and u^r are shown to emphasize the discontinuity in the incident and reflected fields at the incident and reflection shadow boundaries. They are one in their lit regions and zero in their shadow regions. The extent of the regions are determined by geometrical optics. The surfaces used in this report are perfectly conducting and the surrounding medium is free space. An exp $(j\omega t)$ time dependence is assumed throughout and suppressed.

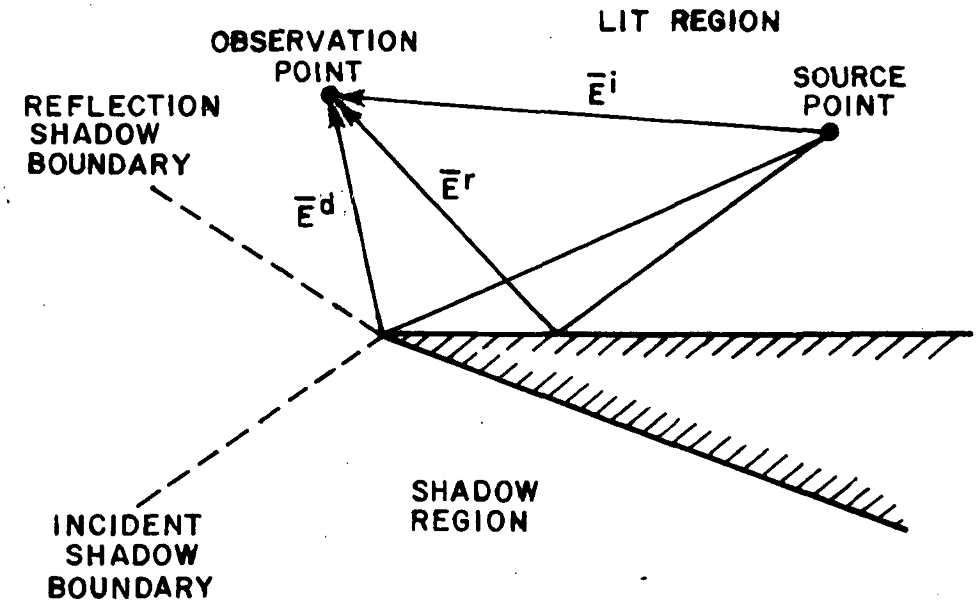

(a) BASIC WEDGE PROBLEM

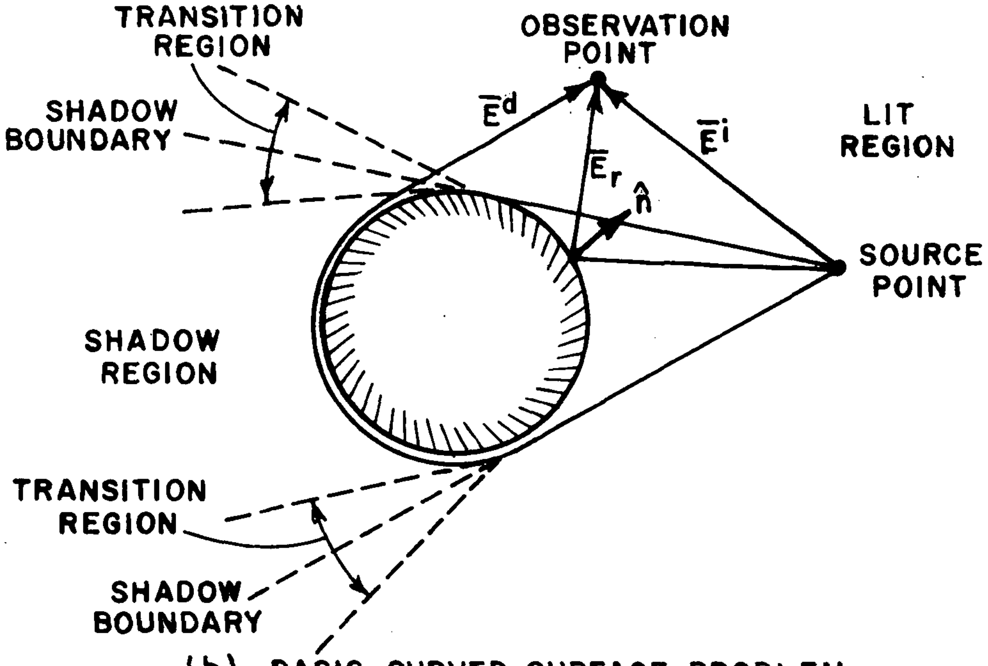

(b) BASIC CURVED SURFACE PROBLEM

Figure 1--Basic diffraction problems.

B. Geometrical-Optics Fields

The incident electric field $\overline{E}^i$ can be produced by an arbitrary electric or magnetic source causing plane, cylindrical, conical, or spherical wave incidence on the scattering structures. In this report the spherical wave case is treated. The far field pattern of the source can be written as

$$\overline{E}^i(\theta,\phi) = [\hat{\theta}F(\theta,\phi) + \hat{\phi}G(\theta,\phi)]\,\frac{e^{-jks}}{s} \quad . \tag{1}$$

The reflected electric field from a curved surface S as shown in Figure 2 is given in terms of geometrical optics by

$$\overline{E}^r(s) = \overline{E}^i(Q_R) \cdot \overline{\overline{R}}\sqrt{\frac{\rho_1^r\rho_2^r}{(\rho_1^r+s)(\rho_2^r+s)}}\; e^{-jks} , \tag{2}$$

where $\overline{E}^i(Q_R)$ is the incident electric field at the point of reflection Q_R and $\overline{\overline{R}}$ is the dyadic reflection coefficient such that

$$\overline{\overline{R}} = \hat{e}_\parallel^i\,\hat{e}_\parallel^r - \hat{e}_\perp\hat{e}_\perp \quad . \tag{3}$$

The vector $\hat{e}_\perp$ is the unit vector perpendicular to the plane of incidence and $\hat{e}_\parallel^i$ and $e_\perp^r$ are the unit vectors parallel to the plane of incidence. The point of reflection Q_R is found from the laws of reflection that state that the angle of incidence is equal to the angle of reflection that is

$$-\hat{I} \cdot \hat{n} = \hat{s} \cdot \hat{n} \tag{4a}$$

and that the incident, reflected, and surface normal vectors must lie in the same plane or in other words

$$\hat{I} \times \hat{n} = \hat{s} \times \hat{n}. \tag{4b}$$

The quantities ρ_1^r and ρ_2^r are the principal radii of curvature of the reflected wavefront at the reflection point Q_R. Kouyoumjian [34] discusses how to find these values for an arbitrary wavefront by diagonalizing the curvature matrix for the reflected wavefront given by Deschamps [35]. Let a wavefront be incident on a curved surface S at Q_R as shown in Figure 2. $\hat{e}_1$ and $\hat{e}_2$ are unit vectors in the principal directions of S at Q_R with principal radii of curvature R_1 and R_2. $\hat{X}_1^i$ and $\hat{X}_2^i$ are the principal directions of

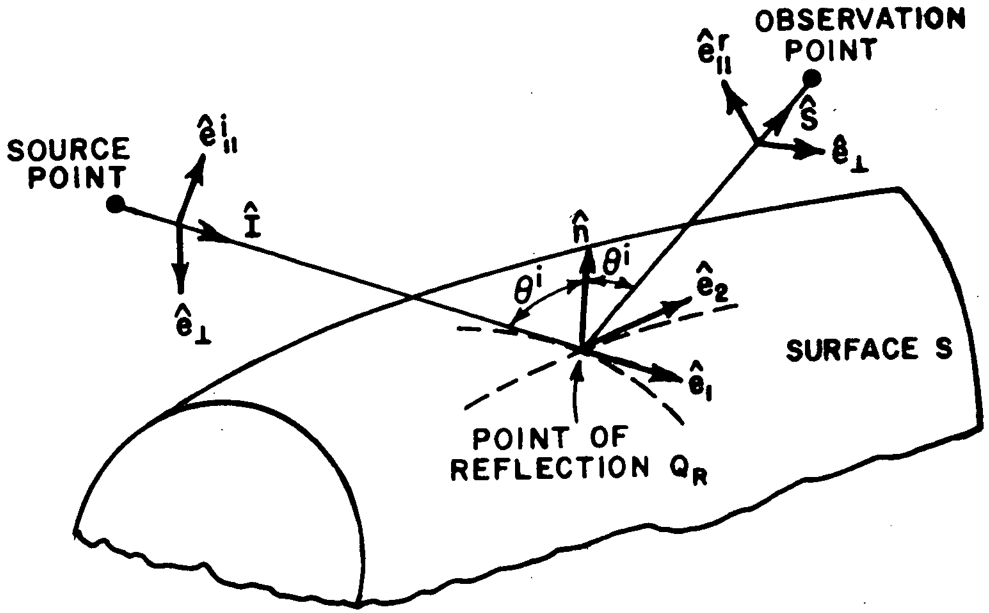

Figure 2--Reflection by a smooth convex surface.

the incident wavefront at Q_R with principal radii of curvature ρ^i_1 and ρ^i_2. The principal radii of curvature of the reflected wave are given by

$$\frac{1}{\rho^r_{1,2}} = \frac{1}{2}\left(\frac{1}{\rho^i_1} + \frac{1}{\rho^i_2}\right) + \frac{\cos\theta^i}{|\theta|^2}\left[\frac{\theta^2_{22}+\theta^2_{12}}{R_1} + \frac{\theta^2_{21}+\theta^2_{11}}{R_2}\right]$$

$$\pm \frac{1}{2}\left\{\left(\frac{1}{\rho^i_1} - \frac{1}{\rho^i_2}\right)^2 + \left(\frac{1}{\rho^i_1} - \frac{1}{\rho^i_2}\right)\frac{4\cos\theta^i}{|\theta|^2}\left[\frac{\theta^2_{22}-\theta^2_{12}}{R_1} + \frac{\theta^2_{21}-\theta^2_{11}}{R_2}\right]\right.$$

$$\left. + \frac{4\cos^2\theta^i}{|\theta|^4}\left[\left(\frac{\theta^2_{22}+\theta^2_{12}}{R_1} + \frac{\theta^2_{21}+\theta^2_{11}}{R_2}\right)^2 - \frac{4|\theta|^2}{R_1R_2}\right]\right\}^{1/2} \quad (5)$$

in which the plus sign is associated with ρ_1^r and the minus sign with ρ_2^r and where

$$\theta_{jk} = \hat{X}_j^i \cdot \hat{e}_k \tag{6a}$$

$$|\theta| = \theta_{11}\theta_{22} - \theta_{12}\theta_{21} \ . \tag{6b}$$

The principal directions of the principal radii of curvature of the reflected wavefront are given by

$$\hat{X}_1^r = \frac{\left[\left(Q_{22}^r - \frac{1}{\rho_1^r}\right)\hat{x}_1^r - Q_{12}^r\,\hat{x}_2^r\right]}{\sqrt{\left(Q_{22}^r - \frac{1}{\rho_1^r}\right)^2 + (Q_{12}^r)^2}} \tag{7a}$$

$$\hat{X}_2^r = -\hat{s} \times \hat{X}_1^r \tag{7b}$$

where

$$\hat{x}_{1,2}^r = \hat{X}_{1,2}^i - 2(\hat{n} \cdot \hat{X}_{1,2}^i)\hat{n} \tag{8}$$

and

$$Q_{11}^r = \frac{1}{\rho_1^i} + \frac{2\cos\theta^i}{|\theta|^2}\left[\frac{\theta_{22}^2}{R_1} + \frac{\theta_{21}^2}{R_2}\right] \tag{9a}$$

$$Q_{12}^r = \frac{-2\cos\theta^i}{|\theta|^2}\left[\frac{\theta_{22}\theta_{12}}{R_1} + \frac{\theta_{11}\theta_{21}}{R_2}\right] \tag{9b}$$

$$Q_{22}^r = \frac{1}{\rho_2^i} + \frac{2\cos\theta^i}{|\theta|^2}\left[\frac{\theta_{12}^2}{R_1} + \frac{\theta_{11}^2}{R_2}\right] \ . \tag{9c}$$

If the incident wavefront is spherical, the equations for the principal radii of curvature of the reflected wavefront are given by

$$\frac{1}{\rho^r_{1,2}} = \frac{1}{s'} + \frac{1}{\cos\theta^i}\left[\frac{\sin^2\theta_2}{R_1} + \frac{\sin^2\theta_1}{R_2}\right]$$
$$\pm\sqrt{\frac{1}{\cos^2\theta^i}\left[\frac{\sin^2\theta_2}{R_1} + \frac{\sin^2\theta_1}{R_2}\right]^2 - \frac{4}{R_1R_2}} \qquad (10)$$

where s' is the radius of curvature of the incident wavefront at Q_R, θ_1 is the angle between the direction of the incident ray $\hat{I}$ and unit vector $\hat{e}_1$ and θ_2 is the angle between the direction of the incident ray $\hat{I}$ and unit vector $\hat{e}_2$.

C. Diffraction by a Wedge

The wings, vertical and horizontal stabilizers on an aircraft can be approximated as flat plates. The Geometrical Theory of Diffraction provides a means of including the three-dimensional effects of the flat plates with straight edges by the use of wedge diffraction. This section briefly discusses this basic diffraction problem.

An asymptotic solution for the diffraction from a conducting wedge was first solved by Sommerfeld [36]. Originally, GTD [37] as applied to diffraction by a wedge was based on plane wave diffraction coefficients; however, as shown in Reference [38] the use of cylindrical wave diffraction coefficients has been found necessary in the treatment of antennas. Consequently, different formulations of wedge diffraction were substituted for the plane wave diffraction coefficient which is the basis for wedge diffraction theory. Pauli [39] introduced the V_B function as a practical formulation to the solution for a finite-angle conducting wedge. Hutchins and Kouyoumjian [40,41], however, have presented a formula for the diffracted field, which significantly improves the accuracy over that obtained from Pauli's form.

This improved diffraction solution [40,41] is better in the transition regions (near the incident and reflected shadow boundaries). It can be written in the form

$$V_B(L,\beta,n) = I_{-\pi}(L,\beta,n) + I_{+\pi}(L,\beta,n)$$

where

$$I_{\pm\pi}(L,\beta,n) \sim \frac{e^{-j(kL+\pi/4)}}{jn\sqrt{2\pi}}\sqrt{a}\,\cos\left(\frac{\pi\pm\beta}{2n}\right)$$

$$\times\ e^{jkLa}\int_{\sqrt{kLa}}^{\infty} e^{-j\tau^2}\,d\tau + [\text{higher order terms}]$$

and where the higher order terms are negligible for large kL and with n defined from the wedge angle WA = $(2-n)\pi$, also

$a = a^{\pm} = 1 + \cos(\beta-2n\pi N^{\pm})$ and

$N^{\pm}$ is a positive or negative integer or zero, whichever most nearly satisfies the equations

$2n\pi N^{-} - \beta = -\pi$ for $I_{-\pi}$

$2n\pi N^{+} - \beta = +\pi$ for $I_{+\pi}$.

The variables L and β are defined below.

The three-dimensional wedge diffraction problem is pictured in Figure 3. A source whose radiated $\overline{E}$ field is given by $\overline{E}^{i}(s)$ is located at point $s'(\rho',\phi',z')$. It can be an arbitrary electric or magnetic source causing plane, cylindrical, conical, or spherical wave incidence on the wedge top. The diffracted vector field at point $s(\rho,\phi,z)$ can be written in terms of a dyadic diffraction coefficient. Kouyoumjian and Pathak [42] have given a more rigorous basis for the GTD formulation and have shown that the diffracted fields may be written compactly if they are in terms of a ray-fixed coordinate system. The ray-fixed coordinate system is centered at the point of diffraction Q_E, (or points of diffraction in the case of plane wave incidence). Q_E is a unique point or points for a given source and observation point. The incident ray diffracts as a cone of rays such that $\beta_o = \beta_o'$ (see Figure 3).

The relationships between the orthogonal unit vectors associated with these coordinates $(\hat{s}',\hat{\beta}_o',\hat{\phi}';\hat{s},\hat{\beta}_o,\hat{\phi})$ are given by

$\hat{I} = -\hat{s}'$

$\hat{I} = \hat{\beta}_o' \times \hat{\phi}'$

$\hat{s} = \hat{\beta}_o \times \hat{\phi}$,

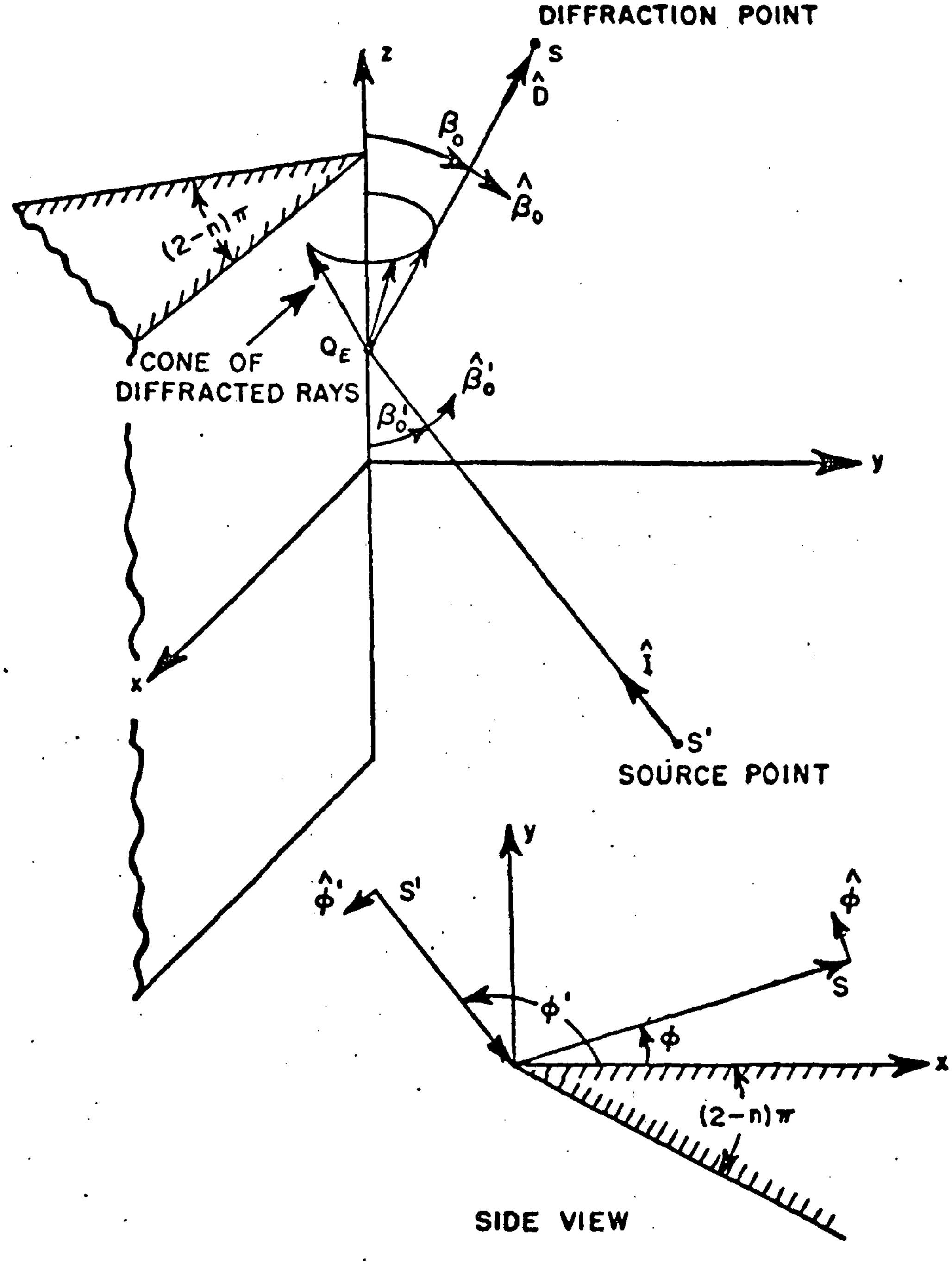

Figure 3--Geometry for three-dimensional wedge diffraction problem.

where $\hat{I}$ is the incident direction unit vector, and $\hat{s}$ is the diffraction direction unit vector. The diffracted field is now given by

$$\overline{E}^d(s) \sim \overline{E}^i(Q_E) \cdot \overline{\overline{D}}_E(\hat{s},\hat{I})A(s)e^{-jks} \tag{11}$$

where

$$\overline{\overline{D}}_E = -\hat{\beta}_o'\hat{\beta}_o D_s - \hat{\phi}'\hat{\phi} D_h$$

and

$$\begin{aligned} D_{s,h}(\phi,\phi',\beta_o) = \frac{-e^{-j\pi/4}}{2n\sqrt{2\pi k}\,\sin\beta_o}\Bigg[&\cot\left(\frac{\pi+\beta^-}{2n}\right)F[kLa^+(\beta^-)] \\ &+ \cot\left(\frac{\pi-\beta^-}{2n}\right)F[kLa^-(\beta^-)] \\ &\mp\left\{\cot\left(\frac{\pi+\beta^+}{2n}\right)F[kLa^+(\beta^+)] + \cot\left(\frac{\pi-\beta^+}{2n}\right)F[kLa^-(\beta^+)]\right\}\Bigg] \end{aligned} \tag{12}$$

and

$$F(X) = 2j\left|\sqrt{X}\right|e^{jX}\int_{\left|\sqrt{X}\right|}^{\infty} e^{-j\tau^2}\,d\tau \tag{13}$$

is called the transition function. This can be shown to be related to the V_B function for a straight wedge as

$$D_{s,h}(\phi,\phi',\beta_o) = [V_B(L,\beta^-) \mp V_B(L,\beta^+)]\,\frac{\sqrt{L}\,e^{jkL}}{\sin\beta_o} \quad .$$

In matrix notation this can be written as

$$\begin{bmatrix} E_{\parallel}^{d}(s) \\ \\ E_{\perp}^{d}(s) \end{bmatrix} \sim \begin{bmatrix} -D_s & 0 \\ \\ 0 & -D_h \end{bmatrix} \begin{bmatrix} E_{\parallel}^{i}(Q_E) \\ \\ E_{\perp}^{i}(Q_E) \end{bmatrix} A(s)e^{-jks}$$

The D_S coefficient (minus sign between V_B terms) applies for the $\overline{E}$-field component parallel to the edge with the boundary condition (acoustically soft)

$$(\overline{E}|_{\text{wedge}}) = 0.$$

The D_h coefficient (plus sign between V_B terms) applies for the $\overline{E}$-field vector perpendicular to the edge with the boundary conditions (acoustically hard)

$$\left(\frac{\partial \overline{E}}{\partial \overline{n}}\bigg|_{\text{wedge}}\right) = 0.$$

The angular relations are expressed by

$$\beta = \beta^{\mp} = \phi \mp \phi' \ .$$

The ϕ-ϕ' terms are associated with the incident field and the $\phi+\phi'$ terms are associated with the reflected field. The quantity A(s) is a ray divergent factor given in general by [34]

$$A(s) = \sqrt{\frac{\rho}{s(\rho+s)}}$$

where for a wedge $\rho = \rho_e^i$ which is the radius of curvature of the incident wavefront in the plane containing the incident ray and the edge. For some specific problems this is given by

$$A(s) = \begin{cases} \dfrac{1}{\sqrt{s}} & \text{plane, cylindrical } (s=\rho)\text{, and conical wave incidence} \\ \sqrt{\dfrac{s'}{s(s'+s)}} & \text{spherical wave incidence.} \end{cases}$$

The quantity L is a distance parameter for a straight wedge given in general for a straight wedge by [34]

$$L = \frac{s(\rho_e^i+s)\rho_1^i\rho_2^i \sin^2\beta_o}{\rho_e^i(\rho_1^i+s)(\rho_2^i+s)} \tag{14}$$

where ρ_1^i, ρ_2^i are the principal radii of curvature of the incident wavefront. For some specific problems this is given by

$$L = \begin{cases} s \sin^2\beta_o & \text{plane wave incidence} \\ \frac{\rho'\rho}{\rho+\rho'} & \text{cylindrical wave incidence} \\ \frac{s's \sin^2\beta_o}{s+s'} & \text{conical and spherical wave incidence.} \end{cases}$$

At grazing incidence, that is when $\phi' = 0$, the expression for D_h and D_s must be multiplied by a factor of 1/2, this comes about because the incident and reflected field merge together and only one-half the total field on the surface is the incident field, the other half is associated with the reflected field.

D. Slope Diffraction by a Wedge

The diffraction coefficient discussed in Section C is only valid for incident fields on an edge that are slowly varying in amplitude. If this is not true, as when a dipole is aligned such that its axis points in the direction of the edge, an additional term is needed that relates the diffracted field to the spatial derivative of the incident field. This term is referred to as the slope diffracted field.

Rudduck and Wu [43] have previously obtained a slope diffracted solution (V_s) for the two dimensional general wedge for the hard boundary condition by differentiating the eigenfunction solution. Karp and Keller [44] first introduced the GTD slope diffracted field; however, this result is not valid at or near the shadow boundary. Recently Mentzer, Peters, and Rudduck [45] obtained a two-dimensional slope diffraction function for the special case of the half plane by differentiating the exact solution given by Sommerfeld. They applied this to horn antennas. Kouyoumjian and Hwang [46,47] have extended the results of Reference [44] such that Equation (15) is now valid even within the transition region adjacent to shadow boundaries. The result presented here is for the diffraction coefficient for the straight wedge case given in Equation (12).

This dyadic slope diffracted field for a dipole whose axis is directed radially toward the edge, that is, such that the amplitude of the incident field is zero at the edge but with a finite incident slope is given by [46,47]

$$\bar{E}^d \sim \frac{\partial \bar{E}^i(Q_E)}{\partial n} \; \frac{1}{jk} \cdot \frac{\partial \bar{\bar{D}}_E}{\partial \phi'} A(s)e^{-jks} \tag{15}$$

where

$$\frac{\partial \bar{\bar{D}}_E}{\partial \phi'} = -\hat{\beta}_o'\hat{\beta}_o \frac{\partial D_s}{\partial \phi'} - \hat{\phi}'\hat{\phi} \frac{\partial D_h}{\partial \phi'} .$$

The slope diffraction coefficient is explicitly given by

$$\frac{\partial D_{s,h}}{\partial \phi'} = -\frac{e^{-j\frac{\pi}{4}}}{4n^2\sqrt{2\pi k}\,\sin^2\beta_o}\left\{\left[\csc^2\left(\frac{\pi+\beta^-}{2n}\right)F_s(kLa^+(\beta^-))\right.\right.$$

$$\left. -\csc^2\left(\frac{\pi-\beta^-}{2n}\right)F_s(kLa^-(\beta^-))\right]$$

$$\left.\pm\left[\csc^2\left(\frac{\pi+\beta^+}{n}\right)F_s(kLa^+(\beta^+)) - \csc^2\left(\frac{\pi-\beta^+}{2n}\right)F_s(kLa^-(\beta^+))\right]\right\}$$

where $\beta^{\mp}$ and $a^{\mp}$ are defined as in Section C and

$$F_s(X) = 2jX + 4X^{3/2}e^{jX}\int_{|\sqrt{X}|}^{\infty} e^{-j\tau^2}d\tau$$

or

$$F_s(X) = 2jX[1 - F(X)]$$

with F(X) defined as in Equation (13).

The partial derivative of the incident field ($\partial/\partial n$) is defined as the derivative taken in the direction normal to the edge-fixed plane of incidence. A very important source type to be considered for general application is the arbitrarily oriented electric and magnetic dipole moment which can be expressed by

$$\hat{u}' p_{\substack{e\\m}} \delta(|s-s'|).$$

Any general source can be approximated by superimposing a weighted set of these dipole moment elements to obtain a sufficiently accurate result for engineering purposes [48].

If the dipole moment has an arbitrary orientation in space with respect to the wedge, the ordinary diffraction effects and the slope diffraction effects should both be considered for completeness. In matrix notation, this may be written, assuming a spherical wavefront incidence, as

$$\begin{bmatrix} E_{\parallel}^{d}(s) \\ \\ E_{\perp}^{d}(s) \end{bmatrix} \sim \begin{bmatrix} -D_s - \frac{1}{jk}\frac{\partial D_s}{\partial \phi'}\frac{\partial}{\partial n} & 0 \\ \\ 0 & -D_h - \frac{1}{jk}\frac{\partial D_h}{\partial \phi'}\frac{\partial}{\partial n} \end{bmatrix} \begin{bmatrix} E_{\parallel}^{i}(Q_E) \\ \\ E_{\perp}^{i}(Q_E) \end{bmatrix}$$

$$\text{x}\sqrt{\frac{s'}{s(s+s')}}\; e^{-jks}. \qquad (16)$$

The dipole moment producing the incident field can be decomposed into three components in the ray-fixed coordinate system. Thus

$$\hat{u}'\, p_{\substack{e\\m}} = p_{\substack{e\\mI}}\, \hat{I} + p_{\substack{e\\m\beta_o'}}\, \hat{\beta}_o' + p_{\substack{e\\m\phi'}}\, \hat{\phi}'$$

where

$$p_{\substack{e\\m}I} = \hat{I} \cdot \hat{u}'\, p_{\substack{e\\m}}$$

$$p_{\substack{e\\m}\beta'_o} = \hat{\beta}'_o \cdot \hat{u}' \, p_{\substack{e\\m}}$$

$$p_{\substack{e\\m}\phi'} = \hat{\phi}' \cdot \hat{u}' \, p_{\substack{e\\m}} \, .$$

The electric field of an electric dipole moment (TM case) can be written in the far field as

$$E^i_{\theta_p} = \eta jk \, p_e \sin \theta_p \frac{e^{-jks}}{4\pi s}$$

where η is the impedance of surrounding media. The far field electric field of a magnetic dipole moment (TE case) can be written as

$$E^i_{\phi_p} = -jk \, p_m \sin \theta_p \frac{e^{-jks}}{4\pi s}$$

where θ_p, ϕ_p are measured with respect to the dipole coordinate system. The non-zero incident fields needed to compute the diffracted field for the electric dipole moment case are

$$E^i_{\parallel} = \hat{\beta}' \cdot \overline{E}^i = \eta jk \, p_{e\beta'} \frac{e^{-jks'}}{4\pi s'}$$

$$E^i_{\perp} = \hat{\phi}' \cdot \overline{E}^i = \eta jk \, p_{e\phi'} \frac{e^{-jks'}}{4\pi s'}$$

$$\frac{\partial E^i_{\perp}}{\partial n} = \phi' \cdot \frac{\partial \overline{E}^i}{\partial n} = \eta jk \, p_{e_I} \frac{e^{-jks'}}{4\pi s'^2} \, .$$

The non-zero incident fields needed to compute the diffracted fields for the magnetic dipole moment case are

$$E_{\parallel}^{i} = \hat{\beta}' \cdot \overline{E}^{i} = -jk\ p_{m\phi'} \frac{e^{-jks'}}{4\pi s'}$$

$$E_{\perp}^{i} = \hat{\phi}' \cdot \overline{E}^{i} = -jk\ p_{m\beta'} \frac{e^{-jks'}}{4\pi s'}$$

$$\frac{\partial E_{\parallel}^{i}}{\partial n} = \hat{\beta}' \cdot \frac{\partial \overline{E}^{i}}{\partial n} = -jk\ p_{mI} \frac{e^{-jks'}}{4\pi s'^{2}} \quad .$$

The above fields may be used in Equation (16) to give the diffracted fields from the edge.

E. Diffraction by a Curved Wedge

The fuselage of a general aircraft is to be modelled in this report as a finite elliptic cylinder. The ends of the cylinder are formed by a flat surface and the elliptic cylinder surface with a resulting curved edge at their junction. The diffracted field due to this curved wedge is analyzed using the GTD techniques developed by Kouyoumjian and Pathak [34].

The curved wedge problem is illustrated in Figure 4. The diffracted field from the curved wedge may be written in the form

$$\overline{E}^{d}(s) \sim \overline{E}^{i}(Q_E) \cdot \overline{\overline{D}}_E(\hat{s},\hat{I}) \sqrt{\frac{\rho}{s(\rho+s)}}\ e^{-jks} \ . \tag{17}$$

The parameter ρ is the distance between the caustic at the edge and the second caustic of the diffracted ray. This is given by

$$\frac{1}{\rho} = \frac{1}{\rho_e^i} - \frac{\hat{n}_e \cdot (\hat{I} - \hat{s})}{a_e \sin^2\beta_o} \tag{18}$$

where ρ_e^i, $\hat{n}_e$, a_e are defined below. The diffraction coefficients for the curved wedge are extended from those in Equation (12) to allow the diffracted field to be continuous at the incident and reflected shadow boundaries. This is accomplished by finding the appropriate distance parameters L in each of the transition functions that make the field continuous. The diffraction coefficient for the curved wedge is given by

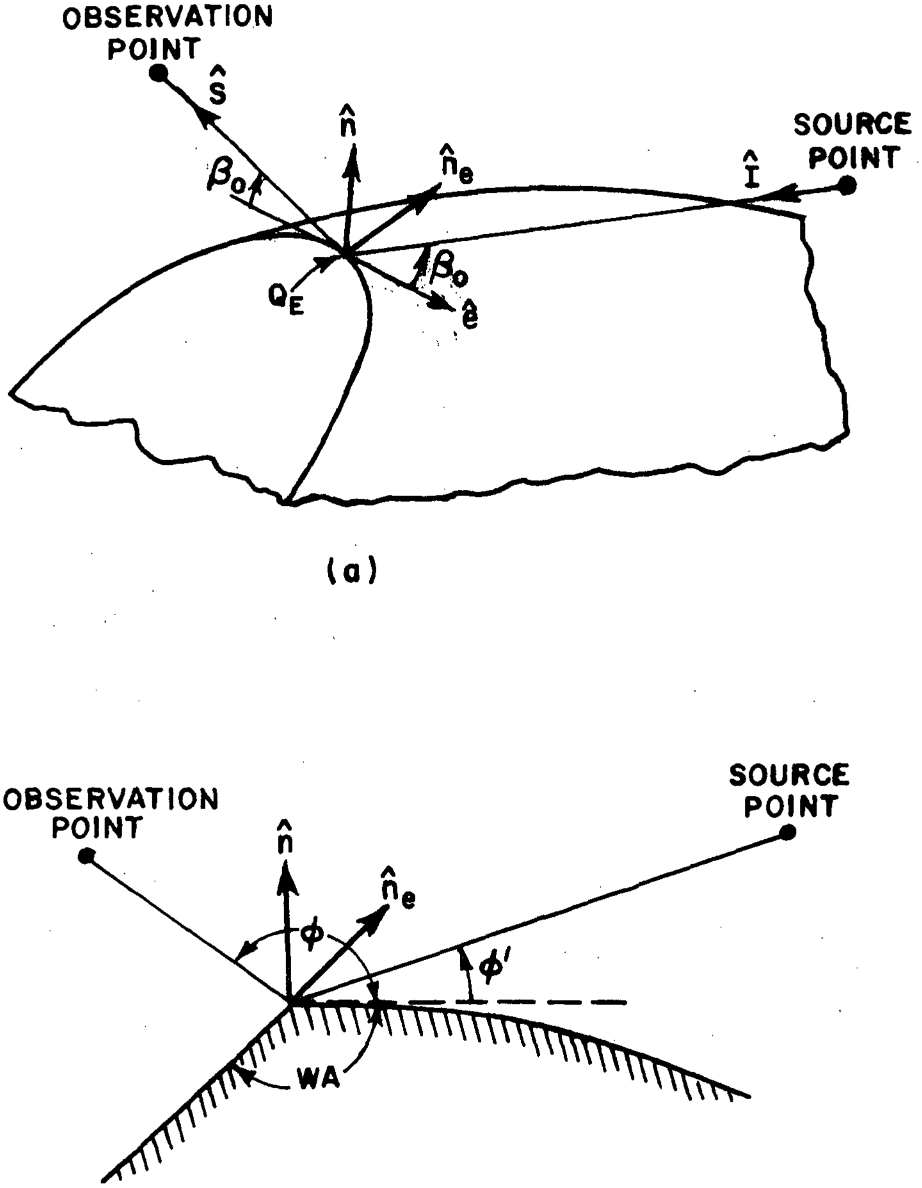

(a)

(b) PLANE PERPENDICULAR TO $\hat{e}$ AT Q_E

Figure 4--Geometry for three-dimensional curved wedge diffraction problem.

$$D_{s,h}(\phi,\phi',\beta_o) = \frac{e^{-j\pi/4}}{2n\sqrt{2\pi k}\,\sin\beta_o}\left[\frac{2\sin\frac{\pi}{n}\,F[kL^{i}a(\beta^{-})]}{\cos\left(\frac{\pi}{n}\right)-\cos\left(\frac{\beta^{-}}{n}\right)}\right.$$

$$\pm\left\{\cot\left(\frac{\pi+\beta^{+}}{2n}\right)F[kL^{rn}a^{+}(\beta^{+})]\right.$$

$$\left.\left.+\cot\left(\frac{\pi-\beta^{+}}{2n}\right)F[kL^{ro}a(\beta^{+})]\right\}\right] \qquad (19)$$

in which $a(\beta) = 2\cos^2 \beta/2$ and $a^+(\beta) = 2\cos^2 \frac{(2\pi n-\beta)}{2}$. The distance parameter associated with the incident field is given by

$$L^i = \frac{s(\rho_e^i+s)\rho_1^i\rho_2^i\sin^2\beta_o}{\rho_e^i(\rho_1^i+s)(\rho_2^i+s)} \quad . \qquad (20a)$$

The distance parameter associated with the reflected field from the surface with superscript 0 (reflection boundary at $\pi-\phi'$) and the reflected field from the surface with superscript n (reflection boundary $(2n-1)\pi-\phi'$) is given by

$$L^r = \frac{s(\rho_e^r+s)\rho_1^r\rho_2^r\sin^2\beta_o}{\rho_e^r(\rho_1^r+s)(\rho_2^r+s)} \quad . \qquad (20b)$$

The parameters ρ_1^i and ρ_2^i are the principal radii of curvature of the incident wavefront at the diffraction point Q_E. The parameter ρ_e^i is the radius of curvature of the incident wavefront at Q_E taken in the plane containing the incident ray and $\hat{e}$ the unit vector tangent to the edge at Q_E. In the case of plane, cylindrical, and conical waves ρ_e^i is infinite and for the case of spherical waves $\rho_e^i=s'$. The parameters ρ_1^r and ρ_2^r are the principal radii of curvature of the reflected wavefront at Q_E, which may be found from Equation (10) for spherical wavefront incidence. The parameter ρ_e^r is the radius of curvature of the reflected wavefront at Q_E taken in the plane containing the reflected ray and $\hat{e}$ the unit vector tangent to the edge at Q_E. This can be found from the expression

$$\frac{1}{\rho_e^r} = \frac{1}{\rho_e^i} - \frac{2(\hat{n}\cdot\hat{n}_e)(\hat{I}\cdot\hat{n})}{a_e \sin^2\beta_o} \tag{21}$$

where $\hat{n}$ is the unit normal to the surface at Q_E, $\hat{n}_e$ is the associated unit normal to the edge directed away from the center of curvature, and $a_e>0$ is the radius of curvature of the edge at Q_E.

A slope wave term can be found for the curved wedge problem; however, for the geometries involved with wing mounted antennas this term does not appear to be a significant contributor to the total scattered field so it will not be used in this study.

F. Diffraction by a Corner

The wings of aircraft are modelled in this study as flat plates. These plates can be thought of as being composed of a series of finite straight edges that join together at the corners of the plate. The diffraction of energy from these edges, as discussed in Section C, is based on diffraction from infinite straight edges. To compensate for the finiteness of the edges, a diffraction coefficient associated with the corners of the plates is needed.

An eigenfunction solution for the scattering from the corner of wedges has been derived by Satterwhite [49]. This solution is extremely cumbersome for numerical calculations. A GTD diffraction coefficient is needed that is numerically efficient in order for the corner effect to be of any practical use in complicated modelling problems. Burnside and Pathak [50] have recently proposed a solution based on the asymptotic evaluation of the radiation integral which employs the equivalent edge currents that would exist in the absence of the corners. The corner diffraction term is then found by appropriately (but presently heuristically) modifying the asymptotic result for the radiation integral which is characterized by a saddle point near an end point. This diffraction coefficient is still in the beginning stages of its development. However, it has been shown to be useful in eliminating discontinuities in the total field associated with the corner effect. For this reason, it is briefly discussed here and has been included in the results as a good engineering approximation to the problem.

The corner diffraction problem is illustrated in Figure 5. The fields associated with one edge of the corner diffraction fields in the far field with spherical wave incidence are given by

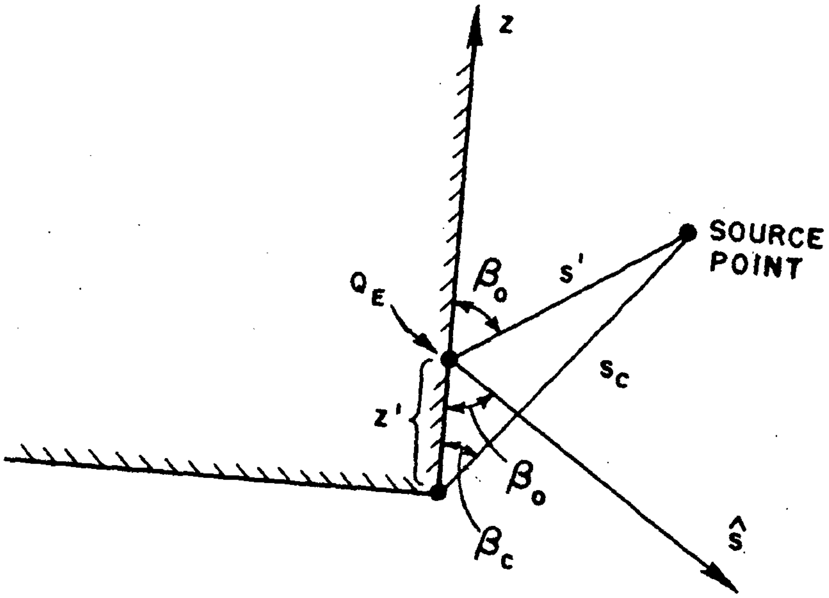

Figure 5--Geometry for corner diffraction problem.

$$\left\{\begin{matrix} E_{\parallel}^{c} \\ E_{\perp}^{c} \end{matrix}\right\} \sim \left\{\begin{matrix} IZ_o \\ MYo \end{matrix}\right\} \frac{\sin\beta_c \, e^{-j\frac{\pi}{4}}}{2\pi(\cos\beta_o - \cos\beta_c)} \quad F[ks_c a(\beta_o - \beta_c)] \, \frac{e^{-jks_c}}{\sqrt{s_c}} \, \frac{e^{-jks}}{s}$$

where

(22a)

$$\left\{\begin{matrix} I \\ M \end{matrix}\right\} = -\left\{\begin{matrix} E^i(Q_E) \\ E^i(Q_E) \end{matrix}\right\} \left\{\begin{matrix} C_s(Q_E)Y_o \\ C_h(Q_E)Z_o \end{matrix}\right\} \sqrt{s'} \, e^{jk(s'+z'\cos\beta_c)} \qquad (22b)$$

and

$$C_{s,h}(Q_E) = \frac{-e^{-j\frac{\pi}{4}}}{2\sqrt{2\pi k}\,\sin\beta_0}\left\{\frac{F[kLa(\beta^-)}{\cos\frac{\beta^-}{2}}\left|F\left[\frac{a(\beta^-)}{ks_c a(\beta_0-\beta_c)}\right]\right|\right.$$

$$\left.\mp\frac{F[kLa(\beta^+)]}{\cos\frac{\beta^+}{2}}\left|F\left[\frac{a(\beta^+)}{ks_c a(\beta_0-\beta_c)}\right]\right|\right\}. \qquad (22c)$$

The function F(x) is defined in Section C by Equation (13), and as before $a(\beta) = 2\cos^2\beta/2$ where $\beta^{\pm} = \phi \mp \phi'$, and $L = s' \sin^2\beta_0$ for spherical wave incidence. The function $C_{s,h}(Q_E)$ is a modified version of the diffraction coefficient in Equation (12) for the half-plane case when n = 2. The modification factor,

$$\left|F\left[\frac{a(\beta)}{ks_c a(\beta_0-\beta_c)}\right]\right| \; F(kLa),$$

is a heuristic function that insures that the diffraction coefficient will not change sign erroneously when it passes through the shadow boundaries of the edge. The F(kLa) in the I and M terms is also heuristic in that it is this term along with the function

$$\cot\left(\frac{\pi-\beta}{2n}\right)$$

that gives the sign change. There is also a corner diffraction term associated with the other edge forming the corner and is found in a similar manner.

Even though further study is needed to improve the diffraction mechanism, it is felt that the benefits obtained from its inclusion warrants its use here. Experimental results in Chapter III, Section B, confirm its utility in engineering applications.

G. Curved Surface Diffraction

The aircraft fuselage is a long cylindrical type structure with a generally convex curved surface. The GTD mechanism that describes the scattering in the shadow of such objects is curved surface diffraction. When an incident ray strikes a smooth curved perfectly conducting surface at grazing incidence, i.e., at the shadow boundary, a part of its energy is diffracted into the shadow region. To describe this phenomenon Keller [51] introduced a class of curved surface diffracted rays. These ray paths include the points Q_1 and Q_2 which form a curve on the diffracting surface as illustrated in Figure 6. The concept of surface rays was actually presented earlier in the creeping waves introduced by Franz and Depperman [52,53]. The results presented in the following discussion are those given by Kouyoumjian [54,55].

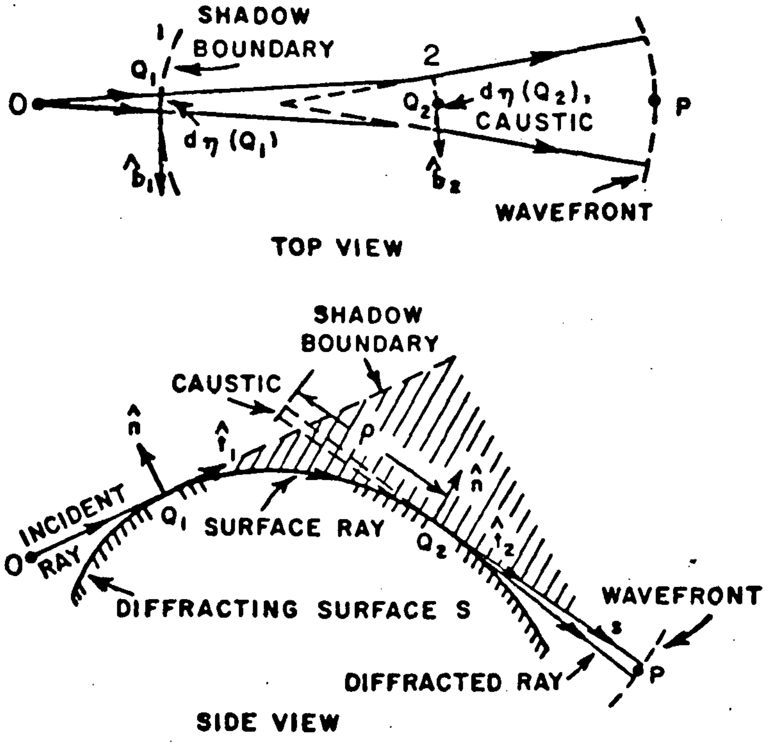

Figure 6--Diffraction by a smooth curved surface.

The diffraction by a smooth curved surface is shown in Figure 6 in which O is the source point and P is the observation point. Applying Fermat's principle, the line OQ_1Q_2P is the shortest distance between O and P which does not penetrate the surface. This is a geodesic path with arclength t on the surface. As the field propagates along the surface it sheds energy tangentially into the shadow region. The preferred coordinate system for this diffraction mechanism is composed of $\hat{t}$ the unit vector in the direction of incidence, $\hat{n}$ the normal to the surface S, and $\hat{b}$ the binomial to the surface ($\hat{b} = \hat{t} \times \hat{n}$). The incident field may be resolved into the normal and tangential components. It is assumed that these two components induce surface ray fields which propagate independently of each other. The diffracted field is given by

$$\overline{E}^d(P) = \overline{E}^i(Q_1) \cdot [\hat{b}_1\hat{b}_2\, u_s + \hat{n}_1\hat{n}_2 u_h]\sqrt{\frac{\rho}{s(\rho+s)}}\, e^{-jks} \tag{23}$$

where

$$u_{s,h} = \sqrt{\frac{d\eta_1}{d\eta_2}}\, e^{-jkt} \sum_m^{\infty} D_m^{s,h}(Q_1) D_m^{s,h}(Q_2) e^{-\int_{Q_1}^{Q_2} \alpha_m^{s,h}(t')dt'} \tag{24}$$

and

$$\hat{n}1,2 = \hat{n}|_{1,2}, \quad \hat{t}_{1,2} = \hat{t}|_{1,2}, \quad \hat{b}_{1,2} = \hat{b}|_{1,2}.$$

The subscripts (superscripts) s,h denote the acoustically soft and hard boundary conditions, respectively. The quantity $D_m(Q)$ is the scalar diffraction coefficient at the point Q and α_m is the attenuation constant which is a function of t because it depends on the local radius of curvature and its derivatives. Voltmer [56] has obtained diffraction coefficients and attenuation constants to order $(2/k\rho_g)^{2/3}$ (where ρ_g = local radius of curvature of the surface along the ray path) which is valid for smooth convex surfaces of non-constant curvature. These curved surface diffraction and attenuation constants [56] were obtained from an extension of the work of Hong [57]. The diffraction coefficients and attenuation constants are given in Table I. Note that even though an infinite number of modes are indicated in Equation (24), it is generally found that sufficiently accurate results for the field in the shadow region are obtained by summing on only the first couple of modes, provided the field point P is far-removed from the shadow boundary.

The parameters $d\eta_1$, $d\eta_2$ and ρ may be found from differential geometry involving the rays and surface; this is discussed at length by Levy and Keller [58]. For the important case of cylinders as considered in this study, it can be shown that

$$\sqrt{\frac{d\eta_1}{d\eta_2}} = \sqrt{\frac{s'}{s'+t}} \tag{25a}$$

and that the caustic distance ρ is given by

TABLE I

GENERALIZED DIFFRACTION COEFFICIENTS AND ATTENUATION CONSTANTS

Surface	SQUARE OF DIFFRACTION COEFFICIENT $D_p^2 =$ (Column A) · (Column B)		ATTENUATION CONSTANT $\alpha_p =$ (Column C) · (Column D)		
	A. Keller's Result	B. Correction Terms	C. Keller's Result	D. Correction Terms	ZEROES OF THE AIRY FUNCTION
Soft Acoustic and Soft EM	$\frac{\pi^{-1/2}2^{-5/6}\rho_g^{1/3}e^{-j\pi/12}}{k^{1/6}(Ai'(-q_p))^2}$	$1+\left(\frac{2}{k\rho_g}\right)^{2/3} q_p\left(\frac{1}{30}+\frac{\rho_g}{4\rho_{tn}}+\dots\right)e^{-j\pi/3}$	$\frac{q_p}{\rho_g}e^{j\pi/6}\left(\frac{k\rho_g}{2}\right)^{1/3}$	$1+\left(\frac{2}{k\rho_g}\right)^{2/3} q_p\left(\frac{1}{60}-\frac{2}{45}\rho_g\ddot{\rho}_g+\frac{4}{135}\dot{\rho}_g^2\right)e^{-j\pi/3}$	$Ai(-q_p)=0$ $q_1=2.33811$ $q_2=4.08795$ $Ai'(-q_1)=.70121$ $Ai'(-q_2)=-.80311$
Hard Acoustic	$\frac{\pi^{-1/2}2^{-5/6}\rho_g^{1/3}e^{-j\pi/12}}{k^{1/6}\bar{q}_p(Ai(-\bar{q}_p))^2}$	$1+\left(\frac{2}{k\rho_g}\right)^{2/3}\left(\bar{q}_p\left(\frac{1}{30}+\frac{\rho_g}{4\rho_{tn}}+\dots\right)-\frac{1}{\bar{q}_p^2}\left(\frac{1}{10}+\frac{\rho_g}{4\rho_{tn}}+\dots\right)\right)e^{-j\pi/3}$	$\frac{\bar{q}_p}{\rho_g}e^{j\pi/6}\left(\frac{k\rho_g}{2}\right)^{1/3}$	$1+\left(\frac{2}{k\rho_g}\right)^{2/3}\left(\bar{q}_p\left(\frac{1}{60}-\frac{2}{45}\rho_g\ddot{\rho}_g+\frac{4}{135}\dot{\rho}_g^2\right)+\frac{1}{\bar{q}_p^2}\left(\frac{1}{10}+\frac{\rho_g}{4\rho_{tn}}-\frac{\rho_g\ddot{\rho}_g}{60}+\frac{\dot{\rho}_g^2}{90}\right)\right)e^{-j\pi/3}$	ZEROES OF THE DERIVATIVE OF THE AIRY FUNCTION $Ai'(-\bar{q}_p)=0$ $\bar{q}_1=1.01879$ $\bar{q}_2=3.24820$ $Ai(-\bar{q}_1)=.53566$ $Ai(-\bar{q}_2)=-.41902$
Hard EM		$1+\left(\frac{2}{k\rho_g}\right)^{2/3}\left(\bar{q}_p\left(\frac{1}{30}+\frac{\rho_g}{4\rho_{tn}}+\dots\right)-\frac{1}{\bar{q}_p^2}\left(\frac{1}{10}-\frac{\rho_g}{4\rho_{tn}}+\dots\right)\right)e^{-j\pi/3}$		$1+\left(\frac{2}{k\rho_g}\right)^{2/3}\left(\bar{q}_p\left(\frac{1}{60}-\frac{2}{45}\rho_g\ddot{\rho}_g+\frac{4}{135}\dot{\rho}_g^2\right)+\frac{1}{\bar{q}_p^2}\left(\frac{1}{10}-\frac{\rho_g}{4\rho_{tn}}-\frac{\rho_g\ddot{\rho}_g}{60}+\frac{\dot{\rho}_g^2}{90}\right)\right)e^{-j\pi/3}$	

ρ_g = radius of curvature along the geodesic

ρ_{tn}^g = radius of curvature perpendicular to the geodesic (transverse curve)

Dots indicate differentiation with respect to the arc length variable

The Miller-type Airy function[illegible] appearing in Column A is given by:

$$Ai(-x) = \frac{1}{\pi}\int_0 \cos\left(\frac{t^3}{3} - xt\right)\,dt.$$

Ai'(-x) denotes the derivative of Ai(-x) with respect to the argument of the Airy function.

$$\rho = s' + t. \tag{25b}$$

where s' is the distance from the source to the point Q_1.

The above discussion has been applied to open curved surface so far. For a closed surface, each surface ray mode produced at Q_1 encircles the surface an infinite number of times. In the present work, the surfaces are large enough, so that these multiple encirclements may be neglected. An additional surface ray field must be added, however, associated with the shadow boundary at the other end of the closed surface to Q_1.

H. Transition Field Associated with Curved Surface Diffraction

In the analysis of the scattered fields from smooth, convex surfaces the pertinent diffraction and reflection coefficients are readily available, but they are only valid away from the shadow boundaries. At and near the shadow boundaries, the GTD ray method fails. Therefore, in this transition region adjacent to the shadow boundary a separate solution is required.

The general problem of the diffraction of waves by smooth, convex surfaces for grazing angles is very complex, and it has been the subject of an investigation by various authors. An extensive bibliography on various aspects of the problem may be found in the papers by Logan [59], and Borovikov and Kinber [60]. The work in these references and others are based on the pioneering work of Fock [61]. In general, due to the mathematical complexity of the solutions, the previous solutions do not appear to be in a tractable form for practical engineering problems.

Pathak [62,63] has modified and extended the transition solution in a systematic fashion via ray optical considerations. His result is in a form suitable to be used in high frequency scattering by arbitrary two-dimensional and three-dimensional smooth convex, conducting surfaces. This study will briefly discuss Pathak's [62, 63] results for diffraction by cylindrical structures. This uniform result yields a finite, continuous variation for the total field across the shadow boundaries within the transition regions. In the lit region, exterior to the transition region the solution reduces to the incident and reflected geometrical optics field as presented in Section B. In the deep shadow region, exterior to the transition region, the solution reduces to the usual GTD surface diffracted ray field as given in Section G. The transition problem is illustrated in Figure 7a for the lit region (also refer to Figure 2) and in Figure 7b for the shadow region (also refer to Figure 6).

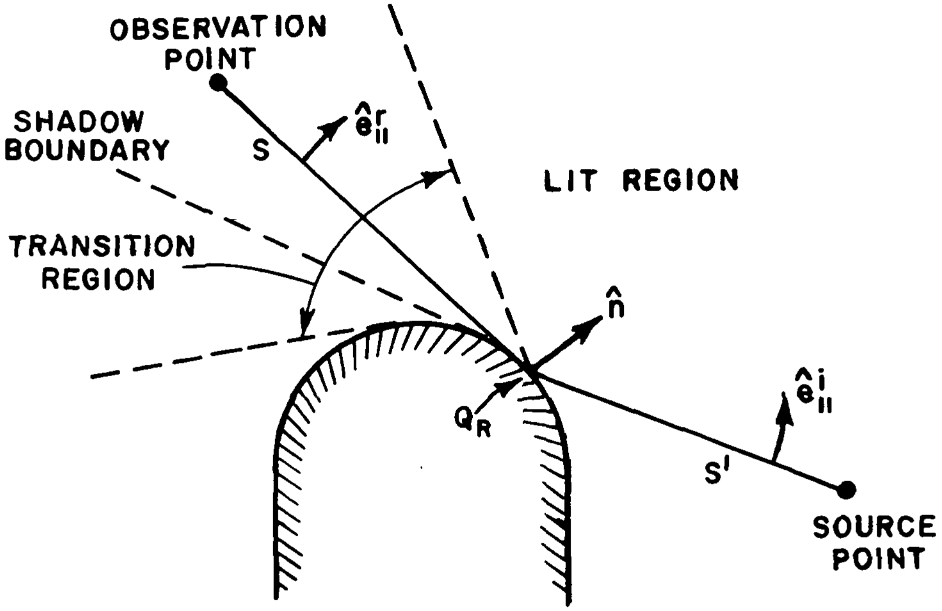

(a) SIDE VIEW OF LIT REGION

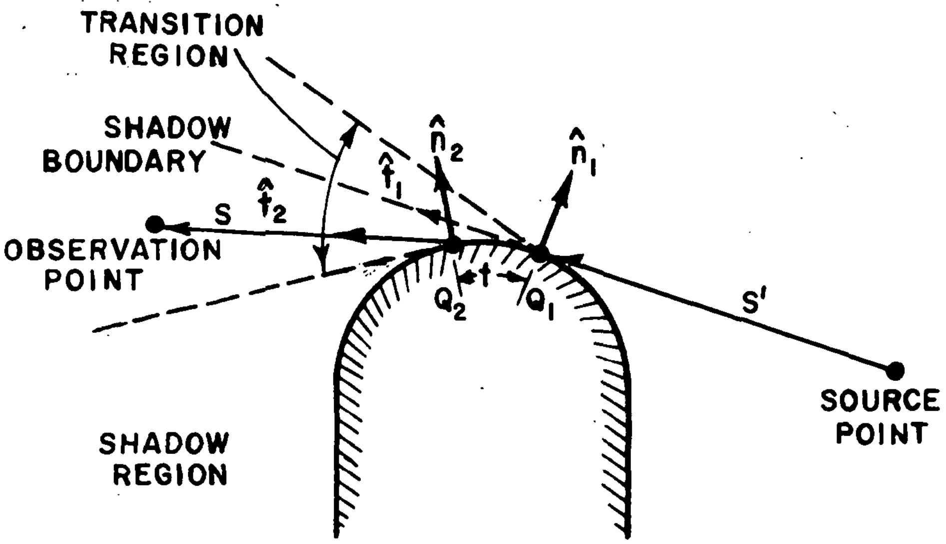

(b) SIDE VIEW OF SHADOW REGION

Figure 7--Curved surface transition function geometry.

The transition field for a cylindrical structure can be written as

$$\vec{E}^{t} \sim \vec{E}^{i}(Q) \cdot [\hat{u}_1\hat{u}_2\, G_s + \hat{v}_1\hat{v}_2 G_h] \tag{26}$$

where

$$Q = \begin{cases} Q_R & \text{for the lit region case} \\ Q_1 & \text{for the shadow region case} \end{cases}$$

and G_s, G_h are curved surface transition coefficients for the soft and hard boundary conditions, respectively. In the lit zone, the transition coefficients are given by

$$G_{s,h} = \left\{ \frac{-m\; e^{-j\left(\frac{\pi}{4} + \frac{\xi_\ell^3}{12}\right)}}{\sqrt{\pi k}} \sqrt{\frac{-2k}{m^2 \xi_\ell}} \left[\frac{-1}{\sqrt{2}\xi_\ell} F\left(\frac{kL\xi_\ell^2}{2m^2}\right) + \sqrt{2\pi} \begin{Bmatrix} p^*(\xi_\ell) \\ q^*(\xi_\Omega) \end{Bmatrix} \right] \right\}$$

$$\times \sqrt{\frac{\rho_1^r \rho_2^r}{(\rho_1^r + s)(\rho_2^r + s)}}\; e^{-jks} \tag{27}$$

where

$$\hat{u}_1 = \hat{e}_{\parallel}^{i}\,, \quad \hat{u}_2 = \hat{e}_{\perp}^{r}$$

and

$$\hat{v}_1 = \hat{e}_{\perp}\,, \quad \hat{v}_2 = \hat{e}_{\perp}\,.$$

The first term in the square brackets is similar to the Kirchhoff edge diffraction coefficient of a half-plane. The function F(X) in this term is the transition function of the wedge in Section C Equation (13). In contrast, the second term in the square brackets is dependent on the electrical properties of the surface; this term becomes dominant far from the shadow boundary. The functions $p^*(\xi)$ and $q^*(\xi)$ are universal functions and are the complex conjugates of the $p(\xi)$ and $q(\xi)$ functions defined by Logan [59]. The functions $e^{-j\pi/4}p^*(\xi)$ and $e^{-j\pi/4}q^*(\xi)$ are plotted in Figures 8a and 8b,

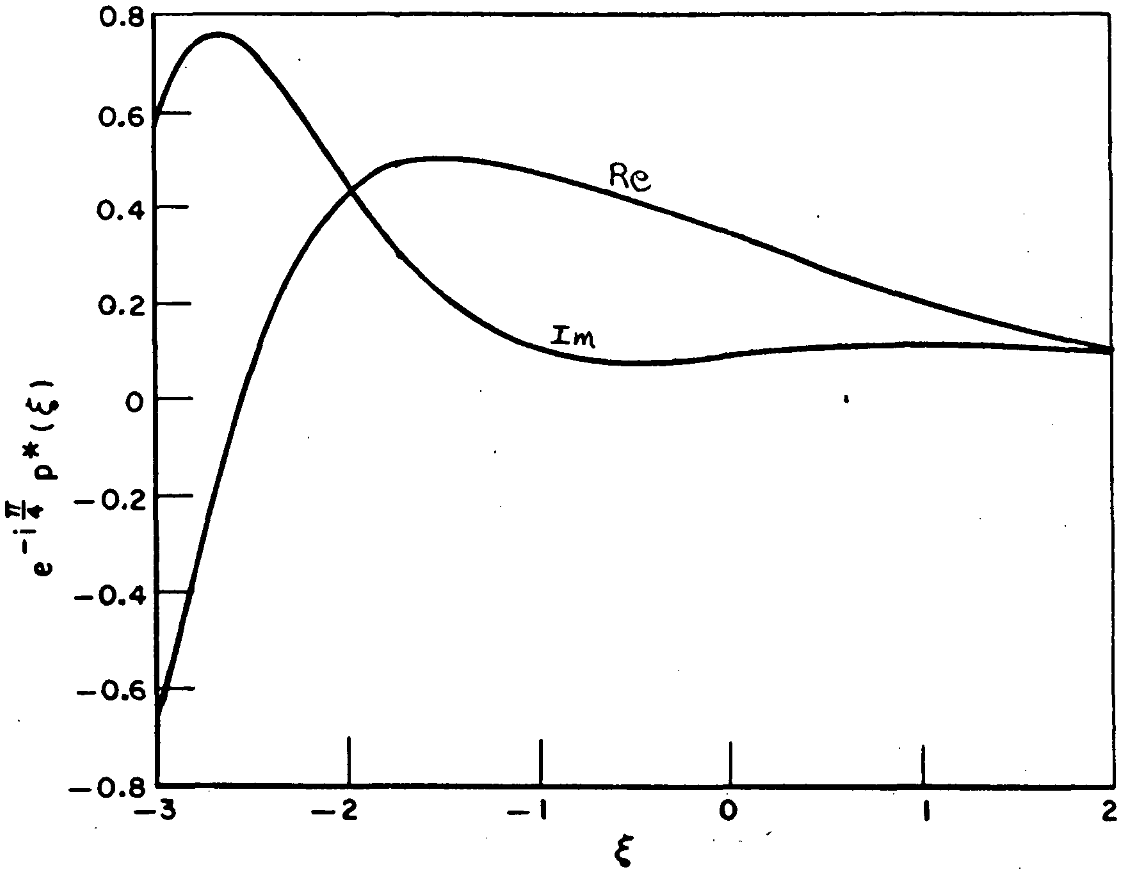

Figure 8a--Plot of $e^{-j\,\pi/4}\,p^*(\xi)$ vs ξ based on Logan's tabulated data [59] for $p(\xi)$.

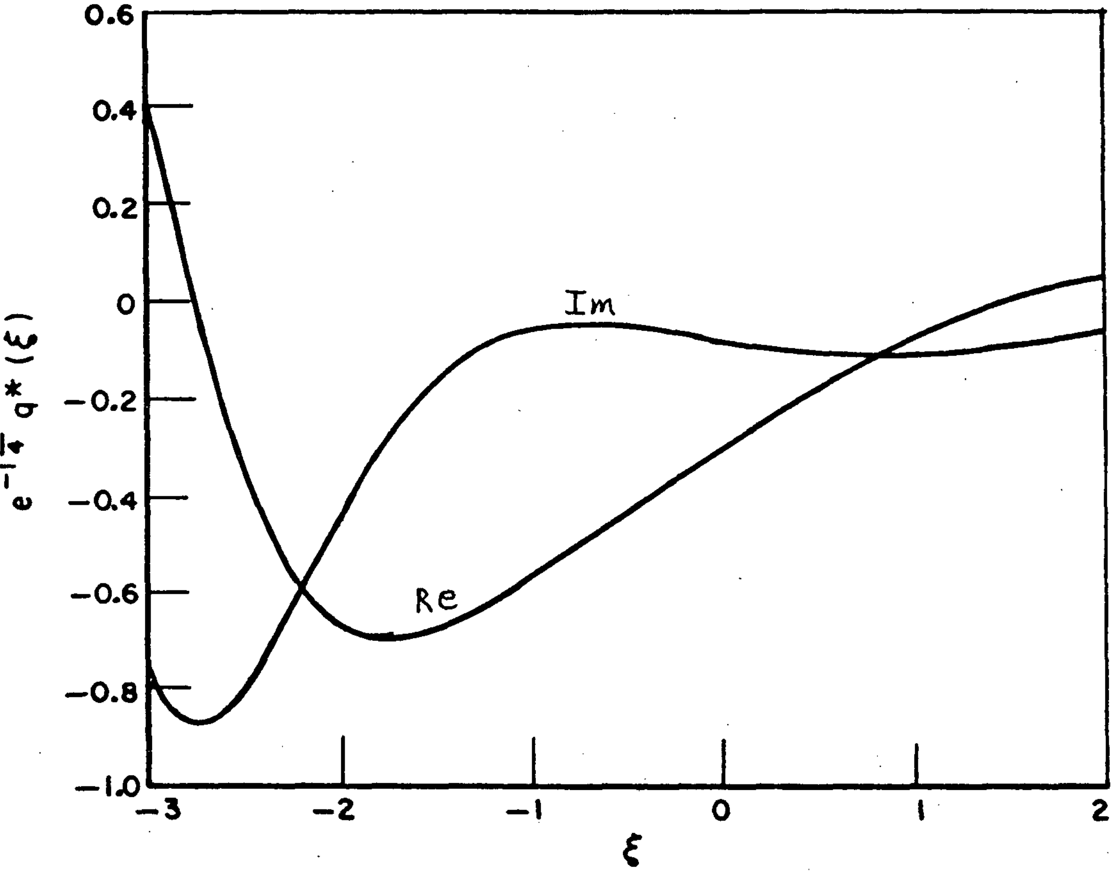

Figure 8b. Plot of $e^{-j\,\pi/4}\,q^*(\xi)$ vs ξ based on Logan's tabulated data [59] for $q(\xi)$.

respectively. For a further discussion of the derivation of these functions see Reference [59]. The other parameters are defined as

$$L = \frac{ss'}{s+s'}$$

$$\xi_\ell = -\frac{2k}{m^2}\left(\frac{s'\rho_1^r}{s'-\rho_1^r}\right)$$

$$m = \left[\frac{k\rho_g(Q_R)}{2}\right]^{1/3}$$

$\rho_g(Q_R)$ = longitudinal radius of curvature of the surface at the point Q

$\rho^r_{1,2}$ are defined in Section B, Equation (10) for spherical wave incidence.

In the shadow zone, the transition coefficients are given by

$$G_{s,h} = \left\{\frac{-(m_1m_2)^{1/2}e^{-j(\pi/4+kt)}}{\sqrt{\pi k}}\left[\frac{-1}{\sqrt{2}\xi_s}\,F\left(\frac{kL\xi_s^2}{2m_1m_2}\right) + \sqrt{2\pi}\begin{Bmatrix} p^*(\xi_s) \\ q^*(\xi_s)\end{Bmatrix}\right]\right\}\sqrt{\frac{d\eta_1}{d\eta_2}}\sqrt{\frac{\rho}{s(\rho+s)}}\,e^{-jks} \tag{28}$$

where

$$\hat{u}_1 = \hat{b}_1,\ \hat{u}_2 = \hat{b}_2$$

and

$$\hat{v}_1 = \hat{n}_1,\ \hat{v}_2 = \hat{n}_2\ .$$

The functions $F(x)$, $p^*(\xi)$ and $q^*(\xi)$ and the parameter L are defined as in the lit case. The other parameters are defined as

$$m_{1,2} = \left[\frac{k\ \rho_g(Q_{1,2})}{2} \right]^{1/3}$$

$$\xi_s = \int_{Q_1}^{Q_2} \frac{1}{\rho_g} \left(\frac{k\rho_g}{2} \right)^{1/3} dt'$$

$\rho_g(t')$ is the radius of curvature on the surface at the point t' on the geodesic path of the ray

and

$d\eta_1$, $d\eta_2$, ρ are defined as in Section G, Equations (25a) and (25b).

CHAPTER III

NEAR FIELD SCATTERING BY A NUMBER OF FLAT PLATES

A. Introduction

The Geometrical Theory of Diffraction as discussed in Chapter II is applied in this chapter to the near field scattering by a number of finite flat plates. This is basically an extension of the scattering by a single finite flat plate considered by Burnside [23].

In this problem the antenna is in the near field of the three-dimensional scattering bodies, and the observation point is in the far field. However, it is assumed that any point on the scattering body is in the far field of the source. Some assumptions have been made about the geometry of the scattering bodies to simplify the analysis, that is to minimize multiple scattering mechanisms. These assumptions are based on geometries that can be used to obtain results for wing mounted antennas.

B. Near Field Scattering by a Number of Finite Plates

The near field scattering by a number of finite flat plates presented here is a practical application of the Geometrical Theory of Diffraction presented earlier. The dimensions of the plates are assumed to be large in terms of the wavelength. The geometry of the plates is specified by the location of their corners in a general coordinate system, as illustrated in Figure 9. The source is defined by its location and far-field pattern. The far field pattern is appropriate since the source is assumed to be $2D^2/\lambda$ away from the edges of the plates, where D is the maximum dimension of the source. The infinitesimal electric and magnetic dipole moments, discussed in Section II-D, are the source types considered in this analysis. These elements, properly weighted and summed, can be used to approximately represent any antenna with a known source distribution.

The high frequency scattering by a number of structures in proximity to each other is, in general, a very complicated problem. All the multiple interactions between the various structures must be included to obtain an exact solution to the problem. This of course is impractical in most instances. For low frequencies the method of moments is used for these types of problems, however, for electrically large sized bodies physical limitations on computer storage and numerical accuracy make this method impractical. The GTD and its ray optical format is ideal for these problems.

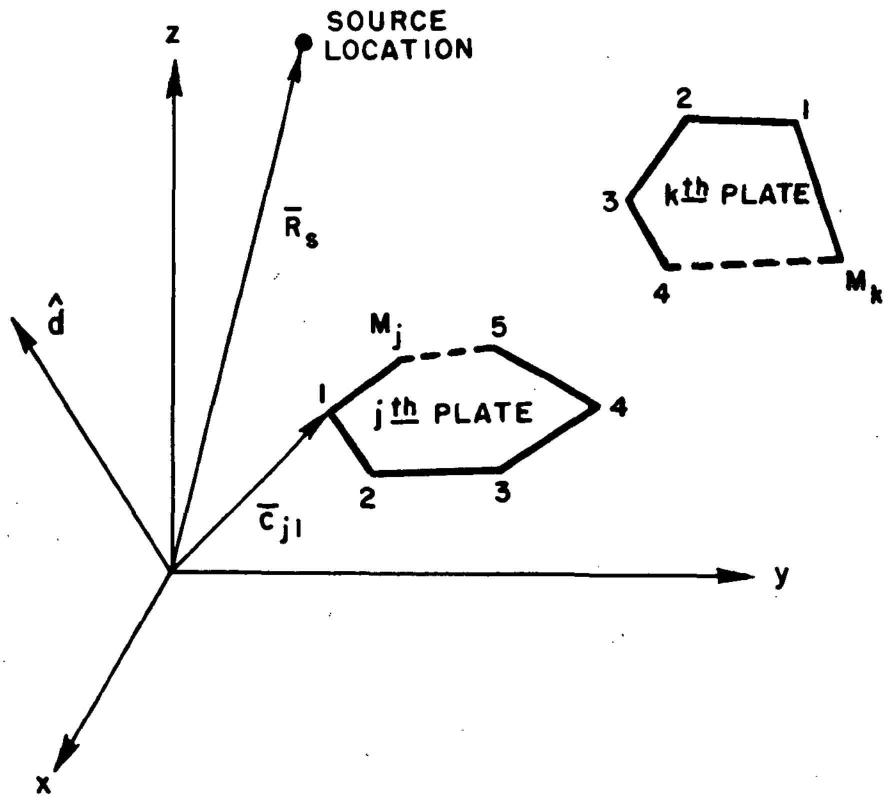

Figure 9--Geometry for the near field scattering by a number of flat plates.

In constructing a solution using GTD, one starts by tracing the most important rays that will contribute to the total field. It is important that all rays be properly shadowed by the scattering structures. This, of course, will produce discontinuous fields at the shadow boundaries. These discontinuities, however, may be compensated, by including the appropriate diffraction mechanisms discussed in Chapter II. As the solution progresses, more and more higher order terms can be added until the resulting patten is relatively smooth. In general, it is impractical to include enough higher order terms to produce a completely continuous field. However, the discontinuities may be kept to a few dB and in fact the general rule is that the actual field normally passes through the average of the discontinuity. The resulting radiation patterns are usually a good engineering approximation to the true fields.

The geometry of the multiple flat plates discussed in this report is assumed to be such that second order interactions only need to be considered. This is a good approximation for the aircraft geometries of interest in that the plates are relatively widely spaced and do not produce strong corner reflector effects for antennas mounted on the wings. The type of interaction terms that have been determined to be important for the geometries in this study are listed in Table II. They comprise the major contributors to the total scattered field from a number of flat plates.

TABLE II

SCATTERED FIELDS INCLUDED IN THE FLAT PLATES SOLUTION

	Symbol	Description	Figure	Equation
1)	$\overline{E}^r$	Simply reflected field off a plate	13	41
2)	$\overline{E}^d$	Diffracted field off an edge	15	46
3)	$\overline{E}^c$	Corner diffracted field off a corner	16	48
4)	$\overline{E}^{rr}$	Double reflected field off a plate after reflection by another plate	21	49
5)	$\overline{E}^{rd}$	Diffracted field off an edge after reflection by a plate	22	50
6)	$\overline{E}^{rc}$	Corner diffracted field off a corner after reflection by a plate	23	51
7)	$\overline{E}^{dr}$	Reflected field off a plate after diffraction by an edge	24	52

The incident field from the source is given by

$$\overline{E}^i(S) = [\hat{\theta}^s F(\theta_s,\phi_s) + \hat{\phi}^s\, G(\theta_s,\phi_s)]\, \frac{e^{-jks}}{s} \quad . \qquad (29)$$

For a far field observation direction given by

$$\hat{d} = \cos\phi_s \sin\theta_s\, \hat{x} + \sin\phi_s \sin\theta_s\, \hat{y} + \cos\theta_s \hat{z},$$

the phase can be referred to the reference coordinate system by the usual far field approximation so that $e^{-jks}/s \approx e^{jk\overline{R}_s \cdot d}\, e^{-jkd}/d$, where d is the distance from the reference point to the far field receiver.

It is essential, in the GTD format, that the source field be set to zero whenever the ray from the source to the receiver passes through any perfectly conducting obstacle. This can be accomplished in many different ways. The scheme used here is to first decide whether the ray direction, representing the field, is pointed in the same half space in which a plate with normal $\hat{n}$ is contained. This is done by comparing the sign of

$$\hat{n} \cdot (\overline{R}_s - \overline{C}_1) \text{ and } \hat{n} \cdot \hat{d}. \tag{30}$$

If they are of the same sign, the ray can not hit the plate. If they are of the opposite sign a further test is needed.

First, the incident ray is projected onto the plane of the plate to find its intersection point, as shown in Figure 10, that is

$$\overline{R}_t = \overline{R}_s - \frac{[\hat{n} \cdot (\overline{R}_s - \overline{C}_1)]\hat{d}}{\hat{n} \cdot \hat{d}} . \tag{31}$$

Now, using an idea based on Cauchy's formula from complex variables, that is

$$\oint_C f(z)dz = \begin{cases} 0, \text{ no pole in } f(z) \\ 2\pi j, \text{ one pole in } f(z) \end{cases}$$

the intersection point can be tested to see whether or not it falls within the limits of the plate. This is illustrated in Figure 11. It is easy to show that

$$\theta_m = \tan^{-1}\left[\frac{(\overline{C}_m - \overline{R}_t) \times (\overline{C}_{m+1} - \overline{R}_t)}{(\overline{C}_m - \overline{R}_t) \cdot (\overline{C}_{m+1} - \overline{R}_t)}\right] \tag{32a}$$

which leads to the test, if

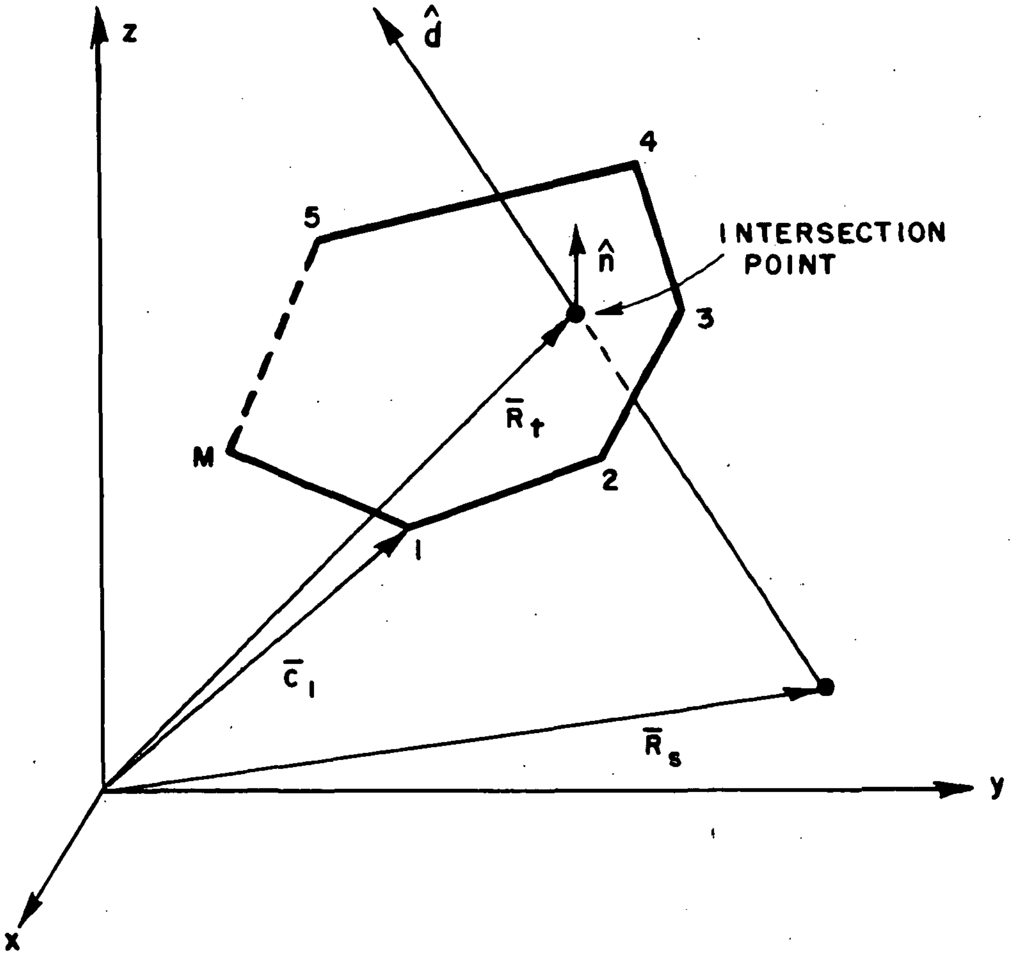

Figure 10--Intersection of scatter direction ray with plate.

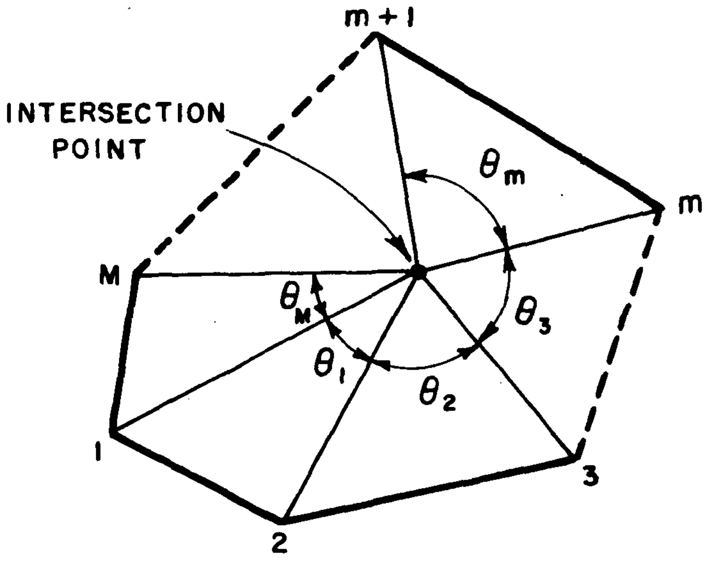

(a) RAY HITS PLATE

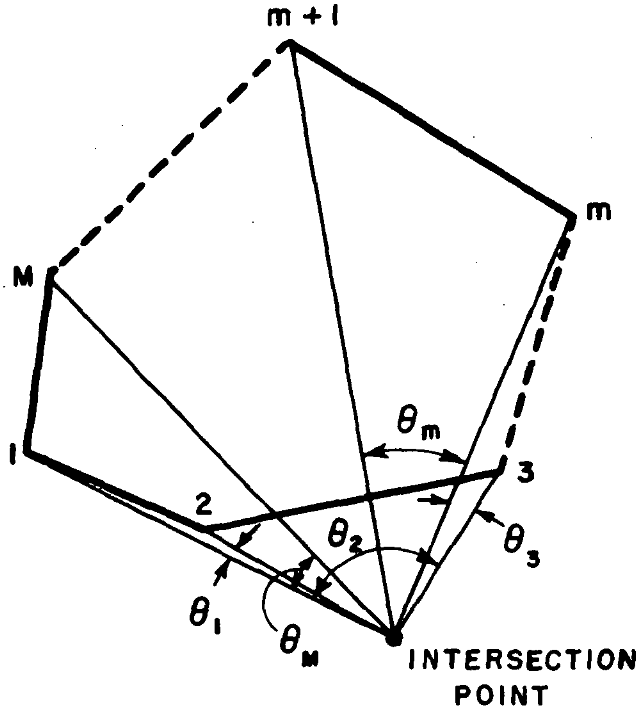

(b) RAY DOES NOT HIT PLATE

Figure 11--Geometry for deciding whether ray does or does not hit plate.

$$\left|\sum_{m=1}^{M} \theta_m\right| \quad \begin{cases} <\pi \text{ , no hit occurs} \\ >\pi \text{ , a hit occurs} \end{cases} \quad . \tag{32b}$$

All the plates may be tested in this way to see if they shadow the ray.

The singly reflected field from a flat plate is considered next. The first step in this calculation is to find the location of the image source, which is uniquely determined once the plane of the flat plate is defined by its normal. In fact, the image is located along a line which is orthogonal to the plate and positioned an equal distance on the opposite side of the plate. This location can be found analytically using the geometry illustrated in Figure 12. The image position vector ($\vec{R}_i$) can be determined using the following expression

$$\vec{R}_i = \vec{R}_s - 2[\hat{n} \cdot (\vec{R}_s - \vec{C}_1)]\hat{n}. \tag{33}$$

With the image position known, one needs to determine if the reflected field contributes to the total scattered field. The reflected field exists if the ray from the image source in the scatter direction passes through the finite limits of the plate. The same procedure outlined in Equations (30-32) is used for this except $\vec{R}_i$ replaces $\vec{R}_S$. In this case if a hit on the plate does occur, reflections could exist. One must also test that the incident ray and the scatter direction ray are not shadowed by another plate. The incident ray ($\bar{I}$) may be found by reflecting the scatter direction ray into the plane of the plate. This is given by the expression

$$\hat{I} = \hat{d} - 2(\hat{n}\cdot\hat{d})\hat{n} .$$

The incident angles for the source may be found from

$$\theta_i = \tan^{-1}\left(\frac{\sqrt{I_x^2+I_y^2}}{I_z}\right)$$

and

$$\phi_i = \tan^{-1}\left(\frac{I_y}{I_x}\right)$$

where

$$\hat{I} = I_x\hat{x} + I_y\hat{y} + I_z\hat{z}$$

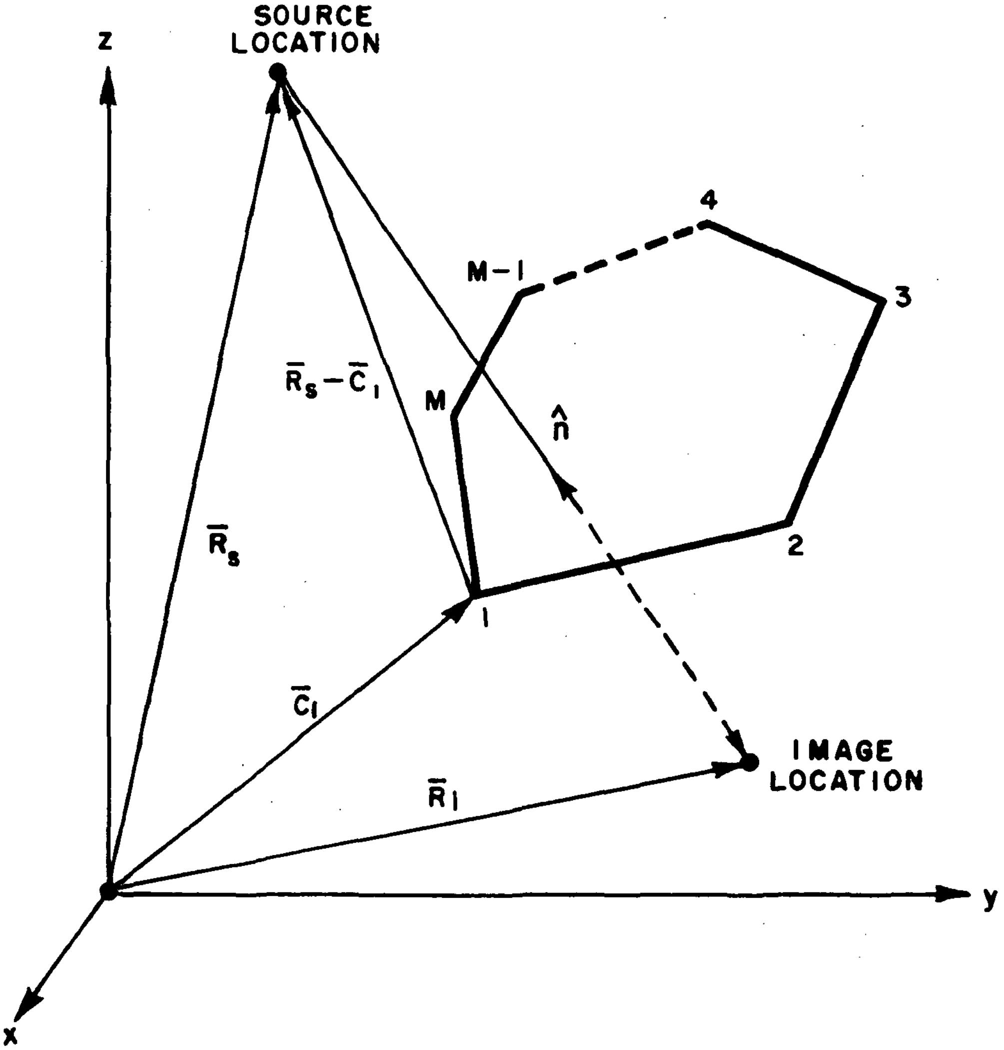

Figure 12--Geometry for location of image source.

or

$$\hat{I} = \cos\phi_i \sin\theta_i \hat{x} + \sin\phi_i \sin\theta_i \hat{y} + \cos\theta_i \hat{z}.$$

Once it is determined that the reflections do occur. the value of the reflected field can be found. For the jth plate the reflected field from the image source can be written as

$$\overline{E}_j^r(\theta_s,\phi_s) = [\hat{\theta}^s F^r(\theta_s,\phi_s) + \hat{\phi}^s G^r(\theta_s,\phi_s)] \frac{e^{-jks}}{s} \quad (34)$$

using the geometry illustrated in Figure 13. The vectors $\hat{\theta}^s$ and $\hat{\phi}^s$ are related to the scatter direction $\hat{d}$ and are given by

$$\hat{\theta}^s = \cos\phi_s \cos\theta_s \hat{x} + \sin\phi_s \cos\theta_s \hat{y} - \sin\theta_s \hat{z}$$

$$\hat{\phi}^s = -\sin\phi_s \hat{x} + \cos\phi_s \hat{y}.$$

The incident field is given by

$$\overline{E}^i(s') = [\theta^i F(\theta_i,\phi_i) + \hat{\phi}^i G(\theta_i,\phi_i)] \frac{e^{-jks'}}{s'} \quad (35)$$

where

$$\hat{\theta}^i = \cos\phi_i \cos\theta_i \hat{x} + \sin\phi_i \cos\theta_i \hat{y} - \sin\theta_i \hat{z}$$

$$\hat{\phi}^i = -\sin\phi_i \hat{x} + \cos\phi_i \hat{y} .$$

A tangent vector $(\hat{t})$ can be found on the plate such that

$$\hat{t} = \frac{\hat{n} \times \hat{d}}{|\hat{n} \times \hat{d}|} . \quad (36)$$

The reflected field can now be found from the boundary conditions that must be satisfied on the perfectly conducting flat plate surfaces. They are given by

$$\hat{n} \cdot \overline{E}^r \text{ (on plate)} = \hat{n} \cdot \overline{E}^i \text{ (on plate)} \quad (37a)$$

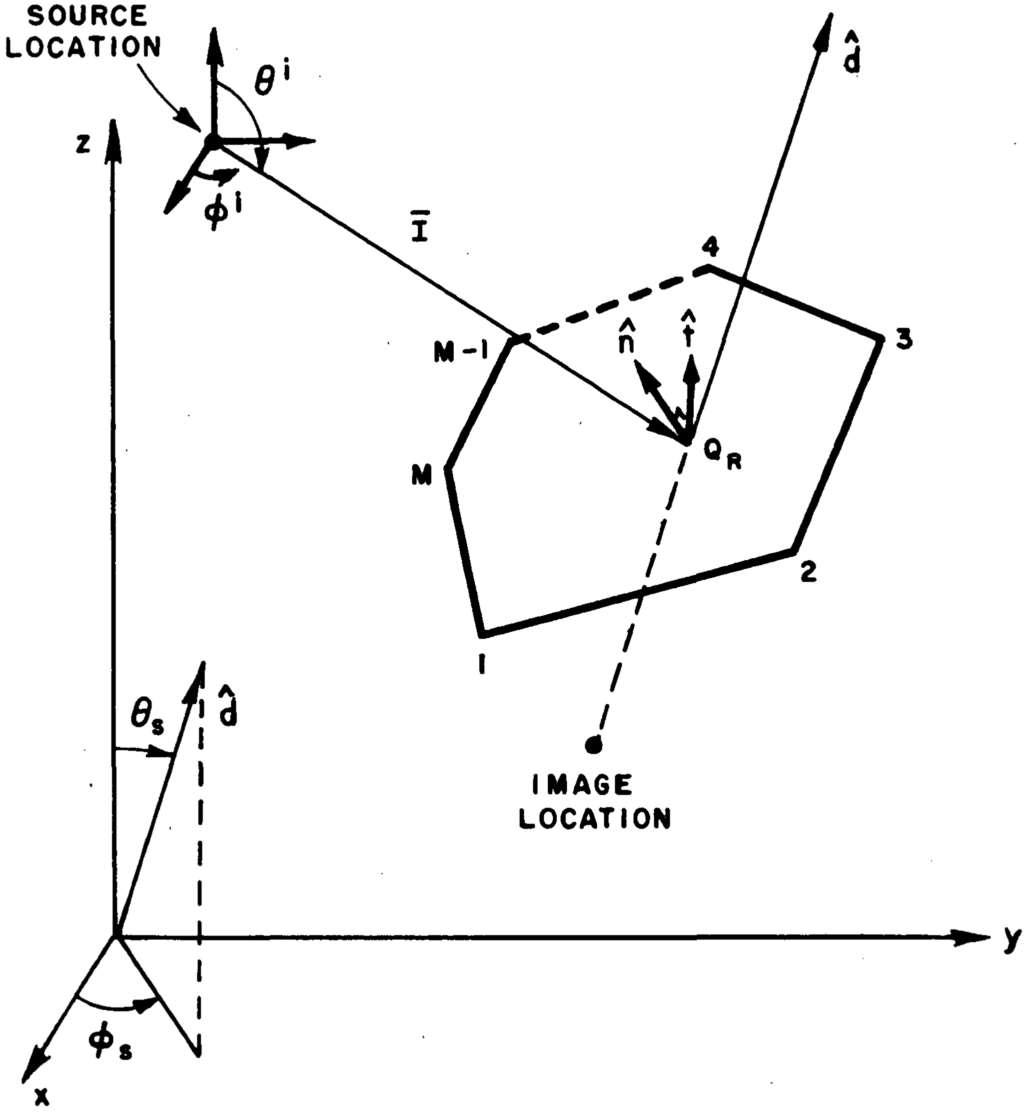

Figure 13--Reflected field geometry.

$$\hat{t} \cdot \bar{E}^r \text{ (on plate)} = - \hat{t} \cdot \bar{E}^i \text{ (on plate)} \qquad (37b)$$

In matrix notation Equations (37a and 37b) can be written, using Equations (34 and 35) and the fact that s=s' on the plate, as

$$\begin{bmatrix} \hat{n} \cdot \hat{\theta}^s & \hat{n} \cdot \hat{\phi}^s \\ \hat{t} \cdot \hat{\theta}^s & \hat{t} \cdot \hat{\phi}^s \end{bmatrix} \begin{bmatrix} F^r \\ G^r \end{bmatrix} = \begin{bmatrix} A^n \\ -A^t \end{bmatrix} \qquad (38a)$$

where

$$\begin{bmatrix} \hat{n} \cdot \hat{\theta}^i & \hat{n} \cdot \hat{\phi}^i \\ \hat{t} \cdot \hat{\theta}^i & \hat{t} \cdot \hat{\phi}^i \end{bmatrix} \begin{bmatrix} F \\ G \end{bmatrix} = \begin{bmatrix} A^n \\ A^t \end{bmatrix} \quad . \qquad (38b)$$

Now solving the above expression for the unknown reflected field pattern functions gives

$$F^r = \frac{(\hat{t}\cdot\hat{\phi}^s)A^n + (\hat{n}\cdot\hat{\phi}^s)A^t}{(\hat{n}\cdot\hat{\theta}^s)(\hat{t}\cdot\hat{\phi}^s) - (\hat{n}\cdot\hat{\phi}^s)(\hat{t}\cdot\hat{\theta}^s)} \qquad (39a)$$

$$G^r = \frac{-[(\hat{n}\ \hat{\theta}^s)A^t + (\hat{t}\cdot\hat{\theta}^s)A^n]}{(\hat{n}\cdot\hat{\theta}^s)(\hat{t}\cdot\hat{\phi}^s) - (\hat{n}\cdot\hat{\phi}^s)(\hat{t}\cdot\hat{\theta}^s)}). \qquad (39b)$$

Thus, in the far field the reflected field from the jth plate can be written using Equations (34 and 39) as

$$\bar{E}_j^r(\theta_s,\phi_s) = [\hat{\theta}^s F^r(\theta_s,\phi_s) + \hat{\phi}^s G^r(\theta_s,\phi_s)] e^{jk\bar{R}_i \cdot \hat{d}} \, \frac{e^{-jkd}}{d} \ . \qquad (40)$$

The total reflected field from the P flat plates is, then, given by

$$\bar{E}^r(\theta_s,\phi_s) = \sum_{j=1}^{P} \bar{E}_j^r(\theta_s,\phi_s) \qquad (41)$$

remembering that if the incident or reflected field is shadowed by any plate,,the reflected field for that plate is taken to be zero. Also, if the source is directly mounted on the surface of a plate, such as a slot antenna, there is assumed to be no reflections from that plate.

The shadowing of the incident and reflected rays by the flat plates is compensated for in the total field by the addition of the three-dimensional wedge diffracted field of Equation (16). It is known that for a given scatter direction there is only one point along an infinitely long straight edge at which the diffracted field can emanate for a near zone source. Thus, one needs to determine whether a diffraction point lies on the finite length of each of the M edges on the P plates so that it can be included in the total scattered field. Note that it is possible for two plates to have a common edge. The common edges are treated as one edge with a wedge angle other than n=2 and therefore it must only be included once in the scattered field.

To determine if a given edge has a diffraction point that will contribute to the total field in the scatter direction, bounds on the possible diffraction cone angles β_0 can be obtained for each of the edges forming the P plates. Diffractions will occur if the following inequality is met

$$\frac{(\bar{C}_m-\bar{R}_s)}{|\bar{C}_m-\bar{R}s|} \cdot \hat{e}_m < \hat{d} \cdot \hat{e}_m < \frac{(\bar{C}_{m+1}-\bar{R}_s)}{|\bar{C}_{m+1}-\bar{R}_s|} \cdot \hat{e}_m \ , \tag{42}$$

otherwise, diffractions for that edge will <u>not</u> occur in the given scatter direction. The diffraction point ($\bar{R}_d$) for an infinite edge and an observation point, as illustrated in Figure 14, can be obtained in a straight-forward manner. For a given edge, a perpendicular vector from the source to the edge can be found from

$$t_p = (\bar{R}_s - \bar{C}_m) \cdot \hat{e}_m, \tag{43a}$$

$$\bar{R}_p = \bar{C}_m + t_p\hat{e}_m. \tag{43b}$$

The scatter direction is known so that

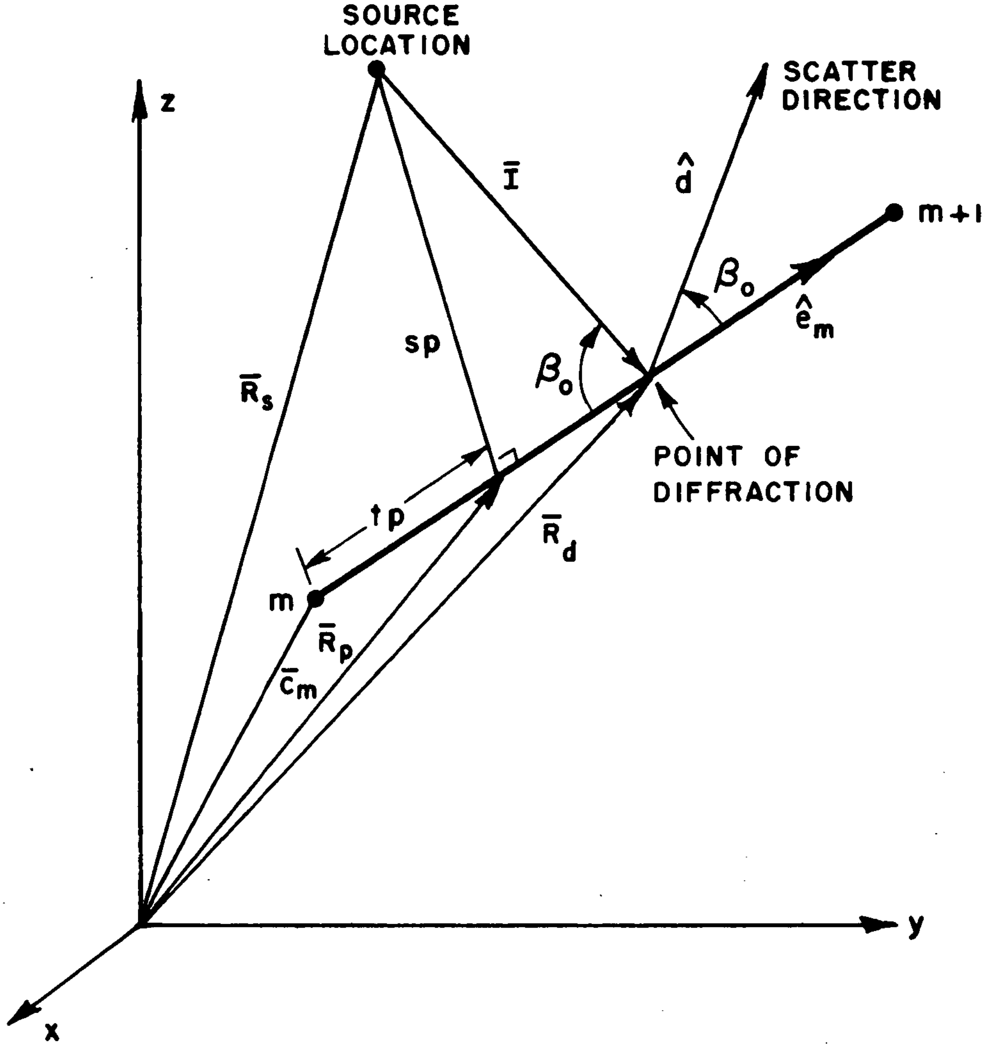

Figure 14--Geometry for diffraction point along the mth edge.

$$\cot \beta_o = \frac{\hat{d} \cdot \hat{e}_m}{\sqrt{1-(\hat{d}\cdot\hat{e}_m)^2}} \quad . \tag{43c}$$

The diffraction point can now be found from

$$\overline{R}_d = \overline{R}_p + s_p \cot \beta_o \, \hat{e}_m \tag{43d}$$

where

$$s_p = |\overline{R}_s - \overline{R}_p| \tag{43e}$$

and the incident vector is given by

$$\overline{I} = \overline{R}_d - \overline{R}_s .$$

As before in the discussion of the reflected field the incident field and diffracted field must be checked to see if they are shadowed by any other structure. This can be done in the same manner given in Equations (30-32). If either field is shadowed the result is set equal to zero for that edge.

Once the diffraction point is known, the diffracted field can be found from Equation (16). Since the source produces a spherical wave incidence and the scatter direction is in the far field ($S\rightarrow\infty$), the diffracted field (with its phase referred to the reference coordinate system) is given by

$$\begin{bmatrix} E_{\parallel}^{d} \\ E_{\perp}^{d} \end{bmatrix} \sim \begin{bmatrix} -D_s - \frac{1}{jk} \frac{\partial D_s}{\partial \phi'} \frac{\partial}{\partial n} & 0 \\ 0 & -D_h - \frac{1}{jk} \frac{\partial D_h}{\partial \phi'} \frac{\partial}{\partial n} \end{bmatrix} \begin{bmatrix} E_{\parallel}^{i}\ (Q_E) \\ E_{\perp}^{i}\ (Q_E) \end{bmatrix}$$

$$\sqrt{s'}\ e^{jk\,\overline{R}_d\cdot\hat{d}}\ \frac{e^{-jkd}}{d} \tag{44}$$

where

$$L = s' \sin^2\beta_o \tag{45a}$$

$$n_w = \text{wedge angle number} = \begin{cases} 2 & \text{for half plane edges} \\ \dfrac{1}{\pi}\tan^{-1}\left(\dfrac{\hat{e}_i \cdot \hat{n}_j}{\hat{n}_i \cdot \hat{n}_j}\right) & \begin{array}{l}\text{for angle between } \hat{n}_i \\ \text{and } n_j \text{ plate with} \\ \text{plates } i \text{ and } j \\ \text{having a common edge}\end{array} \end{cases} \tag{45b}$$

$$E^i_{\parallel}(Q_E) = \overline{E}^i(\theta_i,\phi_i) \cdot \beta'_o \tag{45c}$$

$$E^i_{\perp}(Q_E) = \overline{E}^i(\theta_i,\phi_i) \cdot \phi' \tag{45d}$$

$$s' = |I| \tag{45e}$$

$$\theta_i = \tan^{-1}\left(\frac{\sqrt{(I_x^2+I_y^2)}}{I_z}\right), \tag{45f}$$

and

$$\phi_i = \tan^{-1}\left(\frac{I_y}{I_x}\right). \tag{45g}$$

The incident field is given by

$$\overline{E}^i(\theta_i,\phi_i) = [\hat{\theta}^i F(\theta_i,\phi_i) + \hat{\phi}^i G(\theta_i,\phi_i)]\,\frac{e^{-jks'}}{s'} \quad .$$

In order to define the diffraction angles it is necessary to define a coordinate system at the diffraction point as illustrated in Figure 15. The three orthogonal unit vectors are $\hat{e}_m$, the unit vector along the edge; $\hat{n}$, the normal to the surface; and $\hat{e}_m' = \hat{n} \times \hat{e}_m$, the vector perpendicular to the edge and lying in the plane of the flat plate. The incident vector direction can now be written in terms of this coordinate system as

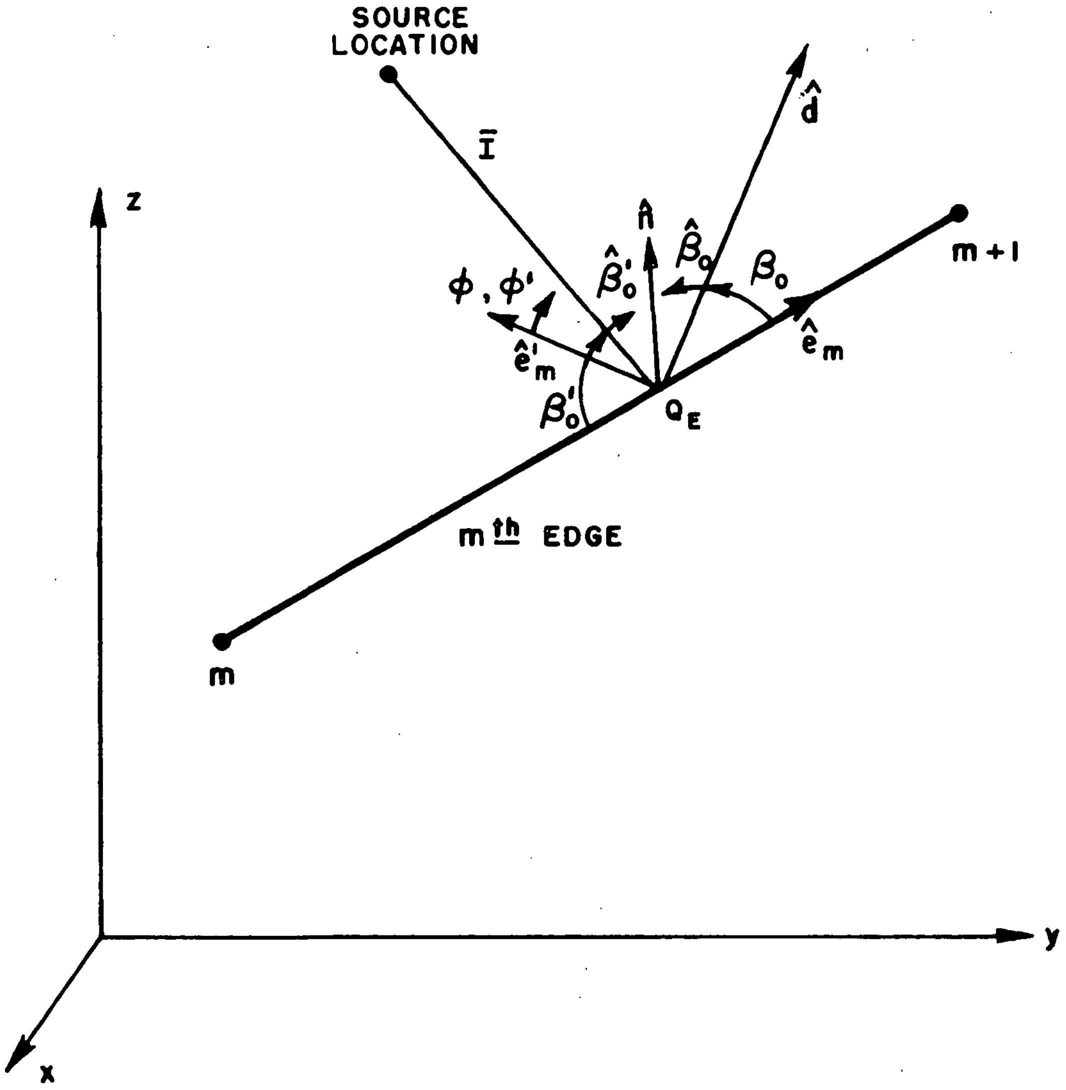

Figure 15--Edge coordinate system at point of diffraction.

$$-\hat{I} = \hat{e}'_m \cos\phi' \sin\beta'_o + \hat{n} \sin\phi' \sin\beta'_o + \hat{e}_m \cos\beta'_o \ .$$

Using the above expression one finds that

$$\phi' = \tan^{-1}\left(\frac{-\hat{I} \cdot \hat{n}}{-\hat{I} \cdot \hat{e}'_m}\right) .$$

The scatter direction unit vector can, also, be decomposed in terms of this coordinate system as

$$\hat{d} = \hat{e}'_m \cos\phi \sin\beta_o + \hat{n} \sin\phi \sin\beta_o + \hat{e}_m \cos\beta_o$$

which results in

$$\phi = \tan^{-1}\left(\frac{\hat{d} \cdot \hat{n}}{\hat{d} \cdot \hat{e}'_m}\right) .$$

The half-cone angle of the diffracted cone of rays is found from

$$\beta_o = \sin^{-1}|\hat{d} \times \hat{e}_m|$$

and the incident cone angle is found from the laws of diffraction to be

$$\beta'_o = \beta_o .$$

The vector directions used to determine the diffracted field are defined by the following expressions:

$$\hat{\phi}' = -\hat{e}'_m \sin\phi' + \hat{n} \cos\phi'$$

$$\hat{\phi} = -\hat{e}'_m \sin\phi + \hat{n} \cos \phi$$

$$\hat{\beta}'_o = \hat{\phi}' \times \hat{I} \quad \text{and} \quad \hat{\beta}_o = \hat{\phi} \times \hat{d}.$$

The total diffracted field from a general mth edge of the jth plate can now be found to be

$$\overline{E}^d_{j,m}(\theta_s,\phi_s) = E^d\hat{\beta}_o + E^d\hat{\phi} \; .$$

The total diffracted field is the superposition of all the diffracted fields from all the edges on the P plates that exist in that direction and is given by

$$\overline{E}^d(\theta_s,\phi_s) = \sum_{j=1}^{P} \sum_{m=1}^{M_j} \overline{E}^d_{j,m}\,(\theta_s,\phi_s). \tag{46}$$

The diffraction from an edge as discussed above is based on an infinite edge. The plates of interest here have finite length edges. The fact that the straight edge diffraction point is lost past the corners of the edge produces a discontinuity that must be compensated for in some way. In the Geometrical Theory of Diffraction this is accomplished using a corner diffraction term. This diffraction mechanism is very small in magnitude except when the source is close to the corner or if the radiation pattern is taken directly across the corner. For wing mounted antennas, this situation occurs frequently enough to warrant the inclusion of this term. As discussed in Chapter II, Section F, the corner diffraction term is available at present as a heuristically derived function. This function has proven to be useful as will be seen below.

The corner diffraction term is assumed to be localized to a small region around the truncation point of the edge, that is, the corner. For each edge on the plates, there are two terms associated with each truncation of the edge. This is illustrated in Figure 16. The diffraction point is found for a given scatter direction using Equations (43a-e). This time, however, the diffraction point is not bound by the finite limits of the edge. It may fall off the edge on an imaginary extension of the real finite edge as shown in Figure 16. Since this term will be small away from the edge, the limits for including the terms associated with the two truncations are given as

$$\frac{(\overline{C}_m-\overline{R}_s)}{|\overline{C}_m-\overline{R}_s|} \cdot \hat{e}_m - 0.1 < \hat{d} \cdot \hat{e}_m < \frac{(\overline{C}_m-\overline{R}_s)}{|\overline{C}_m-\overline{R}_s|} \cdot \hat{e}_m + 0.1 \; ,$$

for the first (mth) corner of the mth edge,

and

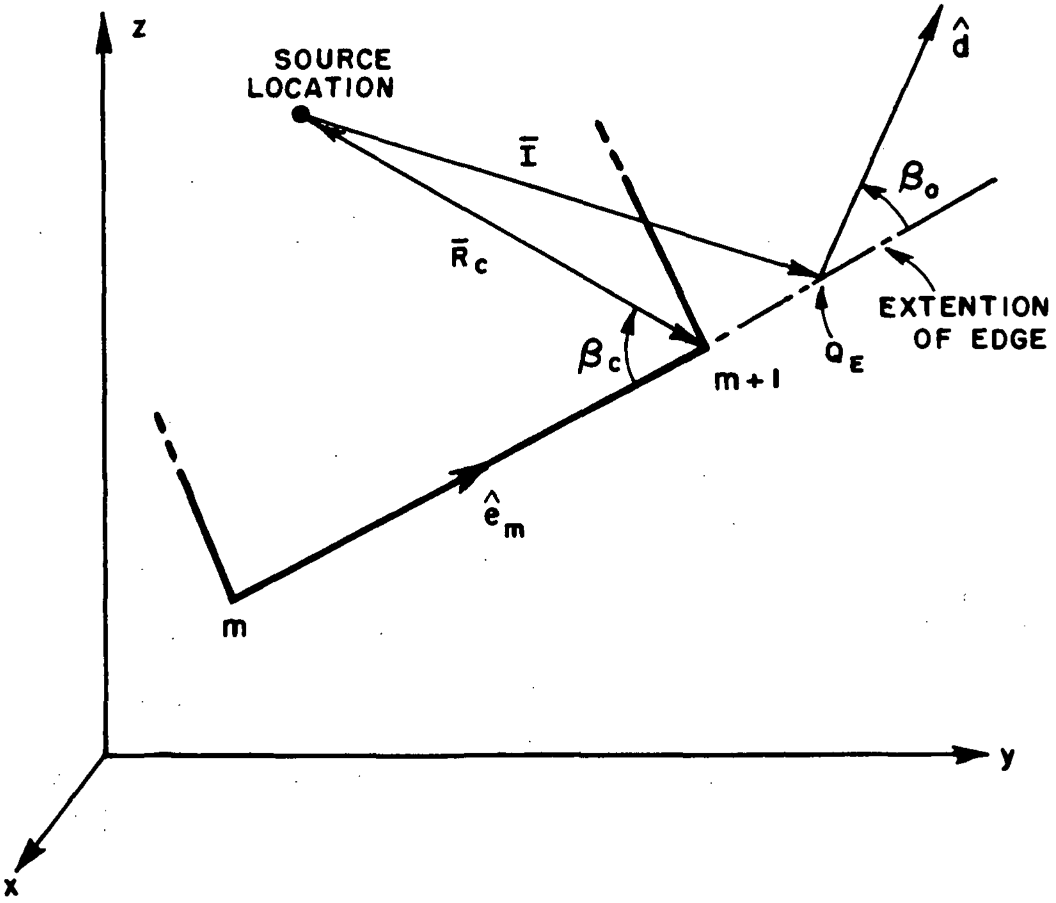

Figure 16--Corner diffracted field geometry.

$$\frac{(\overline{C}_{m+1}-\overline{R}_s)}{|\overline{C}_{m+1}-\overline{R}_s|} \cdot \hat{e}_m - 0.1 < \hat{d} \cdot \hat{e}_m < \frac{(\overline{C}_{m+1}-\overline{R}_s)}{|\overline{C}_{m+1}-\overline{R}_s|} \cdot \hat{e}_m + 0.1 \ ,$$

for the second (m+1st) corner of the mth edge.

This bound has been set heuristically, but it appears to give good results in the cases tried. Once the diffraction point is found, tests are made on the incident direction and scatter direction to see if they are shadowed by any obstacles as was done before.

After it is determined whether the corner terms will contribute to the scatter direction, the terms for the first and second edge truncations of the mth edge are computed from Equation (22a), that is

$$\begin{Bmatrix} E^c_{\parallel} \\ E^c_{\perp} \end{Bmatrix} \sim \begin{Bmatrix} IZ_o \\ MY_o \end{Bmatrix} \frac{\sin\beta_c \, e^{-j\frac{\pi}{4}}}{2\pi(\cos\beta_o - \cos\beta_c)} F[ks_c a(\beta_o - \beta_c)]$$

$$\times \frac{e^{-jks_c}}{\sqrt{s_c}} \, e^{jk\overline{R}_d \cdot \hat{d}} \, \frac{e^{-jkd}}{d} \qquad (47)$$

for a scatter direction in the far field. The quantities I and M are defined in Equations (22b and c).

For the jth plate, the mth edge, and the ith truncation (i=1 or 2) the corner diffracted field can be written as

$$\overline{E}^c_{j,m,i}(\theta_s,\phi_s) = E^c_{\parallel}\,\hat{\beta}_o + E^c_{\perp}\,\hat{\phi}.$$

All the variables are defined as in the discussion for the edge diffraction term defined previously, except for the terms that follow. For the first truncation point (mth corner),

$$\overline{R}_c = \overline{R}_s - \overline{C}_m$$

$$s_c = |\overline{R}_c|$$

$$\cos \beta_c = \frac{\overline{R}_c}{|\overline{R}_c|} \cdot \hat{e}_m$$

$$z' = \overline{C}_m - \overline{R}_d \quad .$$

For the second truncation point (m+1st corner),

$$\overline{R}_c = \overline{R}_s - \overline{C}_{m+1}$$

$$s_c = |\overline{R}_c|$$

$$\cos \beta_c = \frac{\overline{R}_c}{|\overline{R}_c|} \cdot (-\hat{e}_m)$$

$$z' = \overline{C}_{m+1} - \overline{R}_d \; .$$

The corner diffraction term is not presently applicable to corners that are formed by the junction of two plates. The corner term is neglected when this case arises. The total corner diffracted fields of all the corner diffracted fields that exist in the scatter direction is given by

$$\overline{E}^c(\theta_s,\phi_s) = \sum_{j=1}^{P} \sum_{m=1}^{M_j} \sum_{i=1}^{2} \overline{E}^c_{j,m,i} \, (\theta_s,\phi_s). \tag{48}$$

The four terms discussed above comprise all the mechanisms needed to determine the scattered fields for a single plate. The total radiated field in the presence of a single plate is given, using Equations (29), (41), (46), and (48), by

$$\overline{E}(\theta_s,\phi_s) = \overline{E}^i(\theta_s,\phi_s) + \overline{E}^r(\theta_s,\phi_s) + \overline{E}^d(\theta_s,\phi_s) + \overline{E}^c(\theta_s,\phi_s) \; .$$

This solution has been compared with measured results using a short dipole antenna mounted above a flat square plate [23]. This is illustrated in Figure 17 for a dipole mounted above the center of the square plate. To illustrate the effect of including the slope diffraction term, Figure 18 compares the radiated field of a short slot mounted on a plate with and without the slope diffraction term. The effects of the corner diffraction term is shown by obtaining the radiation pattern across the corners of a square plate using a short monopole mounted at the center of the plate, as shown in the insert of Figure 19. The radiation pattern with and without corner diffraction is compared in Figure 19. Note that the discontinuity is completely eliminated. The radiation pattern with corner diffraction is compared with an experimental result in Figure 20. The good agreement in the comparison would tend to confirm the approximation made in the corner diffraction coefficient.

If more than one plate is desired, the interaction between the plates must be included. These higher order terms are obtained in a step by step manner similar to the analysis carried out for the mechanisms discussed above. First, the double reflected fields will be discussed. The double reflected field, as illustrated in Figure 21, can be viewed as a field emanating from a second image obtained by reflecting the first image of the jth plate into the kth plate, that is

$$\overline{R}_{ii} = \overline{R}_i - 2\,[\hat{n}_k \cdot (\overline{R}_i - \vec{C}_{kl})]\hat{n}_k$$

where $\overline{R}_i$ is obtained from Equation (33) for the jth plate and $\hat{n}_{\underline{k}}$ refers to the normal of the kth plate. The ray emanating from $\overline{R}_{ii}$ in the scatter direction $\hat{d}$ must be tested to see if it hits the kth plate. This is done using the procedure outlined in Equations (30-32). If a hit does occur the analysis proceeds to the next step which is to find the incident ray

$$\hat{I}_k = \hat{d} - 2(\hat{n}_k \cdot \hat{d})\hat{n}_k.$$

The ray emanating from $\overline{R}_i$ in the direction $\hat{I}_k$ must be tested to see if it hits the jth plate as was done above. The incident field on the jth plate is then found from

$$\hat{I} = \hat{I}_k - 2(\hat{n}_j \cdot \hat{I}_k)\hat{n}_j \ .$$

Of course, each of the rays must be tested to see that they are not shadowed by any other plate.

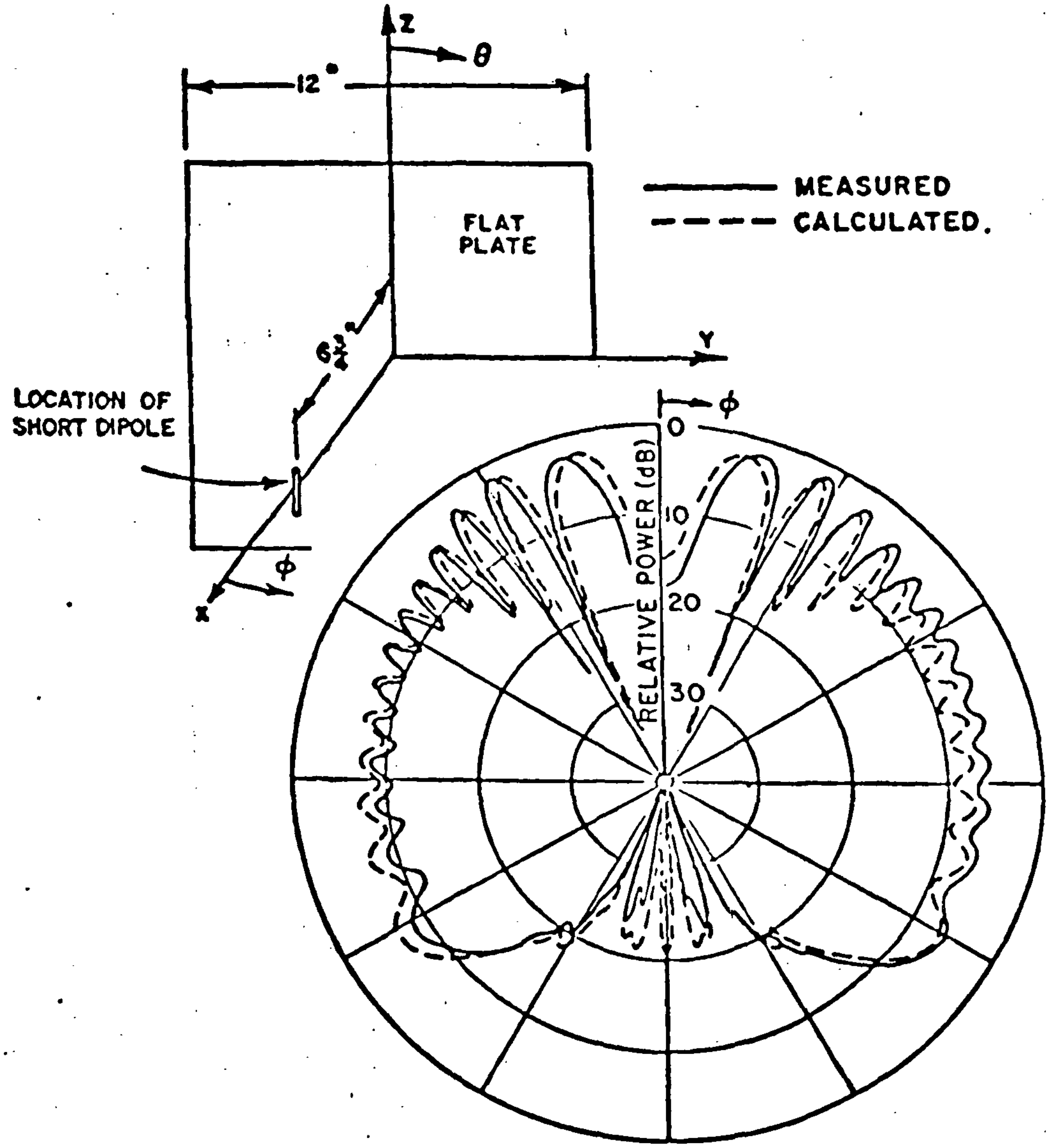

Figure 17--E_θ radiation pattern for a small dipole mounted above a square plate for $\theta_s = 90°$ and $0 \leq \phi_s \leq 360°$ at freq. = 10.43 GHz.

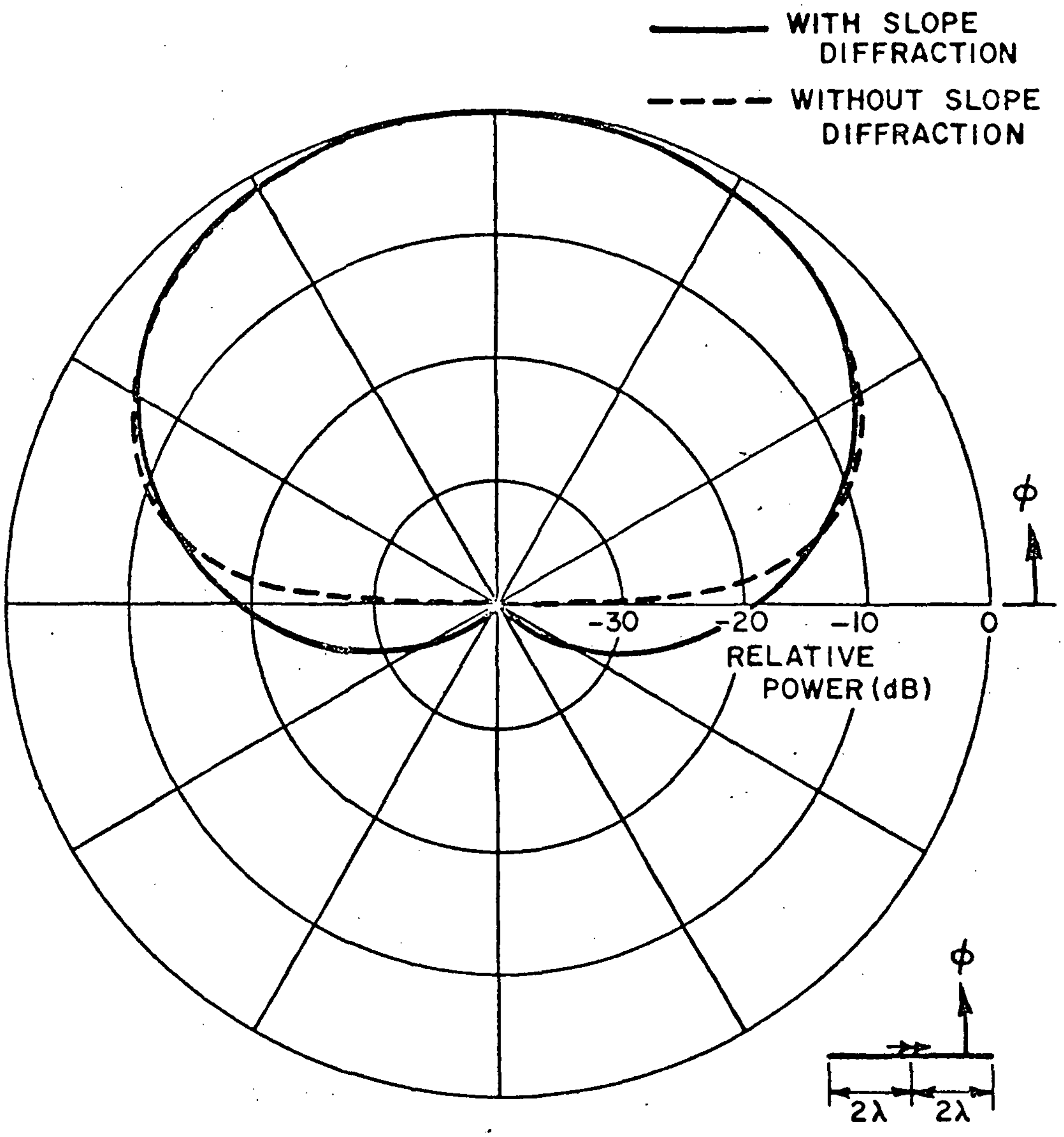

Figure 18--Comparison of the E_θ radiation pattern of a strip slot on a plate with and without slope diffraction.

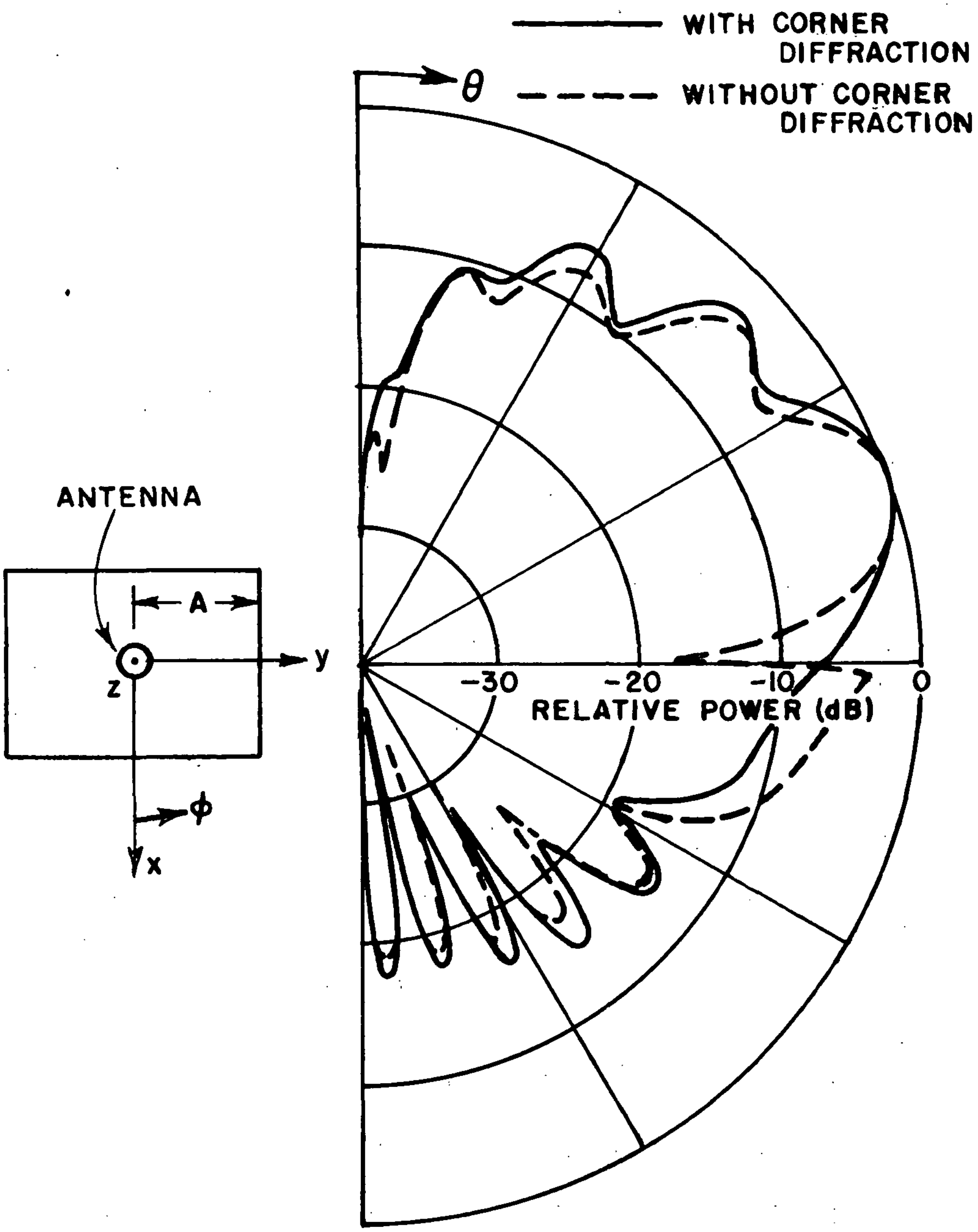

Figure 19--Comparison of the E_θ radiation pattern of a short monopole on a square plate (A=4λ) with or without corner diffraction taken in the plane φ =45°.

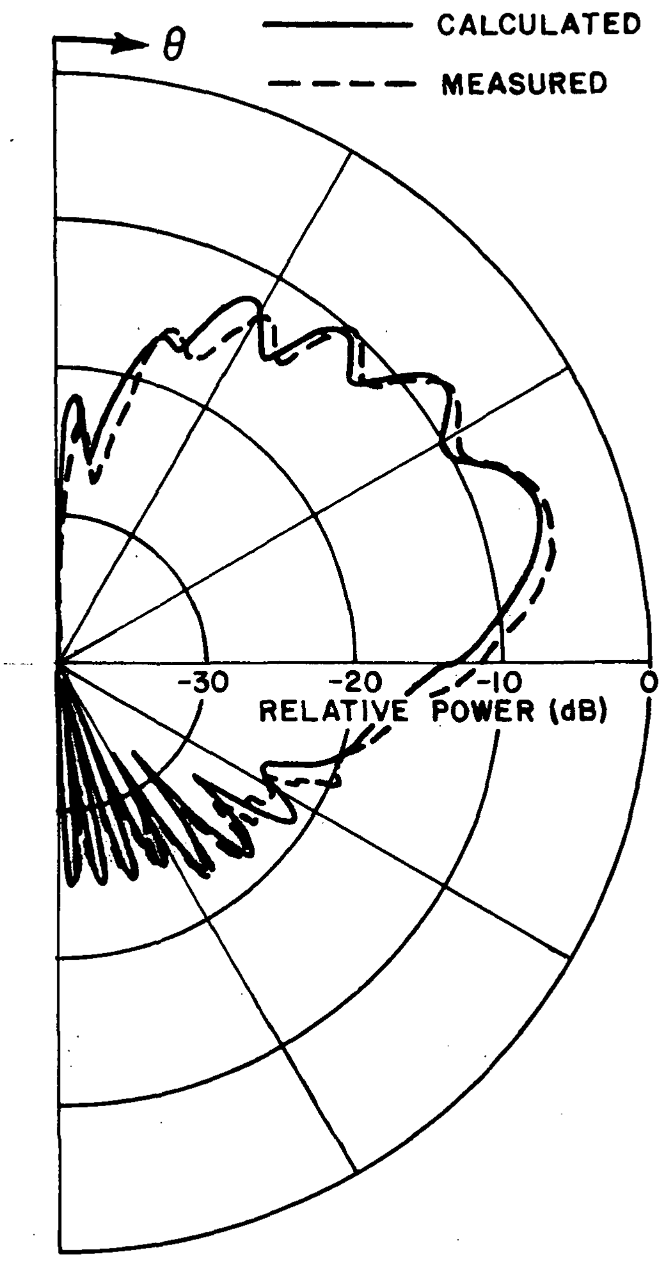

Figure 20--Comparison of the calculated and measured E_θ radiation pattern of a short monopole on a square plate ($A=5.51\lambda$) taken in the plane $\phi=45°$.

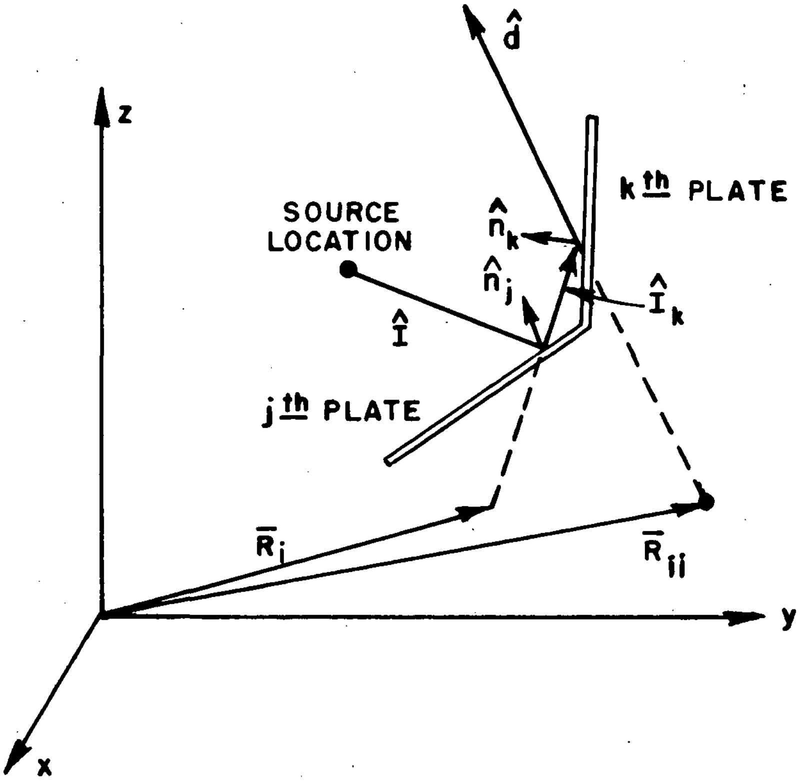

Figure 21--Doubly reflected field geometry.

The doubly reflected field can now be obtained, if all of the tests determine that a field exists. First, the reflected field is obtained from the jth plate as was done in Equations (34-40), except with θ_{ki},ϕ_{ki} substituted for θ_s,ϕ_s where

$$\hat{I}_k = I_{kx}\hat{x} + I_{ky}\hat{y} + I_{kz}\hat{z}$$

$$\theta_{ki} = \tan^{-1}\left(\frac{\sqrt{I_{kx}^2 + I_{ky}^2}}{I_{kz}}\right)$$

$$\phi_{ki} = \tan^{-1}\left(\frac{I_{ky}}{I_{kx}}\right) \quad .$$

This means that the reflected field from the jth plate, which is the incident field on the kth plate, is given by

$$\overline{E}_j^r(\theta_{ki},\phi_{ki}) = [\hat{\theta}_k^i F^r(\theta_{ki},\phi_{ki}) + \hat{\phi}_k^i G^r(\theta_{ki},\phi_{ki})] \frac{e^{-jks'}}{s'} \quad .$$

The boundary conditions on the kth plate are satisfied such that the doubly reflected field is found. In matrix notation this can be written as

$$\begin{bmatrix} \hat{n}_k\cdot\hat{\theta}^s & \hat{n}_k\cdot\hat{\phi}^s \\ \hat{t}_k\cdot\hat{\theta}^s & \hat{t}_k\cdot\hat{\phi}^s \end{bmatrix} \begin{bmatrix} F^{rr} \\ G^{rr} \end{bmatrix} = \begin{bmatrix} A^n \\ -A^t \end{bmatrix}$$

where

$$\begin{bmatrix} \hat{n}_k\cdot\hat{\theta}_k^i & \hat{n}_k\cdot\hat{\phi}_k^i \\ \hat{t}_k\cdot\hat{\theta}_k^i & \hat{t}_k\cdot\hat{\phi}_k^i \end{bmatrix} \begin{bmatrix} F^r \\ G^r \end{bmatrix} = \begin{bmatrix} A^n \\ A^t \end{bmatrix} .$$

Thus, solving the above expression for the unknown reflected field gain functions gives

$$F^{rr} = \frac{(\hat{t}_k\cdot\hat{\phi}^s)A^n + (\hat{n}_k\cdot\hat{\phi}^s)A^t}{(\hat{n}_k\cdot\hat{\theta}^s)(\hat{t}_k\cdot\hat{\phi}^s) - (\hat{n}_k\cdot\hat{\phi}^s)(\hat{t}_k\cdot\hat{\theta}^s)}$$

$$G^{rr} = \frac{-[(\hat{n}_k\cdot\hat{\theta}^s)A^t + (\hat{t}_k\cdot\hat{\theta}^s)A^n]}{(\hat{n}_k\cdot\hat{\theta}^s)(\hat{t}_k\cdot\hat{\phi}^s) - (\hat{n}_k\cdot\hat{\phi}^s)(\hat{t}_k\cdot\hat{\theta}^s)} .$$

In the far field the reflected field from the kth plate after its original reflection from the jth plate can be written as

$$\overline{E}_{jk}^{rr}(\theta_s,\phi_s) = [\hat{\theta}^s F^{rr}(\theta_s,\phi_s) + \hat{\phi}^s G^{rr}(\theta_s,\phi_s)]e^{jk\overline{R}_{ii}\cdot\hat{d}}\,\frac{e^{-jkd}}{d} .$$

The total double reflected field from the P plates is, then, given by

$$\vec{E}^{rr}(\theta_s,\phi_s) = \sum_{\substack{j=1 \\ j\neq k}}^{P} \sum_{k=1}^{P} \overline{E}_{jk}^{rr}(\theta_s,\phi_s), \tag{49}$$

for all the $\overline{E}_{jk}^{rr}$ fields that are not shadowed. Note that there is no double reflection off of the same plate, i.e., when j=k.

The fact that the kth plate has finite limits is compensated by a diffraction term off the M_k edges of the kth plate. Thus, the reflected field from the jth plate must create diffracted fields from the edges composing the kth plate. This reflected-diffracted term is illustrated in Figure 22. In this case, as in the previous case, the reflected field from the jth plate and its image $\bar{R}_i$ may be substituted into the needed equations for the incident field and source point, respectively. That is, bounds for the diffraction point on the mth edge of the kth plate are obtained from

$$\frac{(\bar{C}_{k,m}-\bar{R}_i)}{|\bar{C}_{k,m}-\bar{R}_i|} \cdot \hat{e}_m < \hat{d} \cdot \hat{e}_m < \frac{(\bar{C}_{k,m+1} - \bar{R}_i)}{|\bar{C}_{k,m+1} - \bar{R}_i|} \cdot \hat{e}_m$$

as in Equation (42). The diffraction point $\bar{R}_d$ is found from Equation (43a-e), with $\bar{R}_i$ substituted for $\bar{R}_s$. The incident vector on the edge is given by $\bar{I}_k = \bar{R}_d - \bar{R}_i$.

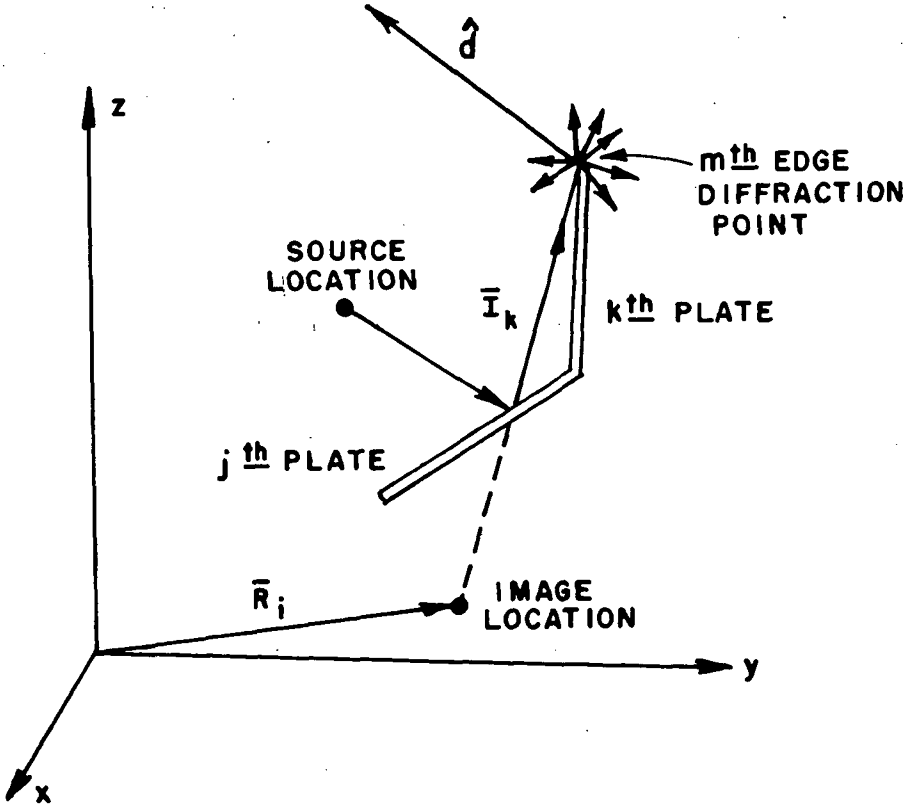

Figure 22--Reflected-diffracted field geometry.

Once the existence tests on the rays are performed, the reflected-diffracted field can be found from

$$\begin{bmatrix} E_{\parallel}^{rd} \\ \\ E_{\perp}^{rd} \end{bmatrix} \sim \begin{bmatrix} -D_s & 0 \\ \\ 0 & -D_h \end{bmatrix} \begin{bmatrix} E_{\parallel}^{r}(Q_E) \\ \\ E_{\perp}^{r}(Q_E) \end{bmatrix} \sqrt{s'}\ e^{jk\,\bar{R}_d \cdot \hat{d}}\ \frac{e^{-jkd}}{d} \quad .$$

Note that the slope term has not been used here. This is due to the fact that the slope term did not appear to be a significant contributor to the fields for the geometries of interest. The incident field (reflected field from the jth plate) on the edge is given by, Equation (40),

$$\bar{E}_j^r(Q_E) = [\hat{\theta}_k^i F^r(\theta_{ki},\phi_{ki}) + \hat{\phi}_k^i G^r(\theta_{ki},\phi_{ki})]\ \frac{e^{-jks'}}{s'}$$

in which case

$$E_{\parallel}^r(Q_E) = \bar{E}_j^r(\theta_{ki},\phi_{ki}) \cdot \hat{\beta}_o'$$

$$E_{\perp}^r(Q_E) = \bar{E}_j^r(\theta_{ki},\phi_{ki}) \cdot \hat{\phi}'$$

$$s' = |\vec{I}_k|$$

$$\theta_{ki} = \tan^{-1}\left(\frac{\sqrt{I_{kx}^2 + I_{ky}^2}}{I_{kz}}\right)$$

$$\phi_{ki} = \tan^{-1}\left(\frac{I_{ky}}{I_{kx}}\right) \quad .$$

All the other parameters are as determined previously.

The reflected-diffracted field from the mth edge of the kth plate is then given as

$$\bar{\vec{E}}^{rd}_{j,k,m}(\theta_s,\phi_s) = E^{rd}_{\parallel}\hat{\beta}_o + E^{rd}_{\perp}\,\hat{\phi}.$$

The total reflected-diffracted field of all the reflected-diffracted fields that exist is given by

$$\bar{\vec{E}}^{rd}(\theta_s,\phi_s) = \sum_{\substack{j=1\\ j\neq k}}^{P} \sum_{k=1}^{P} \sum_{m=1}^{M_k} \bar{E}^{rd}_{j,k,m}(\theta_s,\phi_s)\ . \tag{50}$$

The same procedure for the reflected-diffracted field is applied to the reflected-corner diffracted field so it will not be discussed in detail here. This field is illustrated in Figure 23. The corner diffracted term for the mth edge on the kth plate is found from Equation (47) with the reflected field of the jth plate given by Equation (34) used as the incident field. The total corner diffracted field in the scatter direction is given by

$$\bar{\vec{E}}^{rc}(\theta_s,\phi_s) = \sum_{\substack{j=1\\ j\neq k}}^{P} \sum_{k=1}^{P} \sum_{m=1}^{M_k} \sum_{i=1}^{2} \bar{E}^{rc}_{j,k,m,i}(\theta_s,\phi_s). \tag{51}$$

The diffracted field of the mth edge on the jth plate can be reflected by another plate (call it the kth plate). This diffracted-reflected field is, in general, of the same order of magnitude as the reflected-diffracted field discussed above. This field type is illustrated in Figure 24.

The diffracted point for the mth edge on the jth plate, if it exists, is found using Equation (43a-e), where $\hat{I}_k$ must be substituted for $\hat{d}$. The diffraction direction in this case is the incident direction for reflection of the kth plate and is given by

$$\hat{I}_k = \hat{d} - 2(\hat{n}_k \cdot \hat{d})\hat{n}_k.$$

Once the diffraction point $\bar{R}_d$ is found the imaged diffraction point is given by

$$\bar{R}_{di} = \vec{R}_d - 2(\hat{n}_k \cdot \bar{R}_d)\hat{n}_k.$$

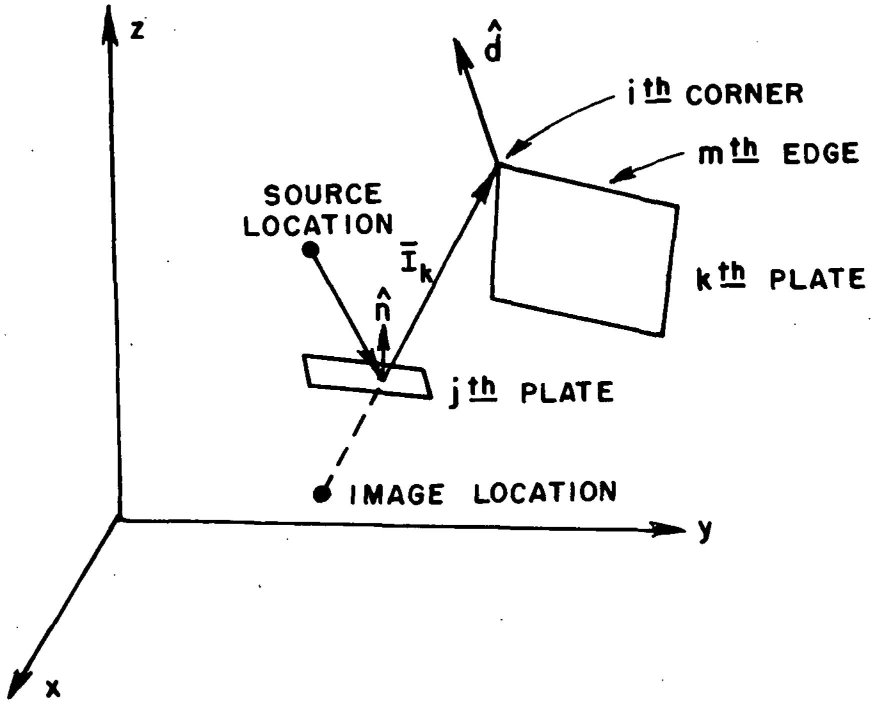

Figure 23--Reflected-corner diffracted field geometry.

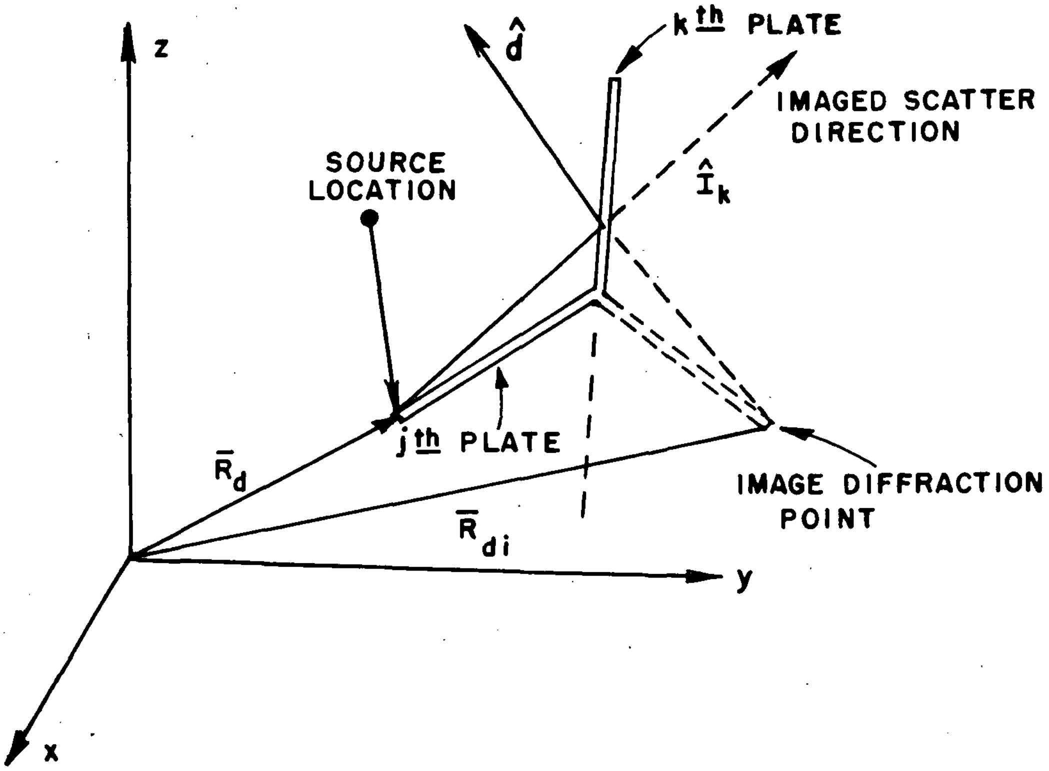

Figure 24--Diffracted-reflected field geometry.

The imaged diffraction point is then used to see if a reflected field exists by virtue of an incident ray hit on the plate. The diffracted field can then be found from Equations (44 and 45a-g), with the appropriate incident direction for the incident field and diffraction direction for the diffracted field. In this case, the slope term is not included. This diffracted field can now be used in Equations (38-40) as the incident field for the reflection mechanism. The details will not be given here.

In the far-field the reflected field of the kth plate from the diffracted field of mth edge on the jth plate is given by

$$\vec{E}^{dr}_{j,m,k}(\theta_s,\phi_s) = [\hat{\theta}^s F^{dr}(\theta_s,\phi_s) + \hat{\phi}^s G^{dr}(\theta_s,\phi_s)] e^{jk\vec{R}_{di}\cdot\hat{d}} \frac{e^{-jkd}}{d} .$$

The total diffracted-reflected field of all the diffracted-reflected fields that exist is given by

$$\vec{E}^{dr}(\theta_s,\phi_s) = \sum_{j=1}^{P} \sum_{\substack{m=1\\ j\neq k}}^{M_j} \sum_{k=1}^{P} \vec{E}^{dr}_{j,m,k}(\theta_s,\phi_s) , \tag{52}$$

where $\vec{E}^{dr}_{j,m,k} = 0$ if the incident, diffracted, or reflected ray is shadowed by any obstacle.

In certain cases, another higher order term can be significant. This is a double diffracted term, illustrated in Figure 25. This term is normally small unless the two edges and the source are close together or one of the edges lies in the shadow boundary of the other edge. In general, this is a fairly complicated ray tracing problem without producing results that are significant to the total field. When the two edges lie in the same plane, the problem simplifies somewhat; however, the results are still not significant except for small angular regions about the shadow boundary. The problem as to when it is necessary to compute this term for a general structure, is under investigation. The double diffracted term has not been added at this time and there has not been substantial deterioration of the patterns.

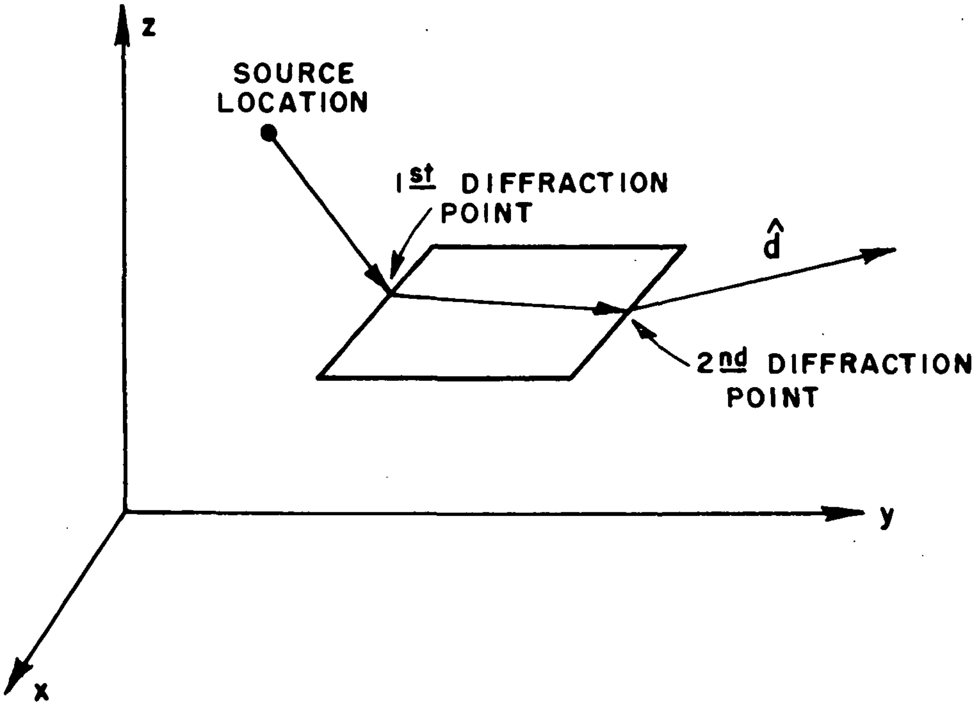

Figure 25--Double diffracted field geometry.

The total field for a source in the presence of a number of plates can now be approximated by superimposing the individual scattered fields listed in Table II, as

$$\vec{E}(\theta_s,\phi_s) = \vec{E}^i + \vec{E}^r + \vec{E}^d + \vec{E}^c + \vec{E}^{rr} + \vec{E}^{rd} + \vec{E}^{rc} + \vec{E}^{dr}. \quad (53)$$

This represents the sum of the most significant terms for a number of plates that are fairly widely separated. In the case of plates with common edges, the angle between the plates should be great enough not to produce a large number of multiple reflections. There is the possibility that other terms will be significant for particular geometrical configurations. These are seen as discontinuities in the pattern. However, using the above prescription, these rays may be identified and included in the total field. An engineering judgment must be made as to whether the time expended in obtaining these higher order terms will produce a corresponding benefit in the final result.

This solution can be used in a wide variety of ways. To illustrate a simple case, this solution is compared with results obtained using the newly developed moment method patch technique [7] as illustrated in Figures 26a and b and 27a and b. Note that for these comparisons the plate dimensions are quite small in terms of the wavelength to accommodate an overlap between the low frequency patch solution and the higher frequency GTD solution. This accounts for the discontinuities in the patterns using the present GTD solution.

More complicated structures can also be analyzed using this solution. For example, the scattering from a building or a ship can be modelled using flat plates. In this study, the plates are used as models for the wings and horizontal and vertical stabilizers of aircraft. They could also be used to model the wing flap, or the stores and engines on the aircraft. Even more complicated structures such as the fuselage of the aircraft can be modelled in a crude way. Such a model was constructed for an F-4 aircraft with a slot mounted on its wing before the more advanced model using an elliptic cylinder discussed in Chapter V was developed [22].

The fuselage of an F-4 aircraft is modelled as a 10-sided flat plate as illustrated in Figure 28. The wing is modelled as in Figure 29, with a 17.5° bend between the two sections about the common edges numbered 11' and 13'. In order to check the validity of the approximation made in the flat plate model of the F-4, experimental measured patterns were taken at the Naval Weapons Center using a scale model of an F-4 aircraft, shown in Figure 30. Four different pattern cuts were made as illustrated in Figures 31a-d. Five different antenna locations on the wing were used as shown in Figure 32. The antenna was a single cavity-backed slot of length 0.748λ in free space with only the first waveguide mode excited. The comparison of experimental and calculated main beam elevation plane pattern results (refer to Figure 31a) for the slot placed at a 45° angle with respect to the fuselage axis at locations #2 and #4 are shown in Figures 33a and b, respectively. The pattern in the main beam roll plane (Figure 31c) for an antenna at location #2 is shown in Figure 33c. The elevation plane pattern (Figure 31b) for slot antenna location #2 is shown in Figure 33d and its roll plane pattern (Figure 31a) is shown in Figure 33e. At the time of the comparisons the slope diffraction, corner diffraction, and double diffraction fields had not been added. The resulting discontinuities are marked on the patterns for illustrative purposes. The overall character of the measured and calculated patterns appear to agree; however, the finer details of the patterns do not compare very well.

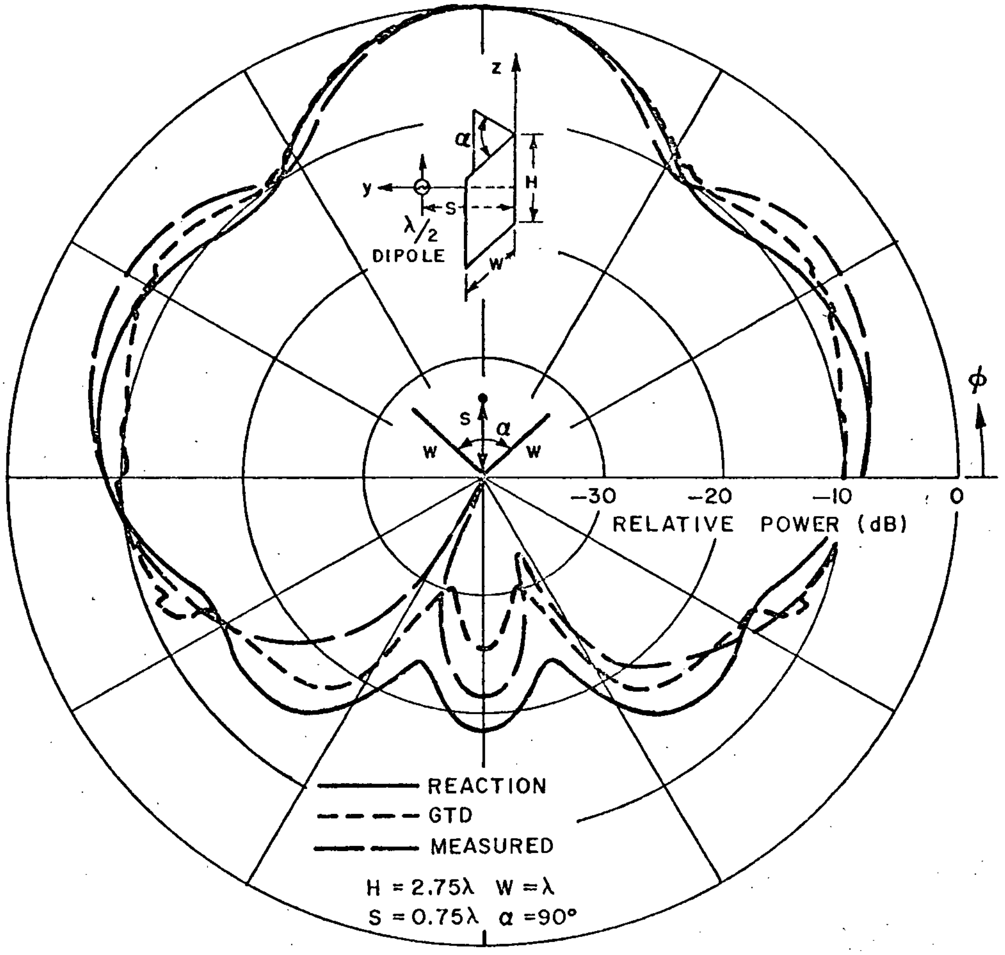

Figure 26a--Comparison of measured, reaction and GTD calculated H-plane pattern results for a λ/2 dipole near a corner reflector.

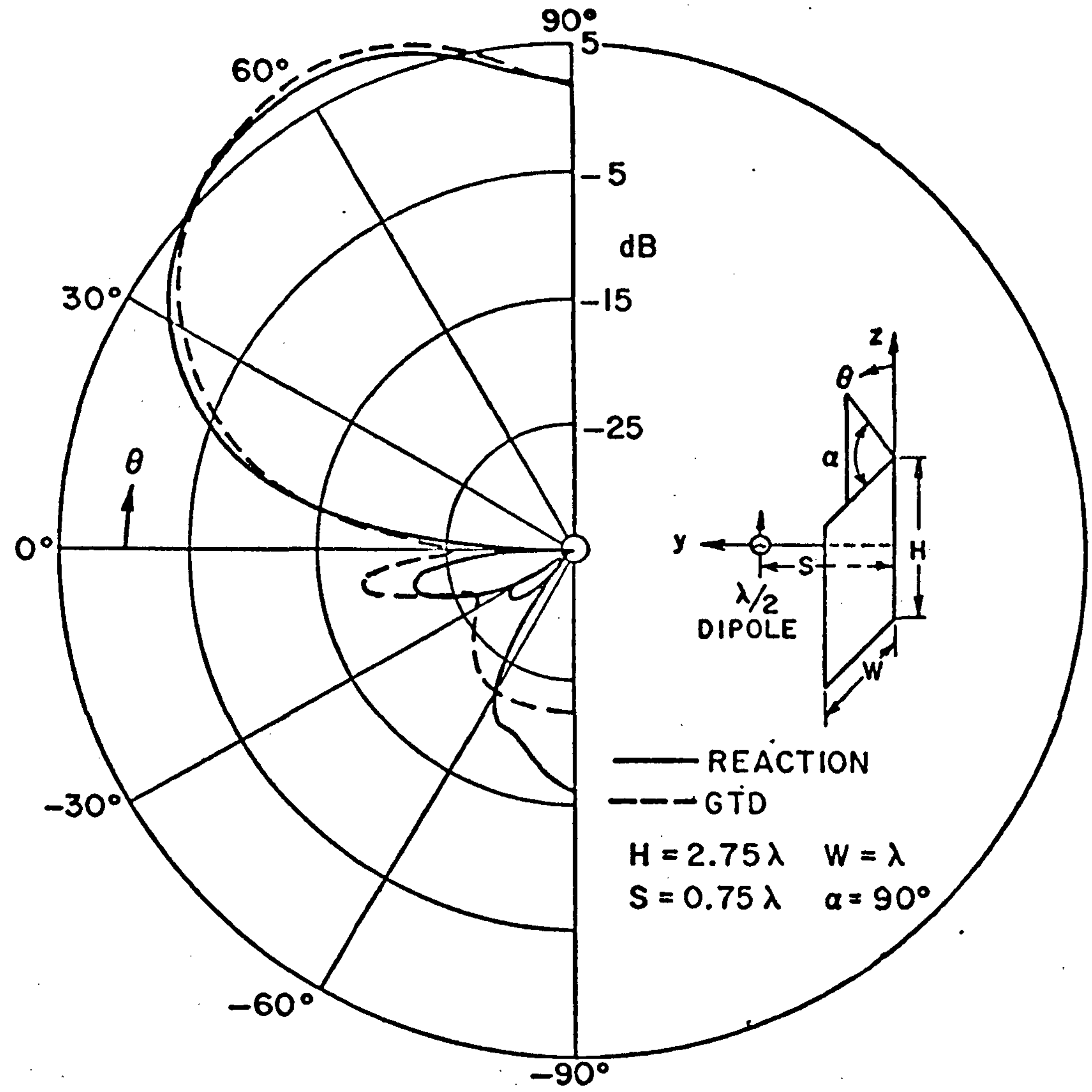

Figure .26b--Comparison of reaction and GTD E-plane pattern results (α=90°).

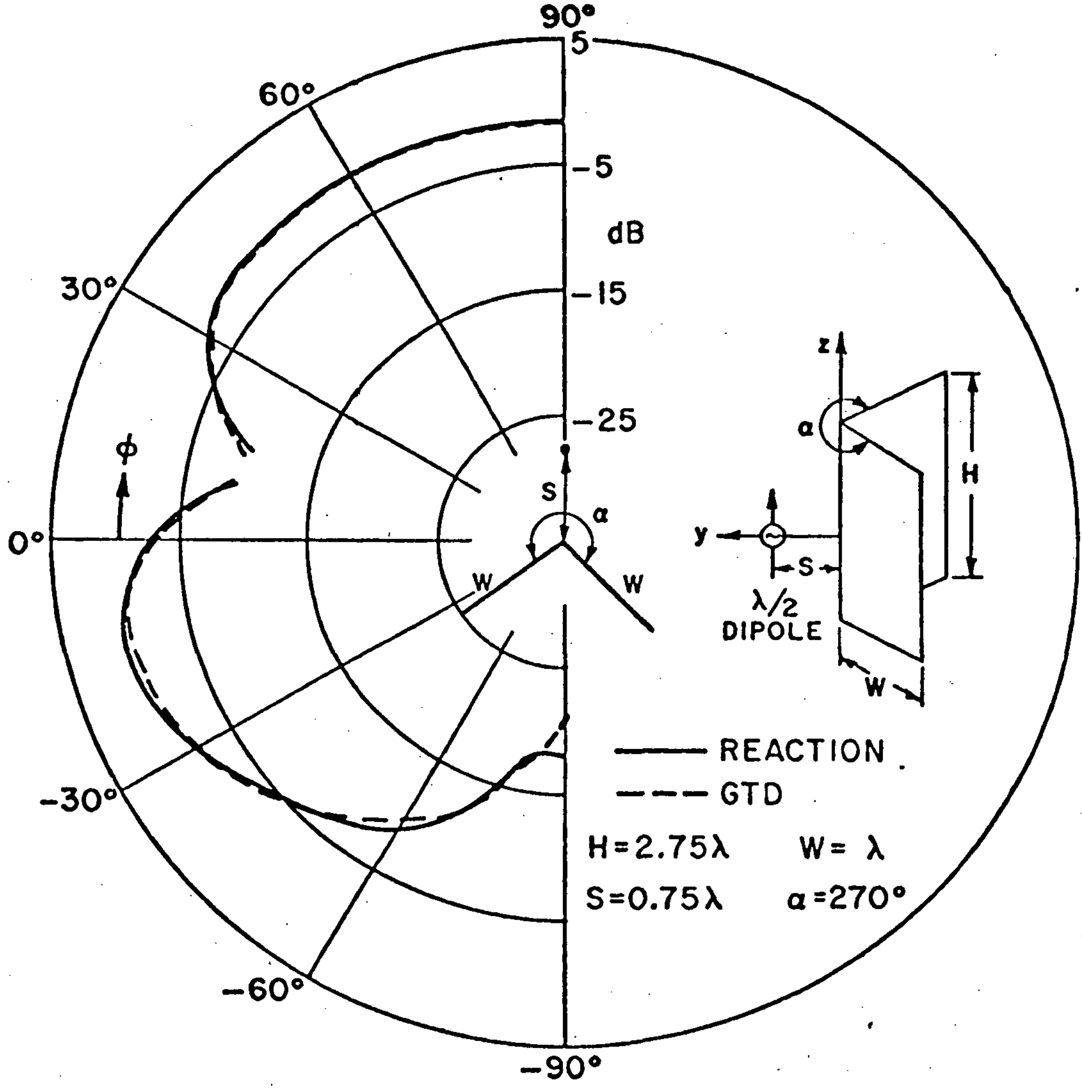

Figure 27a--Comparison of reaction and GTD H-plane pattern results (α=270°).

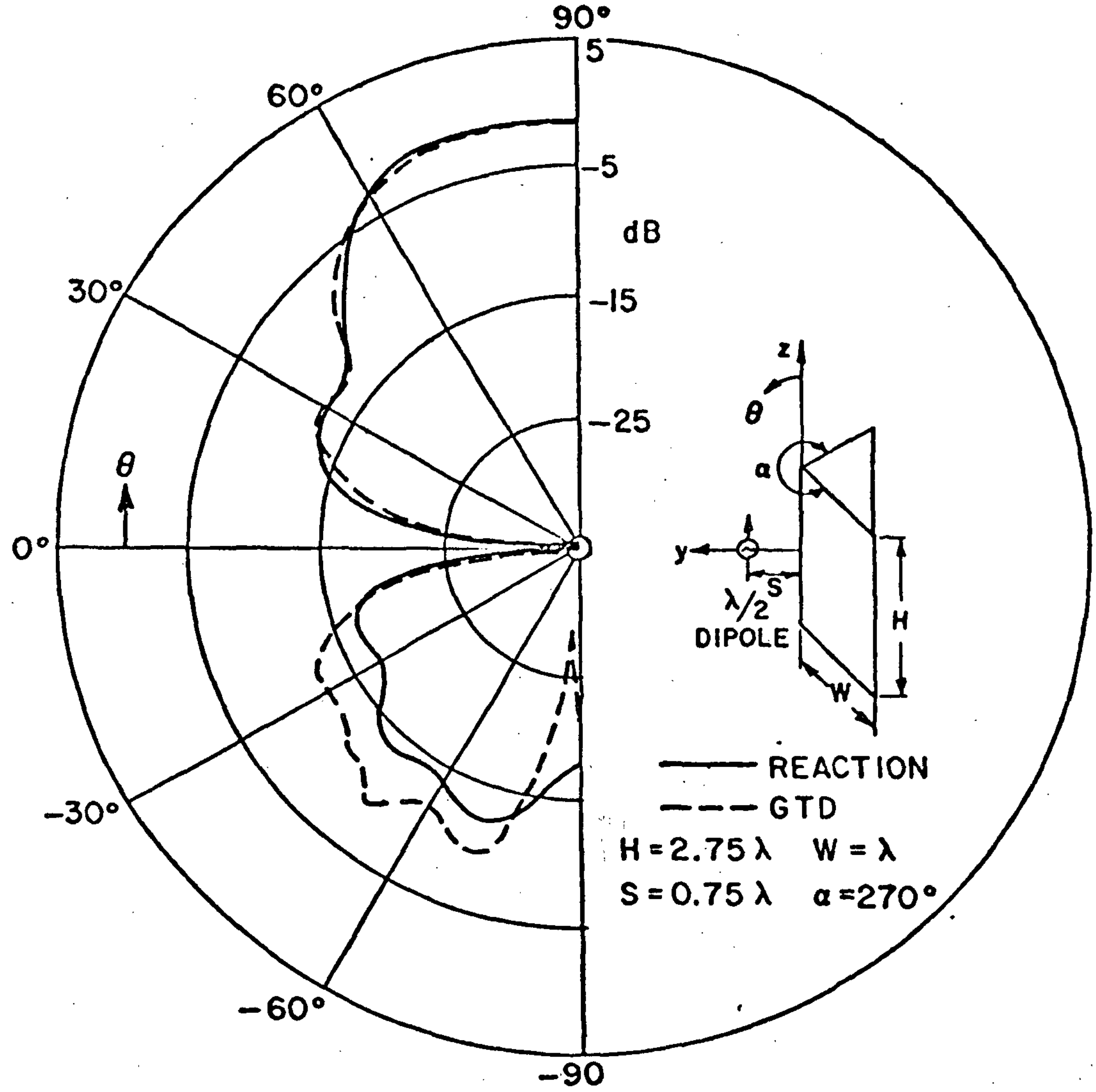

Figure 27b--Comparison of reaction and GTD E-plane pattern results (α=270°).

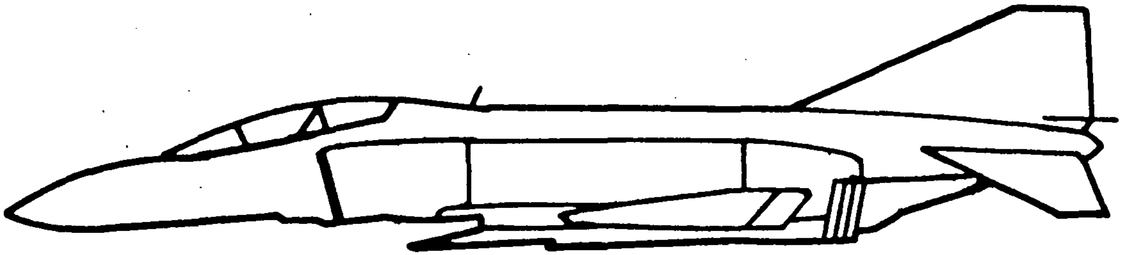

POINT	y	x
1	0.0	0.0
2	0.210	0.045
3	1.650	0.485
4	1.560	1.185
5	1.210	1.220
6	0.090	0.685
7	-1.625	0.700
8	-3.340	0.375
9	-3.310	0.045
10	-1.840	0.090

SCALE 1:126.5

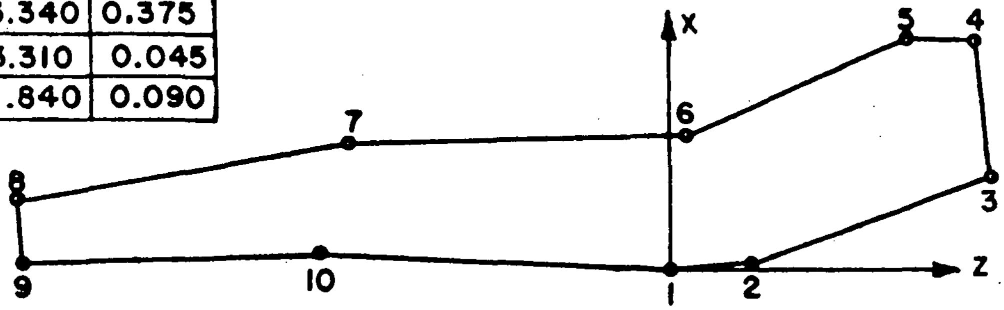

Figure 28--Fuselage geometry for best plate model of F-4 aircraft.

POINT	z	y
10	-1.840	0.0
11	-1.840	0.427
12	-0.240	1.868
13	0,187	1.868
14	-0.050	0.369
15	0.0	0.0
11'	-0.876	1,295
13'	0.0966	1.295

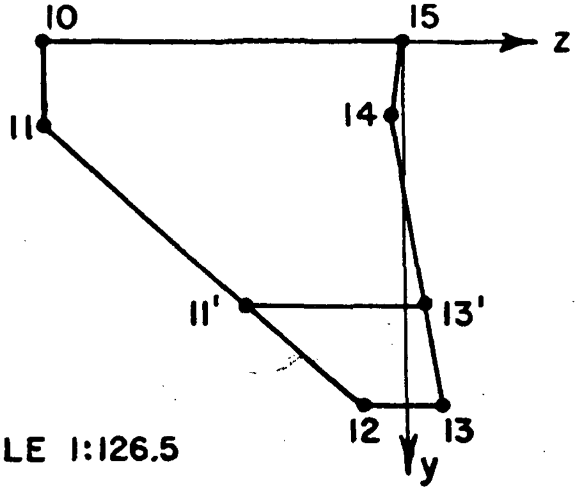

SCALE 1:126.5

Figure 29--Wing geometry of F-4 aircraft bent plate model.

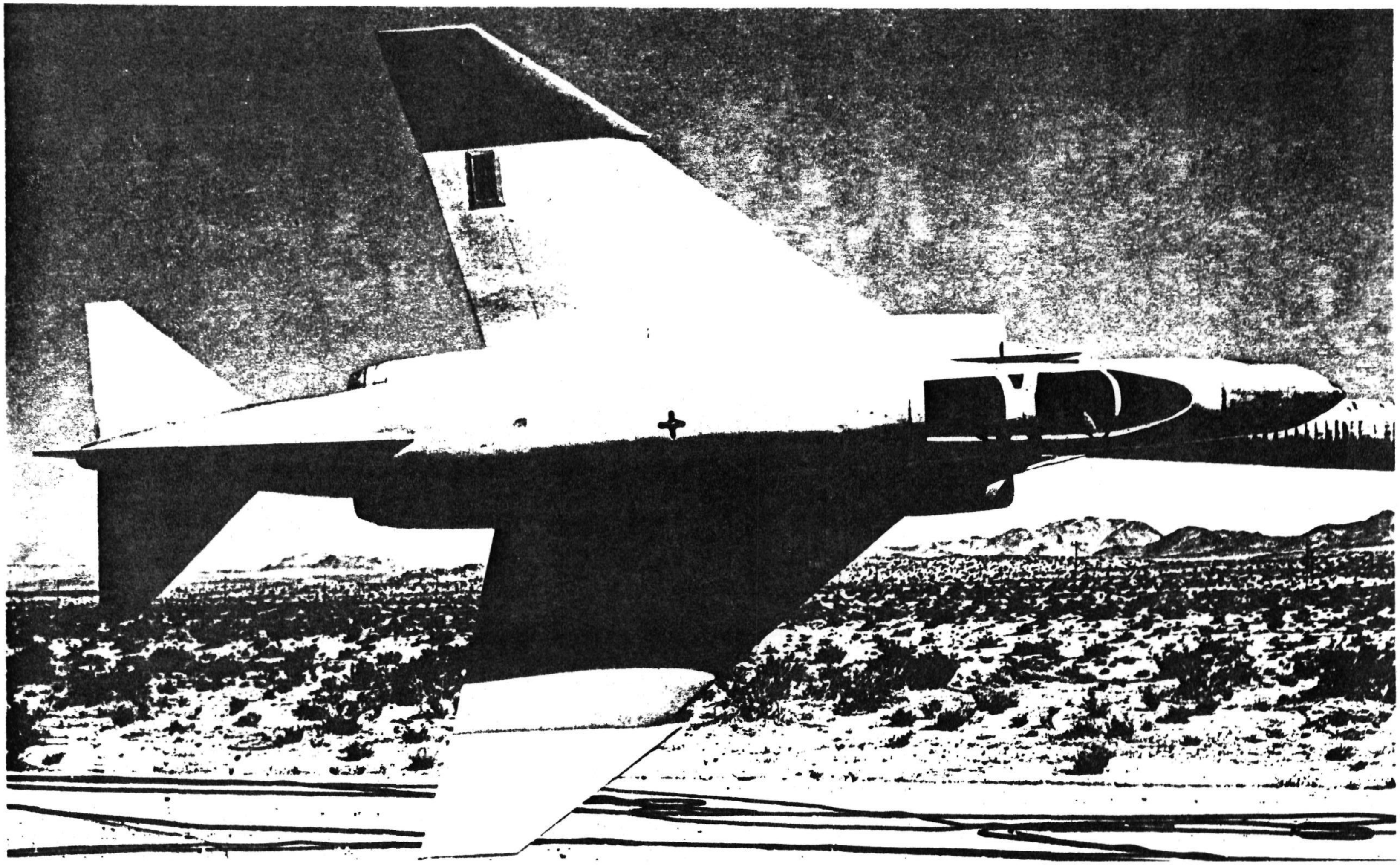

Figure 30--Naval Weapon Center's F-4 aircraft model used in measurements.

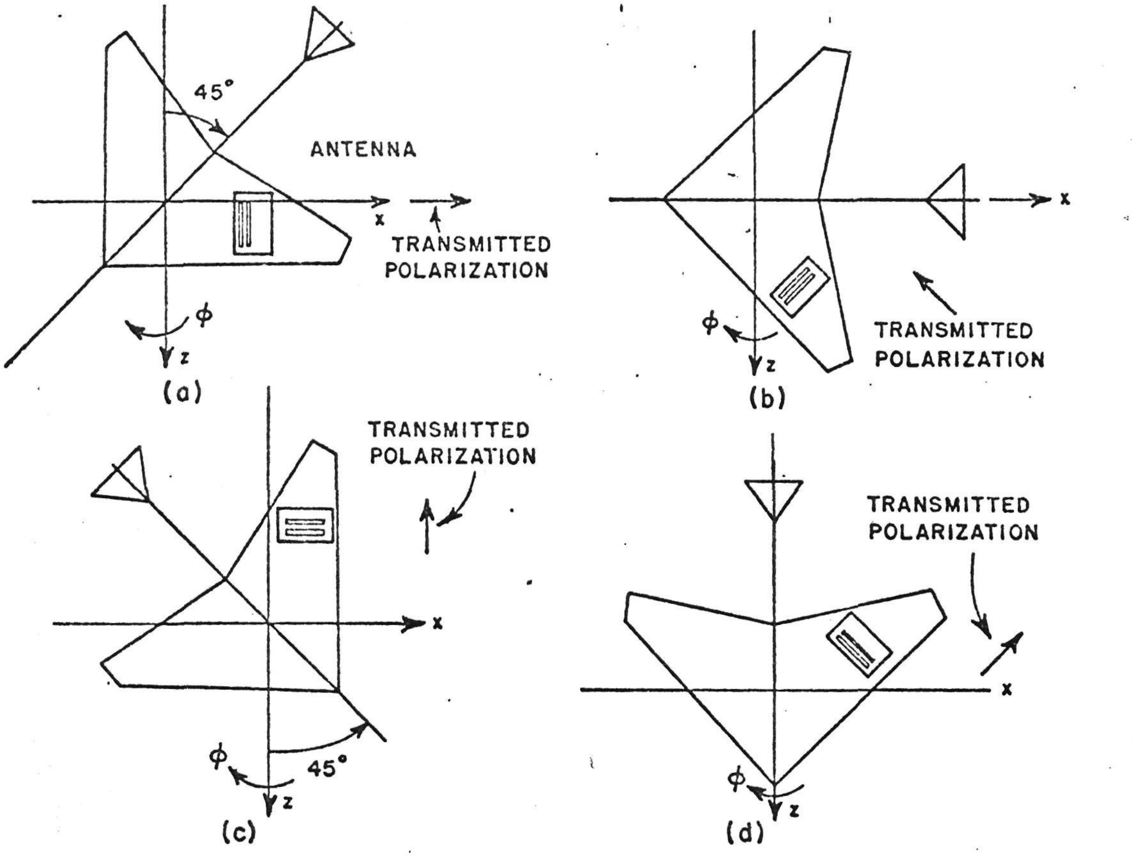

Figure 31--Illustration of pattern cuts and transmitted polarization for measured results:
(a) main beam elevation plane;
(b) elevation plane;
(c) main beam roll plane;
(d) roll plane.

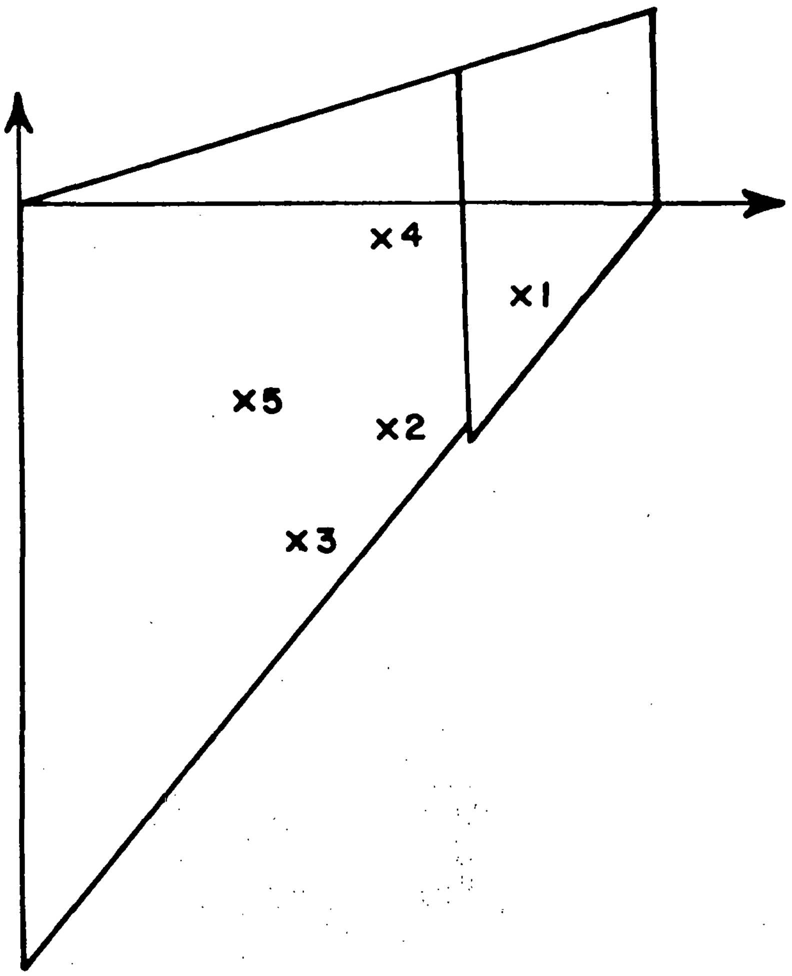

Figure 32--Antenna locations on F-4 wing used in measured results.

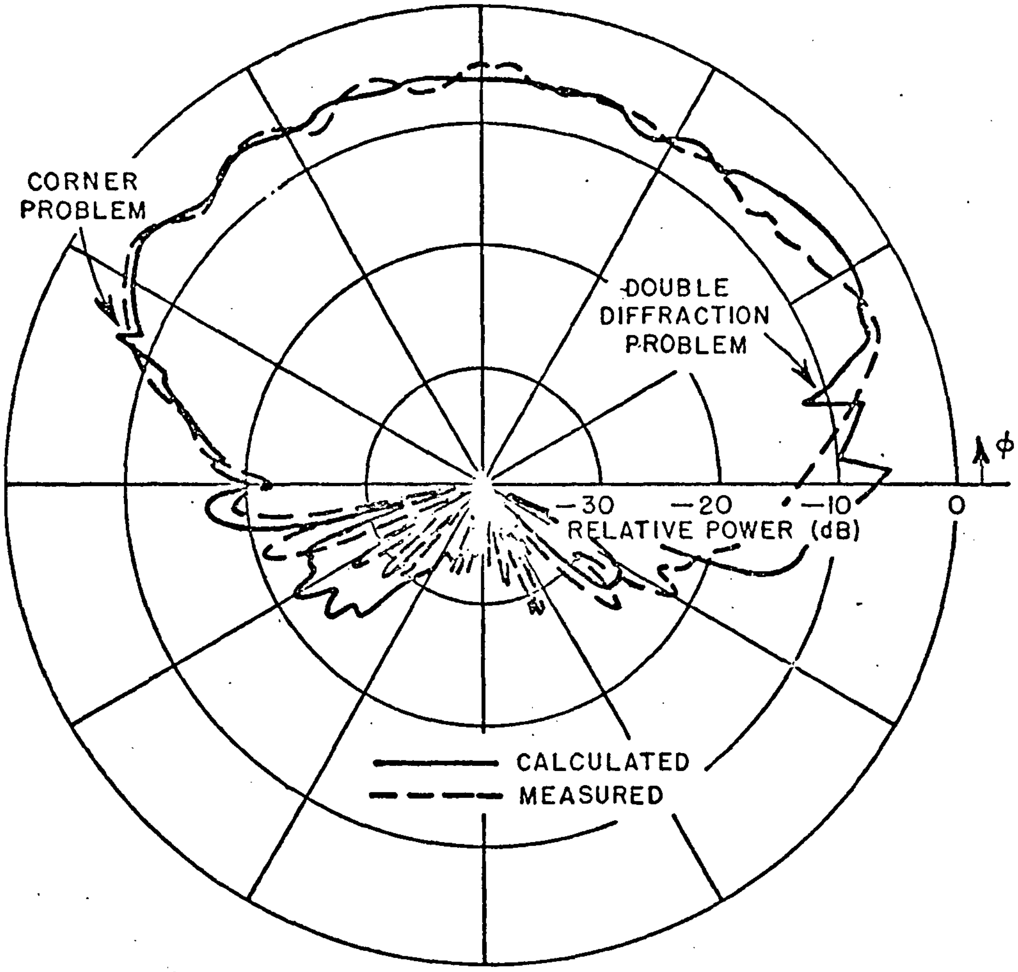

Figure 33a--Main beam elevation plane pattern of single slot mount on F-4 model at location #2 compared with bent plate aircraft result.

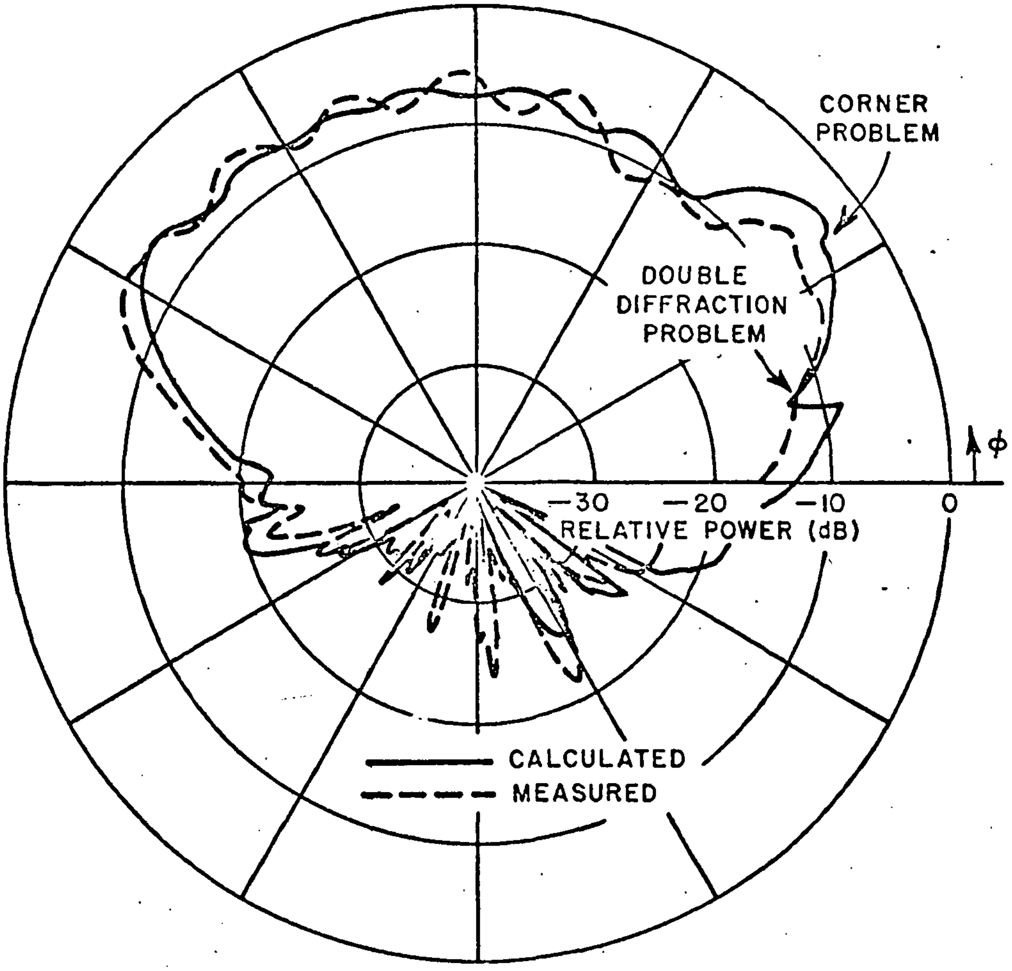

Figure 33b--Main beam elevation plane pattern of single slot mounted on F-4 model at location #4 compared with bent plate aircraft result.

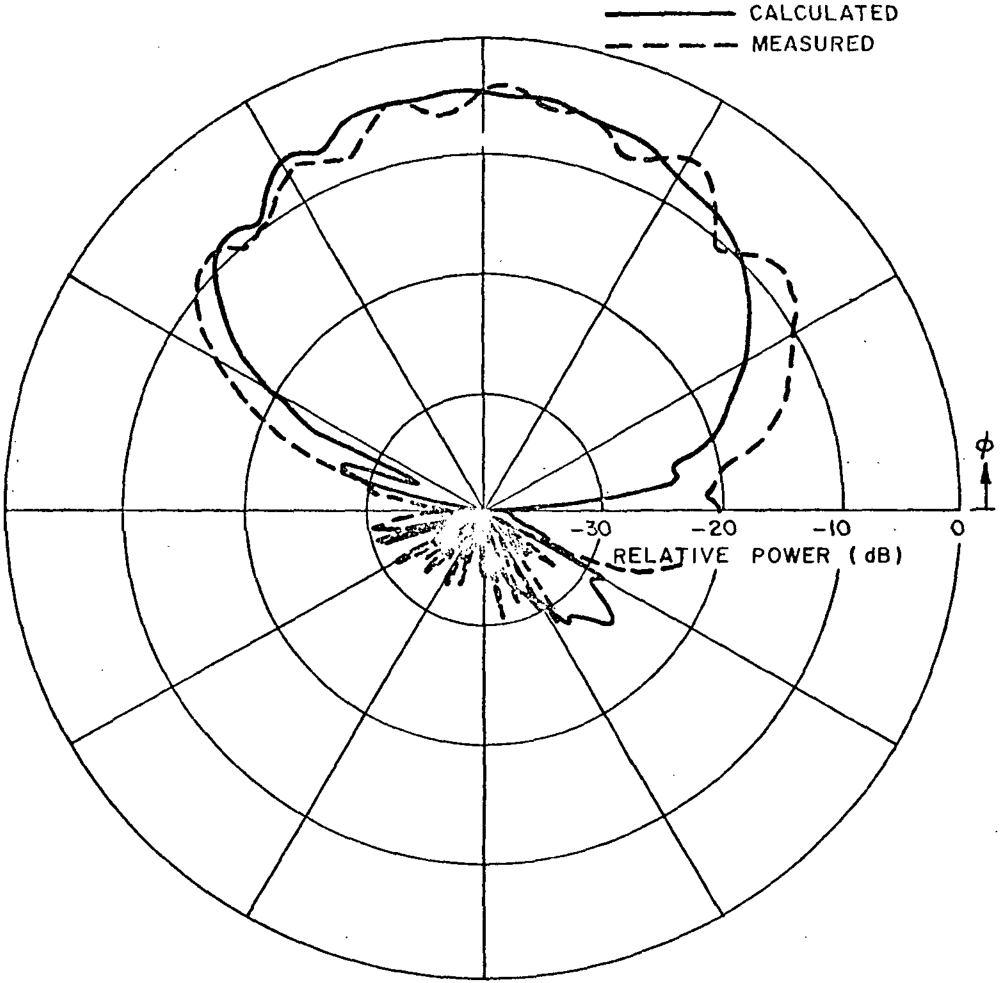

Figure 33c--Main beam roll plane pattern of single slot mounted on F-4 model at location #2 compared with bent plate aircraft result.

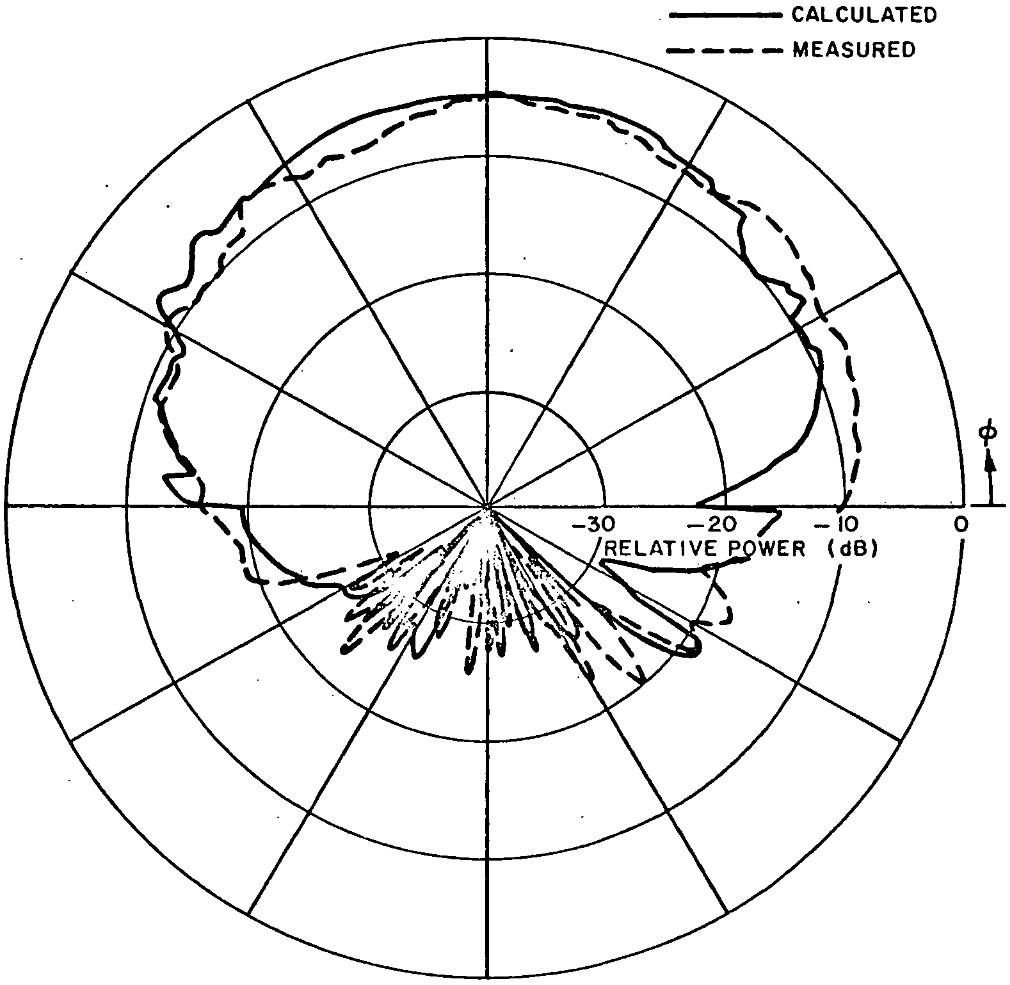

Figure 33d--Elevation plane pattern of single slot mounted on F-4 model at location #2 compared with bent plate aircraft result.

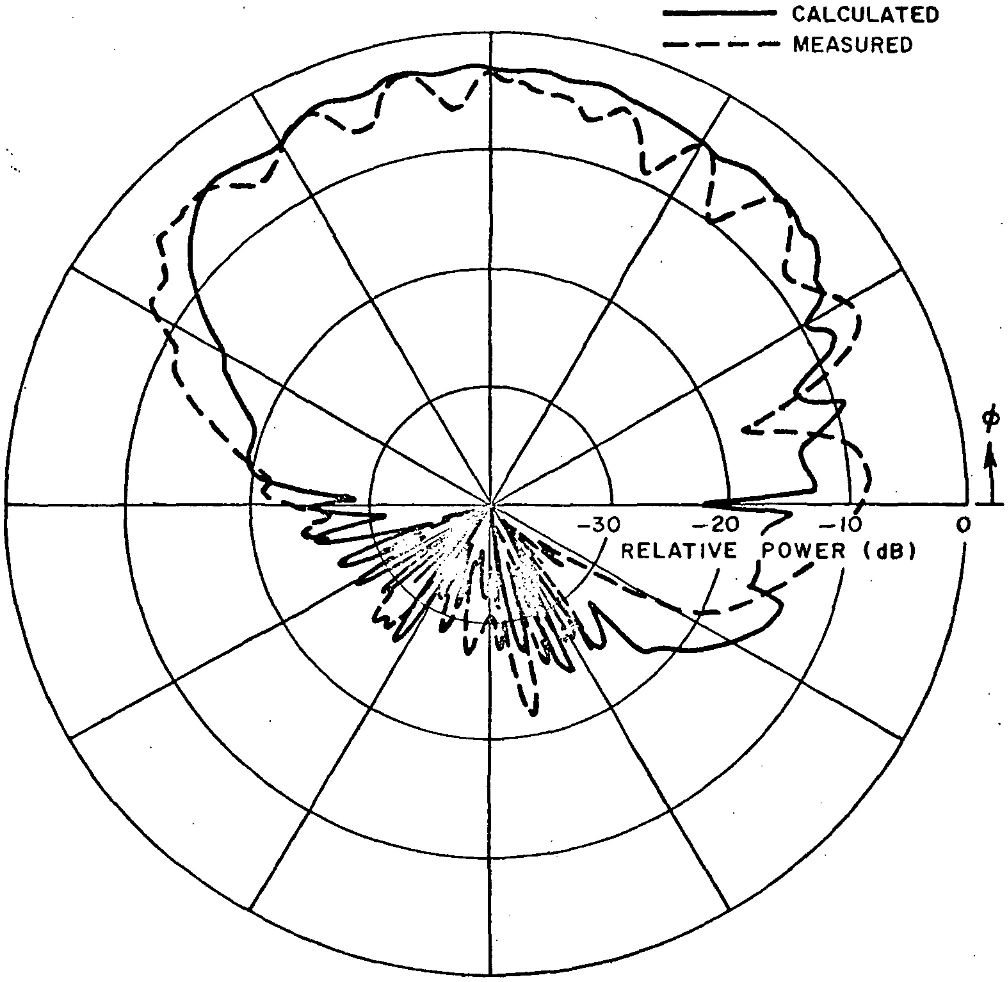

Figure 33e--Roll plane pattern of single slot mounted on F-4 model at location #2 compared with bent plate aircraft result.

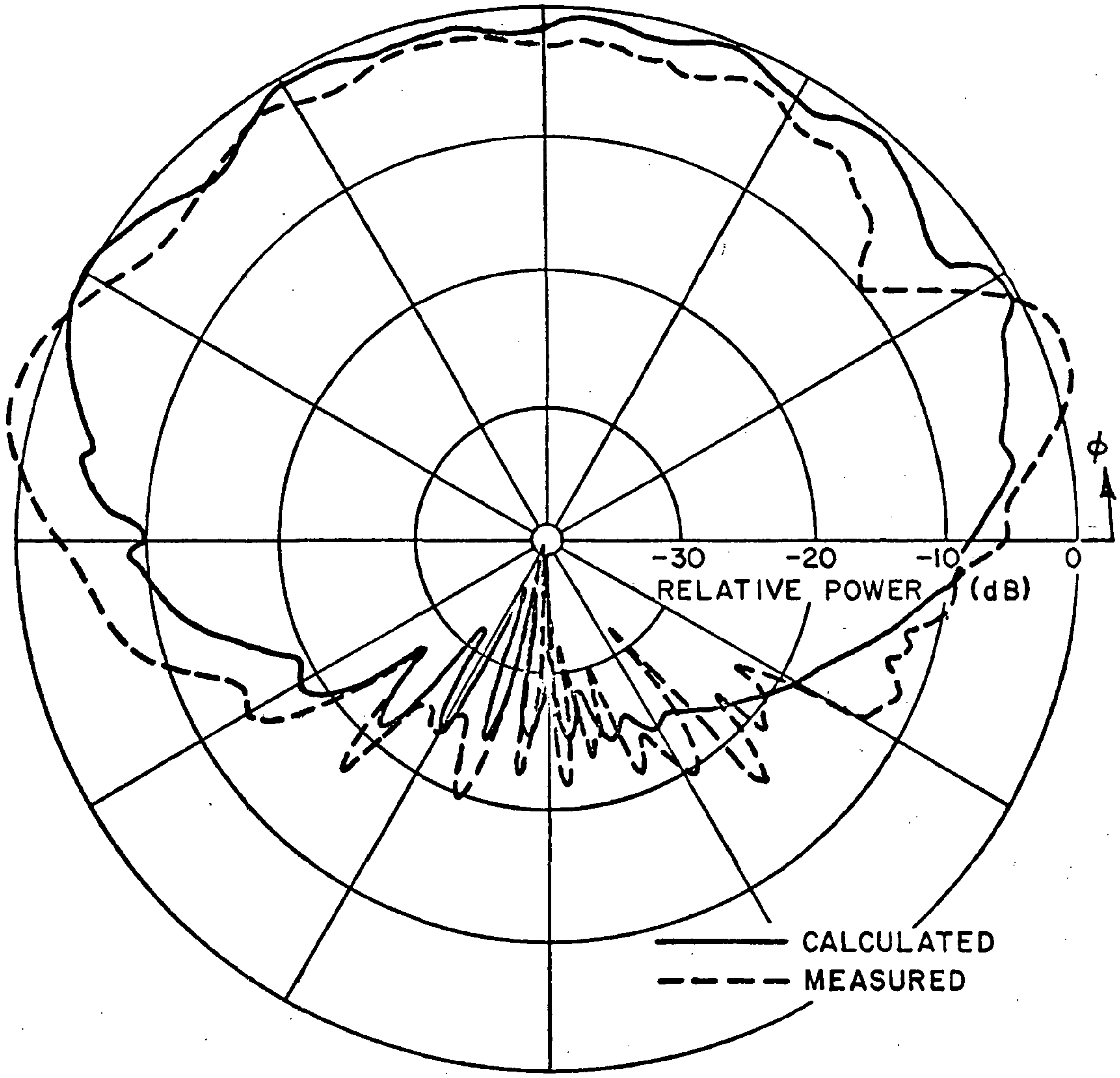

Figure 33f--Elevation plane pattern of single slot mounted on F-4 wing facing aft compared with bent plate aircraft result.

The above comparisons, especially the roll plane result in Figure 33e in which scattering from the fuselage plays an important part, indicate that the flat plate representation does not adequately represent the smooth curved surface of the aircraft fuselage. This leads to the development of a more complex fuselage representation presented in the following Chapters. To minimize the fuselage effects on the flat plate fuselage, a measurement was made on the F-4 model with the antenna main beam pointed straight behind the aircraft. This result is shown in Figure 33f. Some of the detail compares slightly better; however, the shifting of some of the ripple and the broadnesss of the pattern at $\theta = 180°$ indicates a problem with the measurements that turns up in all the comparisons. The problem is that the measurements were taken in the near field of the aircraft. As a result, one cannot directly compare the measured near-field and calculated far-field patterns. Of course, there is also the possibility of slight inaccuracies in the measured results due to variations in placement of the antennas, ground reflections, etc. The comparisons are good enough, however, to show that the flat plate model is moderately successful although it needs improvement for aircraft fuselage modelling.

The question as to whether a flat plate adequately models a wing with finite thickness and a rounded edge with an antenna mounted on its surface is studied [32] by comparing the results of a two dimensional thick wing model with the knife edge used in the flat plate model. The rounded wing tip is modelled by a circular cylinder mounted on a thick wall as shown in the insert of Figure 34. The radiation patterns are compared in Figure 34 for a tip of $1/16\lambda$ radius and the knife edge model. Note there is very little difference in the two results. This implies that the knife edge is a good approximation for a wing tip at the frequencies of interest.

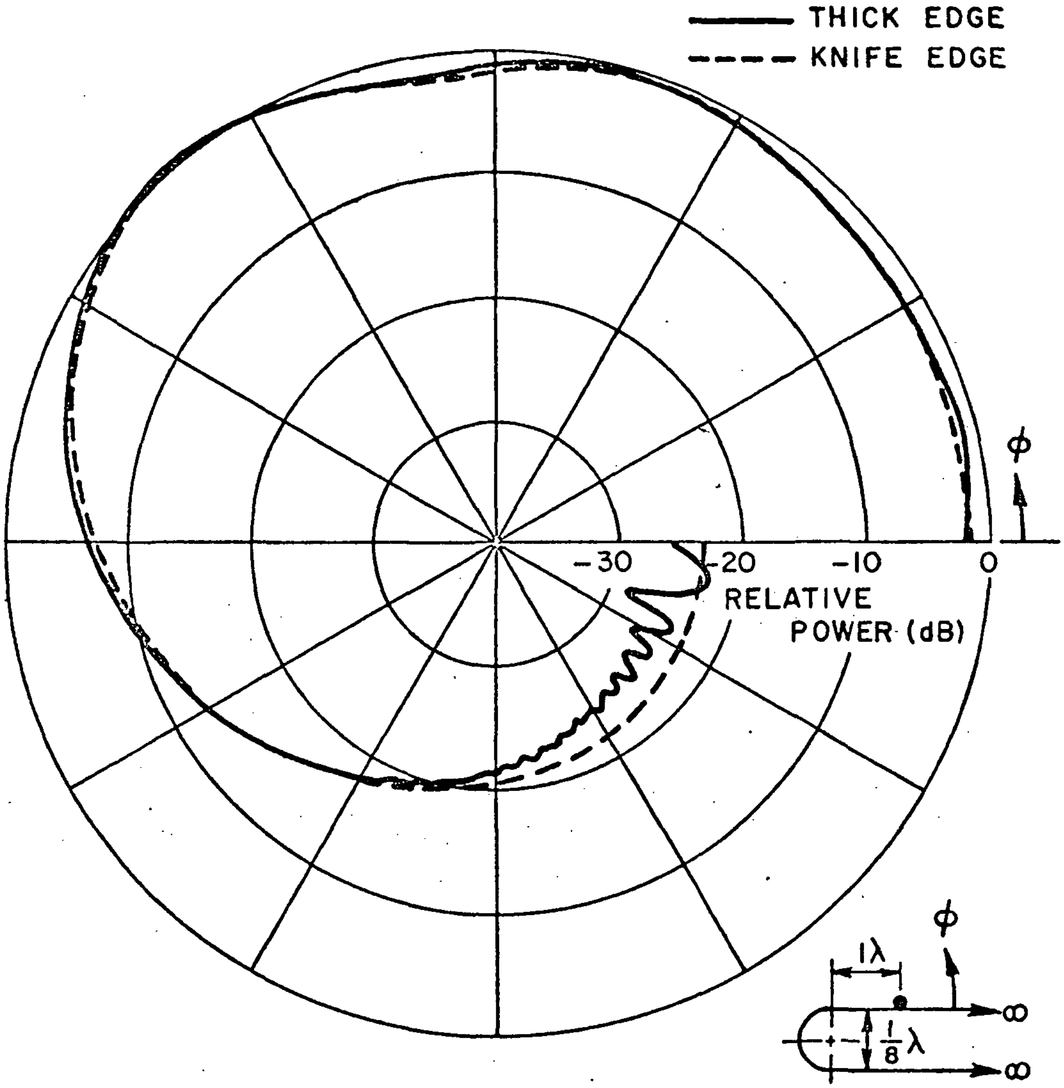

Figure 34--Comparison of the E_ϕ radiation patterns of a slot on a thick edge plate to that of a slot on a knife edge plate.

CHAPTER IV

NEAR FIELD SCATTERING BY A FINITE ELLIPTIC CYLINDER

A. Introduction

The near field scattering by a finite length, perfectly-conducting elliptic cylinder is analyzed using the Geometrical Theory of Diffraction as discussed in Chapter II. The near field scattering from a finite circular cylinder was studied by Burnside [23] using a combination of modal solutions, physical optics, and equivalent currents. The present work is now possible due to the curved wedge diffraction coefficients of Kouyoumjian and Pathak [34] and the curved surface transition function solution of Pathak [62,63].

In this study, the antenna is in the near field of the three dimensional scattering body, but it may not be on the surface of the cylinder. The scattering body is assumed to be in the far field of the source. The observation point is also in the far field.

The finite elliptic cylinder is of interest because it can be used to simulate aircraft fuselages, engines, and stores. The elliptic cylinder geometry allows for variations in its dimensions such that a best fit can be obtained for a variety of actual aircraft fuselage shapes.

B. Near Field Scattering by a Finite Elliptic Cylinder

The finite length, perfectly conducting elliptic cylinder analyzed in this study is composed of a cylinder with elliptic cross-section truncated by two flat end caps, whose normals lie in the x-z plane such that they can make an arbitrary angle with the cylinder axis. The end cap cylinder junction forms a curved wedge. The dimensions of the structure are assumed to be large in terms of the wavelength. The geometry is illustrated in Figure 35. The source is defined by its location and far-field pattern. The source is assumed to be an infinitesimal electric or magnetic dipole moment.

The incident field is given in Equation (29), and as before the scatter direction is given as

$$\hat{d} = \cos\phi_s \sin\theta_s \hat{x} + \sin\phi_s \sin\theta_s \hat{y} + \cos\theta_s \hat{z}. \tag{54}$$

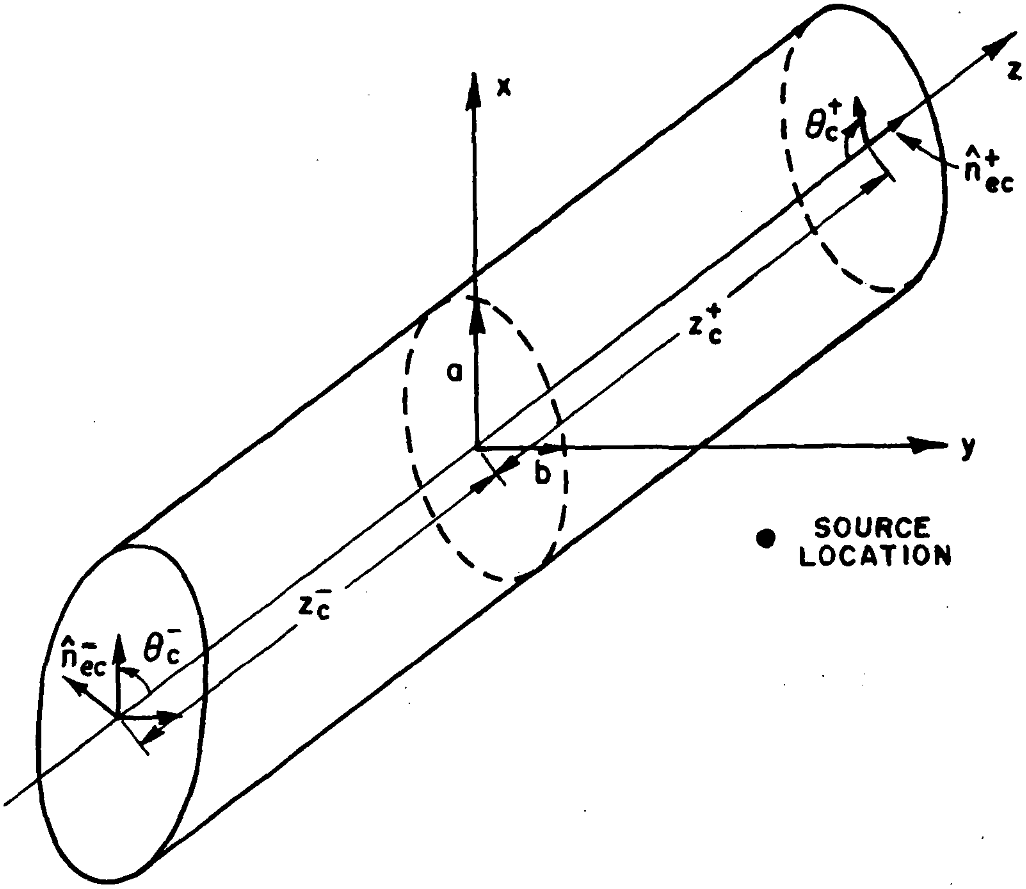

Figure 35--Near field finite elliptic cylinder geometry.

As mentioned previously, it is important that all fields be set to zero if they are shadowed by any obstacle. In this case, the cylinder is assumed to be the only structure present.

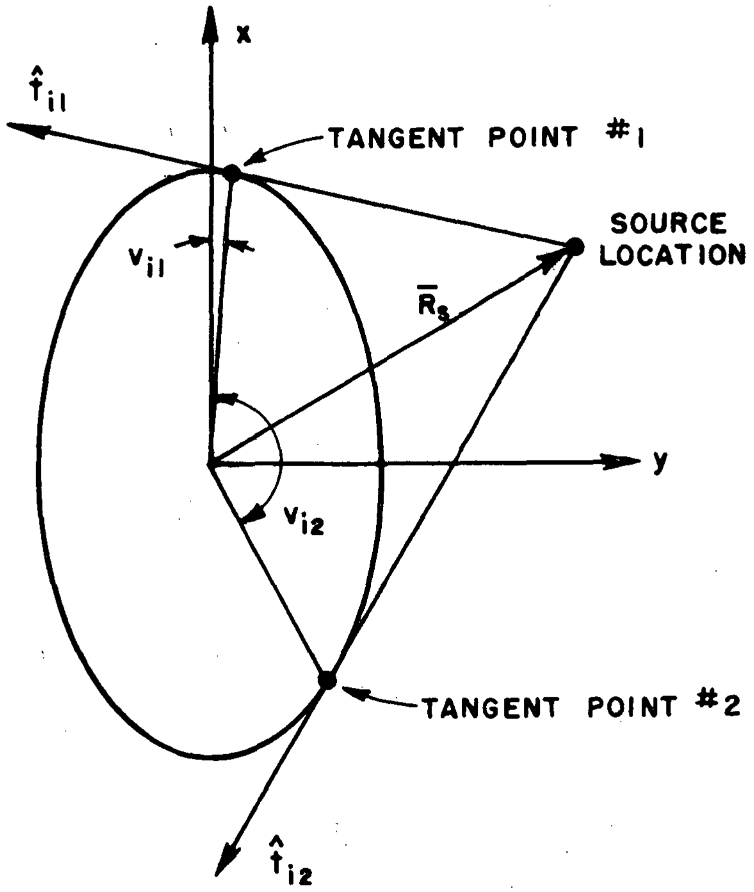

Figure 36--Geometry for tangent directions to elliptic cylinder.

The method used to determine if a ray is shadowed or not by the cylinder is based on limits defined by vectors emanating from the source such that they are tangent to the cylinder surface as shown in Figure 36. These vectors $\hat{t}_{i1}$ and $\hat{t}_{i2}$ define the top and bottom shadow boundaries of the source, respectively. The coordinates of each tangent point associated with the source shadow boundaries can be found by setting an incident vector from the source equal to the general unit tangent vector to the elliptic surface. This is written as

$$\hat{I}_{xy} = \mp\hat{t}_e \tag{55}$$

where the minus sign is associated with the top shadow boundary ($\hat{t}_{i1}$), and the plus sign is for the bottom shadow boundary ($\hat{t}_{i2}$). The general unit tangent vector to the elliptic surface at the point

$$\overline{R}_e = a \cos v \, \hat{x} + b \sin v \, \hat{y} + z_e \hat{z}$$

on the surface is given by

$$\overline{t}_e = \frac{\partial \overline{R}_e}{\partial v} \quad .$$

As a unit tangent vector this is given by

$$\hat{t}_e = \frac{-a \sin v \, \hat{x} + b \cos v \, \hat{y}}{\sqrt{a^2 \sin^2 v + b^2 \cos^2 v}} \quad . \tag{56a}$$

The tangent vector need only be defined in the x-y plane, so the vector emanating from the source is defined only in the x-y plane here as

$$\hat{I}_{xy} = \frac{(a \cos v - x_s)\hat{x} + (b \sin v - y_s)\hat{y}}{\sqrt{(a \cos v - x_s)^2 + (b \sin v - y_s)^2}} \tag{56b}$$

where the source point is given by

$$\overline{R}_s = x_s \hat{x} + y_s \hat{y} + z_s \hat{z}.$$

With the substitutions

$$\cos v = \frac{x_t}{a} \quad \text{and} \quad \sin v = \frac{y_t}{b}$$

in Equations (56a) and (56b) to simply the notation,,Equation (55) can be used to solve for the tangent points (x_t, y_t, z_t) when it can then be used to solve for the tangent points (x_t, y_t, z_t) when it is written as

$$\frac{(x_t-x_s)}{\sqrt{(x_t-x_s)^2+(y_t-y_s)^2}} = \frac{\pm a^2 y_t}{\sqrt{a^4 y_t^2+b^4 x_t^2}} \tag{57a}$$

and

$$\frac{(y_t-y_s)}{\sqrt{(x_t-x_s)^2+(y_t-y_s)^2}} = \frac{\mp b^2 x_t}{\sqrt{a^4 y_t^2+b^4 y_t^2}} \quad . \tag{57b}$$

This is accomplished in the following manner. First, dividing Equations (57a) by (57b) and rearranging the result gives

$$\frac{x_t^2}{a^2} + \frac{y_t^2}{b^2} = \frac{x_t x_s}{a^2} + \frac{y_t y_s}{b^2} \quad .$$

Then, noting that

$$\frac{x_t^2}{a^2} + \frac{y_t^2}{b^2} = 1 \tag{58a}$$

is the equation of an ellipse, this leads to the fact that

$$\frac{x_t x_s}{a^2} + \frac{y_t y_s}{b^2} = 1 \ . \tag{58b}$$

The y-coordinate of the tangent point can be written in terms of the x-coordinate from Equation (58b) as

$$y_t = \frac{b^2}{y_s}\left(1 - \frac{x_t x_s}{a^2}\right) . \qquad (58c)$$

Then, substituting Equation (58c) into Equation (58a) yields the quadratic equation on the x-coordinate

$$\frac{1}{a^2}\left(1 + \frac{b^2}{a^2}\frac{x_s^2}{y_s^2}\right)x_t^2 - \frac{2b^2}{a^2}\frac{x_s}{y_s^2}x_t + \left(\frac{b^2}{y_s^2} - 1\right) = 0.$$

Hence, this can be solved for the x-coordinate of the tangent points so that

$$x_t^{1,2} = \frac{a^2b^2x_s \mp a^2y_s\sqrt{a^2y_s^2 + b^2x_s^2 - a^2b^2}}{(a^2y_s^2 + b^2x_s^2)} . \qquad (59a)$$

The *y-coordinate of the tangent points are found by substituting* this into Equation (58c) which gives

$$y_t^{1,2} = \frac{a^2b^2y_s \pm b^2x_s\sqrt{a^2y_s^2+b^2x_s^2-a^2b^2}}{(a^2y_s^2 + b^2x_s^2)} \qquad (59b)$$

The top tangent point (#1) is defined with the minus sign in Equation (59a) and the plus sign in Equation (59b). The bottom tangent point (#2) is defined with the plus sign in Equation (59a) and the negative sign in Equation (59b). Then

$$v_{i1,2} = \tan^{-1}\left(\frac{ay_t^{1,2}}{bx_t^{1,2}}\right) \qquad (60)$$

so that the tangent vectors are

$$\hat{t}_{i1} = -\hat{t}_e\big|_{v=v_{i1}}$$

$$\hat{t}_{i2} = \hat{t}_e\big|_{v = v_{i2}}$$

where $\hat{t}_e$ is defined in Equation (56a).

The shadowing algorithm follows such that if

$$\hat{t}_{i1} \cdot \hat{d}_{xy} < \hat{t}_{i1} \cdot \hat{t}_{i2} \quad \text{or} \quad \hat{t}_{i2} \cdot \hat{d}_{xy} < \hat{t}_{i1} \cdot \hat{t}_{i2} \tag{61}$$

where $\hat{d}_{xy} = \cos\phi_s\ \hat{x} + \sin\ \phi_s \hat{y}$

the ray in the $\hat{d}_{xy}$ direction does not hit the cylinder, that is shadowing does not occur. This is illustrated in Figure 37. If Equation (61) is not satisfied a further test must be made due to the finite length of the cylinder. The incident vector $\hat{I}_{xy}$, Equation (56b), is assumed to be between the $\hat{t}_{i1}$ and $\hat{t}_{i2}$ directions. The parameter v at which the incident vector would hit the cylinder in two dimensions is found from

$$\bar{I}_{xy} \times \hat{d}_{xy} = 0.$$

This leads to the equation

$$\sin v = \frac{-a \sin\phi_s \cos v + (x_s \sin \phi_s - y_s \cos\phi_s)}{-b \cos\phi_s} \tag{62}$$

Squaring both sides of this equation, and substituting in $\sin^2 v = 1 - \cos^2 v$ and rearranging gives the quadratic equation

$$(a^2\sin^2\phi_s + b^2\cos^2\phi_s)\cos^2 v - 2a \sin\phi_s(x_s\sin {}_s - y_s\phi_s) \cos v$$

$$-b^2\cos^2\phi_s + (x_s\sin\phi_s - y_s \cos\phi_s)^2 = 0 .$$

This may be solved for cos v, then cos v may be substituted into Equation (62) to find sin v. The sign of the quadratic solution is picked such that the $|I_{xy}|$ is a minimum. The z-component of the three dimensional incident vector

$$\bar{I} = (a \cos v - x_s)\hat{x} + (b \sin v - y_s)\hat{y} + (z_e - z_s)\hat{z} \tag{63}$$

can be found from

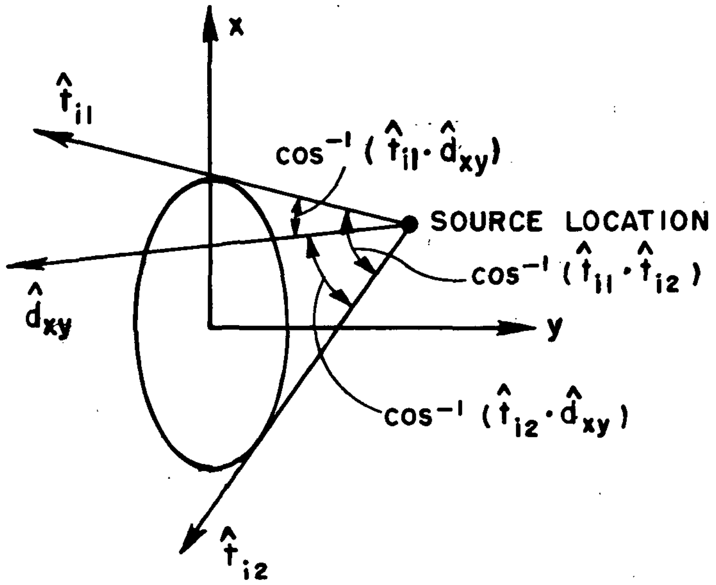

(a) RAY COULD HIT CYLINDER

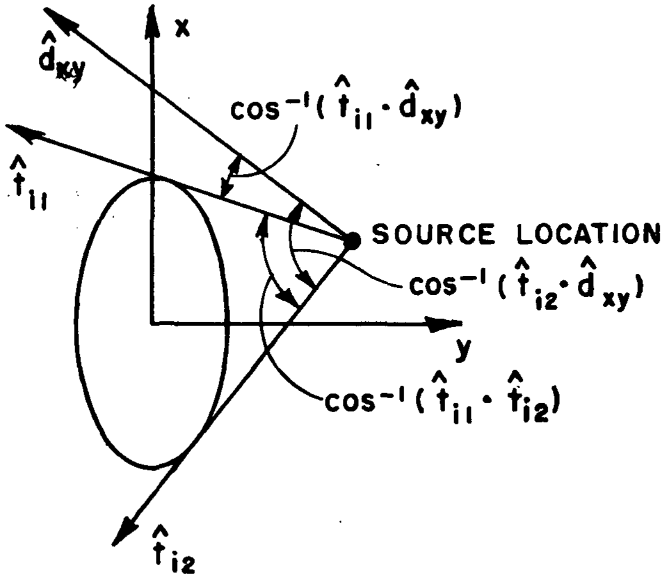

(b) RAY CAN NOT HIT CYLINDER

Figure 37--Geometry for deciding whether ray does or does not hit elliptic cylinder in the x-y plane.

$$z_e = z_s + \frac{\cos\theta_s}{\cos\phi_s \sin\theta_s}(x_e - x_s),$$

where $x_e = a \cos v$. The incident ray hit the cylinder and is shadowed, as in Figure 38, if

$$z_c^- + x_e \cot\theta_c^- < z_e < z_c^+ + x_e \cot\theta_c^+,$$

where

$$z_c^{\pm} = \text{origin of} \begin{Bmatrix} \text{positive} \\ \text{negative} \end{Bmatrix} \text{end cap}$$

$$\theta_c^{\pm} = \text{angle of} \begin{Bmatrix} \text{positive} \\ \text{negative} \end{Bmatrix} \text{end cap with z-axis.}$$

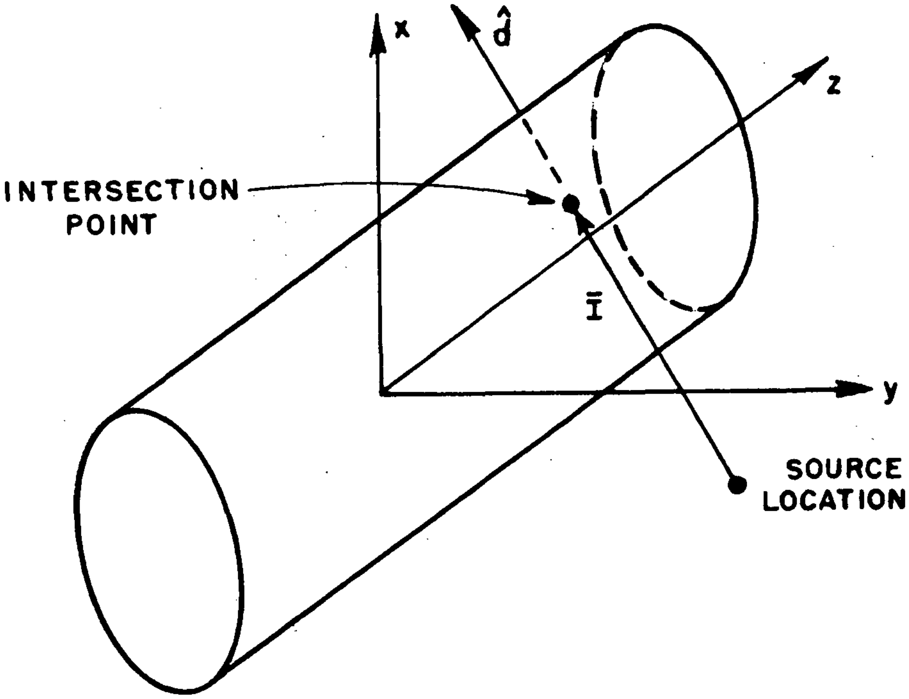

Figure 38--Geometry of intersection point of ray in three dimensions.

Once it is determined the incident field is not shadowed, the far field incident field is given by Equation (29). This shadowing algorithm can be used for any point of origin and type of interaction ray that follows in Chapter V.

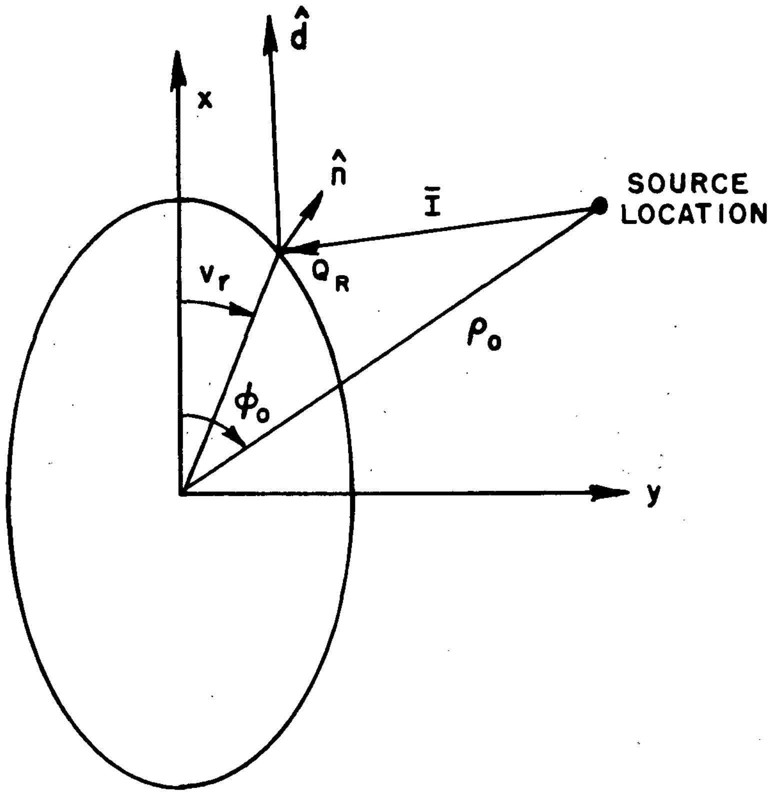

Figure 39--Geometry for determination of reflection point on elliptic cylinder.

In order to find the reflected field off the curved surface of the cylinder in a given scatter direction $\hat{d}$, as shown in Figure 39, the reflection point must first be found. This is assuming that $\hat{d}$ is not in the shadow region, that is, $\hat{d}$ does satisfy the test in Equation (61). If $\hat{d}$ is in the shadow region the reflected field does not exist. To find the reflection point in the lit zone, the laws of reflection as given by Equations (4a and b) are the starting point. These equations are now written such that

$$-\frac{\bar{n} \cdot \vec{I}}{\bar{n} \cdot \vec{d}} = \frac{|\bar{d}|}{|\bar{I}|} = \frac{\bar{n} \times \bar{I}}{\bar{n} \times \bar{d}}$$

or

$$(\bar{n} \times \bar{I})(\bar{n}\cdot\bar{d}) + (\bar{n}\cdot\bar{I})(\bar{n}\times\bar{d}) = 0. \tag{64}$$

Note that the normalization factors may be removed. This will simplify the solutions to follow. The scatter direction given in Equation (54), and the incident vector given in Equation (63) may be written as

$$\bar{d}(\theta_s,\phi_s) = d_x(\theta_s,\phi_s)\hat{x} + d_y(\theta_s,\phi_s)\hat{y} + d_z(\theta_s)\hat{z}$$

and

$$\bar{I}(v,z) = I_x(v)\hat{x} + I_y(v)\hat{y} + I_z(z)\hat{z}.$$

The normal to the curved surface is given in general by

$$\bar{n} = \bar{t}_e \times \hat{z} = b \cos v \; \hat{x} + a \sin v \; \hat{y} \tag{65a}$$

or

$$\bar{n}(v) = n_x(v)\hat{x} + n_y(v)\hat{y}. \tag{65b}$$

Performing the necessary dot and cross products, Equation (64) reduces to two equations,

$$(n_xI_x + n_yI_y)(n_xd_y-n_yd_x) + (n_xd_x + n_yd_y)(n_xI_y-n_yI_x) = 0 \tag{66a}$$

and

$$(n_xI_x + n_yI_y)d_z + (n_xd_x + n_yd_y)I_z = 0. \tag{66b}$$

For a given scatter direction, the location of $\bar{n}$ is usually not known a priori. It has to be solved for using the above two equations. Actually, Equation (66a) contains only one unknown, that is the parameter v. Once this is found the appropriate v may be substituted into Equation (66b) to find the unknown z_e.

Let Equation (66a) be written as

$$\beta_1\beta_2 + \beta_3\beta_4 = 0$$

with

$$x_s = \rho_o \cos \phi_o$$

$$y_s = \rho_o \sin \phi_o$$

$$\beta_1 = a\, b - \rho_o\, (b \cos\phi_o \cos v + a \sin \phi_o \sin v)$$

$$\beta_2 = b \sin\phi_s \cos v - a \cos\phi_s \sin v$$

$$\beta_3 = b \cos\phi_s \cos v + a \sin\phi_s \sin v$$

$$\beta_4 = (b^2-a^2)\cos v \sin v + \rho_o(a \cos\phi_o \sin v - b \sin\phi_o \cos v) \; .$$

Now using the substitution

$$\alpha = e^{jv}$$

or in other words

$$\cos v = \frac{\alpha^2+1}{2\alpha}$$

and

$$\sin v = \frac{-j(\alpha^2-1)}{2\alpha}$$

then

$$\beta_1 = \frac{1}{2\alpha}\{2ab\alpha - \rho_o[(b\ \cos\phi_o - j\ a\ \sin\phi_o)\alpha^2 + (b\ \cos\phi_o + ja\ \sin\phi_o)]\}$$

$$\beta_2 = \frac{1}{2\alpha}\ [(b\ \sin\phi_s + ja\ \cos\phi_s)\alpha^2 + (b\ \sin\phi_s - ja\ \cos\phi_s)]$$

$$\beta_3 = \frac{1}{2\alpha}\ [(b\ \cos\phi_s - ja\ \sin\phi_s)\alpha^2 + (b\ \cos\phi_s + ja\ \sin\phi_s)]$$

$$\beta_4 = \frac{1}{4\alpha^2}[j(a^2-b^2)\alpha^4 - 2\rho_o(b\ \sin\phi_o + ja\ \cos\phi_o)\alpha^3$$

$$- 2\rho_o(b\ \sin\phi_o - ja\ \cos\phi_o)\alpha - j(a^2-b^2)]\ .$$

Multiplying the equations together, collecting terms and setting the equation to zero results in a sixth order polynomial in α given by

$$C_6\alpha^6 + C_5\alpha^5 + C_4\alpha^4 + C_3\alpha^3 + C_2\alpha^2 + C_1\alpha^1 + C_o = 0$$

where

$$C_6 = (a^2-b^2)(a\ \sin\phi_s + j\ b\ \cos\phi_s)$$

$$C_5 = -2\ \rho_o[(a^2+b^2)\sin(\phi_o+\phi_s) + j\ ab\ \cos(\phi_o+\phi_s)]$$

$$C_4 = a(5b^2-a^2)\sin\phi_s + j\ b(5a^2-b^2)\cos\phi_s$$

$$C_3 = 4\rho(a^2-b^2)\sin(\phi_o+\phi_s)$$

$$C_2 = C_4^* \text{ (complex conjugate of } C_4)$$

$$C_1 = C_5^*$$

$$C_o = C_6^* \ .$$

This can be solved using any standard numerical method for the solution of polynomials with complex coefficients. Of course, there will be six roots to this equation, but only one will be physically realizable. This one is found by plugging the v's from

$$v = \tan^{-1}\left(\frac{\text{Imaginary } (\alpha)}{\text{Real } (\alpha)}\right)$$

into the equation for $\bar{I}$ and finding the one which gives the minimum distance $|\bar{I}|$. The parameter z_e can now be found from Equation (66b), that is

$$z_e = z_s - \frac{(n_x I_x + n_y I_y) d_z}{(n_x d_x + n_y d_y)} \quad . \tag{67}$$

The method for finding the reflection point discussed above can be considered an exact solution. There will be some errors involved in practice due to the numerical solution of the polynomial, but these will not be accumulative since the polynomial must be resolved for every scatter direction. This method is time consuming, however, because it must be resolved every time a new pattern direction is considered. Also, more complicated interaction problems involving reflections, as discussed in the next chapter, will not have such a simple solution. It is for these reasons that an approximate method for solving for the reflected field is desirable.

In most radiation pattern calculations, the scatter direction is normally incremented by only a small amount before another field point is desired. This suggests the possibility of using an incremental scheme to find the reflection point on a curved surface. This method is developed based on the first term in a Taylor expansion of the reflection equation

$$f(v,\phi_s) = (n_x I_x + n_y I_y)(n_x d_y - n_y d_x) + (n_x d_x + n_y d_y)(n_x I_y - n_y I_x) = 0, \tag{68}$$

that is

$$f_{j+1} = f_j + df_j$$

where

$$df_j = \frac{\partial f_j}{\partial v} \partial v + \frac{\partial f_d}{\partial \phi_s} \delta\phi_s .$$

Since

$$f_{j+1} \Big|_{\substack{v_j+\delta v \\ \phi_s+\delta\phi_s}} = 0$$

this implies that

$$f_j + df_j \Big|_{\substack{v_j \\ \phi_s}} = 0$$

or

$$f_j + \frac{\partial f_j}{\partial v} \delta v + \frac{\partial f_j}{\partial \phi_s} \delta\phi_s \Big|_{\substack{v_j \\ \phi_s}} = 0$$

so that

$$\delta v = \left. \frac{-f_j - \frac{\partial f_j}{\partial \phi_s} \delta\phi_s}{\frac{\partial f_j}{\partial v}} \right|_{\substack{v_j \\ \phi_s}} .$$

This says that if the reflection point for an observation angle of ϕ_s is at the elliptic angle v_j on the cylinder surface, then the reflection point for an angle of $\phi_s+\delta\phi_s$ is given by

$$v_{j+1} = v_j + \delta v.$$

From Equation (68), it is seen that

$$\frac{\partial f_j}{\partial \phi_s} = (n_x I_x + n_y I_y)\left(n_x \frac{\partial d_y}{\partial \phi_s} - n_y \frac{\partial d_x}{\partial \phi_s}\right)$$

$$+ \left(n_x \frac{\partial d_x}{\partial \phi_s} + n_y \frac{\partial d_y}{\partial \phi_s}\right)(n_x I_y - n_y I_x)$$

and

$$\frac{\partial f_j}{\partial v} = \left(\frac{\partial n_x}{\partial v} I_x + n_x \frac{\partial I_x}{\partial v} + \frac{\partial n_y}{\partial v} I_y + n_y \frac{\partial I_y}{\partial v}\right)\left(n_x d_y - n_y d_x\right)$$

$$+ (n_x d_x + n_y d_y)\left(\frac{\partial n_x}{\partial v} I_y + n_x \frac{\partial I_y}{\partial v} - \frac{\partial n_y}{\partial v} I_x - n_y \frac{\partial I_x}{\partial v}\right)$$

$$+ (n_x I_x + n_y I_y)\left(\frac{\partial n_x}{\partial v} d_y - \frac{\partial n_y}{\partial v} d_x\right)$$

$$+ \left(\frac{\partial n_x}{\partial v} d_x + \frac{\partial n_y}{\partial v} d_y\right)(n_x I_y - n_y I_x)$$

and from Equations (54, 63) and (65a)

$$\frac{\partial n_x}{\partial v} = -b \sin v$$

$$\frac{\partial n_y}{\partial v} = a \cos v$$

$$\frac{\partial I_x}{\partial v} = -a \sin v$$

$$\frac{\partial I_y}{\partial v} = b \cos v$$

$$\frac{\partial d_x}{\partial \phi_s} = -\sin\phi_s$$

$$\frac{\partial d_y}{\partial \phi_s} = \cos\phi_s .$$

Now v_{j+1} may be solved for, and an error computed from

$$\varepsilon = \hat{n} \cdot \hat{I}\Big|_{v_{j+1}} + \hat{n} \cdot \hat{d}\Bigg|_{\substack{v_j+1 \\ \phi_s+\delta\phi_s}} .$$

If the error is not within a given bound, the number of interval steps $\delta\phi_s$ may be halved and the total number of steps doubled so that the new scatter direction is the same but the increments have doubled. This process may be continued until the error bound is reached or the roundoff error in the computer has been reached. The z component of the field may be found from Equation (67) as before.

The assumption in the above method is that the previous reflection point is known accurately. Of course this is not true in general, since the previous reflection point is computed using the same method from its previous point. This means that the process can accumulate error, but this is compensated for by allowing the step size to vary and the fact that the error is computed against the laws of reflection that must be obeyed. In other words, the errors accumulated in calculating the previous point (f_j) are included in the calculation of the next point (f_{j+1}). Thus, as errors grow the interval decreases and tends to correct the total result at (f_{j+1}).

A starting location for the first computation needs to be provided for the incremental method. This is most easily obtained from the fact that the reflection point is known at the shadow boundary, since this is simply the point of tangency from the source to the cylinder. The two points of tangency v_{i1} and v_{i2} were previously found in Equation (60). The scatter direction at the start will be the tangent vectors $\hat{t}_{i1}$ and t_{i2}, respectively. The one closer to the desired direction $\hat{d}$ can be chosen to start the incremental method.

The reflected field from the elliptic cylinder is found using Equation (2). The geometry is illustrated in Figure 40. In this case the observation point is in the far field, $S\to\infty$. Using the usual far-field approximation and referring the phase to the origin

$$\overline{E}^r(\theta_s,\phi_s) = \overline{E}^i(Q_R) \cdot \overline{\overline{R}}\sqrt{\rho_1^r\rho_2^r}\, e^{jk\overline{R}_r\cdot\hat{d}} \; \frac{e^{-jkd}}{d} \tag{69}$$

where $\overline{R}_r$ is the reflection point and $\overline{\overline{R}}$ is the reflection coefficient given by Equation (3). The principal radii of the reflected fields for spherical wave incidence are given in Equation (10), where for an elliptic cylinder $R_2\to\infty$. This gives

$$\rho_2^r = s' \tag{70a}$$

and

$$\rho_1^r = \frac{s'\; R_1\; \cos\theta^i}{R_1\cos\theta^i+2s'\sin^2\theta_2} \quad . \tag{70b}$$

where

$$s' = |\vec{I}| \tag{71a}$$

$$R_1 = \frac{(b^2\cos^2 v_r + a^2\sin^2 v_r)^{3/2}}{a\ b} \tag{71b}$$

$$\cos\theta^i = \hat{n} \cdot \hat{d} \tag{71c}$$

and

$$\sin^2\theta_2 = \sin^2\omega_r + \cos^2\omega_r\ \cos^2\theta^i \tag{71d}$$

$$\cos\omega_r = -\hat{I} \cdot \hat{e}_2 \tag{71e}$$

$$\sin\omega_r = -\hat{I} \cdot \hat{e}_1 \tag{71f}$$

and

$$\hat{e}_1 = \hat{e}_2 \times \hat{n} = e_{1x}\hat{x} + e_{1y}\hat{y} \tag{71g}$$

$$\hat{e}_2 = \hat{z} \tag{71h}$$

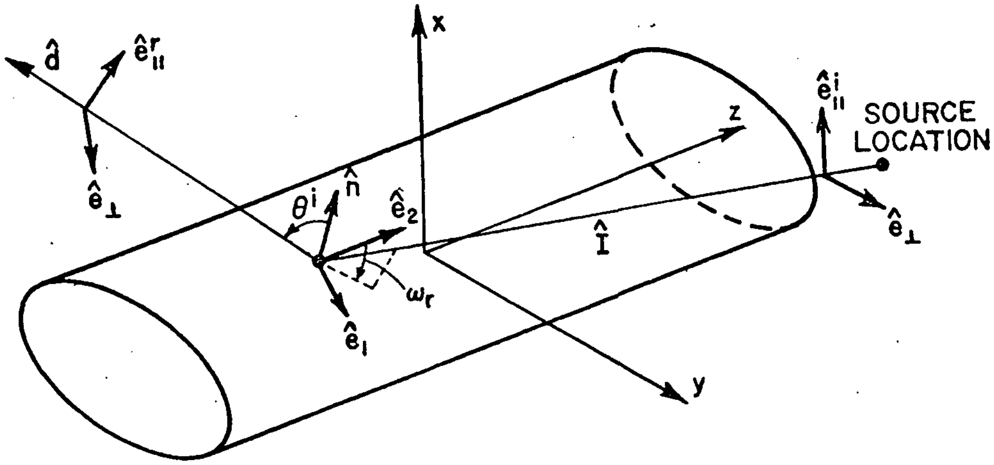

Figure 40--Reflected field geometry for elliptic cylinder.

The vectors that are used in the reflection coefficient are given by

$$\hat{e}_{\perp} = \sin(\omega_r-90°)e_{1x}\hat{x} + \sin(\omega_r-90°)e_{1y}\hat{y} + \cos(\omega_r-90°)\hat{z}, \quad (71i)$$

$$\hat{e}^{i}_{\parallel} = \hat{I} \times \hat{e}_{\perp}, \quad (71j)$$

and

$$\hat{e}^{r}_{\parallel} = \hat{d} \times \hat{e}_{\perp} . \quad (71k)$$

The incident field $\overline{E}^i(Q_R)$ is given as in Equation (1), with the incident vector $\hat{I}$ defining the incident angles.

Reflections can also occur off the flat surface of the end caps. The normals to the end caps are defined as

$$\hat{n}^{+}_{ec} = -\cos\theta^{+}_{c}\hat{x} + \sin\theta^{+}_{c}\hat{z} \quad (72a)$$

and

$$\hat{n}^{-}_{ec} = \cos\theta^{-}_{c}\hat{x} - \sin\theta^{-}_{c}\hat{z}, \quad (72b)$$

where the positive sign refers to the most positive end cap with its origin at $z = z_c^+$ and the negative sign refers to the most negative end cap with its origin at $z=z_c^-$. It is possible for reflections to occur if

$$\hat{I}_c \cdot \hat{n}_{ec} < 0$$

where

$$\overrightarrow{I}_c = z_c\hat{z} - \overline{R}_s .$$

If the above inequality is true, then an image can be found and an intersection point $(\overline{R}_t)$ on the plane of the end cap can be found from Equations (31 and 33) that were used for the flat plates in Chapter III. The test to see if the point of intersection lies in the confines of the end cap, however, is slightly different. First, the distance from the origin of the end cap to the intersection point of the end cap in the plane of the end cap is defined, that is

$$\rho_{tc} = |\overline{R}_t - z_c\hat{z}|.$$

If

$$\rho_{tc} < \min(a \csc\theta_c, b)$$

then a reflection will occur, or if

$$\rho_{tc} > \max(a \csc\theta_c, b)$$

then a reflection will not occur. If

$$\min(a \csc\theta_c, b) < \rho_{tc} < \max(a \csc\theta_c, b)$$

then another test is constructed as follows. Let

$$\overline{R}_t = R_{tx}\hat{x} + R_{ty}\hat{y} + R_{tz}\hat{z}$$

then

$$v_c = \tan^{-1}\left(\frac{a \csc\theta_c \, \overline{R}_t \cdot \hat{y}}{b \, \overline{R}_t \cdot \overline{x}_c}\right)$$

where

$$\hat{x}_c = \begin{cases} \hat{y} \times \hat{n}^{+}_{ec} \\ \hat{n}^{-}_{ec} \times \hat{y} \end{cases} .$$

The radius of the end cap at the angle v_c is then given by

$$\rho_c = \sqrt{a^2 \csc^2\theta_c \cos^2 v_c + b^2 \sin^2 v_c} \; .$$

Thus if

$$\rho_{tc} < \rho_c$$

reflections occur.

The reflected field for both end caps, if they exist, may be found by the same procedure used for the flat plates in Chapter III, Equations (35-39). The total reflected field from the end caps can be written as

$$\vec{E}^{r}_{\text{end cap}}(\theta_s,\phi_s) = \vec{E}^{r+}_{\text{end cap}}(\theta_s,\phi_s) + \vec{E}^{r-}_{\text{end cap}}(\theta_s,\phi_s), \qquad (73)$$

where the plus sign refers to the most positive end cap and the negative sign to the most negative end cap. Usually both end caps will not contribute to the field at the same time.

Curved surface diffraction is used for aspect angles in the deep shadow region. The geometry is illustrated in Figure 41. This diffraction coefficient is discussed in Section G of Chapter II.

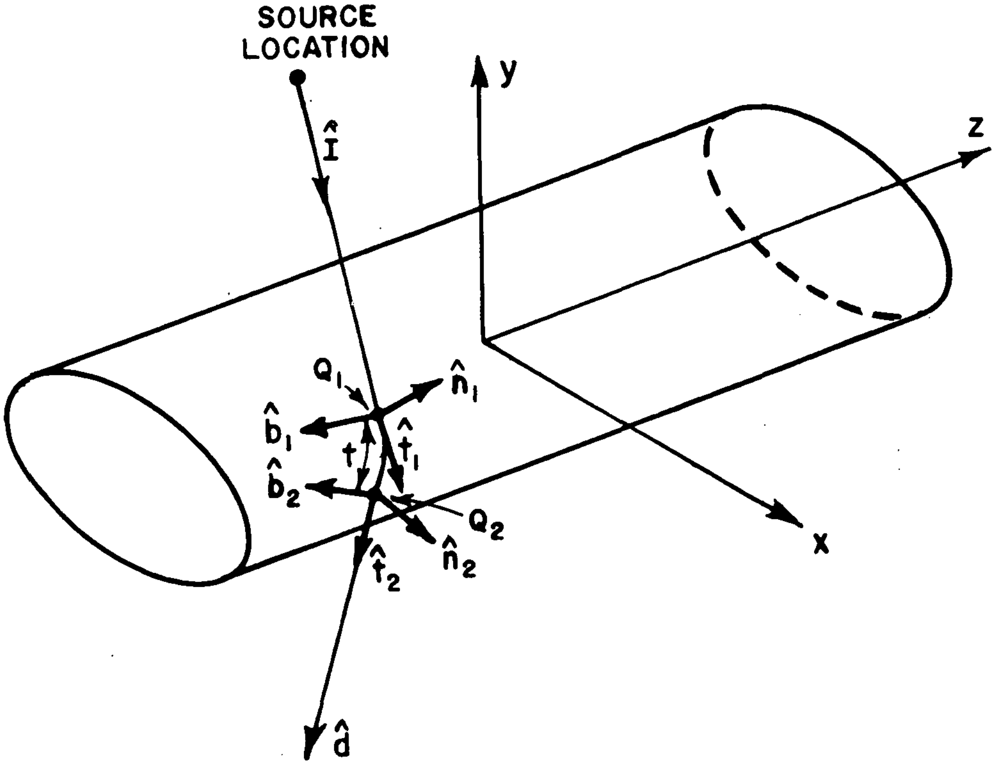

Figure 41--Curved surface diffracted field geometry.

When the scatter direction is in the far-field, Equation (23) is given by

$$\overline{E}^d(\theta_s,\phi_s) = \overline{E}^i(Q_1) \cdot [\hat{b}_1\hat{b}_2u_s + \hat{n}_1\hat{n}_2u_h]\sqrt{\rho}\ e^{jk\,\overline{R}_d\cdot\hat{d}}\ \frac{e^{-jkd}}{d} \qquad (74)$$

where $\overline{R}_d$ is the point at which the ray detaches from the surface (Q_2) and sheds in the scatter direction. The functions u_s and u_h are defined in Equation (24) and ρ is given in Equation (25b) for a cylindrical surface.

The point Q_1 is the incident point and it is found from Equation (60). There are two incident points for a closed convex surface such that energy propagates in a clockwise (cw) and counterclockwise (ccw) sense around the surface so

$$v_i = \begin{cases} v_{i1}, & \text{ccw} \\ v_{i2}, & \text{cw}\ . \end{cases}$$

The surface ray follows a geodesic path along the surface, which is a helical path for a cylinder. The point at which the energy sheds off the cylinder is given by

$$v_f = \begin{cases} \tan^{-1}\left(\dfrac{-b\cos\phi_s}{a\sin\phi_s}\right), & \text{ccw} \\[2ex] \tan^{-1}\left(\dfrac{b\cos\phi_s}{-a\sin\phi_s}\right), & \text{cw}\ . \end{cases}$$

If one defines the geodesic starting direction by the angle α_s = 180°-θ_s, then

$$z = \frac{-\cos\alpha_s}{|\sin\alpha_s|}\int_{v_i}^{v_f}\sqrt{a^2\sin^2 v + b^2\cos^2 v}\ dv \quad \text{(geodesic equation)}\ .$$

This equation can be quickly evaluated using numerical techniques. The important parameters of this problem are listed below:

$$t = \frac{1}{|\sin\alpha_s|} \int_{v_i}^{v_f} \sqrt{a^2\sin^2 v + b^2\cos^2 v}\, dv \quad \text{(arc length)}$$

$$\left.\begin{aligned} \hat{e}_1 &= \frac{-a \sin v\, \hat{x} + b \cos v\, \hat{y}}{\sqrt{a^2\sin^2 v + b^2\cos^2 v}} \\ \hat{e}_2 &= \hat{z} \end{aligned}\right\} \text{(curvalinear coordinates)}$$

$$\hat{t}_{1,2} = \sin\alpha_s \hat{e}_1 - \cos\alpha_s \hat{e}_2 \Big|_{v=v_i}^{v=v_f} \quad \text{(unit tangent vector)}$$

$$\hat{n}_{1,2} = \frac{b \cos v\hat{x} + a \sin v\hat{y}}{\sqrt{a^2\sin^2 v + b^2\cos^2 v}} \Bigg|_{v=v_i}^{v=v_f} \quad \text{(unit normal vector)}$$

$$\hat{b}_{1,2} = t_{1,2} \times \hat{n}_{1,2} = \cos\alpha_s \hat{e}_1 + \sin\alpha_s \hat{e}_2 \Big|_{v=v_i}^{v=v_f} \quad \text{(unit binomial vector)}$$

$$\rho_g = \frac{(a^2\sin^2 v + b^2\cos^2 v)^{3/2}}{a\ b\ \sin^2\alpha_s} \quad \text{(longitudinal radius of curvature)}$$

$$\rho_t = \frac{(a^2\sin^2 v + b^2\cos^2 v)^{3/2}}{ab|\sin^2(\alpha_s - 90°)|} \quad \text{(transverse radius of curvature)}$$

$$\overline{R}_d = a\cos v_f\hat{x} + b\sin v_f\hat{y} + (z_s + |\overline{I}_{xy}|\cot\theta_s + t\cos\theta_s)\hat{z}\ .$$

Using the above relations, Equations (74) can be employed to find the surface diffracted fields from the clockwise ($\overline{E}^d_{cw}$) and counterclockwise ($\overline{E}^d_{ccw}$) propagating rays. The total surface diffracted field from the cylinder, away from the shadow boundaries, is given by

$$\overline{E}^d(\theta_s,\phi_s) = \overline{E}^d_{cw}(\theta_s,\phi_s) + \overline{E}^d_{ccw}(\theta_s,\phi_s). \tag{75}$$

As stated previously, both the reflected field and the surface diffracted fields for the elliptic cylinder are inaccurate close to the shadow boundaries. The transition field solution of Section H in Chapter II for a curved surface is needed in this region. The transition field for a cylindrical structure with the scatter direction in the far field is given in Equation (26) as

$$\overline{E}^t \sim \overline{E}^i(Q) \cdot [\hat{u}_1\hat{u}_2 G_s + \hat{v}_1\hat{v}_2 G_h] \tag{76}$$

where

$$Q = \begin{cases} Q_R, & \text{for the lit region} \\ Q_1, & \text{for the shadow region.} \end{cases}$$

In the lit region, the functions (G_s and G_h) are given by Equation (27), as

$$G_{s,h} = \left\{ \frac{-m\, e^{-j\frac{\pi}{4}}}{\sqrt{\pi k}} \sqrt{\frac{-2k}{m^2 \xi_\ell}} \left[\frac{-1}{\sqrt{2}\xi_\ell} F\left(\frac{kL\xi_\ell^2}{2m^2}\right) + \sqrt{2\pi} \left\{ \begin{matrix} p^*(\xi_\ell) \\ q^*(\xi_\ell) \end{matrix} \right\} \right] \right\} \sqrt{\rho_1^r \rho_2^r}$$

$$\times\ e^{-j\frac{\xi_\ell^3}{12}}\ e^{jk\overline{R}_r \cdot \hat{d}}\ \frac{e^{-jkd}}{d} \tag{77a}$$

and for the shadow region Equation (28) gives

$$G_{s,h} = \left\{ \frac{-(m_1 m_2)^{1/2}\, e^{-j\frac{\pi}{4}}}{\sqrt{\pi k}} \left[\frac{-1}{\sqrt{2}\ \xi_s} F\left(\frac{kL\xi_s^2}{2m_1 m_2}\right) + \sqrt{2\pi} \left\{ \begin{matrix} p^*(\xi_s) \\ q^*(\xi_s) \end{matrix} \right\} \right] \right\}$$

$$\times \sqrt{\frac{d\eta_1}{d\eta_2}} \sqrt{\rho}\, e^{-jkt}\ e^{jk\vec{R}_d \cdot \hat{d}}\ \frac{e^{-jkd}}{d}\ . \tag{77b}$$

The necessary equations to define these functions have been given in Chapter II, Section H and this chapter, where the parameters in the reflected field section are used for the lit region and the parameters in the surface diffracted field section are used in the shadow region.

The transition field solution is accurate at and around the shadow boundaries. As the observation point moves away from the shadow boundary either into the lit region or deep shadow region, the geometrical optics fields and surface diffracted fields, respectively, present a more accurate solution. At some point the solutions are very close together and either solution is valid. This is illustrated in Figure 42 for an elliptically capped thick wall (a=1.59λ). The dipole is on the x-axis, 4.76 from the origin, and parallel to the z-axis. This indicates that the transition region is rather arbitrarily defined in terms of the accuracy of the solutions. A progressive blending function can be constructed, so that the total solution smoothly goes from one type of solution to the next over a small region in the area of common validity.

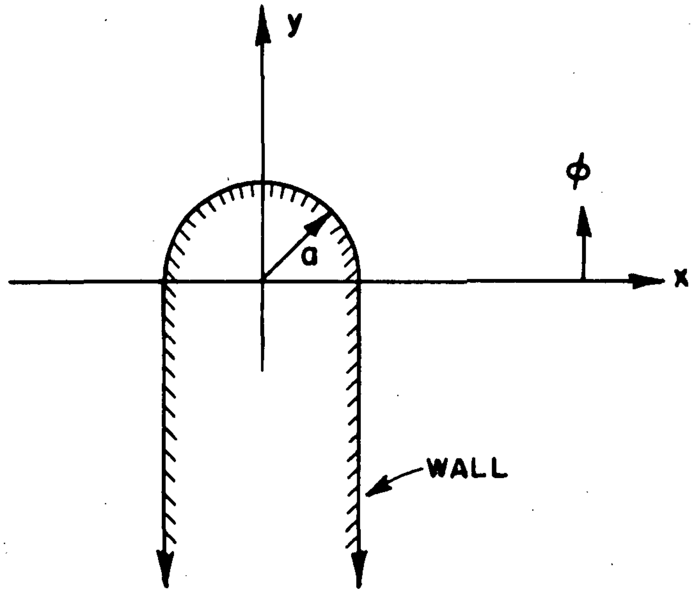

Figure 42a--Cylindrically capped wall configuration excited by a dipole source parallel to z-axis.

For a closed convex surface, there are two shadow boundaries as discussed before so there will be a transition field associated with the top or counterclockwise term ($\vec{E}^t_{ccw}$) and the bottom or clockwise term ($\vec{E}^t_{cw}$). The total transition field, where it exists, is then given by

$$\vec{E}^t(\theta_s,\phi_s) = \vec{E}^t_{cw}(\theta_s,\phi_s) + \vec{E}^t_{ccw}(\theta_s,\phi_s). \tag{78}$$

For an infinitely long cylinder, where the end caps need not be considered, the total field is given by

$$\vec{E}(\theta_s,\phi_s) = \vec{E}^i + \vec{E}^r + \vec{E}^t + \vec{E}^d$$

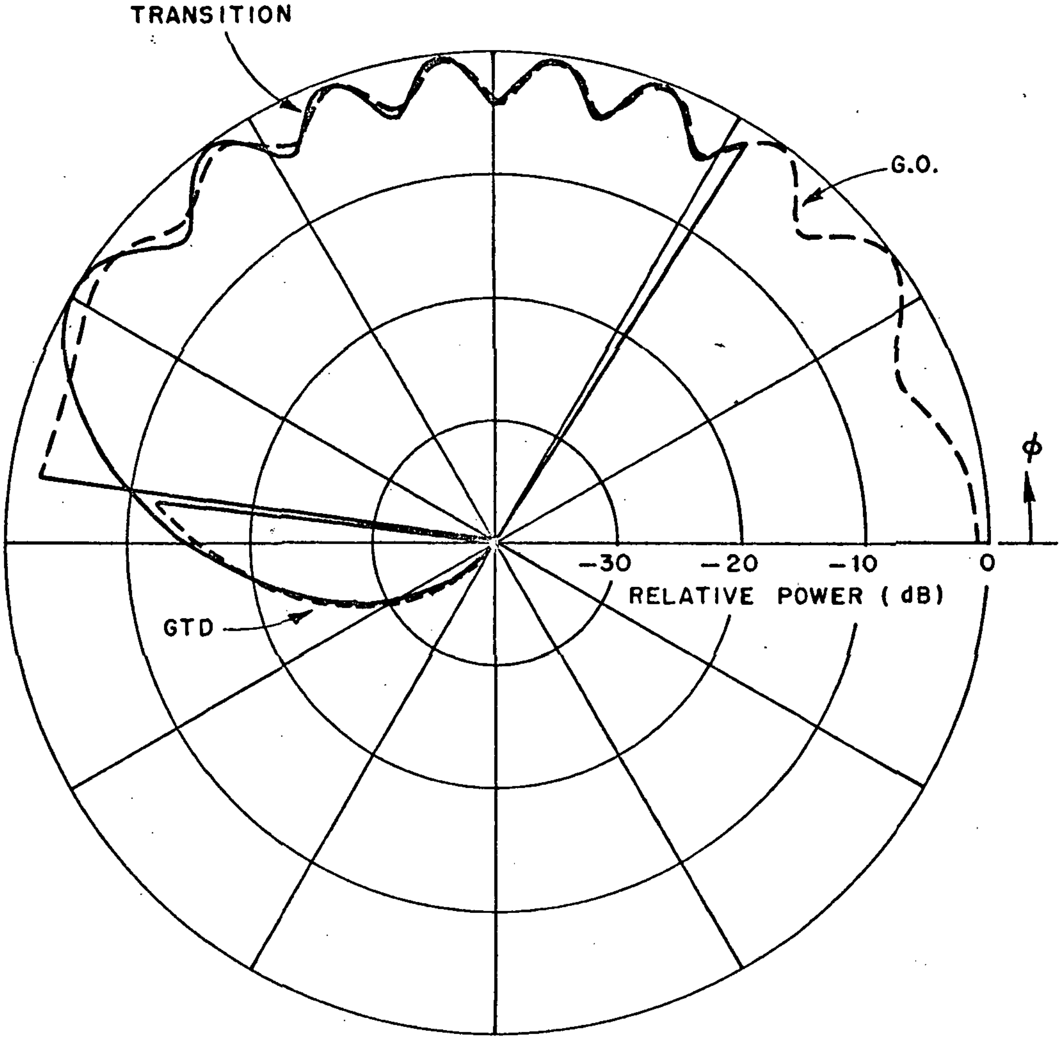

Figure 42b. E_θ radiation pattern of electric dipole source surrounding cylindrically capped wall showing the effects of the three different solutions in their respective regions.

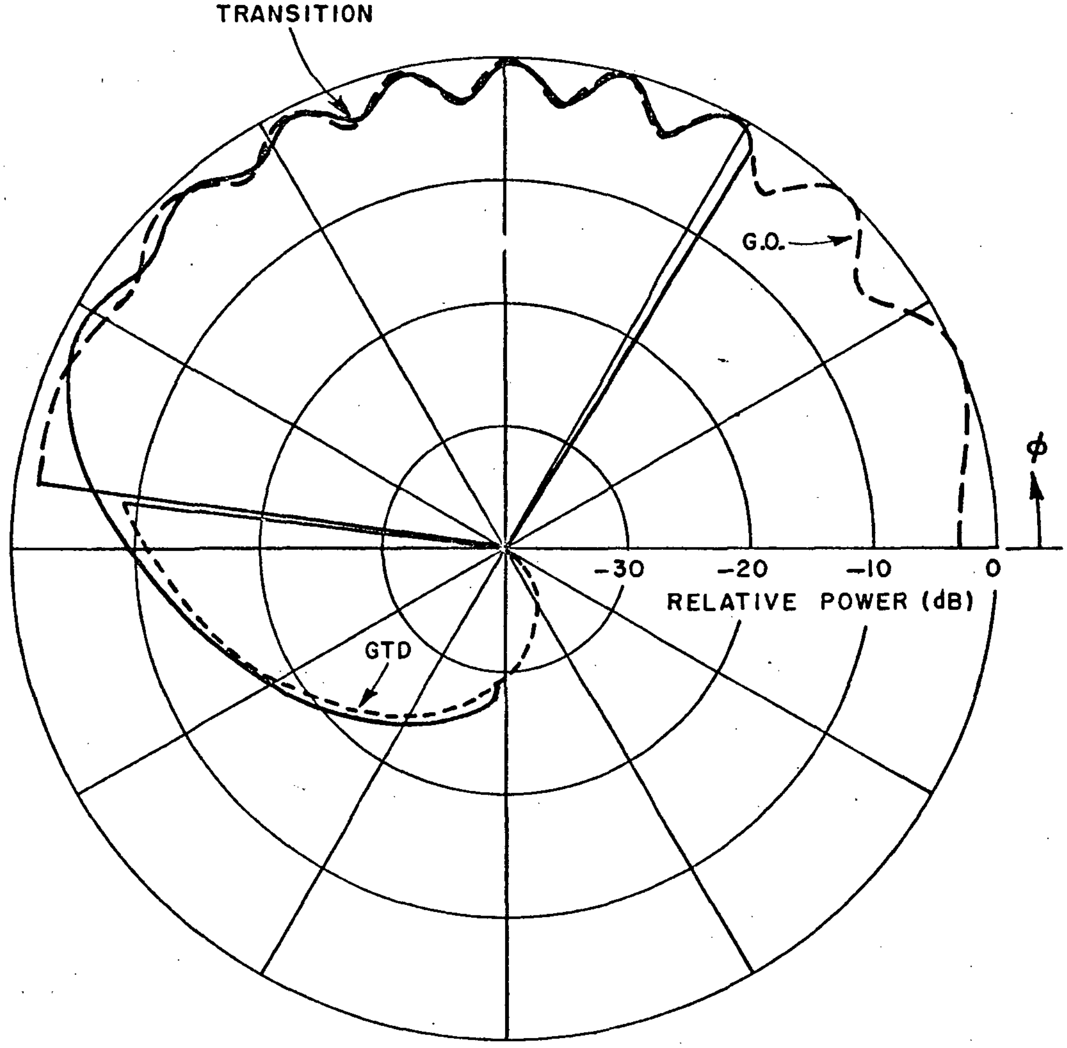

Figure 42c--E_ϕ radiation pattern of magnetic dipole source surrounding cylindrically capped wall showing the effects of the three different solutions in their respective regions.

using Equations (29,69,75,78). The accuracy of this result is confirmed by numerical comparison with the results obtained via an exact eigenfunction solution for a circular cylinder [64] in Figures 43 for the acoustic soft and hard boundary conditions, respectively. The results for the GTD solution are also compared against a moment method (MM) solution for the elliptic cylinder case in Figure 44 for the hard boundary condition and two different source positions. The result in Figure 45 compares the GTD solution with the MM solution for a conical scan angle of $\theta = 45°$. In all the above comparisons the results show excellent agreement.

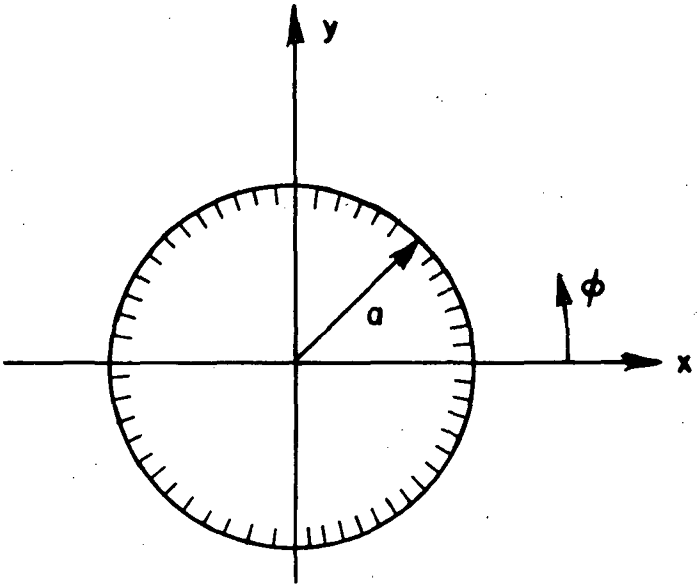

Figure 43a--Circular cylinder configuration excited by a dipole source parallel to z-axis.

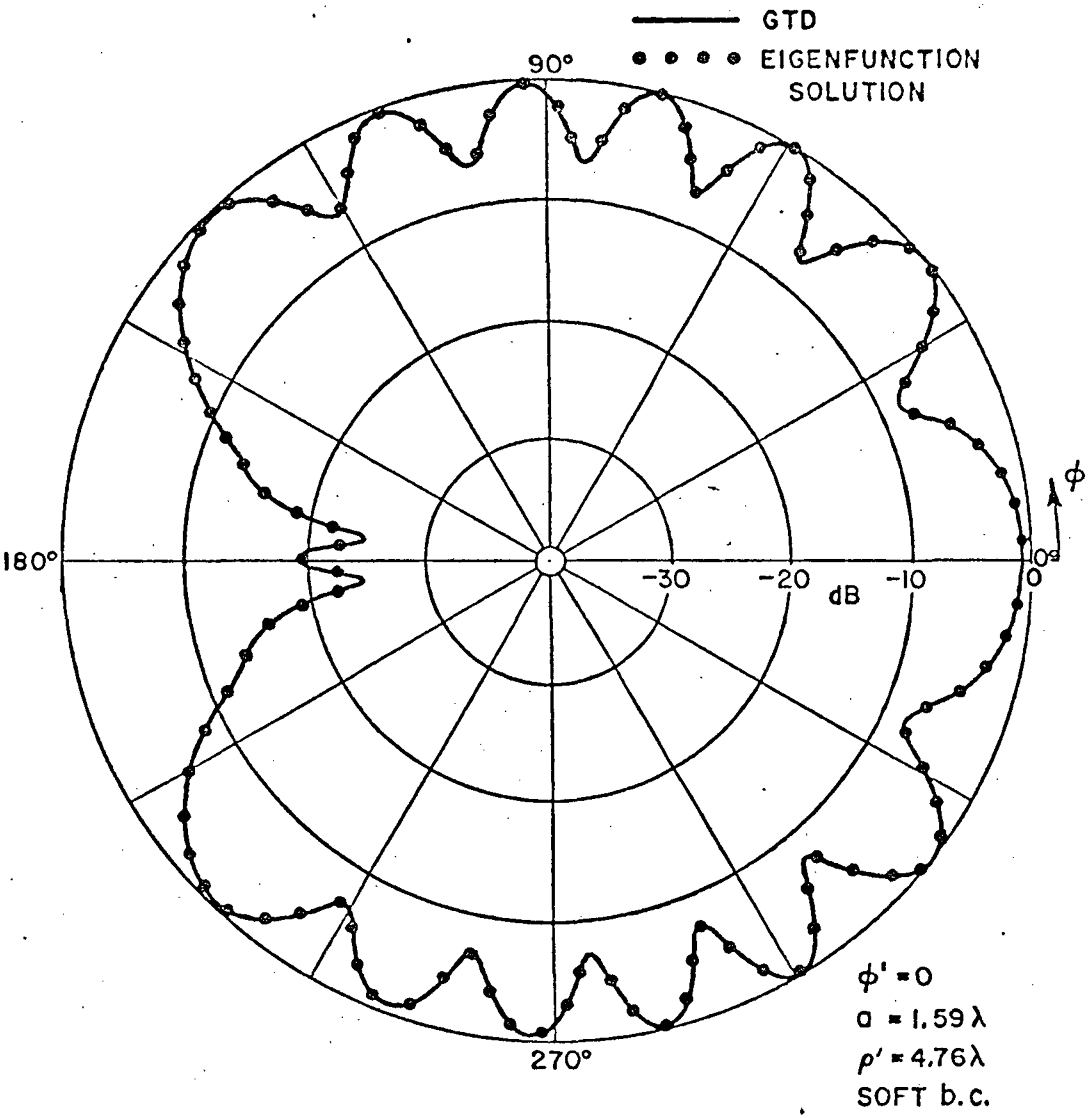

Figure 43b--E_θ radiation pattern of electric dipole surrounding circular cylinder. Here, GTD implies the GTD + transmitter solution.

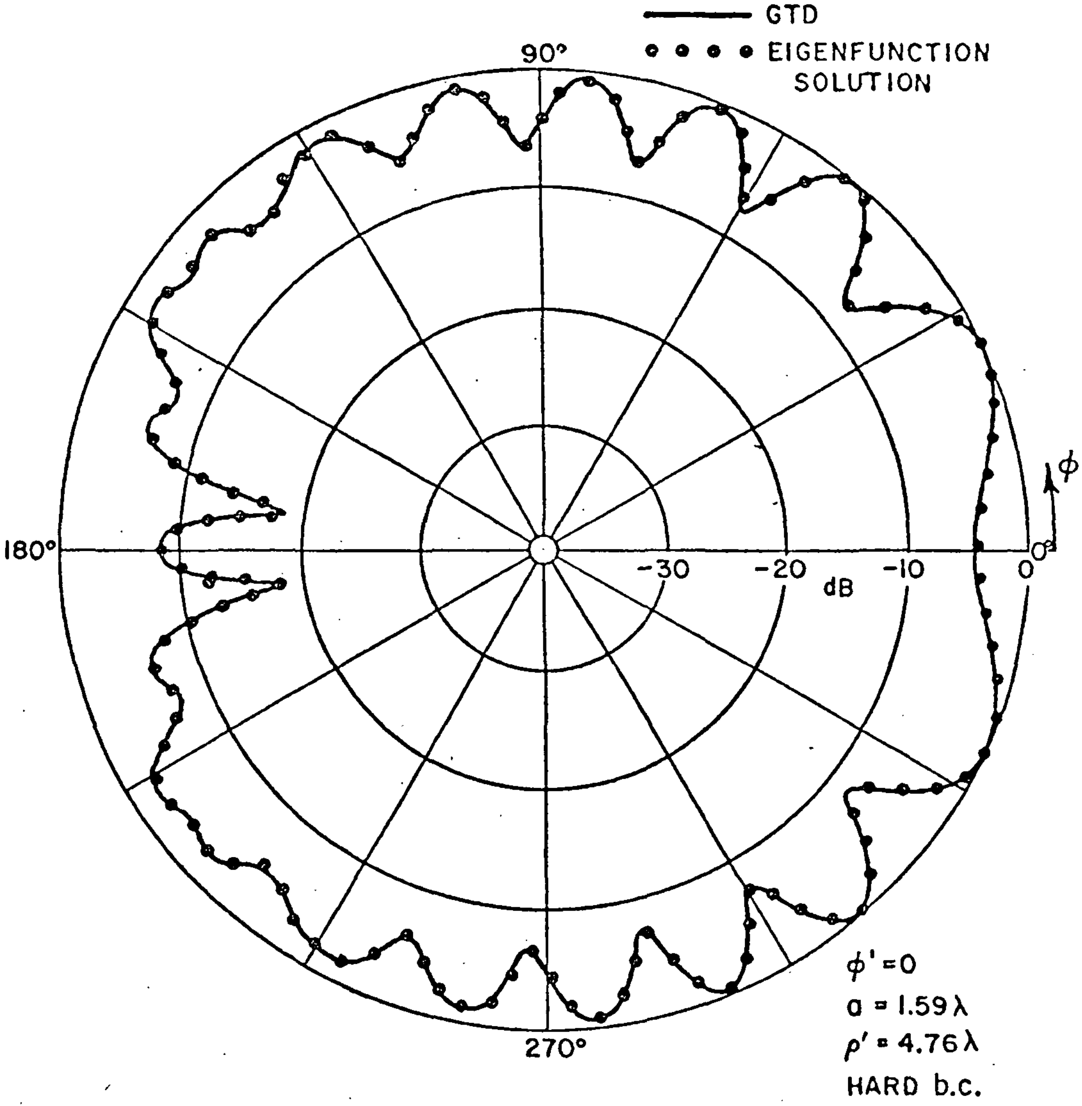

Figure 43c--E_ϕ radiation pattern of magnetic dipole surrounding circular cylinder. Here GTD implies the GTD + transition solution.

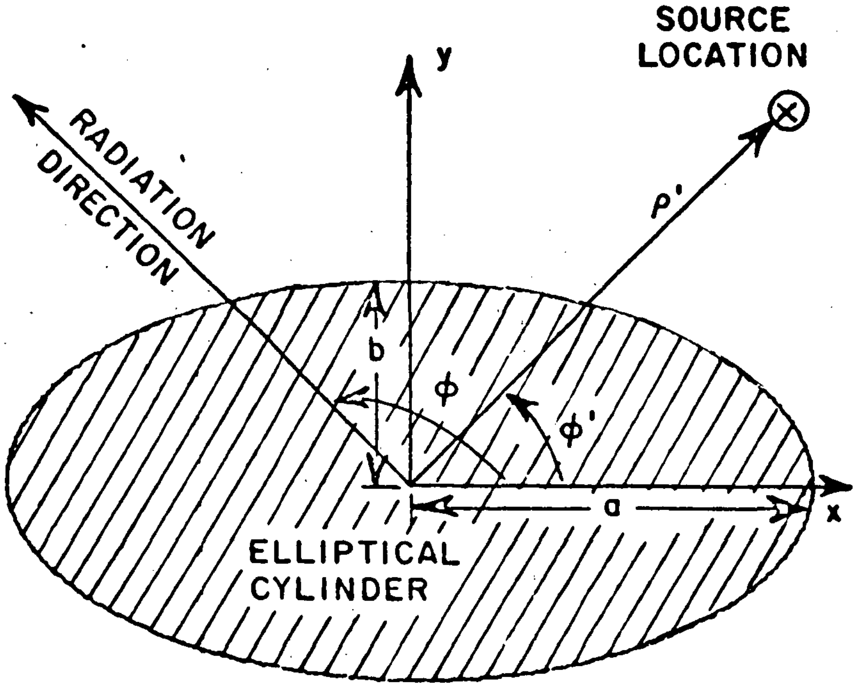

$a = 2\lambda,\ b = 1\lambda,\ \rho' = 4\lambda$

Figure 44a--Elliptic cylinder configuration excited by a magnetic source parallel to the z-axis.

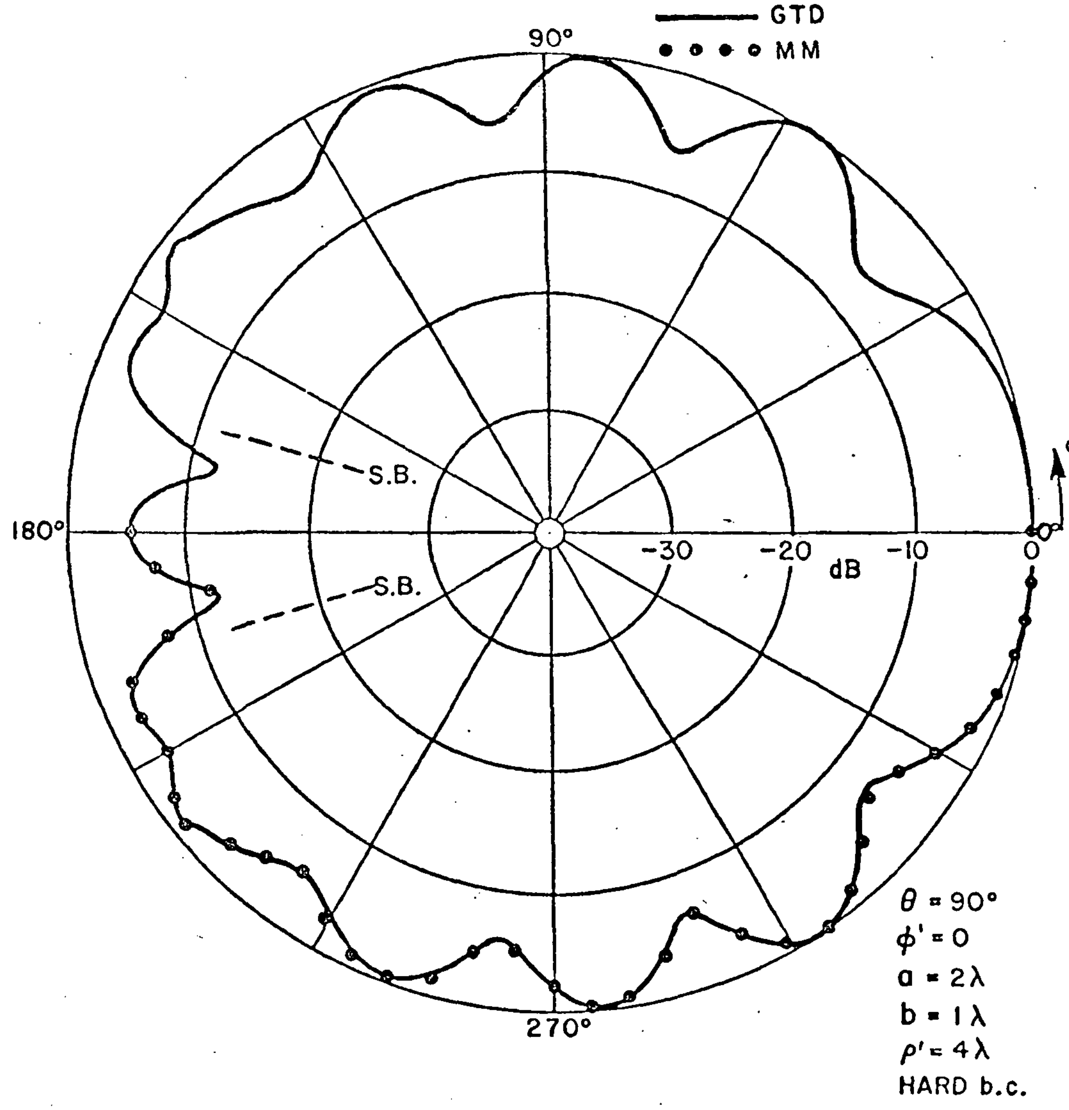

Figure 44b--E_ϕ radiation pattern surrounding the elliptic cylinder. Here GTD implies GTD + transition solution.

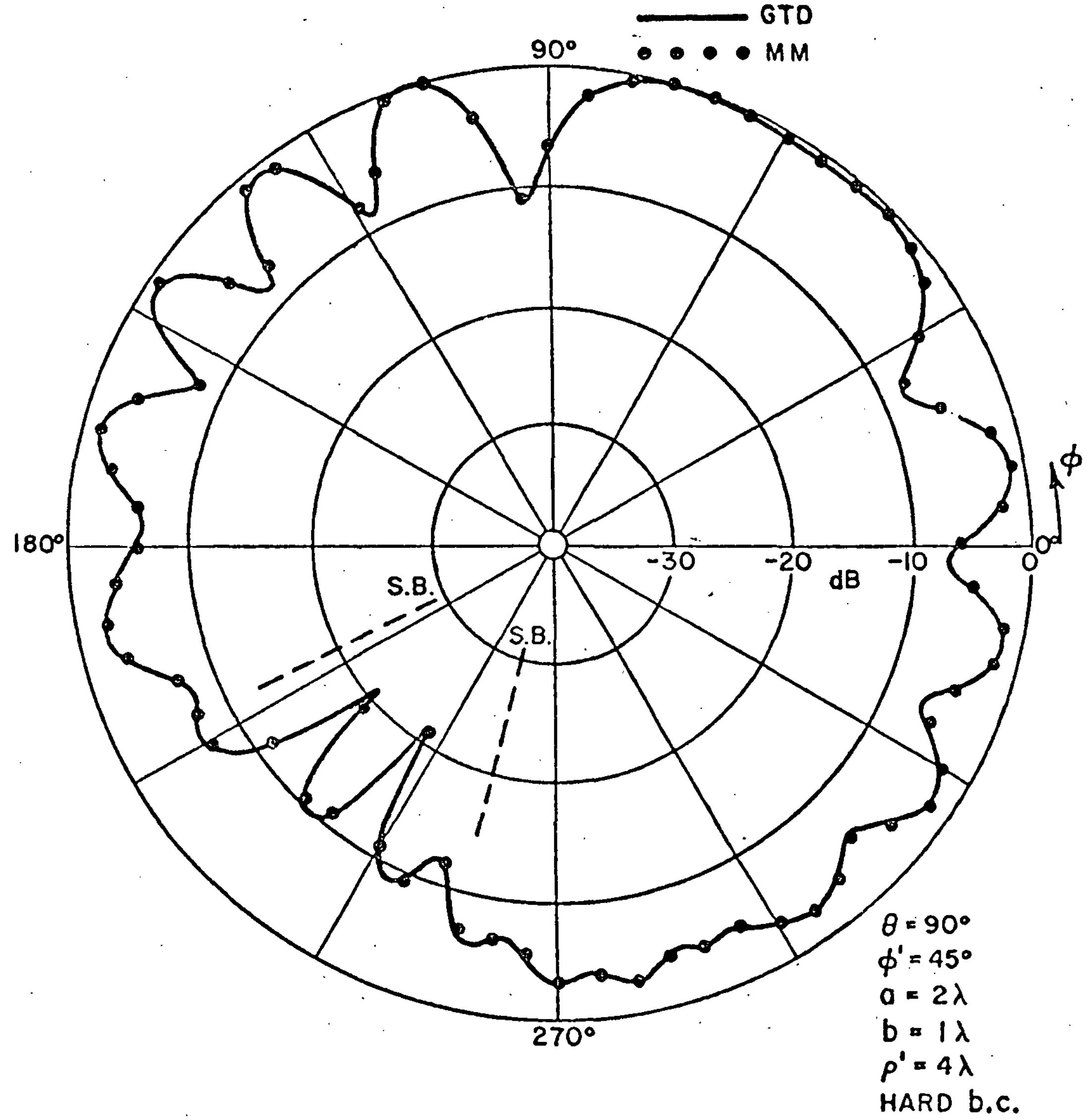

Figure 44c--E_ϕ radiation pattern surrounding the elliptic cylinder. Here GTD implies GTD + transition solution.

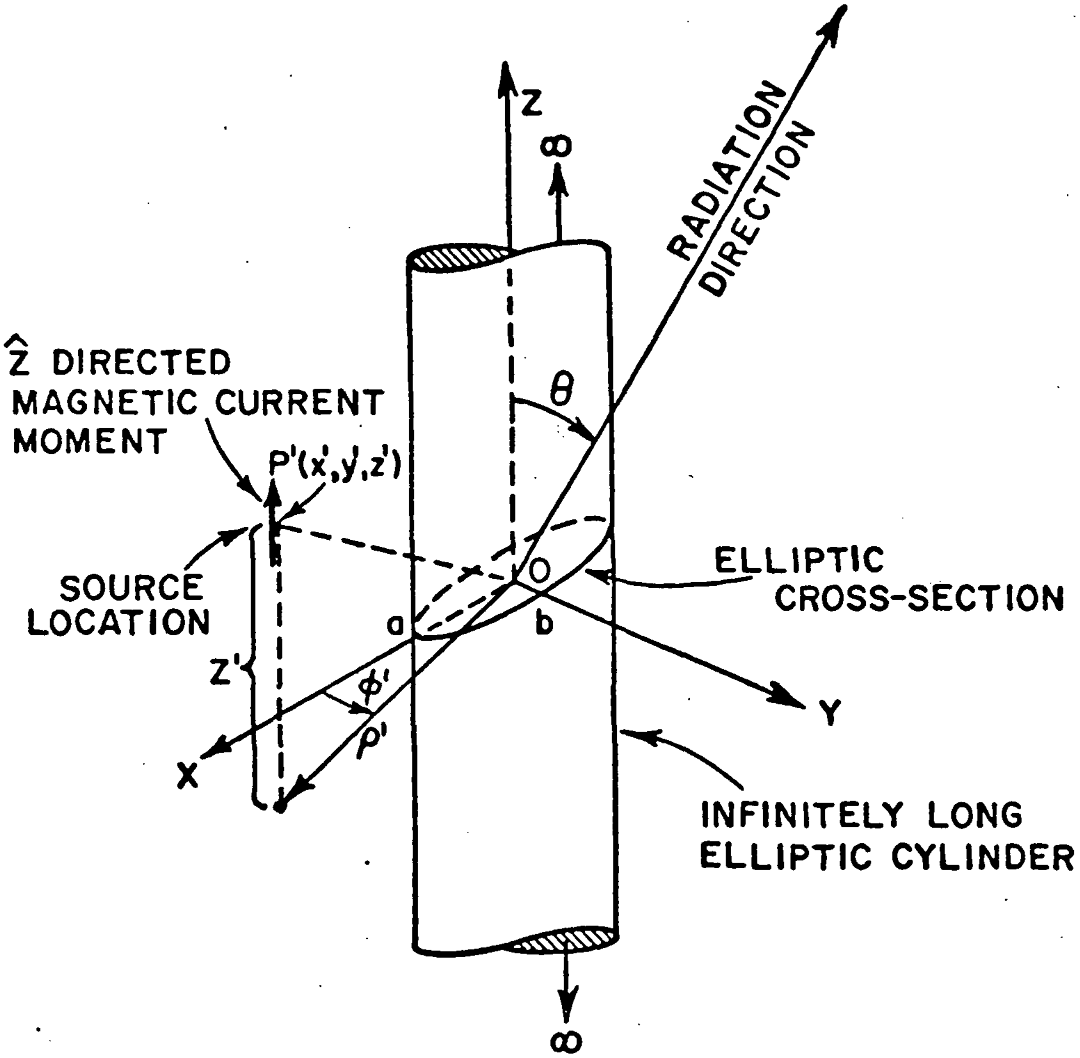

Figure 45a--3-D scattering configuration involving an infinitely long elliptic cylinder.

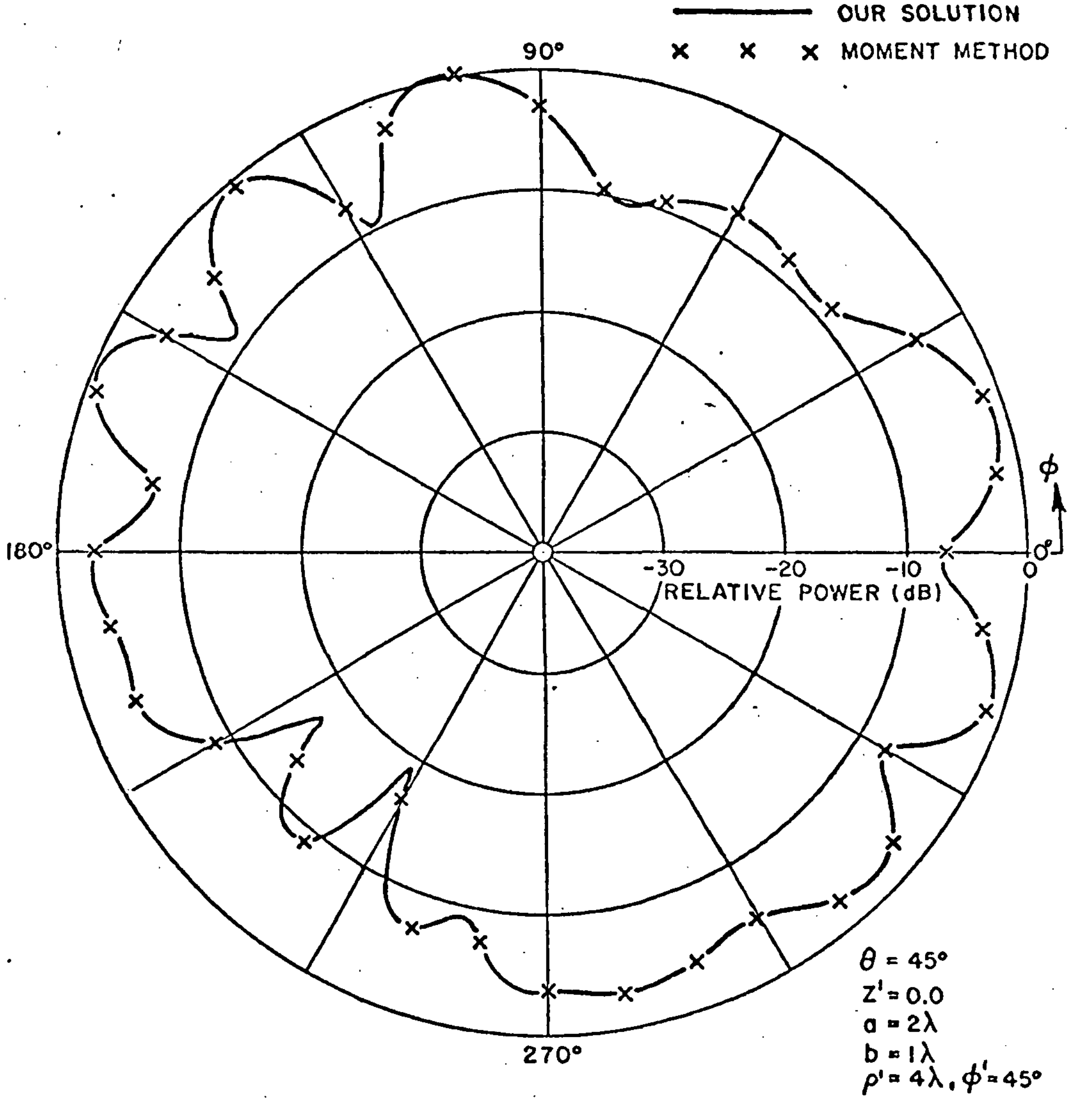

Figure 45b--Conical scan radiation pattern for the 3-D scattering configuration. The pattern of the $\hat{\phi}$ component of the electric field is shown.

The flat end cap and elliptic cylinder junction can be represented by a curved wedge such that one can apply the Geometrical Theory of Diffraction as discussed in Chapter II, Section E. The end caps are defined by their normals as given in Equations (72a and b), and their origin position on the z-axis. The edge of the wedges are given by

$$\vec{e}^{+} = - a \sin v \, \hat{x} + b \cos v \, \hat{y} - a \sin v \cot \theta_c^{+} \, \hat{z}$$

for the most positive end cap and

$$\vec{e}^{-} = a \sin v \, \hat{x} - b \cos v \, \hat{y} + a \sin v \cot \theta_c^{-} \, \hat{z}$$

for the most negative end cap. The diffraction by a curved edge obeys the same laws of diffraction as the straight edge in that the half-angle for a cone of diffracted rays is equal to the angle of incidence. This can be expressed as

$$\hat{e}(v) \cdot \hat{I}(v) = \hat{e}(v) \cdot \hat{d} \, .$$

The location of the diffraction points is more complicated, however, since the edge vector is a function of the parameter v. It can be shown that for a circular or elliptic edge outside the caustic regions there are in general four points of diffraction on the edge of a near field source and a given scatter direction.

The diffraction points can be found in many ways. An exact solution similar to that obtained for the reflection off an elliptic cylinder can be found which in this case is an eighth order polynomial. An incremental solution could also be found for this problem, but this is complicated by the fact that three of the diffraction points can merge into one in certain scatter directions. A search method is another possibility and is used here. The geometry is illustrated in Figure 46.

The search method is based on minimizing the error given by

$$\varepsilon(v) = \hat{e}(v) \cdot \hat{I}(v) - \hat{e}(v) \cdot \hat{d}$$

where

$$\vec{I}(v) = (a \cos v - x_s)\hat{x} + (b \sin v - y_s)\hat{y} + (a \cos v \cot \theta_c + z_c - z_s)\hat{z}$$

as v is incremented from 0° to 360°. A minimum is found using

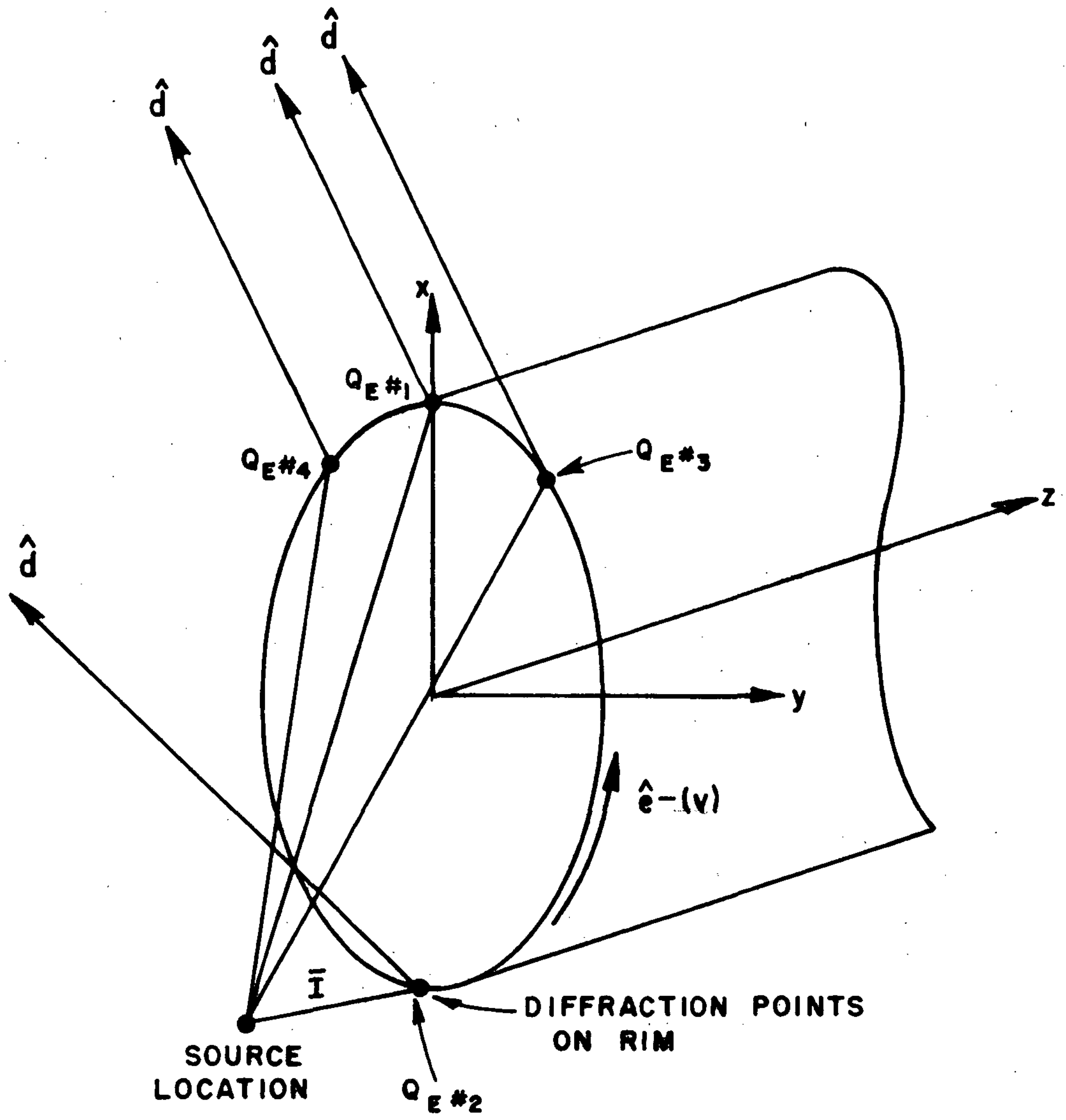

Figure 46--Curved wedge diffraction points on rim of end cap of finite elliptic cylinder.

$$\xi_j = \varepsilon(v_{j-1}) + \varepsilon(v_j) + \varepsilon(v_{j+1}),\ j = 0 \text{ to } 361.$$

If

$$|\xi_j| \le |\xi_{j-1}| \text{ and } |\xi_j| \le |\xi_{j+1}|,$$

then v_j is the closest point to a minimum. An interpolation scheme is used to find the actual minimum based on

$$v_d = v_j + \Delta v$$

where

$$\Delta v = \frac{s'(\bar{e} \cdot \hat{d}) - \bar{e} \cdot \bar{I}}{\bar{e}\cdot\Delta\bar{I}+\Delta\bar{e}\cdot\bar{I}-(\bar{I}\cdot\Delta\bar{I})(\bar{e}\cdot\hat{d})-s'(\Delta\bar{e}\cdot\hat{d})}$$

and

$$s' = |\bar{I}|$$

$$\Delta\bar{I} = -a \sin v\, \hat{x} + b \cos v\, \hat{y} - a \cos v \cot\theta_c \hat{z}$$

$$\Delta\bar{e}^{\pm} = \pm(-a \cos v\, \hat{x} - b \sin v\, \hat{y} - a \cos v \cot\theta_c^{\pm}\, \hat{z}).$$

This process is continued until four points are found or the whole edge has been searched.

Now that the points of diffraction are known the diffracted field can be determined. In the far field, the diffracted field from one of the diffraction points (v_d) is given by, Equation (17),

$$\begin{bmatrix} E_{\parallel}^{d} \\ E_{\perp}^{d} \end{bmatrix} \sim \begin{bmatrix} -D_s & 0 \\ 0 & -D_h \end{bmatrix} \begin{bmatrix} E_{\parallel}^{i}(Q_E) \\ E_{\perp}^{i}(Q_E) \end{bmatrix} \sqrt{\rho}\, e^{jk \vec{R}_d\cdot\hat{d}} \frac{e^{-jkd}}{d} .$$

The diffraction coefficient for the curved wedge are given in Equation (19). The distance parameter associated with the incident field with $s\to\infty$ is given by, Equation (20a),

$$L^i = \frac{\rho_1^i \rho_2^i \sin^2\beta_o}{\rho_e^i} .$$

For spherical wave incidence

$$\rho_1^i = \rho_2^i = \rho_e^i = s'$$

so that L' is given by

$$L^i = s' \sin^2\beta_o .$$

The distance parameter associated with the reflected field with $s \to \infty$ is given by, Equation (20b),

$$L^r = \frac{\rho_1^r \rho_2^r \sin^2\beta_o}{\rho_e^r}$$

where ρ_e^r is given in Equation (21). For the 0 surface, which is the flat end cap, the parameters are simply given by

$$\rho_1^{ro} = \rho_2^{ro} = \rho_e^{ro} = s'$$

so

$$L^{ro} = s' \sin^2\beta_o .$$

For the n surface, which is the curved surface, the parameters ρ_1^{rn} and ρ_2^{rn} are defined in Equations (70a) and (70b), respectively. The parameter ρ_e^{rn} is given by

$$\frac{1}{\rho_e^{rn}} = \frac{1}{s'} - \frac{2(\hat{n}\cdot\hat{n}_e)(\hat{n}\cdot\hat{I})}{a_e \sin^2\beta_o}$$

where $\hat{n}$ is the unit normal to the cylinder at the diffraction point, the normal to the edge is

$$\overline{n}_e = b \cos v_d \sin\theta_c \hat{x} + \frac{a \sin v_d}{\sin\theta_c} \hat{y} + b \cos v_d \cos \theta_c \hat{z},$$

$$a_e = \left. \frac{(a^2 \sin^2 v + b^2 \sin^2 \theta_c \cos^2 v)^{3/2}}{ab \sin^2 \theta_c} \right|_{Q_E},$$

$$\overline{I} = \overline{R}_d - \overline{R}_s,$$

$$\overline{R}_d = a \cos v_d \hat{x} + b \sin v_d \hat{y} + (a \cos v_d \cot \theta_c + z_c)\hat{z}.$$

The caustic distance ρ is given by, Equation (18),

$$\frac{1}{\rho} = \frac{1}{s'} - \frac{\hat{n}_e \cdot (\hat{I} - \hat{d})}{a_e \sin^2 \beta_0} .$$

As for the straight edge a ray fixed coordinate system is used centered about the diffraction point as shown in Figure 47. The necessary equations are given in Chapter III, where here $\hat{e}$ corresponds to $\hat{e}_m$ and $\hat{n}_{ec}$ to $\hat{n}|_{plate}$. The wedge angle number for the curved edge is given by

$$n_w = 1 + \left. \frac{\cos^{-1}(\hat{n} \cdot \hat{n}_{ec})}{\pi} \right|_{v=v_d}.$$

If $\phi' > n_w$ (180°) or $\phi > n_w$ (180°), then the incident or diffracted field, respectively, is shadowed and does not need to be found. In other words, it is assumed that only diffraction points that have an incident field direct from the source is to be found. It is possible to have a diffraction from the curved edge that results from a field that is incident on the edge after it has propagated along the cylinder as a surface diffracted field. This type of field is neglected in this study. The diffracted field from the jth diffraction point on the ith end cap is then given by

$$\overline{E}^{d}_{ij}(\theta_s,\phi_s) = E^{d}_{\parallel}\hat{\beta}_0 + E^{d}_{\perp}\hat{\phi}.$$

As is mentioned above, it is possible for three of the diffraction points to merge into one for certain aspect angles. This represents a pseudo-caustic effect resulting from the disappearance of isolated ray contributions. The GTD fails to describe the transition from the four isolated diffracted ray result to the pseudo-caustic result and hence needs modification. This is presently being studied [65] through the use of equivalent rim currents which indirectly employ the GTD edge diffraction coefficients. The equivalent edge currents are then incorporated in the radiation integrals which yield a smooth behavior for the field across these pseudo-caustic regions. At the present time, this has not been included here.

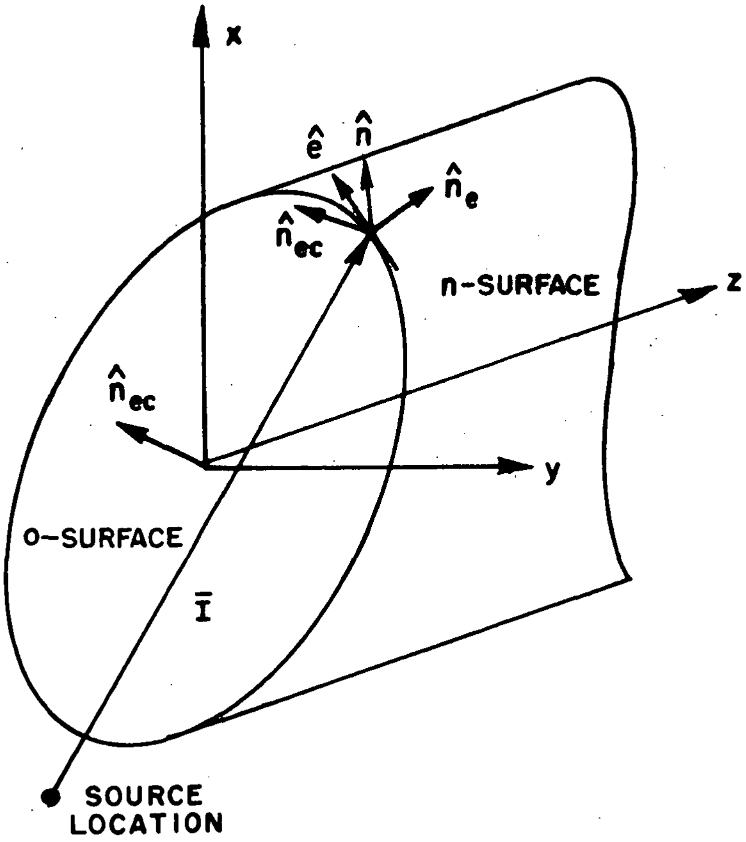

Figure 47--Edge coordinate system at curved wedge diffraction point.

The total diffracted field from the end cap rims, if they exist, can be written as

$$\vec{E}^{d}_{\text{end cap}}(\theta_s,\phi_s) = \sum_{i=1}^{2}\sum_{j=1}^{4} \vec{E}^{d}_{ij} \, . \tag{79}$$

The total scattered field from a finite elliptic cylinder is now given by the sum of all of its individual contributors in their appropriated regions as

$$\vec{E}(\theta_s,\phi_s) = \vec{E}^{i} + \vec{E}^{r} + \vec{E}^{r}_{\text{end cap}} + \vec{E}^{d} + \vec{E}^{t} + \vec{E}^{d}_{\text{end cap.}} \tag{80}$$

The description of the individual scattering contributors from the cylinder are summarized in Table III.

TABLE III
SCATTERED FIELDS INCLUDED IN THE FINITE CYLINDER SOLUTION

	Symbol	Description	Figures	Equation
1)	$\vec{E}^{r}$	Reflected field off the cylinder	40	69
2)	$\vec{E}^{d}$	Diffracted field off the cylinder	41	75
3)	$\vec{E}^{t}$	Transition field off the cylinder	40 & 41	78
4)	$\vec{E}^{r}_{\text{end cap}}$	Reflected field off the end caps	-	73
5)	$\vec{E}_{\text{end cap}}$	Diffracted field off the edges of the end caps	47	79

To illustrate the validity of this near field solution, it is compared with measured results for a finite circular cylinder given in Reference [23]. The geometry is illustrated in Figure 48. For a horizontal dipole parallel to the cylinder axis, the present result is compared with a measured result as shown in Figure 49. Note that the two results are almost identical except about the caustic region where the analytic solution does not accurately describe the field. The same is true for a vertical dipole (parallel to the y-axis) result shown in Figure 50. The caustic region is not extensive for most cases. Leaving this caustic in the solution, does not strongly effect the results in practice as will be seen in the next chapter in which the aircraft problem is studied.

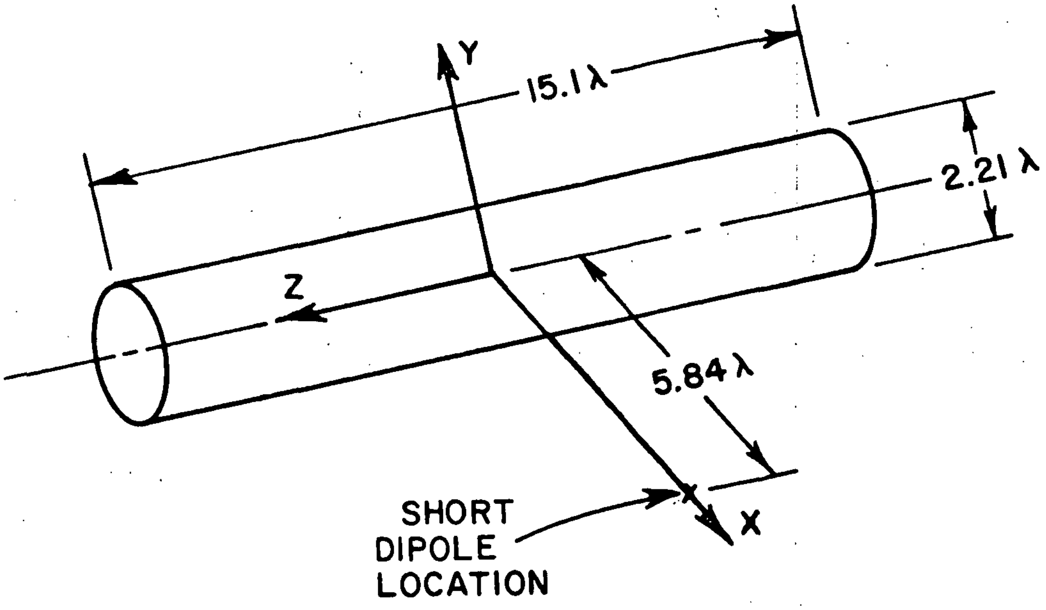

Figure 48--Short dipole illuminating a finite cylinder.

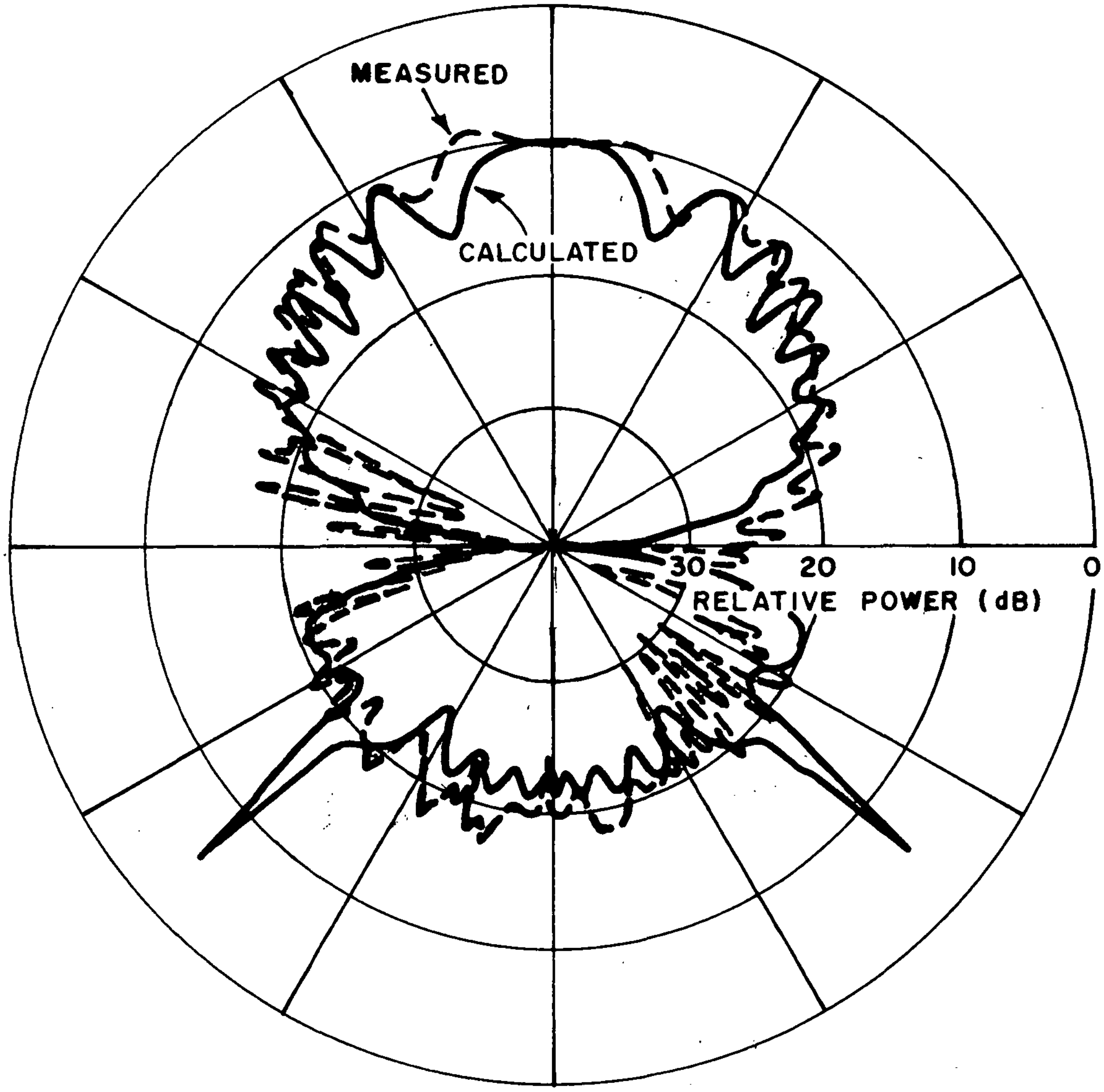

Figure 49--Radiation pattern (E_θ) of a horizontal dipole (parallel to z-axis) in the x-z plane.

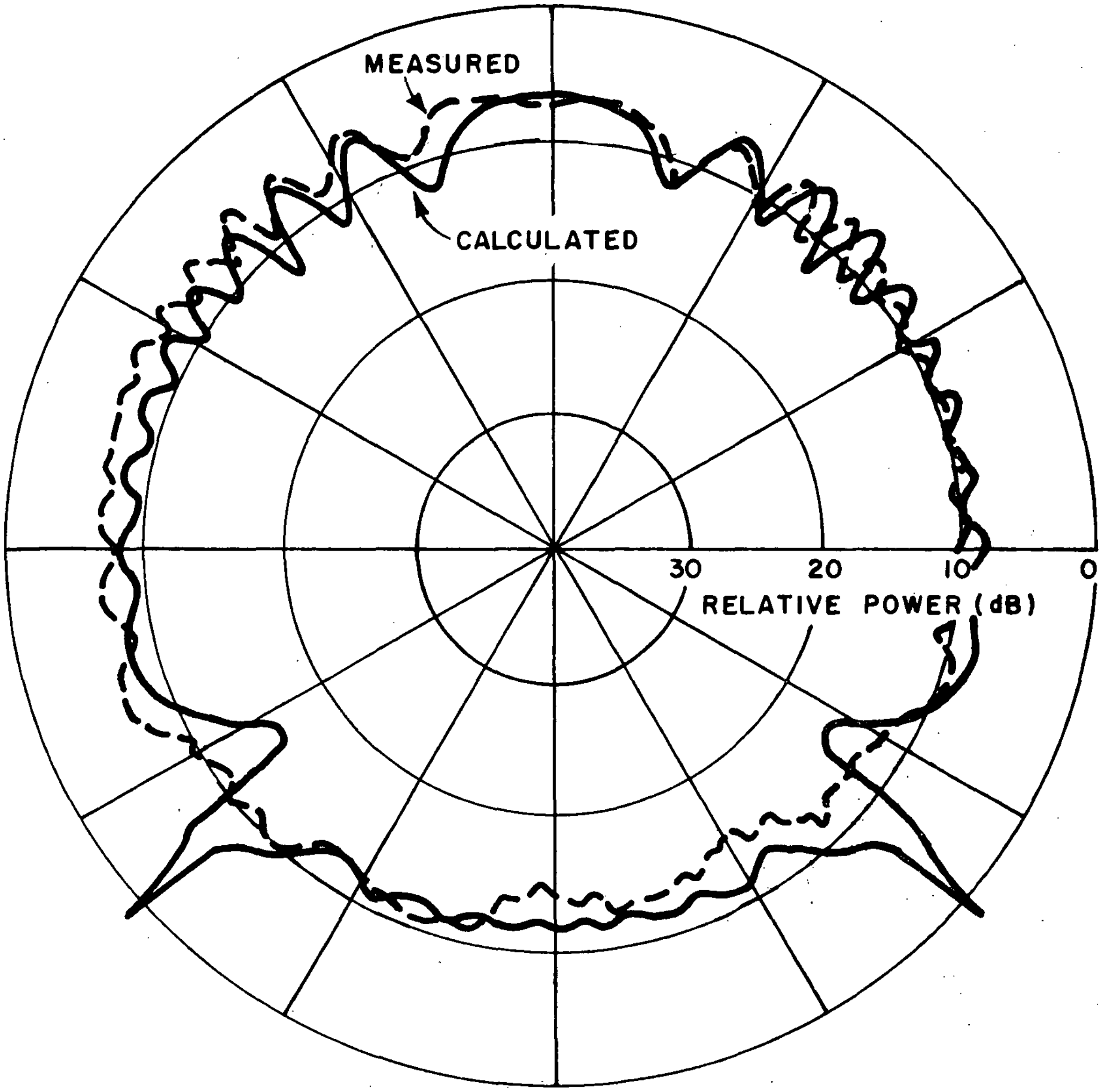

Figure 50--Radiation pattern (E_ϕ) of a vertical dipole (parallel to y-axis) in the x-z plane.

CHAPTER V

ANALYSIS OF WING MOUNTED ANTENNA RADIATION PATTERNS

A. Introduction

The previous chapters have illustrated how the Geometrical Theory of Diffraction is used to study the scattering by basic structures (flat plates and finite cylinders). In this chapter these solutions are extended to determine the radiation patterns of antennas mounted on the wings of aircraft. The analytic aircraft model consists of a finite elliptic cylinder representing the fuselage with flat or bent plate wings and horizontal and vertical stabilizers. Small plates and elliptic cylinders can be used to represent engines and or external stores if necessary.

The basic aircraft shape to be modelled is illustrated in Figure 51. This model is versatile enough to simulate the major scattering contributors of a wide variety of aircraft. The solution is also formulated in such a way that an arbitrary antenna can be considered simply by integrating the equivalent aperture currents. The lower frequency limit of the solution is dictated by the ray optics format which requires that the various scattering centers be no closer than approximately a half wavelength with the overall aircraft being large in terms of the wavelength. The upper frequency limit is dictated by the model representation of the actual aircraft considered.

B. Wing Mounted Antenna Analysis

In general, an antenna mounted near a number of flat plates and an elliptic cylinder is even a more complicated scattering problem than that of a number of flat plates alone as discussed in Chapter III. Again, it is necessary to make a few good engineering assumptions about the problem in order to make it tractable. First it is assumed, at present, that the antenna is mounted on or close to the wing structure, and it is at least a small distance (greater than a quarter wavelength) from the fuselage. This is done merely to reduce the number of scattering mechanisms to be considered. An antenna mounted on the fuselage needs a different treatment as was originally shown in Reference [23]. When the antenna is mounted very close to the fuselage neither solution is applicable in its present form. The antenna is also assumed, at present, to be mounted away from engines and external stores. If the antenna is mounted sufficiently far from these objects,(i.e., the antenna is mounted on the top portion of the wings) their effects will be negligible. If, however, the antenna is mounted on the lower portion of the wing and is close to an obstacle, the scattering effects of that object can be approximated by using small flat plates or elliptic cylinders. This is not done in the present analysis. It should also be possible to easily extend the present solution to antennas mounted on the vertical or horizontal stabilizers.

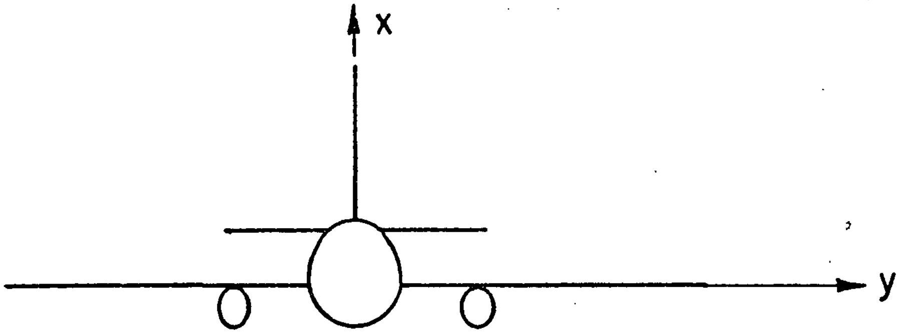

(a) FRONT VIEW

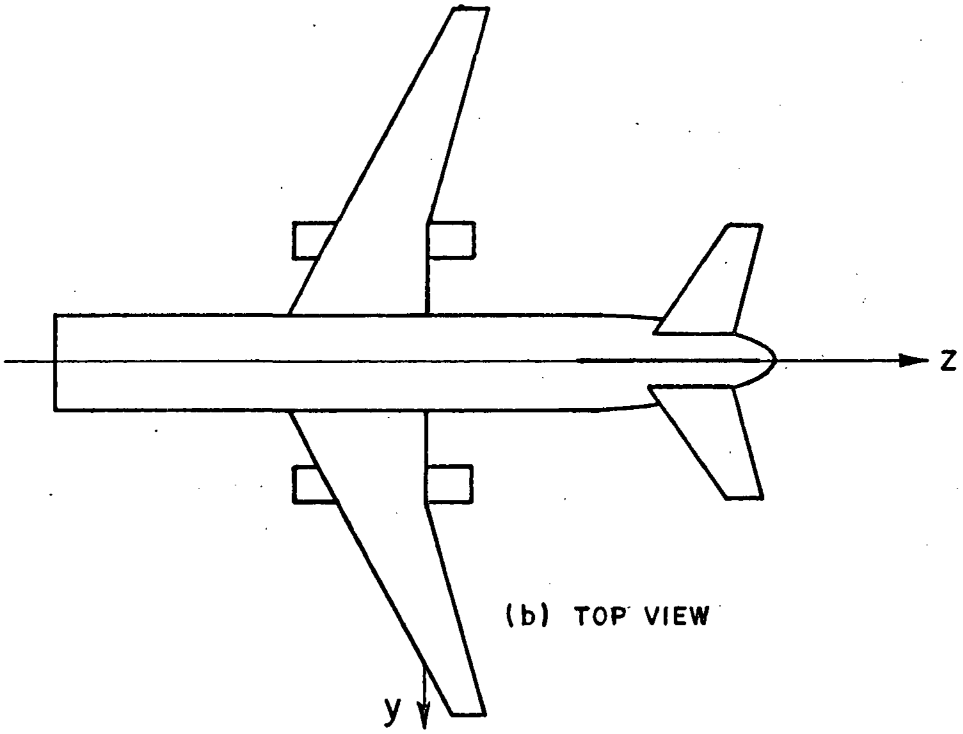

(b) TOP VIEW

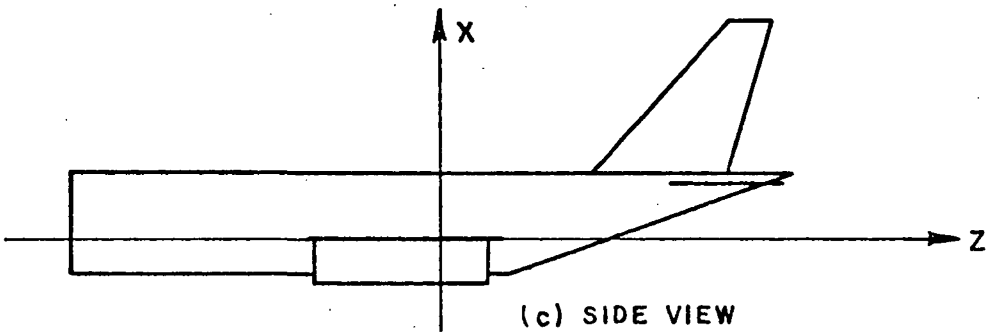

(c) SIDE VIEW

Figure 51--Illustration of general aircraft model for wing mounted antennas.

The scattering mechanisms considered for this model include only first and second order interaction terms with second order being mechanisms like reflected-diffracted or diffracted-reflected fields. All the scattering terms considered for the scattering from a number of plates in Chapter III, Table II, and for the finite elliptic cylinder in Chapter IV, Table III, have been included in this aircraft model. They will not be repeated again. The additional interaction terms that have been found to be important for the aircraft model are shown in Table IV. Subscripts have been added in the notation of the field to distinguish between interactions between the plate (pl.) and the cylinder (cyl.). Note it is assumed that the wing on the opposite side of the structure from the antenna does not contribute to the scattered field. This is a valid assumption in that the surface ray must propagate sufficiently far around the fuselage in order to illuminate the other wing which implies the surface ray attenuates a great deal. Thus, the field illuminating the opposite wing is very weak as well as its scattered field. Also, the wing is assumed to be mounted in the y-z plane, as illustrated in Figure 51, that is at the symmetry point of the cylinder so that image theory can be used to model the wing-cylinder junction. This can be modified by the use of curved wedge diffraction, if the wing must be mounted at an angle. However, this does not appear to be necessary for a practical representation of real aircraft configurations.

As mentioned before, it is important to shadow the fields properly. This can be done by checking the incident ray paths and scattered ray paths for all the interaction mechanisms using both the plate and cylinder shadowing procedures outlined previously. Only those fields that exist should be included in the total field, the shadowed fields must be set to zero. This will help insure that significant terms that are large enough to produce visible discontinuities in the radiation pattern when neglected will be detectable. These higher order terms can then be added to the pattern if they are practical to obtain and are of engineering value in the final result.

Each of the scattered field terms that are to be included for the aircraft model, as listed above, involve a scattering mechanism in which one part of the structure acts as the source of the incident field that illuminates a different part of the structure. The first three scattering mechanisms listed above are simple to determine because they involve reflections off the flat plates such that image theory can be used. As a consequence, the various mechanisms can be viewed as point sources radiating spherical waves originating from their images. This means that the analyses carried out in the previous chapters for the individual scattering terms are applicable here. The procedure for obtaining these fields need not be repeated here. The last two scattered field terms in the list, however, are complicated by the fact that after the first interaction with the structure, the incident field for the second interaction can not be viewed as a point source with a spherical wavefront. These terms must be treated as a source that radiates a wave with two radii of curvature. Consequently the new problems associated with these two scattering mechanisms are considered in great detail.

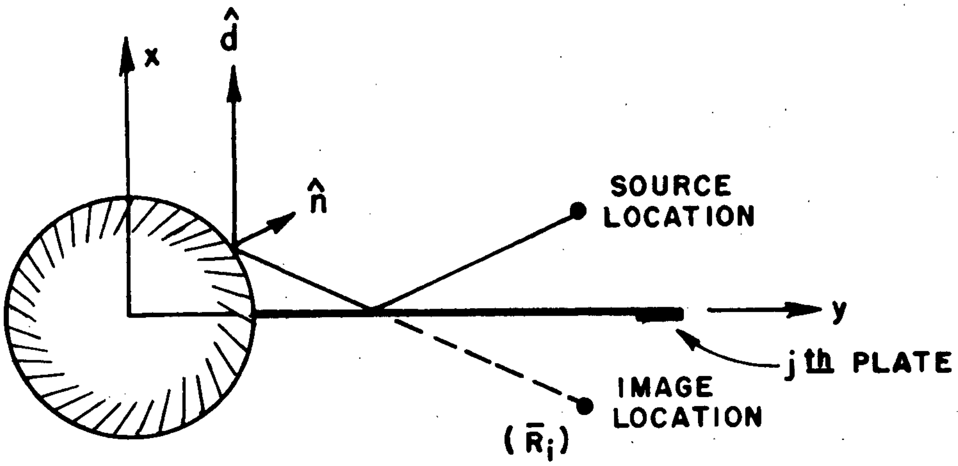

Figure 52--Illustration of reflected field off the cylinder after reflection by a plate.

The first scattering mechanism to be considered is the reflected field of the cylinder after reflection from the jth plate. This is illustrated in Figure 52. The reflected field of the cylinder is given by Equation (69), where the origin of the incident field is the image of the source ($\bar{R}_i$) in the jth plate. The incident field then is the reflected field of the jth plate in the direction from the image to the reflection point of the cylinder and is given by Equation (34), with $\bar{E}^i(Q_E) = \bar{E}^r_j(\theta_i,\phi_i)$. The application of Equations (37-39) to find the reflected fields of the jth plate and the applications of Equations (70) and (71) to find the reflected fields off the cylinder in the scatter direction $\hat{d}$ is a straightforward extension of the above equations and need not be discussed further here. The total field associated with this scattering term is given by

$$\overline{\overline{E}}^{rr}_{pl-cyl}(\theta_s,\phi_s) = \sum_{j=1}^{P} \overline{\overline{E}}^{rr}_{j,cyl}(\theta_s,\phi_s), \tag{81}$$

where $\bar{E}^r_{j,cyl}(\theta_s,\phi_s) = 0$ if it is shadowed in any way.

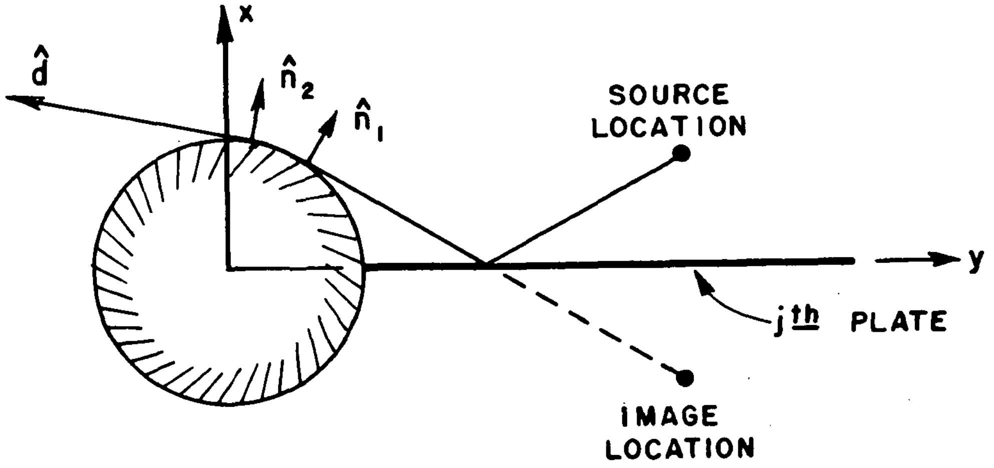

Figure 53--Illustration of transition field off the cylinder after reflection by a plate.

The scattering mechanism to be considered next is the transition field scattered by the cylinder after a reflection by the jth plate. This is illustrated in Figure 53. The transition field of the cylinder is given by Equation (76), and again the image of the source in the jth plate can be viewed at the origin of the incident field. The incident field for this term is then given by Equation (34) which is the reflected field from the jth plate in the direction from the image in the plate to the cylinder scatter point. The cylinder scatter point in the lit region is the point of reflection, and in the shadow region it is the tangent point. The necessary equations for the reflected field from the jth plate are given in Equations (37-39) and the necessary equations for the transition field given in Equations (77a and b). Note that the shadowing procedures determine if the transition field due to both the top part of the cylinder and the bottom part of the cylinder need to be included. The total field associated with this scattering term is given by

$$\vec{E}^{rt}_{pl-cyl}(\theta_s,\phi_s) = \sum_{j=1}^{P} \vec{E}^{rt}_{j,cw} + \sum_{j=1}^{P} \vec{E}^{rt}_{j,ccw} . \tag{82}$$

The scatter terms associated with a reflection off the jth plate after being reflected by the cylinder are illustrated in Figure 54. The reflected field of the cylinder is found in the direction obtained by imaging the scatter direction into the plate using,

$$\hat{d}_r = \hat{d} - 2(\hat{n}\cdot\hat{d})\hat{n} \ .$$

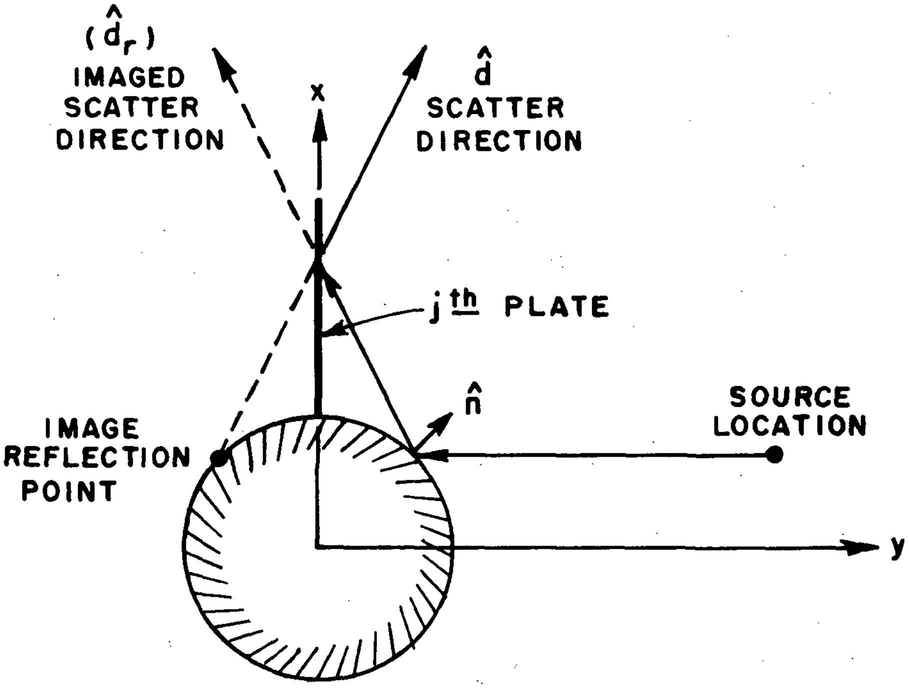

Figure 54--Illustration of reflected field off a plate after reflection by the cylinder.

This reflected field, given by Equations (69), is the incident field on the plate such that

$$\vec{E}^{i}(Q_R) = \vec{E}^{r}_{cyl}(\theta_i,\phi_i) \ .$$

The reflected field off the plate is then computed using Equations (37-39) in the scatter direction. The field appears to be coming from the images in the plate of the two caustics associated with the reflected field off the cylinder. The total field for this scattering term is given by

$$\vec{E}^{rr}_{cyl-pl}(\theta_s,\phi_s) = \sum_{j=1}^{P} \vec{E}^{rr}_{cyl,j}(\theta_s,\phi_s) . \tag{83}$$

The scattering mechanism that corresponds to a diffracted field from an edge after a reflection off the cylinder is illustrated in Figure 55. In order to find this field in a given scatter direction $\hat{d}$, the ray path that the field travels must be determined. This path is governed by the laws of reflection off the cylinder surface and the laws of diffraction along the edge.

The law of reflection on the cylinder can be written as given in Equation (64) such that

$$(\bar{n}x\bar{I})(\bar{n}\cdot\bar{r}) + (\bar{n}\cdot\bar{I})(\bar{n}x\bar{r}) = 0. \tag{84}$$

In this case the ray designated $\bar{r}$ is not known a priori. It is dependent on the diffraction point on the edge. The diffraction point, in turn, is also dependent on the reflection point. This means that the above equation is non-linear. At present, there does not appear to be a way to solve this problem in an exact manner. The incremental method, based on a first order Taylor series approximation, as developed for the reflection point off an elliptic cylinder in Chapter IV may be employed here.

For a cylinder the laws of reflection as governed by Equation (84), reduce to the two equations

$$f(v,z,\theta_s,\phi_s) = (n_xI_x+n_yI_y)(n_xr_y-n_yr_x)+(n_xr_x+n_yr_y)(n_xI_y-n_yI_x)=0. \tag{85a}$$

and

$$g(v,z,\theta_s,\phi_s) = (n_xI_x+n_yI_y)r_z+(n_xr_x+n_yr_y)I_z=0. \tag{85b}$$

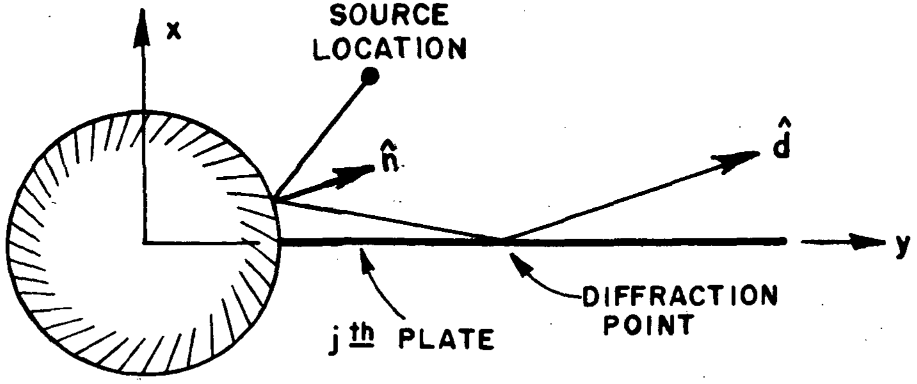

FRONT VIEW

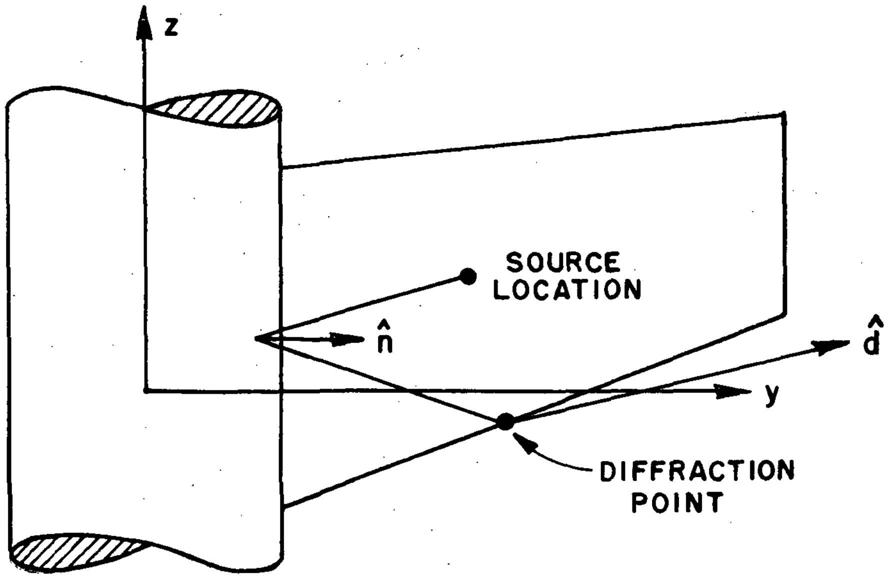

TOP VIEW

Figure 55--Illustration of diffracted field off an edge after reflection by the cylinder.

The normal to the cylinder is given by

$$\overline{n}(v) = n_x(v)\hat{x} + n_y(v)\hat{y}$$

or

$$\overline{n}(v) = b \cos v \; \hat{x} + a \sin v \; \hat{y} \; .$$

The incident vector on the cylinder is given by

$$\vec{I}(v,z) = I_x(v,z)\hat{x} + I_y(v,z)\hat{y} + I_z(v,z)\hat{z} \; ,$$

$$\vec{I}(v,z) = \overline{R}_r(v,z) - \overline{R}_s ,$$

or

$$\vec{I}(v,z) = (a \cos v - x_s)\hat{x} + (b \sin v - y_s)\hat{y} + (z - z_s)\hat{z}$$

where $\overline{R}_r$ is the reflection point and $\overline{R}_s$ is the source location. The reflected ray is given by the vector

$$\overline{r}(v,z,\theta_s,\phi_s) = r_x\hat{x} + r_y\hat{y} + r_z\hat{z}$$

or

$$\overline{r}(v,z,\theta_s,\phi_s) = \overline{R}_d - \overline{R}_r$$

where $\overline{R}_d$ is the diffraction point on the mth edge and is given by

$$\overline{R}_d = \overline{C}_m + t_p(v,z)\hat{e}_m + s_p(v,z) \cot\beta_o(\theta_s,\phi_s)\hat{e}_m$$

and

$$t_p = (\overline{R}_r - \overline{C}_m) \cdot \hat{e}_m \; ,$$

$$s_p = |\overline{R}_r - t_p \hat{e}_m - \overline{C}_m| \quad ,$$

$$\cot\beta_o = \frac{\hat{d} \cdot \hat{e}_m}{\sqrt{1-(\hat{d}\cdot\hat{e}_m)^2}} \quad .$$

Since $\overline{r}$ is dependent on v and z, Equations (85a and b) are not separable and must be solved together. Expanding these two equations in terms of a first order Taylor series gives

$$f_{j+1} = f_j + \frac{\partial f_j}{\partial v}\,\delta v + \frac{\partial f_j}{\partial z}\,\delta z + \frac{\partial f_j}{\partial \theta_s}\,\delta\theta_s + \frac{\partial f_j}{\partial \phi_s}\,\delta\phi_s + O(\delta^2)$$

$$g_{j+1} = g_j + \frac{\partial g_j}{\partial v}\,\delta v + \frac{\partial g_j}{\partial z}\,\delta z + \frac{\partial g_j}{\partial \theta_s}\,\delta\theta_s + \frac{\partial g_j}{\partial \phi_s}\,\delta\phi_s + O(\delta^2)$$

Since from the laws of reflection

$$f_{j+1} = 0$$

$$g_{j+1} = 0$$

and since $\delta\theta_s$, $\delta\phi_s$, v_j, z_j, f_j and g_j are assumed to be known the above equations can be written in matrix form such that

$$\begin{bmatrix} \frac{\partial f_j}{\partial v} & \frac{\partial f_j}{\partial z} \\ \frac{\partial g_j}{\partial v} & \frac{\partial g_j}{\partial z} \end{bmatrix} \begin{bmatrix} \delta v \\ \delta z \end{bmatrix} = \begin{bmatrix} -f_j - \frac{\partial f_j}{\partial \theta_s}\,\delta\theta_s - \frac{\partial f_j}{\partial \phi_s}\,\delta\phi_s \\ -g_j - \frac{\partial g_j}{\partial \theta_s}\,\delta\theta_s - \frac{\partial g_j}{\partial \phi_s}\,\delta\phi_s \end{bmatrix} .$$

This two by two matrix is easily solved to give

$$\delta v = \frac{1}{\Delta}\left[\left(g_j \frac{\partial f_j}{\partial z} - f_j \frac{\partial g_j}{\partial z}\right) + \left(\frac{\partial f_j}{\partial z}\frac{\partial g_j}{\partial \theta_s} - \frac{\partial g_j}{\partial z}\frac{\partial f_j}{\partial \phi_s}\right)\delta\theta_s + \left(\frac{\partial f_j}{\partial z}\frac{\partial g_j}{\partial \phi_s} - \frac{\partial g_j}{\partial z}\frac{\partial f_j}{\partial \phi_s}\right)\delta\phi_s\right] \qquad (86a)$$

$$\delta z = \frac{1}{\Delta}\left[\left(f_j \frac{\partial g_j}{\partial v} - g_j \frac{\partial f_j}{\partial v}\right) + \left(\frac{\partial g_j}{\partial v} \frac{\partial f_j}{\partial \theta_s} - \frac{\partial f_j}{\partial v} \frac{\partial g_j}{\partial \theta_s}\right)\delta\theta_s\right.$$

$$\left. + \left(\frac{\partial g_j}{\partial v}\frac{\partial f_j}{\partial \phi_s} - \frac{\partial f_j}{\partial v} \frac{\partial g_j}{\partial \phi_s}\right)\delta\phi_s\right] \tag{86b}$$

where

$$\Delta = \left(\frac{\partial f_j}{\partial v}\frac{\partial g_j}{\partial z} - \frac{\partial f_j}{\partial z}\frac{\partial g_j}{\partial v}\right) .$$

The partial derivatives are given by

$$\frac{\partial f_j}{\partial v} = \left(\frac{\partial n_x}{\partial v} I_x + n_x \frac{\partial I_x}{\partial v} + \frac{\partial n_y}{\partial v} I_y + n_y \frac{\partial I_y}{\partial v}\right)(n_x r_y - n_y r_x)$$

$$+ \quad (n_x I_x + n_y I_y)\left(\frac{\partial n_x}{\partial v} r_y + n_x \frac{\partial r_y}{\partial v} - \frac{\partial n_y}{\partial v} r_x - n_y \frac{\partial r_x}{\partial v}\right)$$

$$+\left(\frac{\partial n_x}{\partial v} r_x + n_x \frac{\partial r_x}{\partial v} + \frac{\partial n_y}{\partial v} r_y + n_y \frac{\partial r_y}{\partial v}\right)(n_x I_y - n_y I_x)$$

$$+ \quad (n_x D_x + n_y D_y)\left(\frac{\partial n_x}{\partial v} I_y + n_x \frac{\partial I_y}{\partial v} - \frac{\partial n_y}{\partial v} I_x - n_y \frac{\partial I_x}{\partial v}\right)$$

$$\frac{\partial f_j}{\partial z} = \left(n_x \frac{\partial I_x}{\partial z} + n_y \frac{\partial I_y}{\partial z}\right)(n_x r_y - n_y r_x)$$

$$+ (n_x I_x + n_y I_y)\left(n_x \frac{\partial r_y}{\partial z} - n_y \frac{\partial r_x}{\partial z}\right)$$

$$+\left(n_x \frac{\partial r_x}{\partial z} + n_y \frac{\partial r_y}{\partial z}\right)(n_x I_y - n_y I_x)$$

$$+ (n_x r_x + n_y r_y)\left(n_x \frac{\partial I_y}{\partial z} - n_y \frac{\partial I_x}{\partial z}\right)$$

$$\frac{\partial f_j}{\partial \beta} = (n_x I_x + n_y I_y)\left(n_x \frac{\partial r_y}{\partial \beta} - n_y \frac{\partial r_x}{\partial \beta}\right)$$

$$+\left(n_x \frac{\partial r_x}{\partial \beta} + n_y \frac{\partial r_y}{\partial \beta}\right)(n_x I_y - n_y I_x)$$

with $\beta = \theta_s, \phi_s$ and

$$\frac{\partial g_j}{\partial v} = \left(\frac{\partial n_x}{\partial v} I_x + n_x \frac{\partial I_x}{\partial v} + \frac{\partial n_y}{\partial v} I_y + n_y \frac{\partial I_y}{\partial v}\right) r_z$$

$$+ (n_x I_x + n_y I_y) \frac{\partial r_z}{\partial v}$$

$$+\left(\frac{\partial n_x}{\partial v} r_x + n_x \frac{\partial r_x}{\partial v} + \frac{\partial n_y}{\partial v} r_y + n_y \frac{\partial r_y}{\partial v}\right) I_z$$

$$+ (n_x r_x + n_y r_y) \frac{\partial r_z}{\partial v}$$

$$\frac{\partial g_j}{\partial z} = \left(n_x \frac{\partial I_x}{\partial z} + n_y \frac{\partial I_y}{\partial z}\right) r_z + (n_x I_x + n_y I_y) \frac{\partial r_z}{\partial z}$$

$$+\left(n_x \frac{\partial r_x}{\partial z} + n_y \frac{\partial r_y}{\partial z}\right) I_z + (n_x r_x + n_y r_y) \frac{\partial I_z}{\partial z}$$

$$\frac{\partial g_j}{\partial \beta} = (n_x I_x + n_y I_y) \frac{\partial r_z}{\partial \beta} + \left(n_x \frac{\partial r_x}{\partial \beta} + n_y \frac{\partial r_y}{\partial \beta} \right) I_z$$

with $\beta = \theta_s, \phi_s$ where

$$\frac{\partial n_x}{\partial v} = -b \sin v$$

$$\frac{\partial n_y}{\partial v} = a \cos v$$

$$\frac{\partial I_x}{\partial v} = -a \sin v$$

$$\frac{\partial I_y}{\partial v} = b \cos v$$

$$\frac{\partial I_z}{\partial z} = 1$$

$$\frac{\partial \bar{r}}{\partial \alpha} = \frac{\partial \bar{R}_d}{\partial \alpha} - \frac{\partial \bar{R}_r}{\partial \alpha}$$

with $\alpha = v, z$

$$\frac{\partial \bar{R}_r}{\partial v} = -a \sin v \hat{x} + b \cos v \hat{y}$$

$$\frac{\partial \overline{R}_r}{\partial z} = \hat{z}$$

$$\frac{\partial \overline{R}_d}{\partial \alpha} = \frac{\partial t_p}{\partial \alpha}\hat{e}_m + \frac{\partial s_p}{\partial \alpha}\cot\beta_o\,\hat{e}_m$$

$$\frac{\partial t_p}{\partial \alpha} = \frac{\partial \overline{R}_r}{\partial \alpha}\cdot\hat{e}_m$$

$$\frac{\partial s_p}{\partial \alpha} = \frac{\frac{\partial \overline{R}_r}{\partial \alpha}\cdot(\overline{R}_r-\overline{C}_m) - \left(\frac{\partial \overline{R}_r}{\partial \alpha}\cdot\hat{e}_m\right)(\overline{R}_r-\overline{C}_m)\cdot\hat{e}_m}{\sqrt{(\overline{R}_r-\overline{C}_m)\cdot(\overline{R}_r-\overline{C}_m) - [(\overline{R}_r-\overline{C}_m)\cdot\hat{e}_m]^2}}$$

$$\frac{\partial \overline{r}}{\partial \beta} = s_p\,\frac{\partial(\cot\beta_o)}{\partial \beta}\,\hat{e}_m$$

with $\beta = \theta_s, \phi_s$ and

$$\frac{\partial(\cot\beta_o)}{\partial \beta} = \frac{\frac{\partial \hat{d}}{\partial \beta}\cdot\hat{e}_m}{[1-(\hat{d}\cdot\hat{e}_m)^2]^{3/2}} \quad .$$

These equations can then be used to find δv and δz changes associated with the reflection point on the cylinder surface due to $\delta\theta_s$ and $\delta\phi_s$ changes in the scatter direction. The new reflection point is found from the previous reflection point using

$$v_{j+1} = v_j + \delta v$$

and

$$z_{j+1} = z_j + \delta z \ .$$

Once the reflection point on the cylinder is known the diffraction point on the edge can, also, be determined.

Errors can be computed to see how accurately the values are determined using

$$\varepsilon_c = \hat{n} \cdot \hat{I} \Bigg|_{\substack{v_j+1 \\ z_j+1}} + \hat{n} \cdot \hat{r} \Bigg|_{\substack{v_{j+1},\ z_{j+1} \\ \theta_s+\delta\theta_s, \phi_s+\delta\phi_s}}$$

and

$$\varepsilon_d = \hat{e}_m \cdot \hat{r} \Bigg|_{\substack{v_{j+1}, z_{j+1} \\ \theta_s+\delta\theta_s, \phi_s+\delta\phi_s}} - \hat{e}_m \cdot \hat{d} \Bigg|_{\substack{\theta_s+\delta\theta_s \\ \phi_s+\delta\phi_s}} .$$

If the errors are not within a predetermined bound the interval steps $\delta\theta_s$ and $\delta\phi_s$ can be halved and the procedure repeated until the desired scatter direction is obtained and the desired error bounds are achieved.

A known starting location needs to be obtained for the first computation of the incremental method. This can be found in this instance by noting that the corner points of the edges are known and in fact they provide definite bounds on the permissible range for the reflection-diffraction path. With the corner points known, as shown in Figure 56, Equations (85a and b) can be solved by means of the polynomial solution technique derived in Chapter IV.

If the mth corner is given by

$$\overline{C}_m = x_c\hat{x} + y_c\hat{y} + z_c\hat{z}$$

then

$$\overline{r} = (x_c - a \cos v)\hat{x} + (y_c - b \sin v)\hat{y} + (z_c - z)\hat{z}$$

with $\overline{n}$ and $\overline{I}$ defined above. These values are substituted into Equation (85a) along with the fact that

$$\alpha = e^{jv}.$$

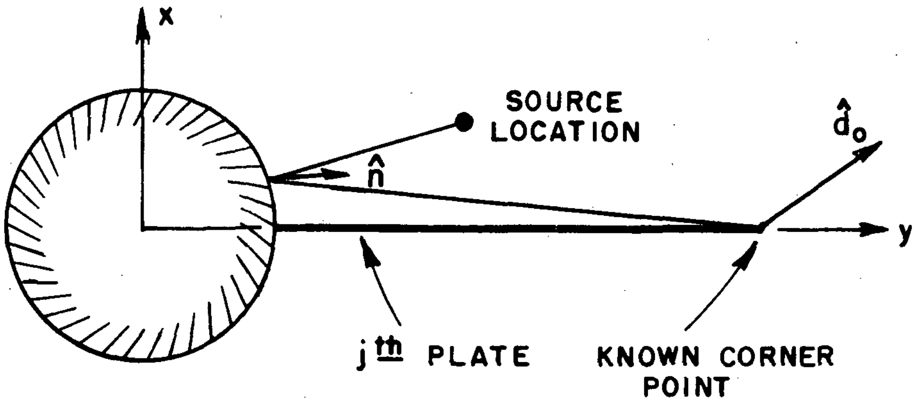

FRONT VIEW

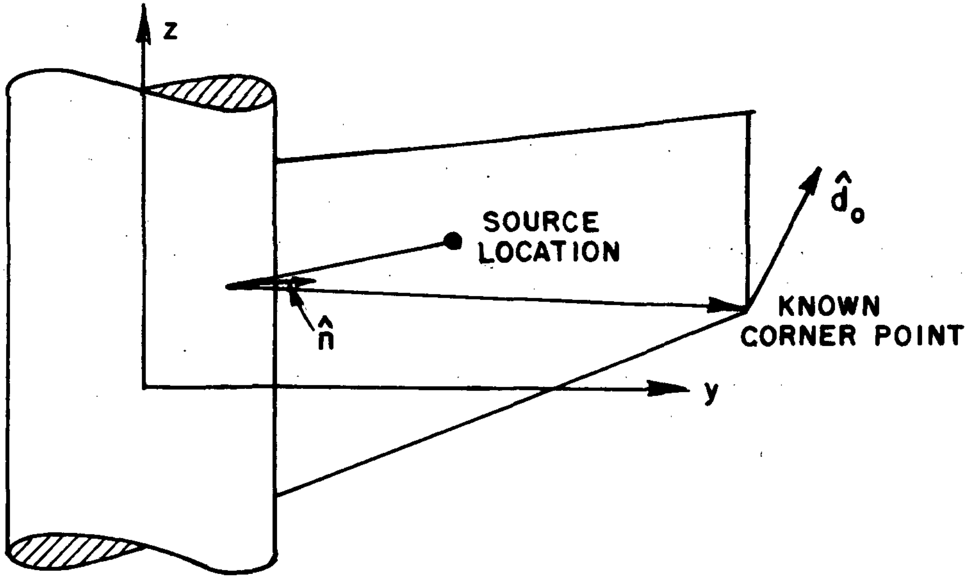

TOP VIEW

Figure 56--Illustration of starting point for finding diffraction point on an edge and the reflection point on the cylinder for the reflection-diffraction problem.

The equation is multiplied thru and like terms in α are collected so that a sixth order polynomial is obtained given by

$$C_6\alpha^6 + C_5\alpha^5 + C_4\alpha^4 + C_3\alpha^3 + C_2\alpha^2 + C_1\alpha^1 + C_o = 0$$

where

$$C_6 = (a^2-b^2)[a(y_c+y_s)+jb(x_c+x_s)]$$

$$C_5 = -2(a^2+b^2)(x_s y_c+y_s x_c)-j\ 4ab[(a^2-b^2)+(x_s x_c-y_s y_c)]$$

$$C_4 = a(5b^2-a^2)(y_c+y_s) + jb(5a^2-b^2)(x_c+x_s)$$

$$C_3 = 4(a^2-b^2)(x_s y_c+y_s x_c)$$

$$C_2 = C_4^* \quad \text{(complex conjugate of } C_4\text{)}$$

$$C_1 = C_5^*$$

$$C_0 = C_6^* \ .$$

The six roots of the polynomial correspond to v in that

$$v = \tan^{-1}\left(\frac{\text{Im }(\alpha)}{\text{Re }(\alpha)}\right) \ .$$

The physically realizable value which is the true reflection point is found by finding the v that minimizes the distance given by

$$|\vec{I}| + |\bar{r}| ,$$

which is necessary to satisfy Fermat's principle. Using this parameter (v_r) representing the reflection point in the x-y plane, the z-coordinate can be found from Equation (85b) to be

$$z_r = \frac{(n_x r_x + n_y r_y) z_s - (n_x I_x + n_y I_y) z_c}{(n_x r_x + n_y r_y) - (n_x I_x + n_y I_y)} \quad .$$

With the reflection point on the surface of the cylinder known for a given corner on the mth edge, the vector $\hat{r}$ represents a bound on the possible incident rays on the edge. The angle of the diffracted cone of rays from the mth edge at the corner is given by

$$\cos \beta_o = \hat{r} \cdot \hat{e}_m \; .$$

One of the rays defined by this cone angle can be used as the starting scatter direction for the incremental method. It is defined by

$$\hat{d}_o \cdot \hat{e}_m = \hat{r} \cdot \hat{e}_m \tag{87}$$

and the fact that the closest ray on the cone to the initial desired scatter direction $\hat{d}$ should be chosen. In other words, $\hat{d}_o$ should be chosen to maximize $\hat{d} \cdot \hat{d}_o$ with the constraint that $\hat{d}_o \cdot \hat{e}_m = \cos \beta_o$. This implies that the following equations need to be solved

$$\frac{\partial(\hat{d} \cdot \hat{d}_o + \lambda \hat{d}_o \cdot \hat{e}_m)}{\partial \theta_o} = 0$$

$$\frac{\partial(\hat{d} \cdot \hat{d}_o + \lambda \hat{d}_o \cdot \hat{e}_m)}{\partial \phi_o} = 0 \; ,$$

where

$$\hat{d} = d_x\hat{x} + d_y\hat{y} + d_z\hat{z}$$

$$\hat{d}_o = \cos\phi_o \sin\theta_o\hat{x} + \sin\phi_o \sin\theta_o\hat{y} + \cos\theta_o\hat{z}$$

$$\hat{e}_m = e_x\hat{x} + e_y\hat{y} + e_z\hat{z} \quad .$$

This can be solved to give

$$\cos\phi_o = \frac{d_x + \lambda e_x}{\pm\sqrt{(d_x+\lambda e_x)^2+(d_y+\lambda e_y)^2}}$$

$$\sin\phi_o = \frac{d_y + \lambda e_y}{\pm\sqrt{(d_x+\lambda e_x)^2+(d_y+\lambda e_y)^2}}$$

$$\cos\theta_o = \frac{d_z + \lambda e_z}{\pm\sqrt{(d_x+\lambda e_x)^2+(d_y+\lambda e_y)^2+(d_z+\lambda e_z)^2}}$$

and

$$\sin\theta_o = \frac{\sqrt{(d_x+\lambda e_x)^2 + (d_y +\lambda e_y)^2}}{\sqrt{(d_x+\lambda e_x)^2+(d_y+\lambda e_y)^2+(d_z+\lambda e_z)^2}} \quad .$$

The parameter λ is found by substituting these equations into Equation (87), which gives

$$\lambda = -(\hat{d}\cdot\hat{e}_m) \pm (\hat{r}\cdot\hat{e}_m)\sqrt{\frac{1-(\hat{d}\cdot\hat{e}_m)^2}{1-(\hat{r}\cdot\hat{e}_m)^2}} \quad .$$

The signs are chosen such that $\hat{d}\cdot\hat{d}_0$ is maximized. This $\hat{d}_0$ and its corresponding reflection point and diffraction point (corner point) are used as the starting parameters in the incremental method.

Now that the reflection point and diffraction point are known the field can be found. The reflected field off the elliptic cylinder is in the form of Equation (2), where the distance from the cylinder to the edge is finite. The diffracted field from the edge is given by Equation (11), where the incident field on the edge is the reflected field off the cylinder, and therefore, the wavefront incident on the edge has two radii of curvature. This field is given by

$$\bar{E}^{rd}_{cyl,j,m} = \bar{E}^{i}(Q_R)\cdot\bar{\bar{R}}\cdot\bar{\bar{D}}\sqrt{\frac{\rho_1^r\rho_2^r}{(\rho_1^r+s')(\rho_2^r+s')}}\sqrt{\rho_e^i}\, e^{-jks'}\frac{e^{-jks}}{s}$$

where s is in the far-field and therefore

$$\frac{e^{-jks}}{s} \cong e^{jk\,\bar{R}_d\cdot\hat{d}}\ \frac{e^{-jkd}}{d} \quad .$$

The parameters needed to find the reflected field off the elliptic cylinder are given in Equations (70a,b) and (71a-k) and the parameters for the diffracted field associated with the edge are given by Equations (45a-g) except for the distance parameter L and the caustic distances. The incident field on the edge has two radii of curvature as stated earlier such that the distance parameter given in Equation (14) must be used where $s\to\infty$ or in other words

$$L = \frac{\rho_1^i\,\rho_2^i\,\sin^2\beta_o}{\rho_e^i} \quad .$$

The incident radii of curvature at the edge are due to the radii of curvature at the surface of the cylinder plus the distance from the point of reflection to the diffraction point or

$$\rho_1^i = \rho_1^r + s'$$

$$\rho_2^i = \rho_2^r + s' \quad .$$

The caustic ρ_e^i is the radius of curvature of the incident wave at the edge in the plane of the edge and incident ray and is given by Eulers Theorem [66], as

$$\frac{1}{\rho_e^i} = \frac{1}{\rho_1^i} \cos^2\alpha + \frac{1}{\rho_2^i} \cos^2\beta \ .$$

The angles are defined by the edge and the principal directions of the reflected wavefront such that

$$\cos\alpha = \vec{X}_1^r \cdot \hat{e}_m$$

$$\cos\beta = \vec{X}_2^r \cdot \hat{e}_m \ .$$

The principal directions of the reflected wavefront are found from Equations (7-9) given in Chapter II.

The total field for this scattering mechanism is the sum of all the contributions from the edges, if they exist, and is given by

$$\vec{E}^{rd}_{cyl-pl}(\theta_s,\phi_s) = \sum_{j=1}^{P} \sum_{m=1}^{M_j} \vec{E}^{rd}_{cyl,j,m}(\theta_s,\phi_s). \qquad (88)$$

The scattering mechanism that corresponds to the reflected field off the cylinder after being diffracted by an edge is illustrated in Figure 57. The first step in finding the field is to determine its ray path for a given scatter direction $\hat{d}$. In this case the incident vector is dependent on the edge diffraction point which in turn is dependent on the reflection point on the cylinder. Again, the incremental method must be employed to solve this non-linear problem.

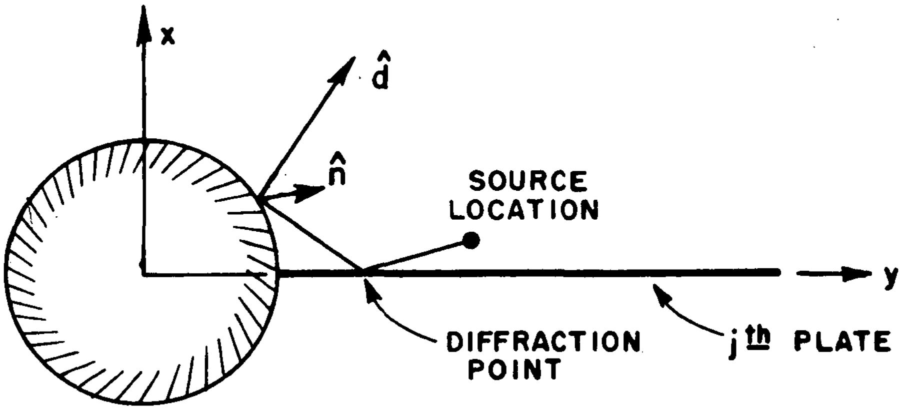

FRONT VIEW

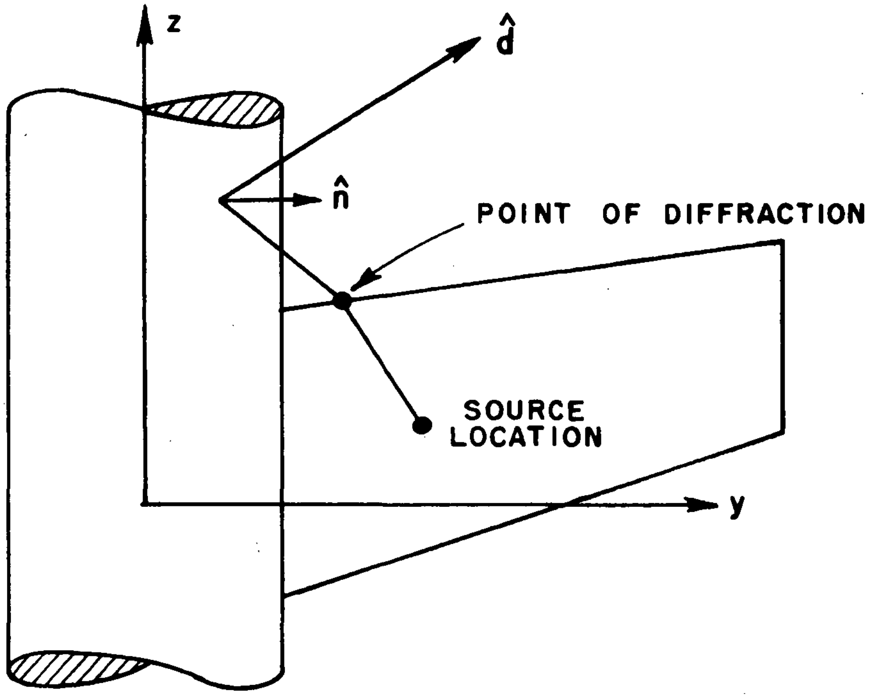

TOP VIEW

Figure 57--Illustration of reflected field off the cylinder after diffraction by an edge.

The laws of reflection for the reflection off the cylinder require that the following equations be satisfied:

$$f(v,z,\theta_s,\phi_s) = (n_xI_x+n_yI_y)(n_xd_y-n_yd_x)$$

$$+(n_xd_x+n_yd_y)(n_xI_y-n_yI_x) = 0$$

and

$$g(v,z,\theta_s,\phi_s) = (n_xI_x+n_yI_y)d_z+(n_xd_x+n_yd_y)I_z=0.$$

The functions f and g can be expanded in a first order Taylor series and solved for δv and δz as was done previously in Equations (86a and b). The answer is the same and does not need to be repeated here. The partial derivatives in this case are given by

$$\frac{\partial f_j}{\partial v} = \left(\frac{\partial n_x}{\partial v}\ I_x+n_x\frac{\partial I_x}{\partial v} + \frac{\partial n_y}{\partial v}\ I_y + n_y\frac{\partial I_y}{\partial v}\right)(n_xd_y-n_yd_x)$$

$$+(n_xI_x+n_yI_y)\left(\frac{\partial n_x}{\partial v}\ d_y - \frac{\partial n_y}{\partial v}\ d_x\right)$$

$$+ (n_xd_x+n_yd_y)\left(\frac{\partial n_x}{\partial v}\ I_y + n_x\frac{\partial I_y}{\partial v} - \frac{\partial n_y}{\partial v}\ I_x - n_y\frac{\partial I_x}{\partial v}\right)$$

$$+ (n_xI_y-n_yI_x)\left(\frac{\partial n_x}{\partial v}\ d_x + \frac{\partial n_y}{\partial v}\ d_y\right)$$

$$\frac{\partial f_j}{\partial z} = (n_xd_y-n_yd_x)\left(n_x\frac{\partial I_x}{\partial z} + n_y\frac{\partial I_y}{\partial z}\right) + (n_xd_x+n_yd_y)\left(n_x\frac{\partial I_y}{\partial z} - n_y\frac{\partial I_x}{\partial z}\right)$$

$$\frac{\partial f_j}{\partial \phi_s} = (n_xI_x+n_yI_y)\left(n_x\frac{\partial d_y}{\partial \phi_s} - n_y\frac{\partial d_x}{\partial \phi_s}\right) + (n_xI_y-n_yI_x)\left(n_x\frac{\partial d_x}{\partial \phi_s} + n_y\frac{\partial d_y}{\partial \phi_s}\right)$$

$$\frac{\partial f_j}{\partial \theta_s} = 0 \quad \text{(since } \sin\theta_s \text{ dependence can be removed from this equation)}$$

and

$$\frac{\partial g_j}{\partial v} = \left(\frac{\partial n_x}{\partial v} I_x + n_x \frac{\partial I_y}{\partial v} + \frac{\partial n_y}{\partial v} I_y + n_y \frac{\partial I_y}{\partial v} \right) dz$$

$$+ \left(\frac{\partial n_x}{\partial v} d_x + \frac{\partial n_y}{\partial v} d_y \right) I_z + (n_x d_x + n_y d_y) \frac{\partial I_y}{\partial v}$$

$$\frac{\partial g_j}{\partial z} = \left(n_x \frac{\partial I_x}{\partial z} + n_y \frac{\partial I_y}{\partial z} \right) dz + (n_x d_x + n_y d_y) \frac{\partial I_z}{\partial z}$$

$$\frac{\partial g_j}{\partial \phi_s} = \left(n_x \frac{\partial d_x}{\partial \phi_s} + n_y \frac{\partial d_y}{\partial \phi_s} \right) I_z$$

$$\frac{\partial g_j}{\partial \theta_s} = (n_x I_x + n_y I_y) \frac{\partial d_z}{\partial \theta_s} + \left(n_x \frac{\partial d_x}{\partial \theta_s} + n_y \frac{\partial d_y}{\partial \theta_s} \right) I_z \ .$$

The definitions of $\vec{n}$ and $\hat{d}$ and their derivatives have been given before, however, the determination of $\bar{I}$, $\partial\bar{I}/\partial v$, and $\partial\bar{I}/\partial z$ need to be derived.

The incident vector (for the ray incident on the cylinder) is given by

$$\vec{I}(v,z) = \bar{R}_r(v,z) - \bar{R}_d(v,z) \tag{89}$$

where $\bar{R}_r$ is the reflection point and the edge diffraction point is given by

$$\bar{R}_d(v,z) = \bar{R}_p + s_p \frac{\hat{I}(v,z) \cdot \hat{e}_m}{\sqrt{1-[\hat{I}(v,z)\cdot\hat{e}_m]^2}} \; \hat{e}_m, \tag{90}$$

$$\bar{R}_p = \bar{C}_m + [(\bar{R}_s-\bar{C}_m) \cdot \hat{e}_m]\hat{e}_m$$

$$s_p = |\bar{R}_s - \bar{R}_p| \; .$$

This leads to the equation

$$|\bar{I}| \; \hat{I} = (\bar{R}_r-\bar{R}_p) - \frac{s_p(\hat{I}\cdot\hat{e}_m)}{\sqrt{1-(\hat{I}\cdot\hat{e}_m)^2}} \; \hat{e}_m \tag{91a}$$

and

$$|\bar{I}|^2=\bar{I}\cdot\bar{I} = |\bar{R}_r-\bar{R}_p|^2 - \frac{2s_p(\hat{I}\cdot\hat{e}_m)[(\bar{R}_r-\bar{R}_p)\cdot\hat{e}_m]}{\sqrt{1-(\hat{I}\cdot\hat{e})^2}} + s_p^2 \frac{(\hat{I}\cdot\hat{e})^2}{1-(\hat{I}\cdot\hat{e})^2} \; . \tag{91b}$$

Taking the dot product of Equation (91a) and $\hat{e}_m$ and then squaring the equation gives

$$|\bar{I}|^2 \; (\hat{I}\cdot\hat{e}_m)^2 = [(\bar{R}_r-\bar{R}_p)\cdot\hat{e}_m]^2 - 2s_p[(\bar{R}_r-\bar{R}_p)\cdot\hat{e}_m] \frac{(\hat{I}\cdot\hat{e}_m)}{\sqrt{1-(\hat{I}\cdot\hat{e}_m)^2}}$$

$$+ \frac{s_p^2(\hat{I}\cdot\hat{e}_m)^2}{1 - (\hat{I}\cdot\hat{e}_m)^2} \; . \tag{92}$$

Now, substituting Equation (91b) into Equation (92) then squaring the equation again to remove the square root term, the equation can be regrouped in the form

$$C_2\alpha^4 + C_1\alpha^2 + C_o = 0$$

where

$$\alpha = (\hat{I} \cdot \hat{e}_m)$$

$$C_2 = (s_p^2 - |\overline{R}_r - \overline{R}_p|^2)^2 + 4s_p^2[(\overline{R}_r - \overline{R}_p) \cdot \hat{e}_m]^2$$

$$C_1 = -2(s_p^2 + |\overline{R}_r - \overline{R}_p|^2)$$

$$C_0 = [(\overline{R}_r - \overline{R}_p) \cdot \hat{e}_m]^4 .$$

This can be solved using the quadratic formula solution and is given by

$$(\hat{I} \cdot \hat{e}_m) = \pm \sqrt{\frac{-C_1 \pm \sqrt{C_1^2 - 4\, C_o C_2}}{2\, C_2}} \quad . \tag{93}$$

This can be used in Equations (90) to find the diffraction point and hence in Equation (89) to find the incident vector. The signs are chosen in Equation (93) to minimize the distance from the source to the edge to the reflection point.

The derivatives of the incident vector are found next. The normalized incident vector is given by

$$\hat{I} = \frac{\overline{I}}{|\overline{I}|} = \frac{\overline{I}}{\sqrt{\overline{I} \cdot \overline{I}}}$$

so

$$\frac{\partial \hat{I}}{\partial \beta} = \frac{\frac{\partial \vec{I}}{\partial \beta} - \left(\frac{\partial \vec{I}}{\partial \beta} \cdot \hat{I}\right)\hat{I}}{|\vec{I}|} \tag{94}$$

where $\beta = v$ or z.

Now, from Equation (89) the partial derivative is given by

$$\frac{\partial \bar{I}}{\partial \beta} = \frac{\partial \bar{R}_r}{\partial \beta} - \frac{s_p\left(\frac{\partial \hat{I}}{\partial \beta} \cdot \hat{e}_m\right)\hat{e}_m}{[1-(\hat{I}\cdot\hat{e}_m)^2]^{3/2}} \quad . \tag{95}$$

Substituting Equation (95) into Equation (94), gives

$$\frac{\partial \hat{I}}{\partial \beta} = \frac{1}{|\bar{I}|}\left\{\frac{s_p\left(\frac{\partial \hat{I}}{\partial \beta} \cdot \hat{e}_m\right)}{\sqrt{1-(\hat{I}\cdot\hat{e}_m)^2}}\left[1 + \frac{(\hat{I}\cdot\hat{e}_m)^2}{1-(\hat{I}\cdot\hat{e}_m)^2}\right][\hat{I}(\hat{I}\cdot\hat{e}_m)-\hat{e}_m] + \frac{\partial \bar{R}_r}{\partial \beta} - \left(\frac{\partial \bar{R}_r}{\partial \beta} \cdot \hat{I}\right)\hat{I}\right\} . \tag{96}$$

Taking the dot product with respect to the edge vector $\hat{e}_m$ of Equation (96) and then rearranging gives

$$\frac{\partial \hat{I}}{\partial \beta} \cdot \hat{e}_m = \frac{\left(\frac{\partial \bar{R}_r}{\partial \beta} \cdot \hat{e}_m\right) - \left(\frac{\partial \bar{R}_r}{\partial \beta} \cdot \hat{I}\right)(\hat{I} \cdot \hat{e}_m)}{|\bar{I}| + \frac{s_p}{\sqrt{1-(\hat{I}\cdot\hat{e}_m)^2}}} \quad . \tag{97}$$

Substituting Equation (97) into Equation (95) gives the solution for the partial derivatives of the incident vector. These can be used to find δv and δz and hence the reflection point and diffraction point using the same prodecure discussed for the previous scattering mechanism.

A known starting location for the first computation is found next. This can be found by defining a fixed point on the cylinder and from this define the diffraction point and scatter direction $\hat{d}_0$ for this point. The best location to define a known point $\bar{R}_0$ on the cylinder for this problem is a point on the end cap rim. The diffraction point is given by

$$\overline{R}_d = \overline{R}_p + t_s \hat{e}_m$$

where

$$t_s = \frac{s_s t_e}{s_s + s_o}$$

$$t_e = (\overline{R}_o - \overline{R}_s) \cdot \hat{e}_m$$

$$s_s = |\overline{R}_s - \overline{R}_p|$$

$$s_o = |\overline{R}_o - \overline{R}_{po}|$$

$$\overline{R}_p = [(\overline{R}_s - \overline{C}_m) \cdot \hat{e}_m]\hat{e}_m + \overline{C}_m$$

$$\overline{R}_{po} = [(\overline{R}_o - \overline{C}_m) \cdot \hat{e}_m]\,\hat{e}_m + \overline{C}_m.$$

This is illustrated in Figure 58. When the diffraction point is found then the scatter direction can be found from the following equations:

$$\hat{I} = \frac{\overline{R}_o - \overline{R}_d}{|\overline{R}_o - \overline{R}_d|}$$

$$\phi_{so} = \tan^{-1}\left[\frac{(n_x^2 - n_y^2) I_y - 2 n_x n_y I_x}{-(n_x^2 - n_y^2) I_x + 2 n_x n_y I_y}\right]$$

$$\theta_{so} = \cos^{-1}(I_z)$$

$\hat{d}_o = \cos\phi_{so} \sin\theta_{so}\hat{x} + \sin\phi_{so}\sin\theta_{so}\hat{y} + \cos\theta_{so}\hat{z}$. This $\hat{d}_o$ and its corresponding reflection point $(\bar{R}_o)$ and diffraction point are used as the starting parameters in the incremental method.

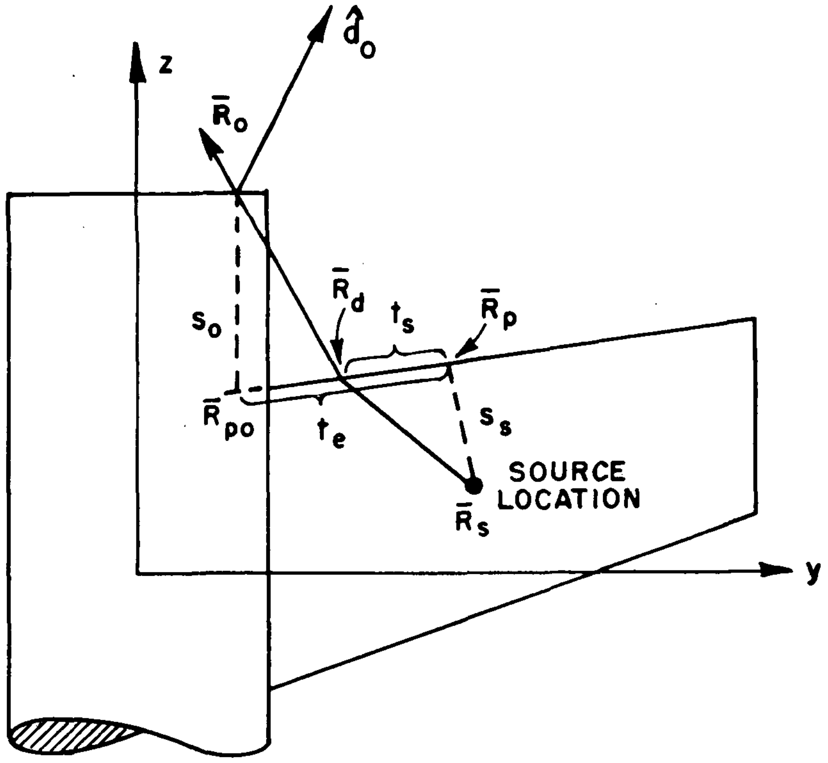

Figure 58--Illustration of starting point for finding diffraction point on an edge and the reflection point on the cylinder for the diffraction-reflection problem.

Once the reflection point and diffraction points are determined the field can be found. The diffracted field of the edge is in the form of Equation (11), where the distance from the edge to the cylinder is finite. The reflected field of the cylinder is given by Equation (2), where the incident field on the cylinder is the diffracted field from the edge. This incident field has two principal radii of curvature. The diffracted-reflected field is given by

$$\vec{E}^{dr}_{j,m,cyl} = \vec{E}^{i}(Q_E) \cdot \bar{\bar{D}} \cdot \bar{\bar{R}} \sqrt{\frac{s'}{s''(s'+s'')}} \sqrt{\rho_1^r \rho_2^r}\, e^{-jks''} \frac{e^{-jks}}{s}$$

where s is in the far field and therefore

$$\frac{e^{-jks}}{s} \cong e^{jk \vec{R}_r \cdot \hat{d}} \quad \frac{e^{-jkd}}{d} \quad .$$

The parameters needed to find the diffracted field from an edge are given in Equations (45a-g), except the distance parameter needed here is in the near field and is given by

$$L = \frac{s's''}{s'+s''} \sin^2\beta_o$$

where s' is the distance from the source to the diffraction point and s" is the distance from the diffraction point to the reflection point. The parameters for the reflected field are given in Equations (71a-k) except the incident field has two radii of curvature so the reflection caustic distances need to be found from Equation (5) with $R_2 \to \infty$ which is given by

$$\frac{1}{\rho^r_{1,2}} = \frac{1}{2}\left(\frac{1}{\rho_1^i} + \frac{1}{\rho_2^i}\right) + \frac{\cos^{i}}{|\theta|^2}\left(\frac{\theta_{22}^2 + \theta_{12}^2}{R_1}\right)$$

$$\pm \frac{1}{2}\sqrt{\left(\frac{1}{\rho_1^i} - \frac{1}{\rho_2^i}\right)^2 + \left(\frac{1}{\rho_1^i} - \frac{1}{\rho_2^i}\right)\frac{4\cos\theta^i}{|\theta|^2}\left(\frac{\theta_{22}^2 - \theta_{12}^2}{R_1}\right) + \frac{4\cos^2\theta^i}{|\theta|^4}\left(\frac{\theta_{22}^2 + \theta_{12}^2}{R_1}\right)^2}$$

where

$\rho_1^i = s''$, in the principal direction $\hat{\phi}$

$\rho_2^i = s''+s'$, in the principal direction $\hat{\beta}_o$.

The parameter $\cos\theta^i$ is found in Equation (71c), R_1 in Equation (71b), and θ_{ij}, $|\theta|$ in Equations (6a and b).

The total field for this scattering mechanism is the sum of all the contributions from the edges if they exist and is given by

$$\overline{E}^{dr}_{pl-cyl}(\theta_s,\phi_s) = \sum_{j=1}^{P} \sum_{m=1}^{M_j} \overline{E}^{dr}_{j,m,cyl}(\theta_s,\phi_s). \tag{98}$$

The total field for the aircraft model is the sum of all the scattered fields from the finite plates, listed in Table II, represented by $\overline{E}_{pl}$; from the finite elliptic cylinder, listed in Table III, represented by $\overline{E}_{cyl}$; and from the plate-cylinder interaction terms, listed in Table IV. This total field can therefore be written as

$$\overline{E}(\theta_s,\phi_s) = \overline{E}^{i} + \overline{E}_{pl} + \overline{E}_{cyl} + \overline{E}^{rr}_{pl-cyl} + \overline{E}^{rt}_{pl-cyl} + \overline{E}^{rr}_{cyl-pl} + \overline{E}^{rd}_{cyl-pl} + \overline{E}^{dr}_{pl-cyl} .$$

TABLE IV

SCATTERED FIELDS INCLUDED INVOLVING PLATE-CYLINDER INTERACTIONS

	Symbol	Description	Figure	Equation
1)	$\overline{E}^{rr}_{pl-cly}$	Reflected field off the cylinder after reflection by a plate	52	81
2)	$\overline{E}^{rt}_{pl-cyl}$	Transition field off the cylinder after reflection by a plate	53	82
3)	$\overline{E}^{rr}_{cyl-pl}$	Reflected field off a plate after reflection by the cylinder	54	83
4)	$\overline{E}^{rd}_{cyl-pl}$	Diffracted field off an edge after reflection by the cylinder	55	88
5)	$\overline{E}^{dr}_{pl-cyl}$	Reflected field off the cylinder after diffraction by an edge	57	98

This result, then, includes the principal contributors to the scattered fields from the finite plates, finite elliptic cylinder, and plate-cylinder interaction terms. They have been found by first tracing the ray paths for a given scatter direction, then testing these ray paths to see whether or not the fields are shadowed by any obstacle along the ray path. The non-shadowed fields are then computed using geometrical optics and/or the geometrical theory of diffraction and superimposed to give the total field.

To illustrate the effects that some of these scattering mechanisms have on the radiation pattern of an antenna mounted near a plate-cylinder structure, a simple model consisting of a flat plate attached to a finite elliptic cylinder in the y-z plane, as shown in Figure 59, is studied. The elevation plane (x-z plane) radiation pattern for an infinitesimal slot mounted parallel to the y-axis is shown in Figure 60a. The cylinder has little effect on the radiation pattern in this plane. The roll plane (x-y plane) radiation pattern for the same source is shown in Figure 60b. The need for a corner diffraction term is shown by the discontinuity in the right side of the backlobe of the pattern. The result using the recently developed corner diffraction term is shown as the dotted line in the same figure. The discontinuity in the left side of the backlobe is due to shadowing by the cylinder. The mechanism to compensate for this discontinuity has not been studied at this time, but it will have only a small effect other than the discontinuity. The roll plane radiation pattern for an infinitesimal slot located parallel to the z-axis is shown in Figure 60c. The lack of a reflected-diffracted term is apparent by the large discontinuity in the solid line at $\phi = 90°$. The smoothing out of the discontinuity by including the reflected-diffracted term is shown by the dotted line. Even for this simple structure the interactions between the different parts are apparent in their area of greatest influence. The way that the GTD compensates for these discontinuities, however, is also quite apparent. This is useful to keep in mind as the structures become more complicated, and consequently, the interaction terms become more involved and less practical to include in the solution.

To test the validity of the approximations involved in the finite elliptic cylinder aircraft model, an experimental model that resembles the computer model was built and tested. The model consisted of a finite cylinder with two flat plates resembling wings as shown in the insert of Figure 61. The comparison of calculated and measured results for the roll plane radiation pattern is shown in Figure 61. The overall agreement between the two results is very good, even down to some of the small backlobes. The disagreement at $\phi = -90°$ is due to the lack of a diffracted-reflected-diffracted term. This third-order term is hard to calculate and seems to be important only in this

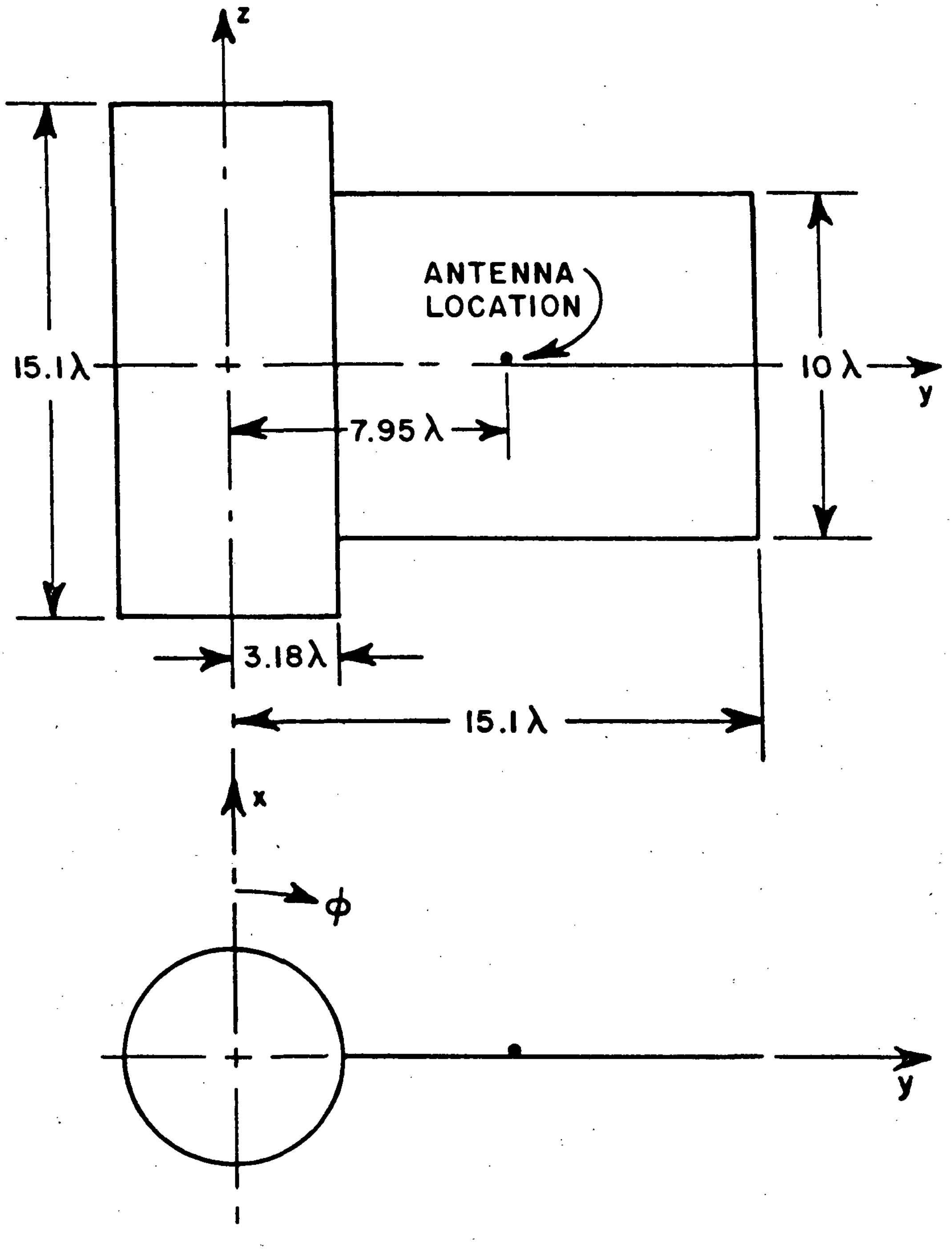

Figure 59--Geometry of a preliminary model.

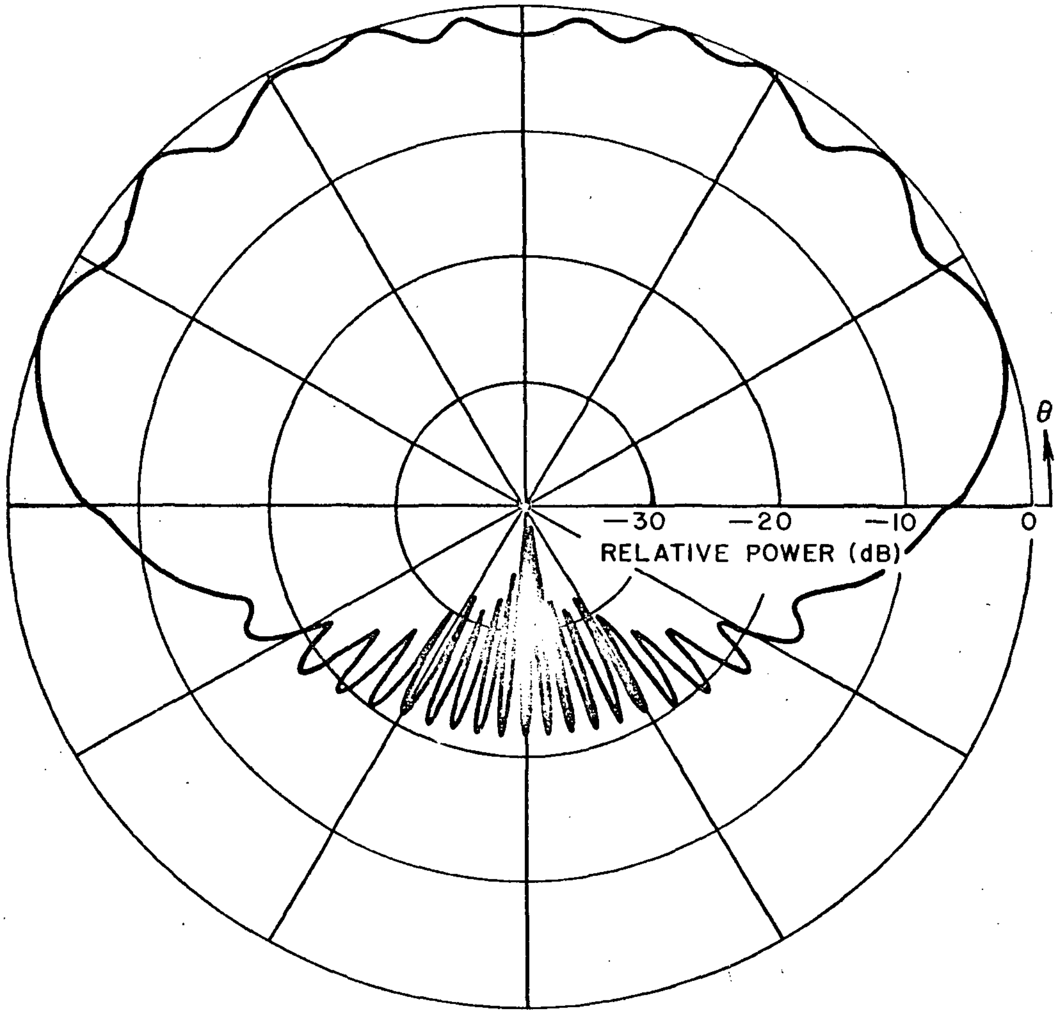

Figure 60a--Elevation plane radiation pattern (E_θ) of small slot mounted parallel to y-axis on plate.

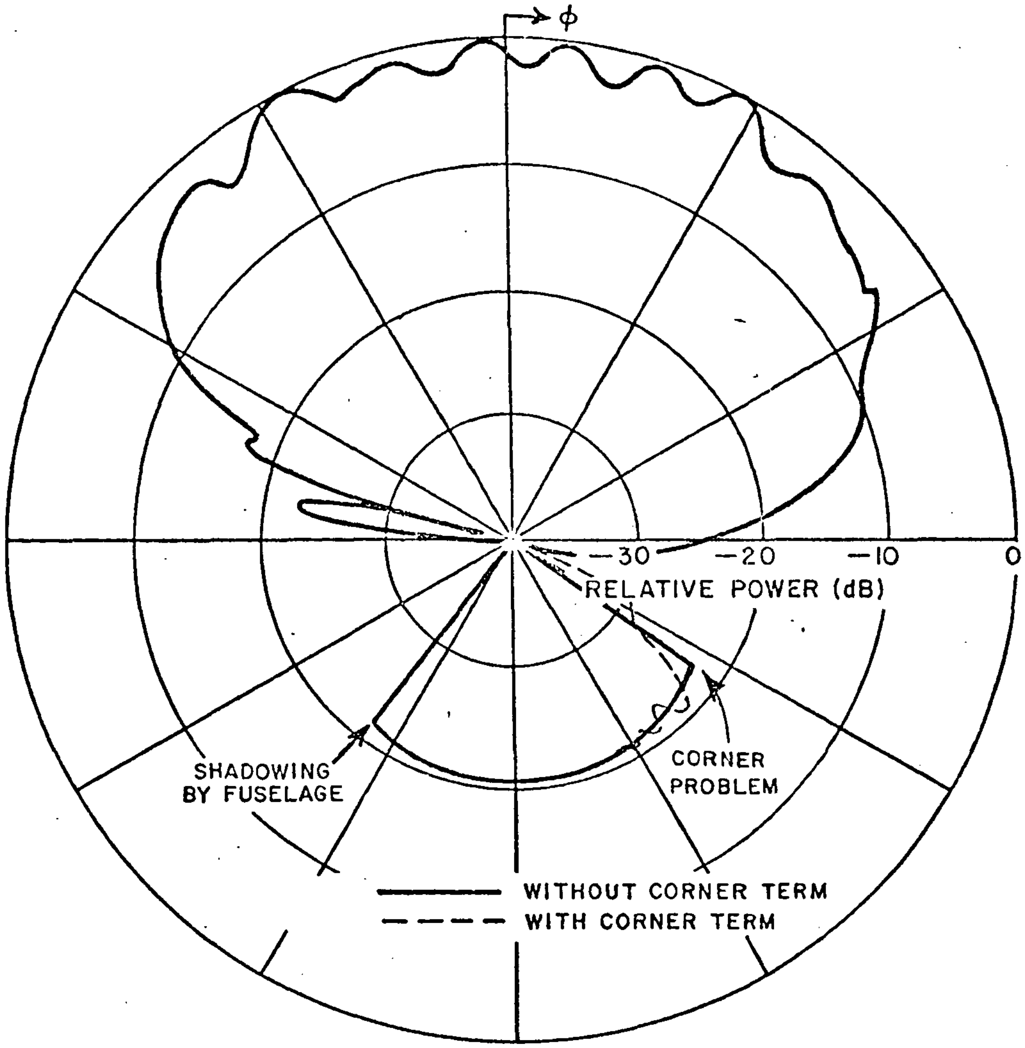

Figure 60b--Roll plane radiation pattern (E_θ) of small slot mounted parallel to y-axis on plate, showing effect of corner diffraction term.

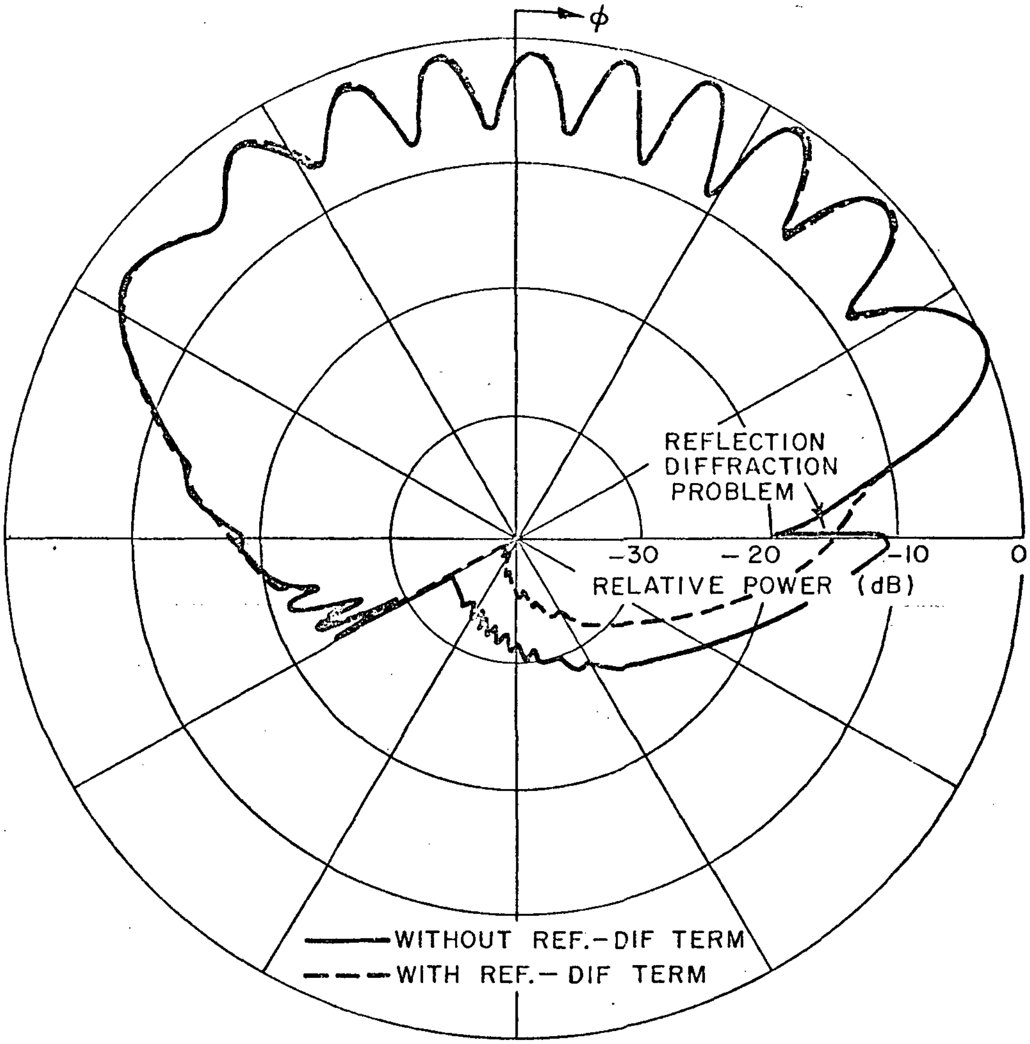

Figure 60c--Roll plane radiation pattern (E_ϕ) of small slot mounted parallel to z-axis on plate, showing effect of reflected-diffracted term.

particular pattern cut. Therefore, it does not seem necessary to include this term at this time. The discontinuity at $\phi = 120°$ is due to some higher order terms involving the second wing which is not included. Again, these do not appear to be of engineering significance so they have been left out of the solution. This comparison indicates that the theory can predict patterns for simple structures resembling the analytic model.

It is interesting, at this point, to compare the results in Figure 61 with the flat plate computer representation of the simple aircraft model as shown in the insert to Figure 62. This emphasizes the difficulties involved in representing a smooth convex surface by a flat plate as was previously used for the F-4 aircraft in Figures 33a-f. The radiation pattern for the flat plate version of the simple aircraft model is shown in Figure 62. The major features of the patterns are quite different. This is simply due to the fact that the specular reflection off the flat plate does not adequately approximate the specular reflection off of the cylinder as might be expected. This flat plate model can then be expected only to give a crude approximation to an aircraft only if the curved surfaces are not strongly illuminated.

The next question that needs to be resolved is how well does the finite elliptic cylinder model predict the radiation patterns of antennas mounted on real aircraft shapes. The finite elliptic cylinder aircraft model has been used to compute some of the patterns that were measured at NWC using a single slot on the wing of the F-4 scale model as discussed in Chapter III. The geometry of this theoretical model is shown in Figure 63. The dimensions for the model are listed in Table V. The antenna locations are shown in Figure 32. A comparison of the measured and calculated radiation patterns for the main beam elevation plane for the slot at location #2 (refer to Figure 31a) is shown in Figure 64a. This result can be compared with the flat plate result that was used to crudely model the aircraft in Figure 33a. Note that the ripple level, in the region $\phi = 60°$ to $150°$, due to the reflections off the fuselage has been improved as expected. The same problem of comparing near field measured results and far field computed results still exists in all these patterns. However, a few of the results for the various cases will be shown here for illustrative purposes. In each case, Figures 31a-d show the aircraft pattern orientation. The polarization of the received signal is computed in the same way the measurements were taken, that is, with the probe aligned with the antenna to give the dominant polarization.

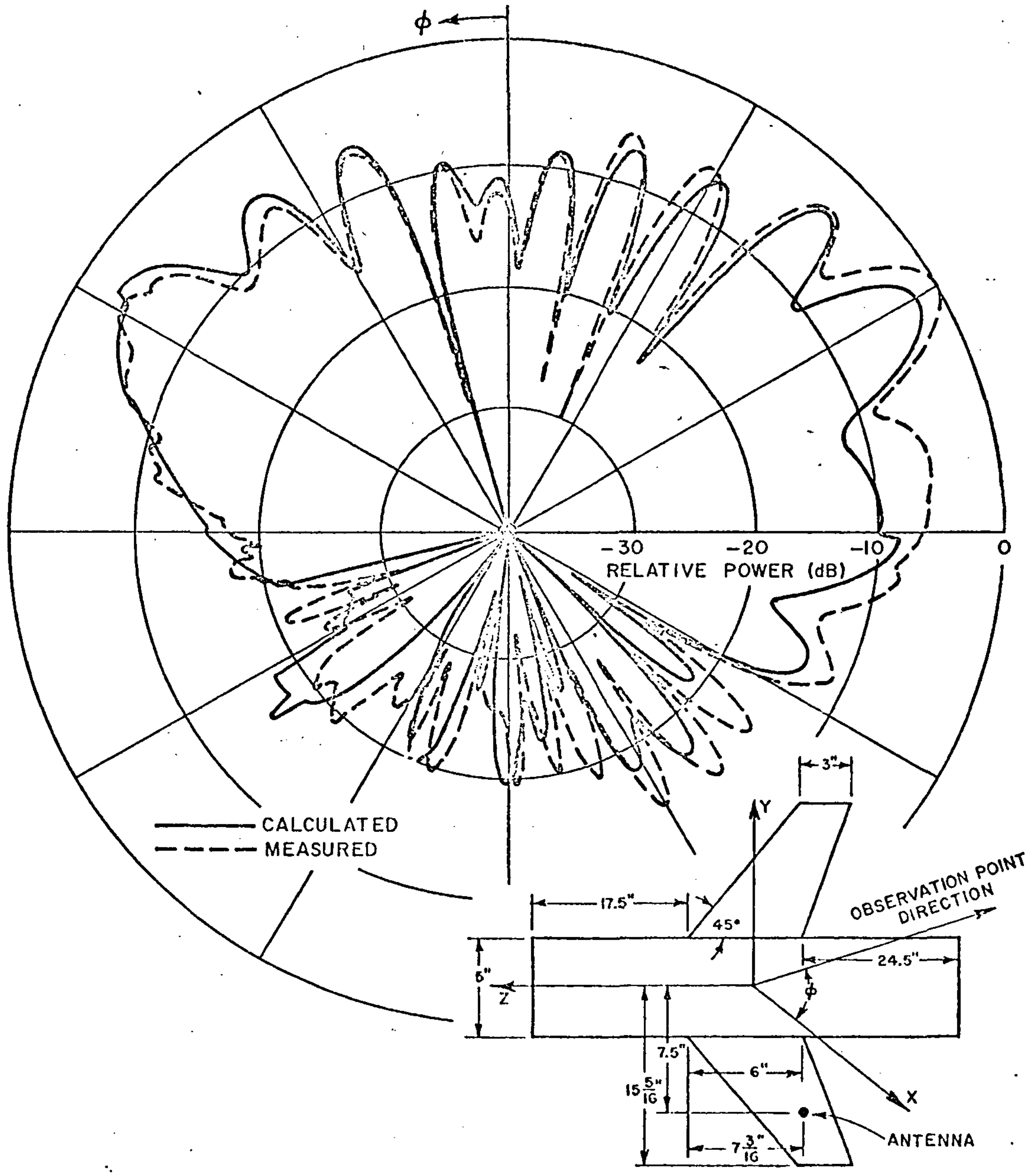

Figure 61--Comparison of measured and calculated results for the roll plane radiation pattern (E_ϕ) of a simple aircraft model with a short monopole mounted on its wing. (freq = 10.87 GHz).

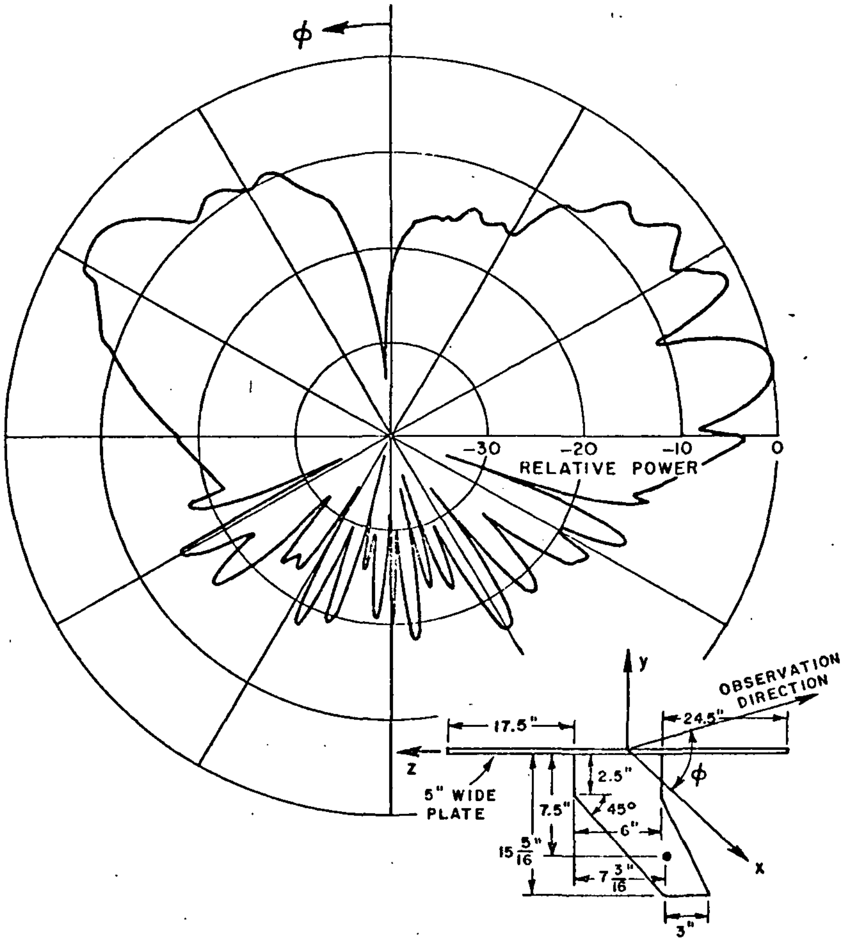

Figure 62--Roll plane radiation pattern (E_ϕ) of a flat plate representation of the simple aircraft model with a short monopole mounted on its wing.

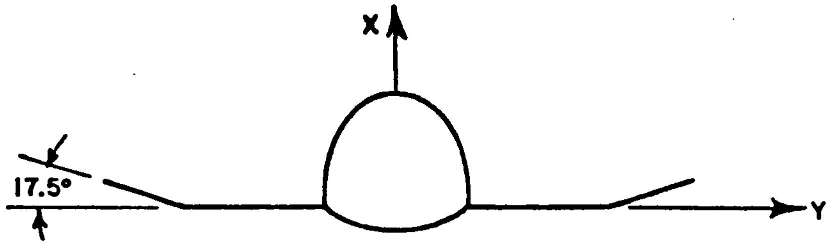

(a) FRONT VIEW

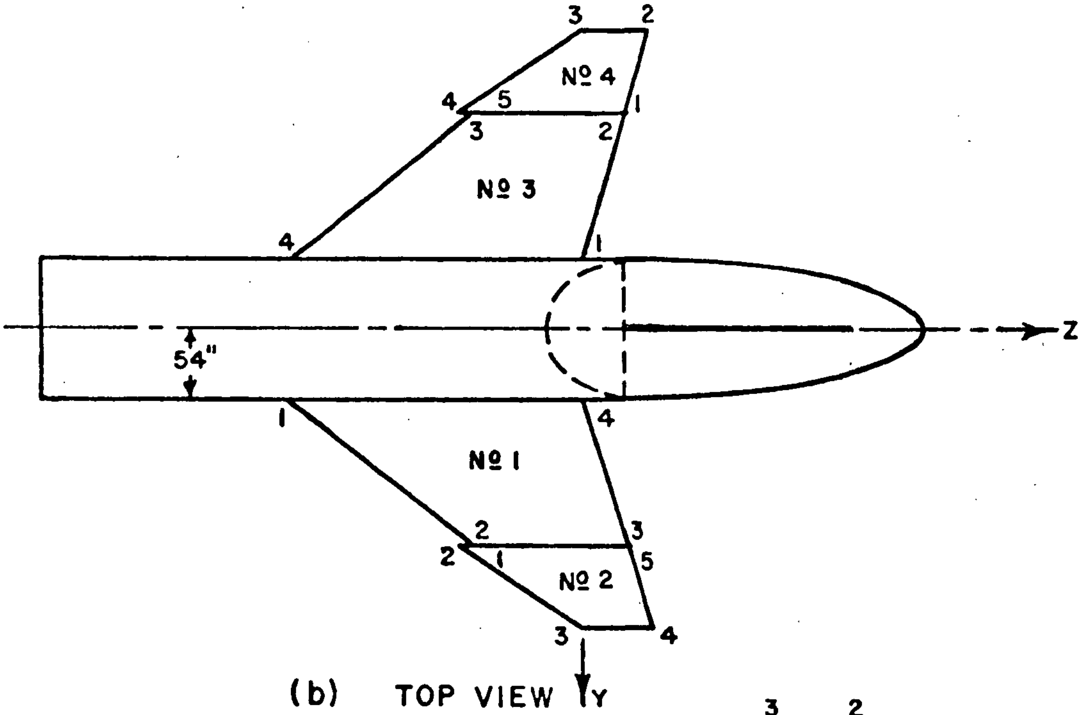

(b) TOP VIEW

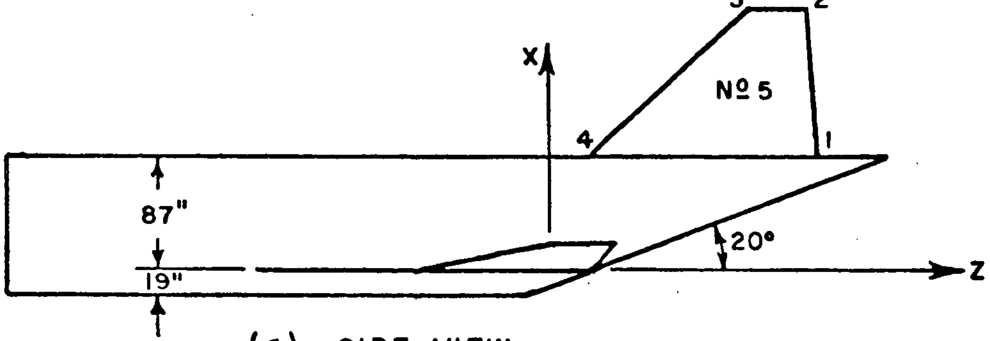

(c) SIDE VIEW

Figure 63--Illustration of geometry of F-4 aircraft model used in finite elliptic cylinder model.

TABLE V

DIMENSIONS FOR FINITE ELLIPTIC CYLINDER MODEL OF F-4

All Dimensions in Inches for Full Scale Model

Fuselage

$A_{Top} = 87.$

$A_{Bottom} = 19.$

$B = 54.$

$Z_{End\ Cap\ Nose} = -420.$, $a_{Nose} = 90°$

$Z_{End\ Cap\ Tail} = 26.6$, $a_{Tail} = 20°$

Wings

Plate 1

Corner	X	Y	Z
1	0.	54.	-228.
2	0.	166.2	- 86.2
3	0.	166.2	32.8
4	0.	54.	0.

Plate 2

Corner	X	Y	Z
1	0.	166.2	- 86.2
2	0.	166.2	- 96.2
3	19.7	228.7	0.
4	19.7	228.7	53.4
5	0.	166.2	32.8

TABLE V cont.

Plate 3

Corner	X	Y	Z
1	0.	-54.	0.
2	0.	-166.2	32.8
3	0.	-166.2	-86.2
4	0.	-54.	-228.

Plate 4

Corner	X	Y	Z
1	0.	-166.2	32.8
2	19.7	-228.7	53.4
3	19.7	-228.7	0.
4	0.	-166.2	-96.2
5	0.	-166.2	-86.2

Plate 5

Corner	X	Y	Z
1	87.	0.	205.1
2	149.9	0.	197.3
3	154.3	0.	153.1
4	87.	0.	11.4

Source Coordinates

Source	X	Y	Z
1	5.14	182.5	-36.91
2	0.00001	149.1	-73.6
3	0.00001	126.3	-102.5
4	0.00001	150.3	-4.6
5	0.00001	111.	-74.1

The comparison of the main beam elevation plane pattern with a slot antenna at location #4 is shown in Figure 64b. This result can be compared with Figure 33b. The pattern in the main beam roll plane (Figure 31c) for a slot antenna at location #2 is shown in Figure 64c and compares with Figure 33c. The elevation plane pattern (Figure 31b) for a slot antenna at location #2 is shown in Figure 64d and compares with Figure 33d. Its roll plane pattern (Figure 31a) is shown in Figure 64e and compares with Figure 33e. The roll plane result especially emphasizes the specular reflection off the fuselages curved surface. The elevation plane result for a slot antenna oriented such that its maximum radiation points aft of the aircraft at location #5 is shown in Figure 64f and compares with Figure 33f.

In all of the above results, the major characteristics of the patterns do show some agreement. In this model the horizontal stabilizers have little effect so they are neglected for this problem. Some higher interaction terms that were not included are significant in small angular regions in some of the various pattern cuts; however, it is not deemed feasible to include them at this time.

In order to further test the finite elliptic cylinder model's ability to predict radiation patterns of antennas mounted on the wings of real aircraft, pattern measurements of a slot antenna mounted on the wing of a 1/20 scale model of a Boeing 737 were taken at NASA (Hampton, Va.). The geometry of the finite elliptic cylinder model of the Boeing 737 is shown in Figure 65. The dimensions used for this model are given in Table VI with a frequency of 1.75 GHz, which corresponds to 35 GHz for the scale model. The source is a Ka band waveguide mounted parallel to the y-axis in Figure 65 with the location given in Table VI. The patterns are presented with respect to the coordinate system in Figure 66. The $E_{\theta'}$ radiation patterns are shown in Figures 67a-e for patterns cut at angles $\phi' = 0°$ to $\phi' = 150°$ in steps of 30°, respectively. The patterns have been normalized to the maximum of the pattern in the $\phi' = 0°$ cut. The pattern at $\phi' = 90°$ has not been shown since for this pattern cut the amplitude of the $E_{\theta'}$ polarized field is below -30 dB which is in the noise region for the measured pattern. In all of the patterns shown, the finite elliptic cylinder model tends to predict very well the frequency and level of the ripple in the patterns in most regions. Some of the discrepancies can be attributed to the following reasons. The high frequency of the ripple in the patterns means that any misalignment in the experimental measurements could cause shifts in the actual placement of the peaks and nulls. Also, the support structure appears to cause some scattering in the $\theta' = 150°$ to 210° region in all the patterns. The measurements in the $\phi' = 30°$ and $\phi' = 150°$ pattern cuts in the $\theta' = -90°$ and $\theta' = 90°$ regions have pointed out that the nose and tail configurations of the finite elliptic cylinder model are not completely adequate to predict all the detail accurately. However, the discrepencies do not appear to be severe.

Overall, the agreement between the calculated and (NWC and NASA) measured results appears to be good for engineering applications. They both point out that the fuselage can strongly effect the patterns of antennas mounted on the wings of aircraft. In particular the reflections off the fuselage and other higher order interactions tend to cause a lot of ripple in the patterns. This can be detrimental to system performance in many instances. However, if the antennas are made directive such that they do not illuminate the fuselage strongly and the antenna locations are chosen judiciously the ill effects of the fuselage and other scatters can be minimized. Thus using this numerical solution, the antenna designer can begin to consider antenna locations on the aircraft wing without having to make numerous scale model measurements.

As a practical example of how the finite elliptic cylinder model can be used to solve an aircraft antenna design problem, the design of an antenna system to give coverage in the aft region of an F-4 aircraft for quadrant detection at UHF, as undertaken in Reference [33], is briefly discussed. Classical array analysis was used to find the element spacing, scan angle, and distribution of a two-element array to obtain a desired pattern shape above the wing. The array was then located on the wing using the finite elliptic cylinder model to optimize the antenna pattern. The optimum location was found to be at location #2 of Figure 32 with the array being mounted at 45° with respect to the fuselage. The volumetric pattern predicted for this antenna system on the F-4 is plotted in Figure 68 in terms of its directive gain with respect to the coordinate system in Figure 66. The desired region of coverage is shown as the rectangular box in the figure. The directivity, which is the maximum directive gain, for the antenna system in place on the aircraft was determined to be 12.3 dB. The directive gain is plotted in Figure 68 using different colors to represent the different gain levels. Each change in color represents a 5 dB window showing regions of farther reduction in the gain. The volumetric pattern shows that the two-element array design does a realistic job of approximating the desired objectives. Other optimum antenna designs can be accomplished in a similar efficient manner on a digital computer using the finite elliptic cylinder model and then tested experimentally to verify the findings.

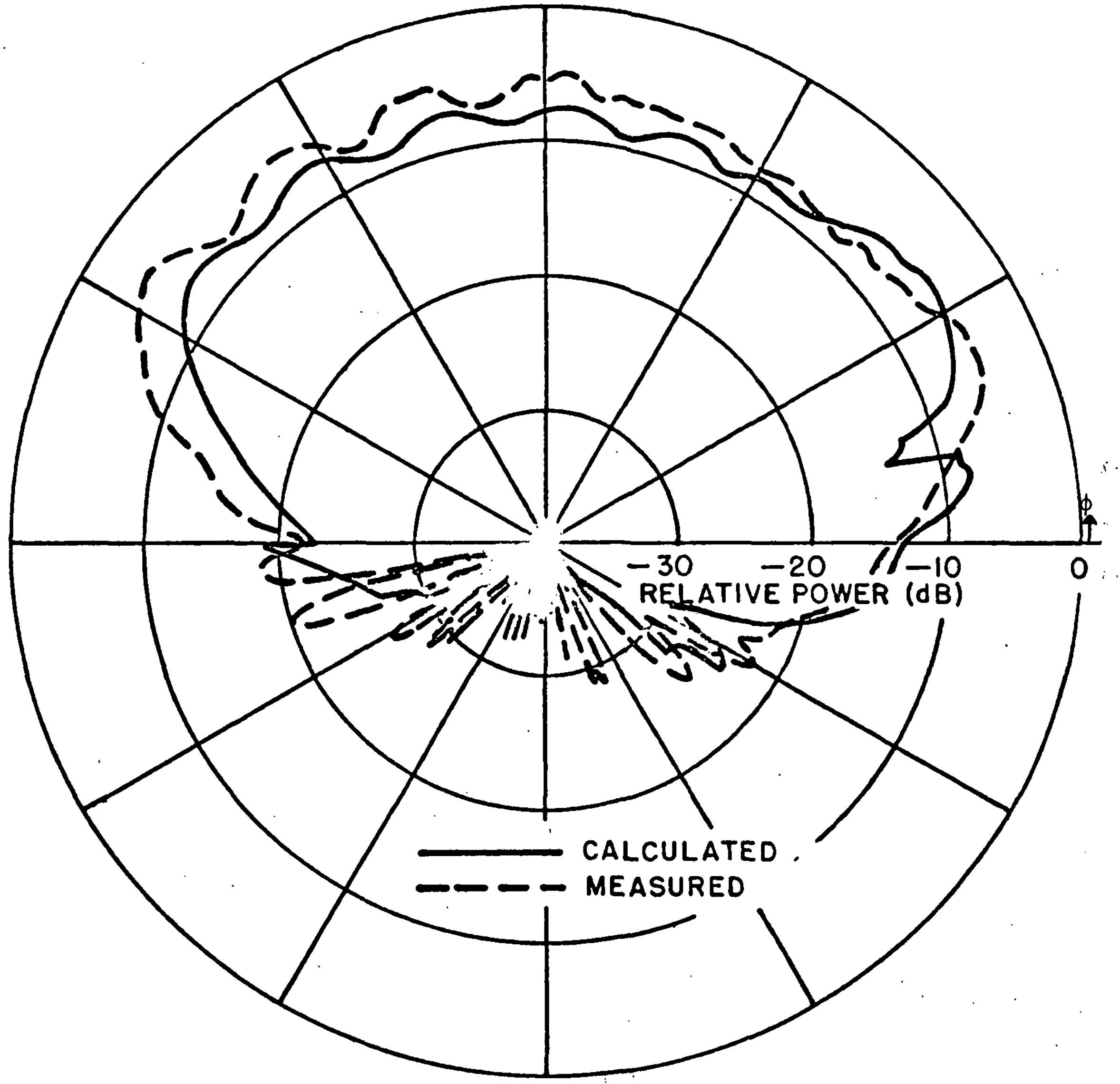

Figure 64a--Comparison of NWC measured results on an F-4 model with the finite elliptic cylinder model results of main beam elevation plane radiation pattern for antenna location #2.

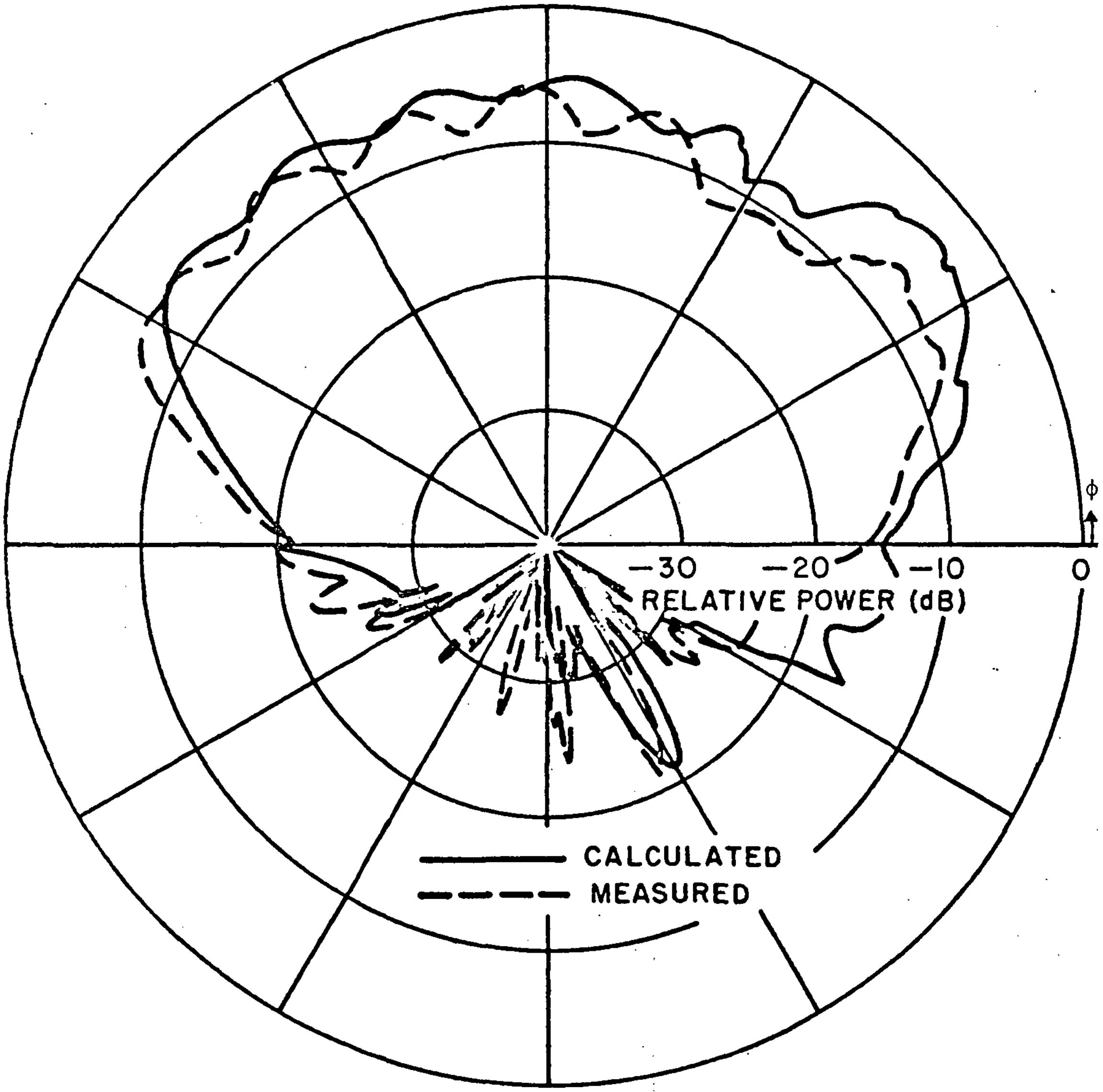

Figure 64b--Comparison of measured and calculated results of main beam elevation plane pattern for antenna location #4.

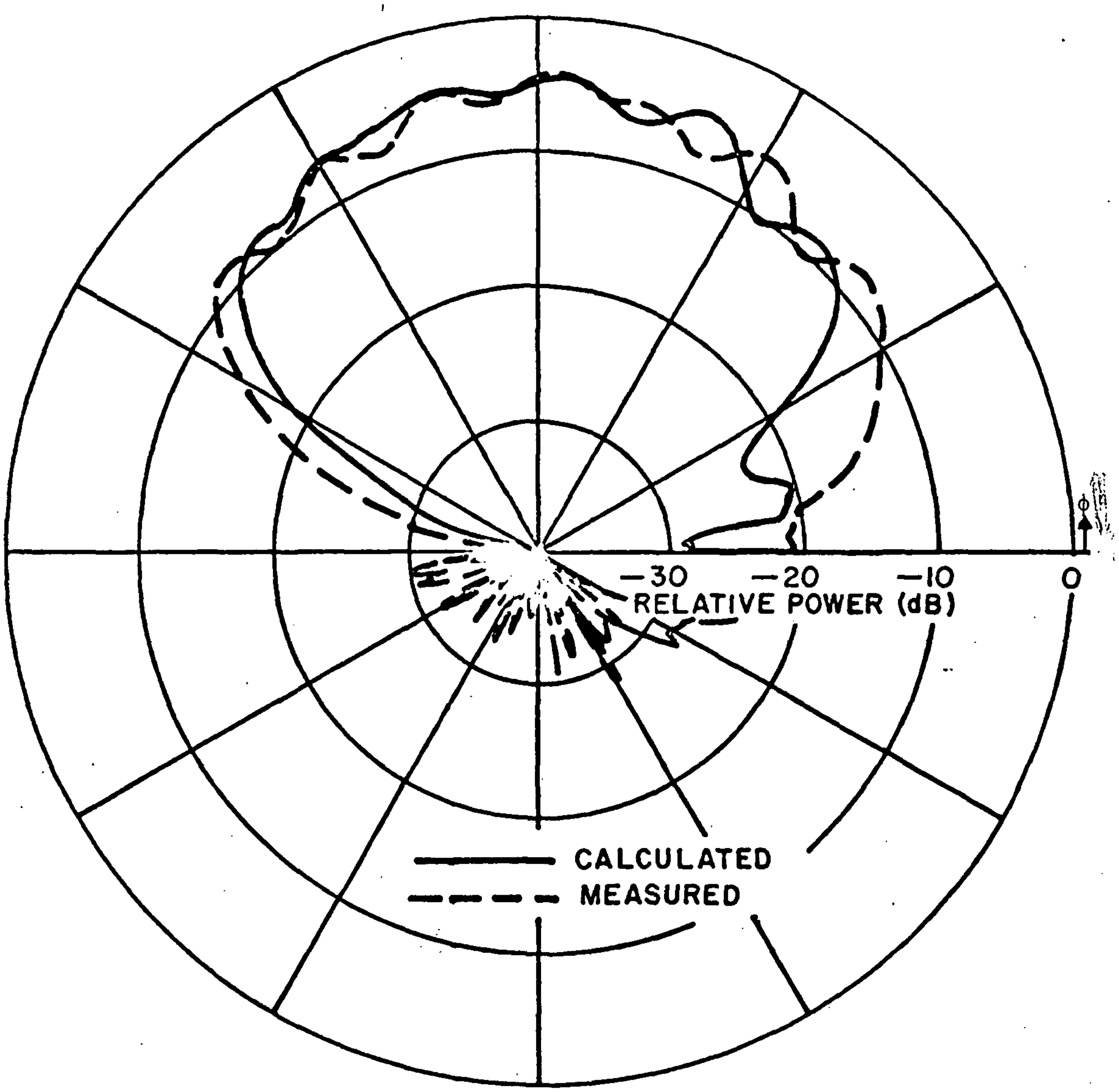

Figure 64c--Comparison of measured and calculated results of main roll plane pattern for antenna location #2.

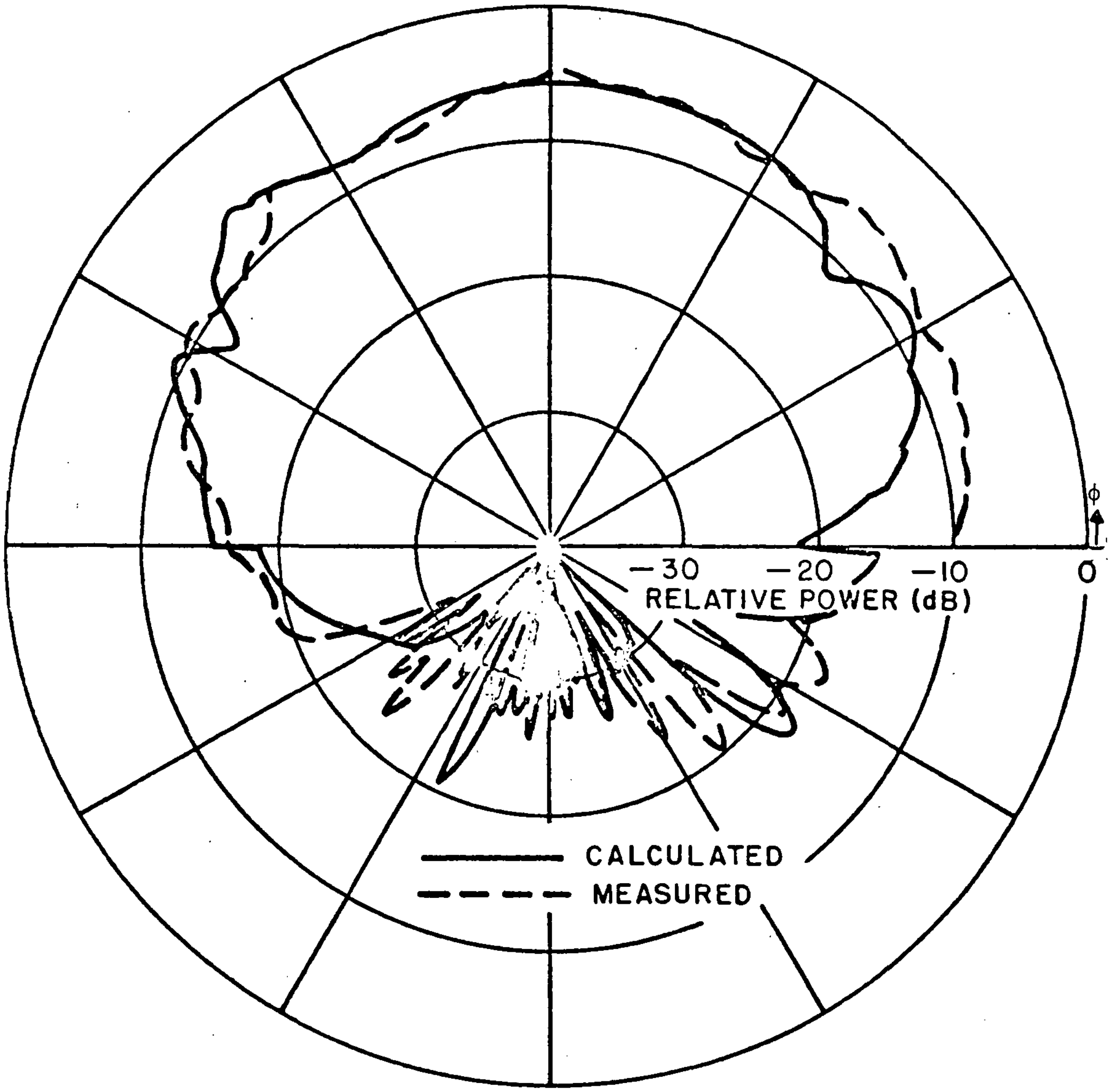

Figure 64d--Comparison of measured and calculated results of elevation plane pattern for antenna location #2.

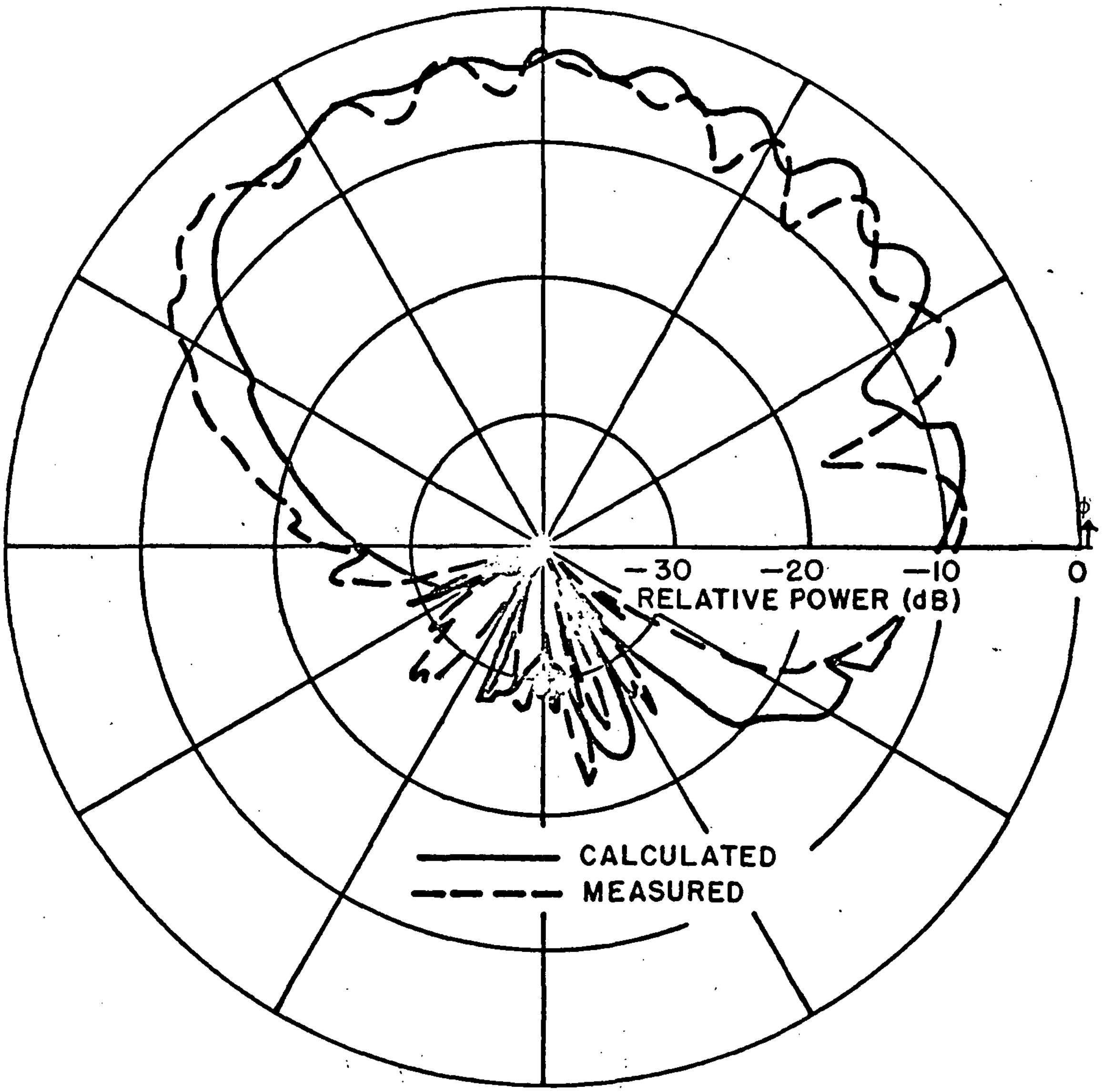

Figure 64e--Comparison of measured and calculated results of roll plane pattern for antenna location #2.

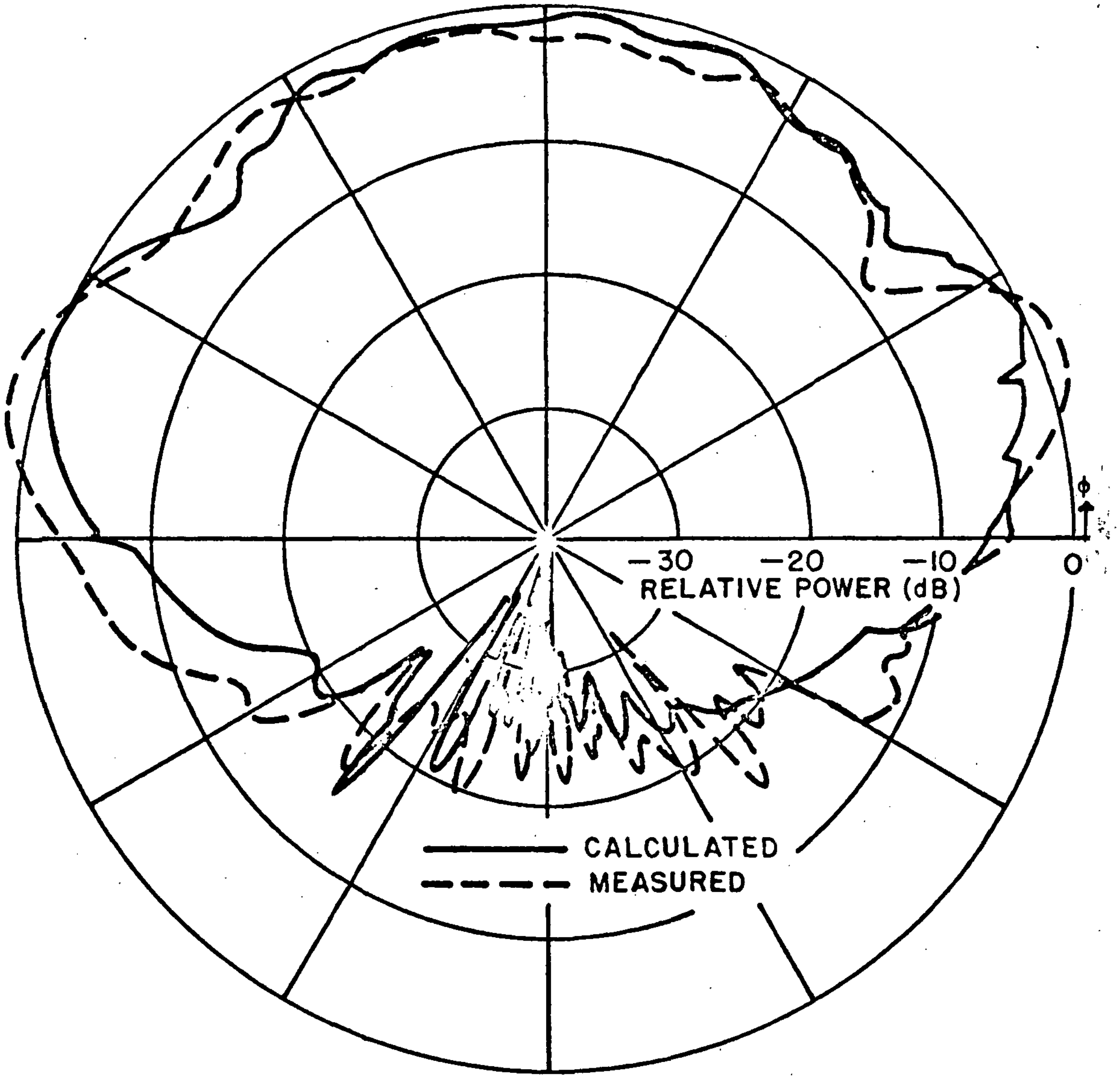

Figure 64f--Comparison of measured and calculated results of of elevation plane pattern for antenna location #5 with the slot pointed straight aft of aircraft.

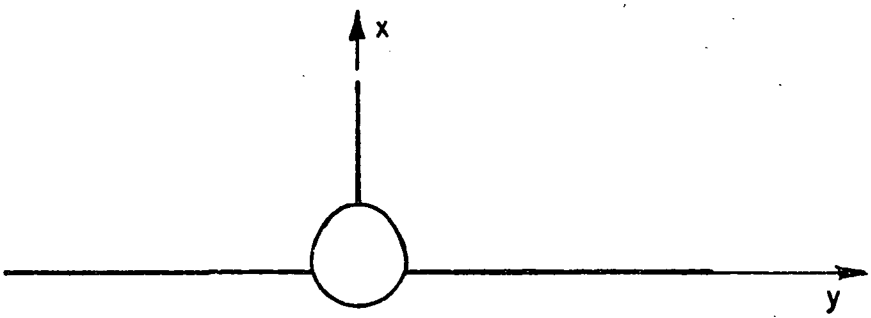

(a) FRONT VIEW

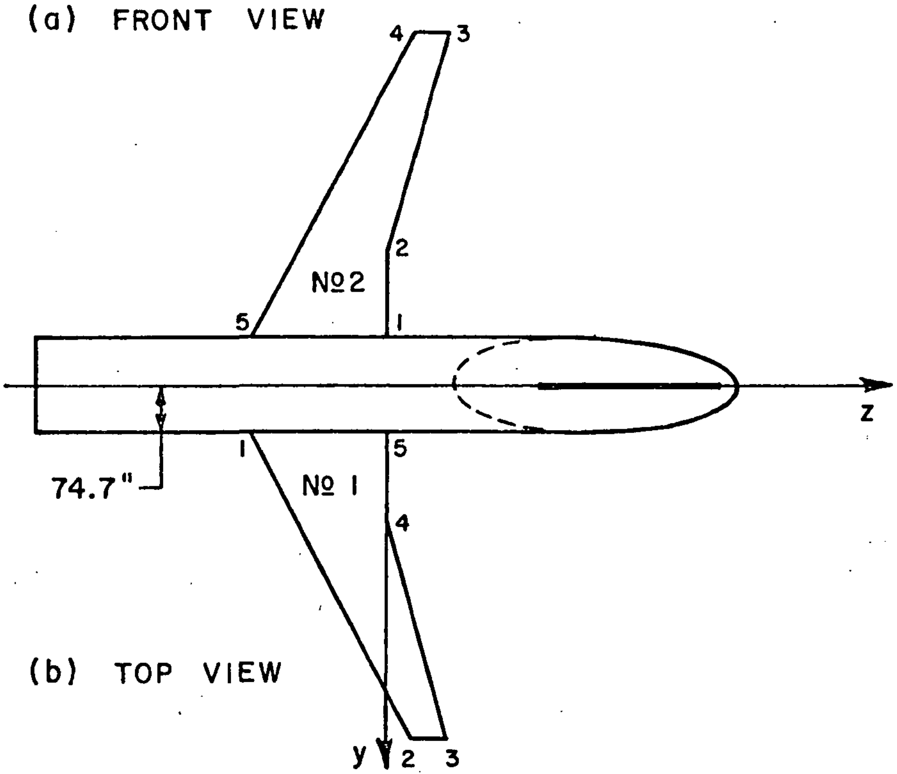

(b) TOP VIEW

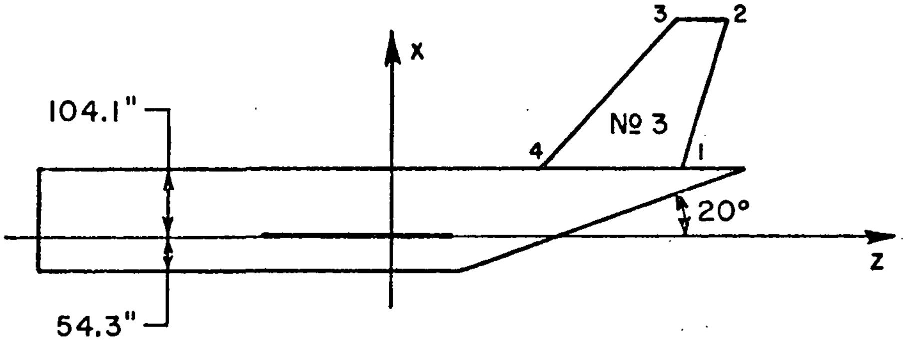

(c) SIDE VIEW

Figure 65--Illustration of geometry of Beoing 737 aircraft model used in finite elliptic cylinder model.

TABLE VI

DIMENSIONS FOR FINITE ELLIPTIC CYLINDER MODEL OF BOEING 737

All Dimensions in Inches for Full Scale Model

Fuselage

$A_{Top} = 104.1$

$A_{Bottom} = 54.3$

$B = 74.7$

$Z_{end\ cap\ nose} = -570.5$, $\theta_{nose} = 90°$

$Z_{end\ cap\ total} = 260.4$, $\theta_{tail} = 20°$

Wings

Plate 1

Corner	X	Y	Z
1	0.	74.7	-212.8
2	0.	547.9	40.8
3	0.	547.9	95.1
4	0.	203.8	0.
5	0.	74.7	0.

Plate 2

Corner	X	Y	Z
1	0.	-74.7	0.
2	0.	-203.8	0.
3	0.	-547.9	95.1
4	0.	-547.9	40.8
5	0.	-74.7	-212.8

Plate 3

Corner	X	Y	Z
1	104.1	0.	448.3
2	344.1	0.	516.2
3	344.1	0.	443.7
4	104.1	0.	235.5

Source Coordinates

Source	X	Y	Z
1	0.000001	312.4	-45.3

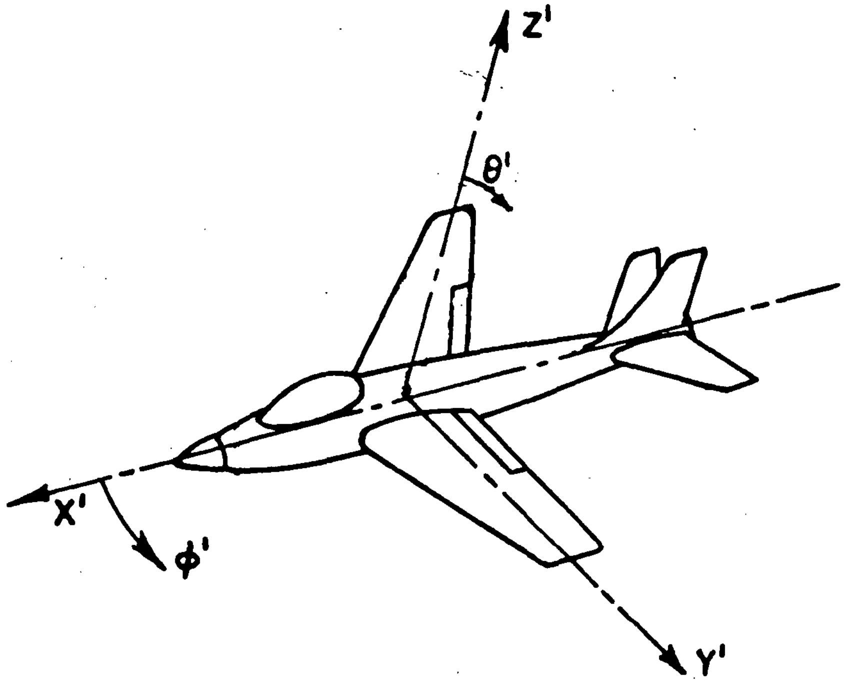

Figure 66--Coordinate system used for volumetric patterns.

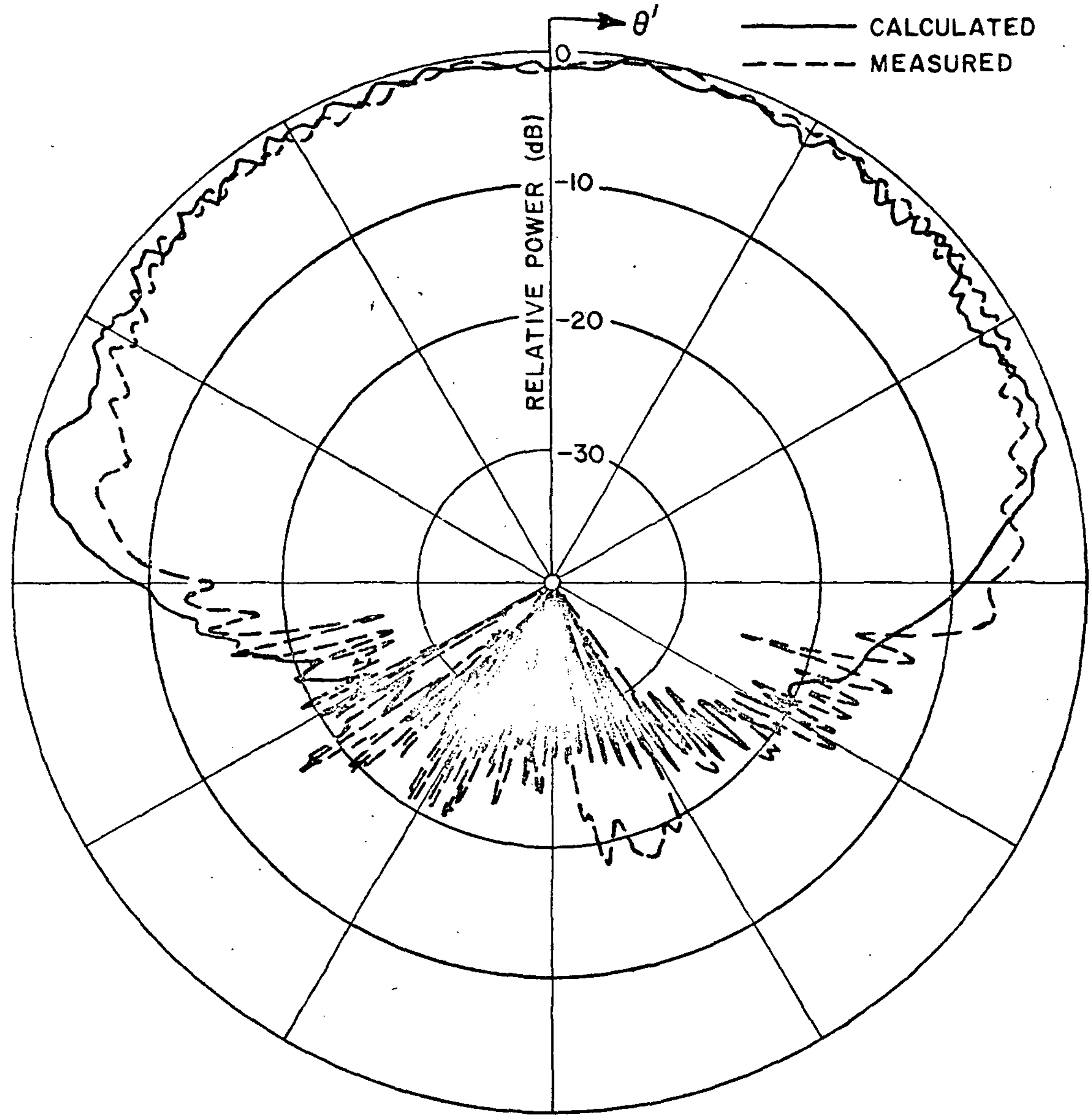

Figure 67a--Comparison of NASA's measured $E_{\theta'}$ results on a Boeing 737 model with the finite elliptic cylinder model results at $\phi' = 0$.

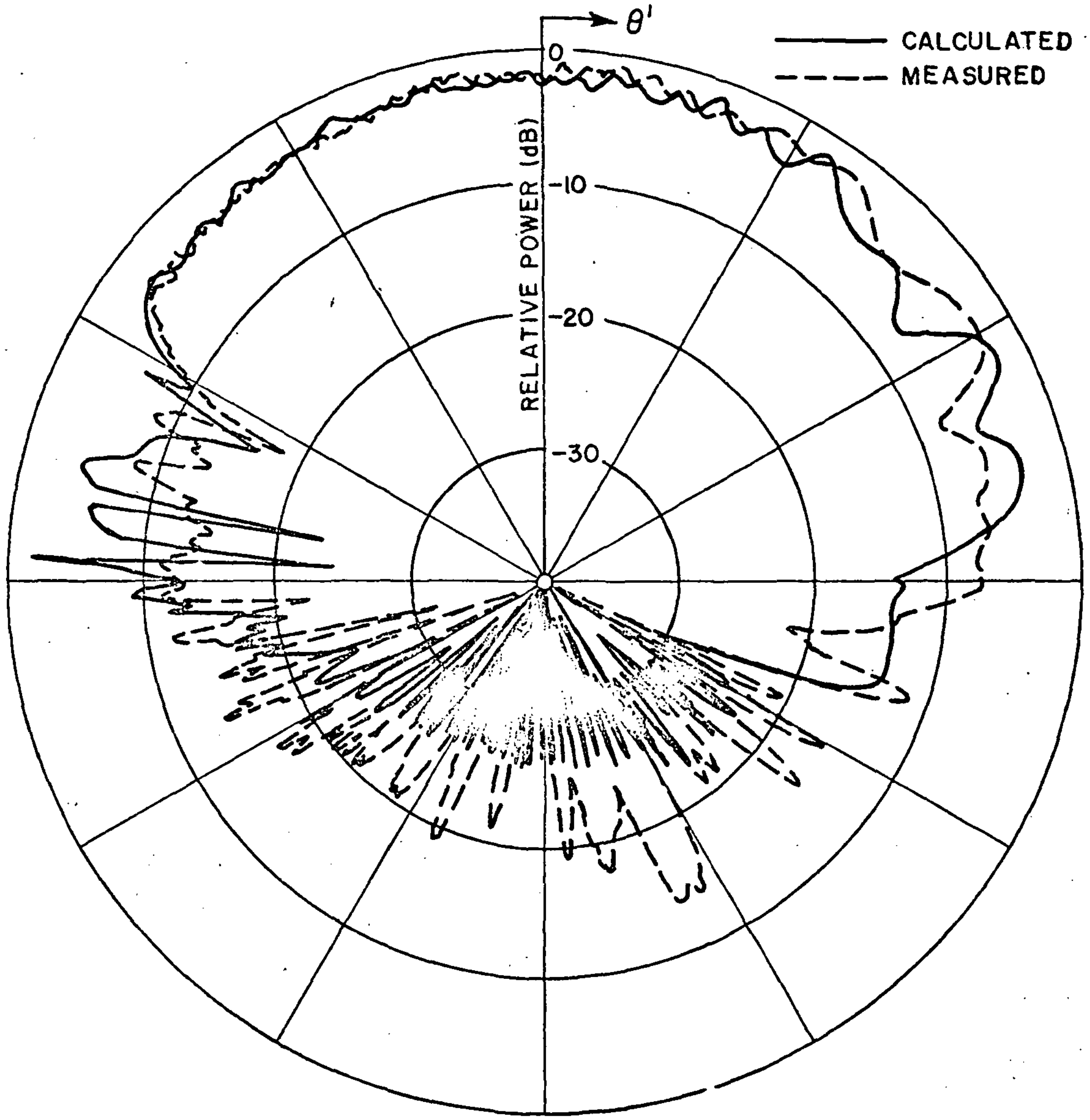

Figure 67b--Comparison of measured and calculated E_{θ}' results for $\phi' = 30°$.

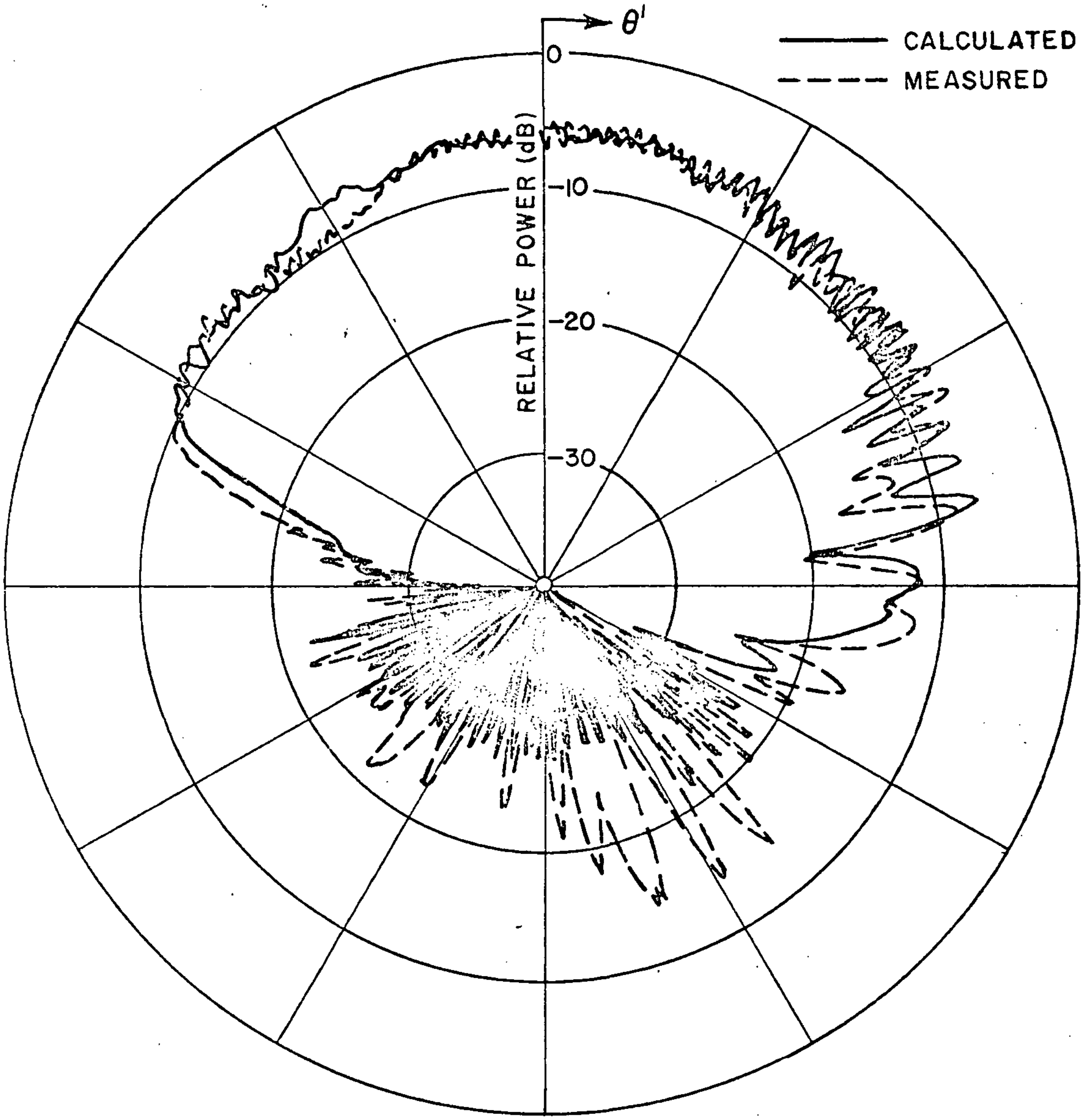

Figure 67c--Comparison of measured and calculated $E_{\theta'}$ results for $\phi' = 60°$.

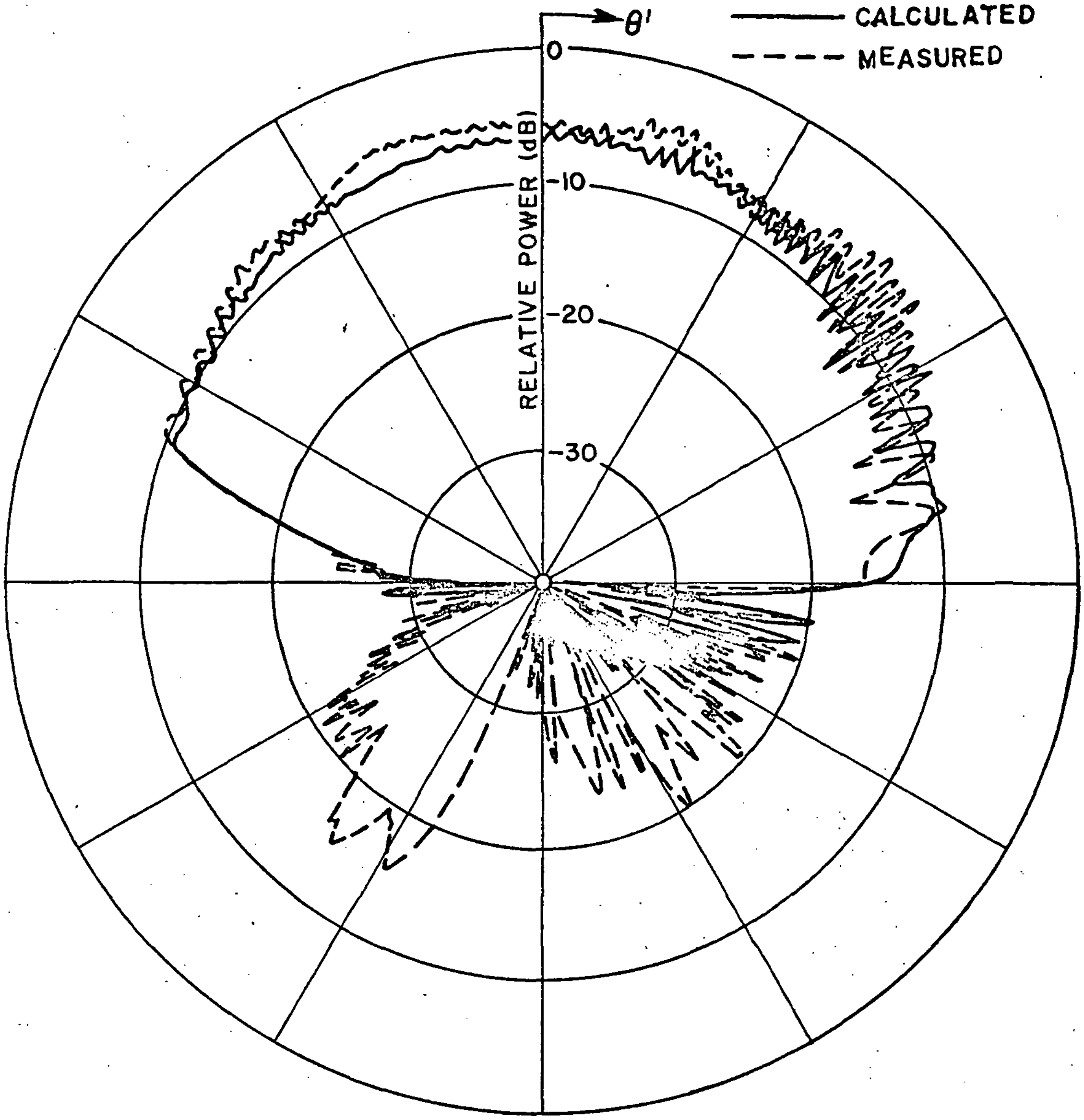

Figure 67d--Comparison of measured and calculated $E_{\theta'}$ results for ϕ' = 120°.

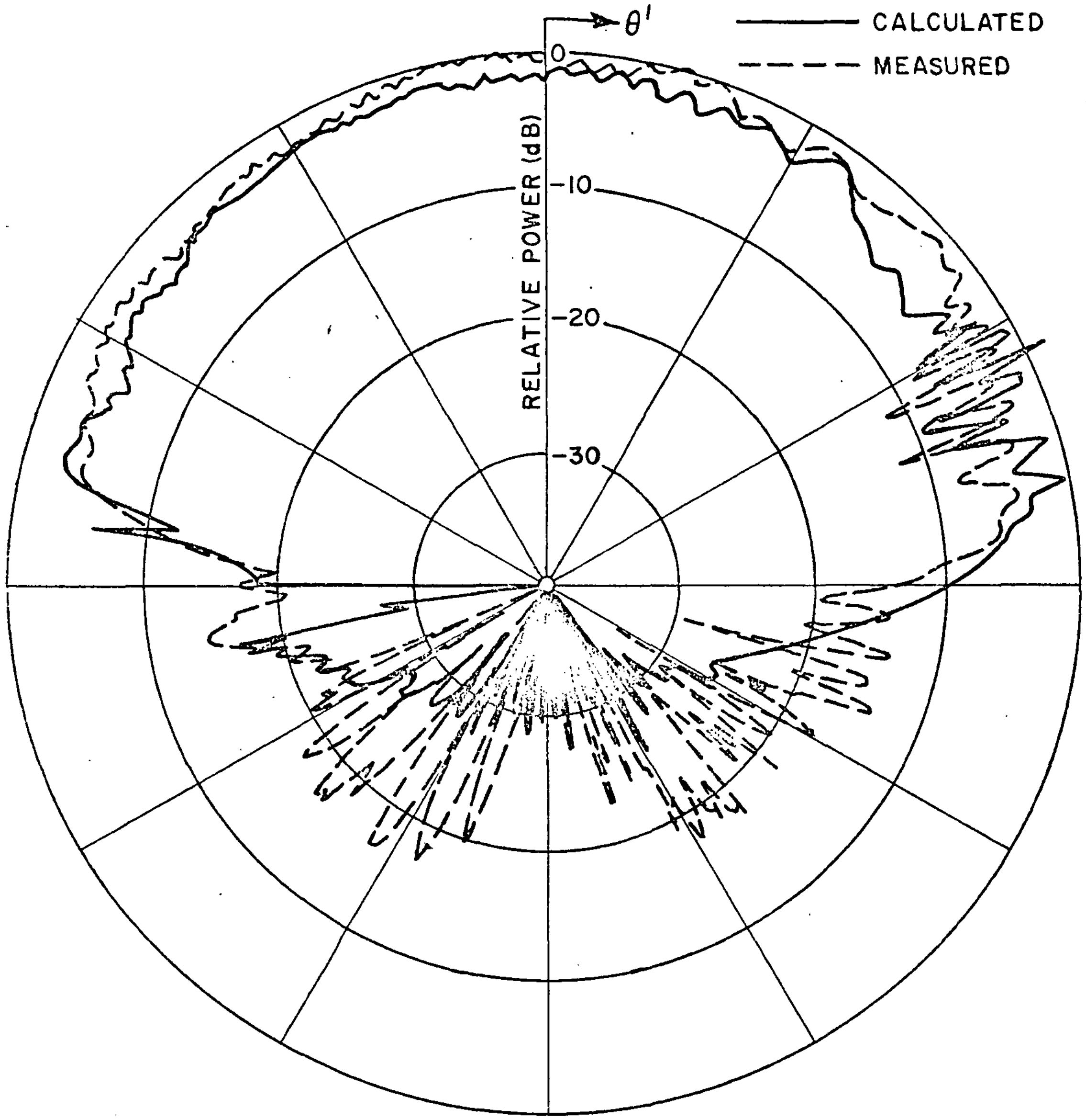

Figure 67e--Comparison of measured and calculated $E_{\theta'}$ results for $\phi' = 150°$.

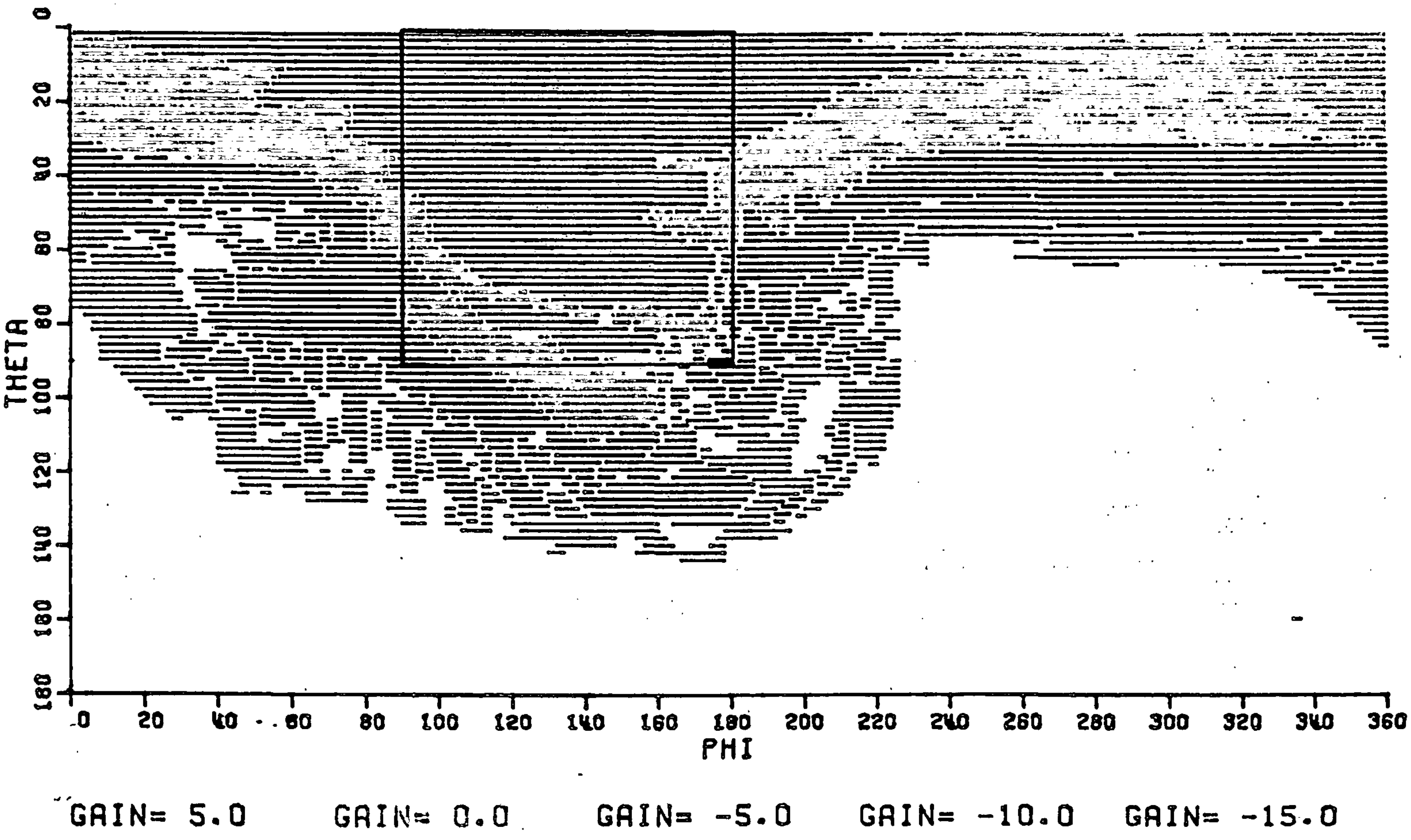

Figure 68. Volumetric directive gain results with various gain levels represented in different colors for optimum two element array design mounted on the wing of an F-4 model.

CHAPTER VI

SUMMARY AND CONCLUSIONS

The object of this research has been to analyze radiation patterns for aircraft wing mounted antennas. This is an analytical study of basic antenna types for frequencies above about 100 megahertz in which the antenna is mounted on or near a wing. The aircraft is modelled in its most basic form so that the study is applicable to general-type aircraft. The fuselage is modelled as a perfectly conducting finite elliptic cylinder. The wings and horizontal and vertical stabilizers are modelled as perfectly conducting "n" sided flat plates that can be arbitrarily attached to the fuselage or to themselves. Presently, the antenna locations are assumed to be on the upper surfaces of the wings or at locations removed from engines and stores such that these effects are negligible. The theory, however, is applicable to the addition of engine and store effects by modelling these structures as flat plates or small finite elliptic cylinders.

The basic approach applied in this study has been to separately analyze the basic scattering shapes making up the computer simulation model of an aircraft. The single structures are analyzed using the ray optics approach such that only the dominant effects are included. The scattered fields of the various component parts of the structure are found using the Geometrical Theory of Diffraction. The basic solutions needed for this study were briefly discussed in Chapter II. This includes the geometrical optics reflected fields from curved surfaces, the diffraction by a wedge and curved wedge, and the slope diffraction by a wedge using arbitrarily oriented dipole moment sources. A heuristic corner diffraction coefficient was, also, introduced. Curved surface diffraction was presented along with a newly developed transition function which describe the scattered field behavior around the shadow boundaries of curved surfaces.

The scattering from a number of finite flat was discussed in Chapter III. The plates can have an arbitrary orientation in space and can be attached to form bent plates. The present solution is restricted in that only first and second order terms are included except for double diffraction which is normally negligible. This solution is useful for antennas mounted near a flat plate, corner reflectors, and even a crude flat plate aircraft. These plates are used to model wings and horizontal and vertical stabilizers on the finite elliptic cylinder model of an aircraft. They can, also, be used to model other scattering objects such as buildings or ships with some modification.

The scattering from a finite elliptic cylinder was discussed in Chapter IV. The end caps of the cylinder can form an angle with the cylinder axis. The scattered fields are found using geomerical optics, the Geometrical Theory of Diffraction and a curved surface transition function. The validity of the solution was shown by comparing the results against exact and moment method solutions and experimental results. The finite elliptic cylinder is used to model the fuselage of an aircraft and can be used to model engines and stores. The solution can also be used to model other objects such as ship masts or hulls.

The combination of the above scattering objects to form a general-type aircraft model is discussed in Chapter V. Measured results for a simple aircraft-like model that resembles the finite elliptic cylinder model verified the approximations in the theoretical solutions. Measurements taken at NWC and NASA on actual aircraft models verified the usefulness of the finite elliptic cylinder model in predicting the radiation patterns for wing-mounted antennas.

In general, the results show that an antenna mounted on a wing can interact strongly with the fuselage and wings causing large amounts of ripple in the pattern. This suggests that proper element design especially directive antennas that do not illuminate the fuselage strongly, and proper placement of the antenna on the wings to minimize the interference problems are important considerations that must be taken into account when designing wing mounted antenna systems. The finite elliptic cylinder model should prove to be a very useful tool to an antenna designer in anticipating these problems in a very economical and efficient manner. The computer code used to generate a pattern for one antenna element typically takes only 30 seconds or less on an IBM 370 digital computer.

A brief discussion of a practical antenna design problem is presented to show the usefulness of the finite elliptic cylinder model. The model was used to optimize the design of a quadrant detection antenna mounted on the wing of an F-4 aircraft. A volumetric pattern of the predicted antenna systems performances illustrated how closely the antenna design can come to the ideal characteristics of a quadrant detection antenna.

The versatility of the present solution can be increased in many ways. The engine and store effects can be added to the aircraft model by using small finite elliptic cylinders or plates to represent these objects. The comparisons of model measurements with the finite elliptic cylinder have indicated that the nose and tail representation are not always adequate in some small angular regions. This could be improved by including equivalent currents to remove caustic effects and perhaps by alternative representations of the nose and tail. The solution can also be extended to allow the analysis of tail mounted antennas.

REFERENCES

[1] Carter, P. S., "Antenna Arrays Around Cylinders," Proc. IRE, Vol. 31, December 1943, pp. 671-693.

[2] Carter, P. S., "Antenna and Cylindrical Fuselage," Report No. 895-11, RCA Laboratories, Rocky Point, N.Y.; December 24, 1943.

[3] Sinclair, G., "The Patterns of Antennas Located Near Cylinders of Elliptical Cross Section," Proc. IRE, Vol. 39, No. 6, June 1951.

[4] Richmond, J. H., "A Wire-Grid Model for Scattering by Conducting Bodies," IEEE Trans. Antennas and Propagation, Vol. AP-14, pp. 782-786, November 1966.

[5] Richards, G. A., "A Boundary-Value Technique for Computing the Patterns of an Antenna Near a Conducting Body of Arbitrary Shape," Report 2235-2, 11 September 19767, The Ohio State University ElectroScience Laboratory, Department of Electrical Engineering; prepared under Contract N10019-67-C-0063 for Naval Air Systems Command.

[6] Richmond, J. R., "Computer Analysis of Three-Dimensional Wire Antennas," Report 2708-4, 22 December 1969, The Ohio State University ElectroScience Laboratory, Department of Electrical Engineering; prepared under Contract DAAD 05-69-C-0031 for Ballistic Research Laboratory.

[7] Wang, N. N., Richmond, J. H., and Gilreath, M. C., "Sinusoidal Reaction Formulation for Radiation and Scattering from Conducting Surfaces," IEEE Trans. on Antennas and Propagation, Vol. AP-23, No. 3 (May 1975), pp. 376-382.

[8] Ryan, C. E., Jr., and Rudduck, R. C., "Calculation of the Radiation Pattern of a General Parallel-Plate Waveguide Aperture for the TEM and TE_{01} Waveguide Modes," Report 1693-4, 10 September 1964, The Ohio State University ElectroScience Laboratory, Department of Electrical Engineering; prepared under Contract N62269-2183 for U. S. Naval Air Development Center, Johnsville, Pennsylvania.

[9] Ryan, C. E., Jr., and Rudduck, R. C., "A Wedge Diffraction Analysis of the Radiation Patterns of Parallel-Plate Waveguides," IEEE Trans. on Antennas and Propagation Comm., Vol. AP-16, No. 4, July 1968.

[10] Wu, D. C. F., Rudduck, R.C., and Pelton, E. L., "Application of a Surface Integration Technique to Parallel-Plate Waveguide Radiation Pattern Analysis," IEEE Trans. Antennas and Propagation, Vol. AP-17 (May 1969), pp. 280-285.

[11] Burnside, W. D. and Pelton, E. L., "Wedge Diffraction Theory Analysis of Parallel-Plate Waveguide Arrays," Report 2382-14, 25 September 1969, The Ohio State University ElectroScience Laboratory, Department of Electrical Engineering; prepared under Contract F33615-67-C-1507 for the Air Force Avionics Laboratory at Wright-Patterson Air Force Base, Ohio. (AFAL-TR-69-240)(AD 860082)

[12] Burnside, W. D., Pelton, E. L., and Peters, L., Jr., "Analysis of Finite Parallel-Plate Waveguide Arrays," to be published as a Communication in IEEE Trans. on Antennas and Propagation.

[13] Yu, J. S., Rudduck, R. C., and Peters, L., Jr., "Comprehensive Analysis for E-Plane of Horn Antennas for Edge Diffraction Theory," IEEE Trans. on Antennas and Propagation, Vol. AP-14, (March 1966) pp. 138-149.

[14] Yu, J. S., and Rudduck, R. C., "H-Plane Pattern of a Pyramidal Horn," IEEE Trans. on Antennas and Propagation Comm., Vol. AP-17, No. 5, September 1969.

[15] Ratnasiri, P. A. J., Kouyoumjian, R. G., and Pathak, P. H., "The Wide Angle Side Lobes of Reflector Antennas," Report 2183-1, 23 March 1970, The Ohio State University ElectroScience Laboratory, Department of Electrical Engineering; prepared under Contract AF 19(628)-5929 for Air Force Cambridge Research Laboratories.

[16] Mentzer, C. A., Pathak, P. H., and Peters, L., Jr., "Pattern Analysis of an Offset Fed Parabolic Reflector Antennas," Report 3220-2, June 1972, The Ohio State University ElectroScience Laboratory, Department of Electrical Engineering; prepared under Contract N00178-71-C-0264 for U. S. Naval Weapons Laboratory.

[17] Ryan, C. E., Jr., and Rudduck, R. C., "Radiation Patterns of Rectangular Waveguides," IEEE Trans. on Antennas and Propagation Comm., Vol. AP-16 (July 1968), pp. 488-489.

[18] Balanis, C. A., and Peters, L., Jr., "Analysis of Aperture Radiation from an Axially Slotted Circular Conducting Cylinder Using Geometrical Theory of Diffraction," IEEE T-AP-17, January 1969, pp. 93097.

[19] Balanis, C. A., and Peters, L., Jr., "Aperture Radiation from an Axially Slotted Elliptical Conducting Cylinder Using Geometrical Theory of Diffraction," IEEE T-AP-17, July 1969, pp. 507-513.

[20] Balanis, C. A., and Peters, L., Jr., "Radiation from TE_{10} Mode Slots on Circular and Elliptical Cylinders," IEEE T-AP-18, No. 3, May 1970, pp. 400-403.

[21] Ryan, C. E., Jr., "Analysis of Radiation Patterns of Antennas on Finite Circular Cylinders and Conically-Capped Cylinders," Report 2805-2, 25 September 1970, The Ohio State University ElectroScience Laboratory, Department of Electrical Engineering; preapred under Contract DAA21-69-C-0535 for Picatinny Arsenal. (AD 875581L)

[22] Burnside, W. D., Gilreath, M. C., Marhefka, R. J., and Yu, C. L., "A Study of KC-135 Aircraft Antenna Patterns," IEEE Trans. on Antennas and Propagation, Vol. AP-23, No. 3, May 1975, pp. 309-16.

[23] Burnside, W. D., "Analysis of On-Aircraft Antenna Patterns," Report 3390-1, August 1972, The Ohio State University ElectroScience Laboratory, Department of Electrical Engineering; prepared under Contract N62269-72-C-0354 for Naval Air Development Center. (AD 777 989)

[24] Yu, C. L., and Burnside, W. D., "Volumetric Pattern Analysis of Fuselage Mounted Airborne Antennas," Report 2902-24, April 1976, The Ohio State University ElectroScience Laboratory, Department of Electrical Engineering; prepared under Grant NGL 36-003-138 for National Aeronautics and Space Administration, Langley Research Center.

[25] Marhefka, R. J., "Roll Plane Analysis of On-Aircraft Antennas," Report 3188-1, December 1971, The Ohio State University ElectroScience Laboratory, Department of Electrical Engineering; prepared under Contract N62269-71-C-0296 for Naval Air Development Center.

[26] Yu, C. L., and Burnside, W. D., "Elevation Plane Analysis of On-Aircraft Antennas," Report 3188-2, January 1972, The Ohio State University ElectroScience Laboratory, Department of Electrical Engineering; prepared under Contract N62269-71-C-0296 for Naval Air Development Center.

[27] Burnside, W. D., Marhefka, R. J., and Yu, C. L., "Roll Plane Analysis of On-Aircraft Antennas," IEEE Trans. on Antennas and Propagation, Vol. AP-21, November 1973, pp. 780-786.

[28] Marhefka, R. J., and Burnside, W. D., "Numerical Solutions to Some On-Aircraft Antenna Pattern Problems," Technical Report 3390-4, October 1973, Department of Electrical Engineering; prepared under Contract N62269-72-C-0354 for Naval Air Development Center. (AD 777977)

[29] Yu, C. L., and Burnside, W. D., "MLS Airborne Antenna Research," Semi-Annual Report 2902-22, May 1975, The Ohio State University ElectroScience Laboratory, Department of Electrical Engineering; prepared under Grant NGL 36-003-138 for National Aeronautics and Space Administration, Langley Research Center. (NASA-CR-145398) (N 76-10378)

[30] Yu, C. L., and Burnside, W. D., "Research on MLS Airborne Antenna," Semi-Annual Report 2902-23, April 1976, The Ohio State University ElectroScience Laboratory, Department of Electrical Engineering; prepared under Grant NGL 36-003-138 for National Aeronautics and Space Administration, Langley Research Center.

[31] Marhefka, R. J., and Burnside, W. D., "Vertically Polarized IFF Antennas Mounted on the Leading Edge of Wings," Report 2836-2, August 1970, The Ohio State University ElectroScience Laboratory, Department of Electrical Engineering; prepared under Contract N62269-69-C-0533 for Naval Air Development Center.

[32] Yu, C. L., "Wedge Diffraction Analysis of Antennas of Simulated Wing Models," Report 2836-3, September 1970, The Ohio State University ElectroScience Laboratory, Department of Electrical Engineering; prepared under Contract N62269-69-C-0533 for Naval Air Development Center.

[33] Marhefka, R. J. and Burnside, W. D., "Pattern Optimization of Wing-Mounted Array Antennas at UHF," Report 3884-1, January 1976, The Ohio State University ElectroScience Laboratory, Department of Electrical Engineering; prepared under Contract N00163-74-C-1580 for Naval Regional Procurement Office, Long Beach, California.

[34] Kouyoumjian, R. G., and Pathak, P,, "A Uniform Geometrical Theory of Diffraction for an Edge of a Perfectly Conducting Surface," Proc. of the IEEE, Vol. 62, No. 11, November, 1974, pp. 1448-1461.

[35] Deschamps, G., "Ray Techniques in Electromagnetics," Proc. IEEE, Vol. 60, pp. 1022-1035, September 1972.

[36] Sommerfeld, A., Optics, Academic Press, Inc., New York, 1954, pp. 245-265.

[37] Keller, J. B., "Geometrical Theory of Diffraction," Jour. Optical Soc. Amer., 52 (February 1962), pp. 116-130.

[38] Rudduck, R. C., "Application of Wedge Diffraction to Antenna Theory," Report 1691-13, 30 June 1965, The Ohio State University ElectroScience Laboratory, Department of Electrical Engineering; prepared under Grant NSF-338 for National Aeronautics and Space Administration, Washington, D. C. Also published as NASA Report CR-372.

[39] Pauli, W., "An Asymptotic Series for Functions in the Theory of Diffraction of Light," Phys. Rev., 54 (1 December 1938), pp. 924-931.

[40] Hutchins, D. L., and Kouyoumjian, R. G., "A New Asymptotic Solution to the Diffraction by a Wedge," URSI 1967 Spring Meeting, Ottawa, Canada, pp. 154-155.

[41] Hutchins, D. L., "Asymptotic Series Describing the Diffraction of a Plane Wave by a Two-Dimensional Wedge of Arbitrary Angle," Ph.D. Dissertation, The Ohio State University, Department of Electrical Engineering, 1967.

[42] Pathak, P. H., and Kouyoumjian, R. G., "The Dyadic Diffraction Coefficient for a Perfectly Conducting Wedge," Scientific Report No. 5, Report 2183-4, 5 June 1970, The Ohio State University ElectroScience Laboratory, Department of Electrical Engineering; prepared under Contract AF19(628)-5929 for Air Force Cambridge Research Laboratories. (AFCRL-69-0546) (AD 707821)

[43] Rudduck, R. C. and Wu, D. C. F., "Slope Diffraction Analysis of TEM Parallel-Plate Guide Radiation Patterns," IEEE Trans. Antennas Propagat. (Commun.), Vol. AP-17, pp. 797-799, November 1969.

[44] Karp, S. N. and Keller, J. B.: Optica Acta 8, 61 (1961).

[45] Mentzer, C. A., Peters, L., Jr., and Rudduck, R. C., "Slope Diffraction and Its Application to Horns," IEEE Trans. Antennas Propagat., Vol. AP-23, No. 2, pp. 153-158, March 1975.

[46] Hwang, Y. M. and Kouyoumjian, R. G., "A Dyadic Diffraction Coefficient for an Electromagnetic Wave Which is Rapidly Varying at an Edge," USNC-URSI 1974 Annual Meeting, Boulder, Colorado, October 1974.

[47] Hwang, Y. M. and Kouyoumjian, R. G., "On the Dyadic Slope Diffraction Coefficient," USNC-URSI Meeting, Urbana, Illinois, June 1975.

[48] Walter, C. H., Traveling Wave Antennas, Dover Publications, Inc., New York, 1970, pp. 15-16.

[49] Satterwhite, R., "Diffraction by a Quarter Plane, the Exact Solution, and Some Numerical Results," IEEE Trans. Antenna and Propagation, Vol. AP-22, No. 3, pp. 500-502, May 1974.

[50] Burnside, W. D., personal communications.

[51] Keller, J. B., "Diffraction by a Convex Cylinder," Trans. IRE, Vol. AP-24, 1956, pp, 312-321.

[52] Franz, W., and Depperman, K., "Theorie der Baugang Am Zylinder unter Berucksichtigung der Kreichwelle," Am. Physik, Vol. 10, June 1952, pp. 361-373.

[53] Franz, W., and Depperman, K., "Theorie der Beugang der Kugel unter Berucksichtigung der Kreighwelle," Ann. Physik, Vol. 14, June 1954, pp. 253-264.

[54] Kouyoumjian, R. G., "Asymptotic High-Frequency Methods," Proc. of the IEEE, Vol. 53, No. 8, August 1965, pp. 864-876.

[55] Kouyoumjian, R. G., "The Geometrical Theory of Diffraction and Its Applications," Numerical and Asymptotic Techniques in Electromagnetics, edited by R. Mittra, Spring-Verlag, New York, 1975.

[56] Voltmer, D., "Diffraction by Doubly Curved Convex Surfaces," Ph.D. Dissertation, The Ohio State University, 1970.

[57] Hong, S., J. Math. Phys. 8, 1223 (1967).

[58] Levy, B. R. and Keller, J. B., "Diffraction by a Smooth Object," Institute of Mathematical Sciences, New York University, published under Contract No. AF 19(604)-1717; December 1957. Also in Comm. Pure Appl. Math., 12, 1959, pp. 159-209.

[59] Logan, N. A., "General Research in Diffraction Theory," Vol. I, LMSD-288087; and Vol. II, LMSD-288088, Missiles and Space Division, Lockheed Aircraft Corp., December 1959.

[60] Borovikov, A. A., and Kinber, B. Y., Proc. IEEE, Vol. 62, No. 11, November 1974, pp. 1416-1437.

[61] Fock, V. A., Diffraction, Refraction, and Reflection Waves: Thirteen Papers, Air Force Cambridge Research Center Report AFCRC-TN-57-102, June 1975 (AD 117276).

[62] Pathak, P. H., and Burnside, W. D., "A Uniform Asymptotic Result for the Scattering of Plane Waves by a Circular Cylinder," Report 3973-1, March 1976, The Ohio State University ElectroScience Laboratory, Department of Electrical Engineering; prepared under Contract N62269-74-C-0788 for Naval Air Development Center.

[63] Pathak, P. H., and Burnside, W. D., "A Uniform Asymptotic Result for the Scattering by Smooth, Convex Surfaces," in preparation.

[64] Pathak, P. H., "On-Aircraft Antennas," Report 3973-2, January 1976, The Ohio State University ElectroScience Laboratory, Department of Electrical Engineering; prepared under Contract N62269-74-C-0788 for Naval Air Development Center.

[65] Greer, E., personal communications.

[66] Lipschutz, M. M., Theory and Problems of Differential Geometry, Schaum's Outline Series, McGraw-Hill, New York, 1969, pg. 196.